UNIVERSITY OF SOUTHAMPTON

FACULTY OF ENGINEERING, SCIENCE AND MATHEMATICS

School of Civil Engineering and the Environment

Air Entrainment, Splash and Energy Dissipation in Breaking Waves

by

Christopher Edwin Blenkinsopp

Thesis for the degree of Doctor of Philosophy

January 2007

UNIVERSITY OF SOUTHAMPTON

ABSTRACT

FACULTY OF ENGINEERING, SCIENCE & MATHEMATICS
SCHOOL OF CIVIL ENGINEERING AND THE ENVIRONMENT

Doctor of Philosophy

AIR ENTRAINMENT, SPLASH AND ENERGY DISSIPATION IN BREAKING WAVES

by Christopher Edwin Blenkinsopp

Wave breaking is a complex natural phenomenon that has significant influence on many oceanic processes. The action of wave breaking leads to the entrainment of large quantities of air at the ocean surface which contributes to energy dissipation during breaking and enhances rates of air-sea gas transfer. A detailed knowledge of the distribution of air entrained by breaking waves would contribute to a better understanding of the wave breaking process and its effect on these physical processes, but largely due to practical difficulties existing information is limited.

This thesis presents detailed laboratory measurements of the time-varying distribution of void fractions and bubble sizes within the dense bubble plumes generated immediately beneath breaking waves in a 2D laboratory wave flume. The measurements were made using a novel optical fibre probe technique, which was shown to perform well under violent, aerated flow conditions and produced results to a resolution not achieved by previous studies. In addition, the technique allowed the distribution of water droplets within the splash generated by breaking waves to be measured, to this author's knowledge for the first time.

The results obtained from these experiments demonstrated that the properties of the two-phase flow generated by breaking waves evolve rapidly as simple functions of time and behave in a similar manner for all of the breaker types under examination. The measurements indicated that the energy expended in entraining air accounted for a minimum of 4% to 9% of the total energy dissipated during breaking, and that the contribution of the air entrainment mechanism was greater as the breaker type changed from spilling to plunging. In addition, it was estimated that the generation of splash contributes between 2.5% to 5% of the total dissipation.

Additional measurements in artificial and natural seawater demonstrated that entrained bubble plumes evolve in an almost identical manner to those in freshwater, although small differences were observed in the distribution of bubble sizes. This is a significant result as the vast majority of laboratory studies are completed using freshwater and these measurements confirm the general applicability of freshwater model studies of violent, air entraining flows in many situations. To further assess the applicability of laboratory measurements of aerating flows to field conditions, an analysis of the effect of scale was completed using a Lagrangian bubble tracking model and it was shown that the post breaking evolution of entrained bubble plumes is subject to significant scale effects.

TABLE OF CONTENTS

LIST OF FIGURES

LIST OF TABLES

ACKNOWLEDGEMENTS

The work presented in this thesis would not have been possible without the support of a number of people. I would therefore like to take to the opportunity to express my gratitude to the following people who have assisted me during the course of my PhD.

Professor John Chaplin for his excellent guidance, encouragement and most of all patience during this research project.

Dr Gerald Müller for his advice and numerous interesting discussions.

Dr Kerry Black, Dr Shaw Mead and the ASR guys for their support and advice.

Dr David Woolf for his advice on bubble tracking models.

Dr Gilberto Brambilla and Michael Röelens who produced the optical fibre phase detection probes, without which this study would have been impossible.

Dr Dave Smallman and Dr Ana Simoes for their assistance in obtaining artificial seawater and the analysis of the natural seawater sample.

The laboratory staff, Harvey Skinner, Mike Rowe, Martin Colvill, Earl Peters, Ken Yeates and Dave Lynnock for practical assistance with my experiments.

All of my friends who helped me to make the most of my time in Southampton, particularly my girlfriend Meera, my housemates and the guys I went surfing with (SCHM) to keep me sane.

My family who have given me amazing support through all stages of my life and education, and for putting up with me during the writing of this document.

EPSRC and the School of Civil Engineering and the Environment for their financial support.

LIST OF NOTATION

Notation	Description
a_i	Incident wave amplitude (m)
a_r	Reflected wave amplitude (m)
A	Wave amplitude (m)
A_b	Cross-sectional area of the bubble plume (m^2)
A_s	Cross-sectional area of the splash-up (m^2)
A_v	Vortex area (m^2)
b	Intercept of interface velocity calibration curve
B	Breaking coefficient
c	Phase speed (ms^{-1})
c_b	Phase speed at breaking (ms^{-1})
c_o	Phase speed of the dominant waves (ms^{-1})
C	Aqueous concentration (mol m^{-3})
C_g	Group velocity (ms^{-1})
d	Bubble diameter
d_m	Mean bubble diameter (mm)
d_{po}	Cavity pinch off depth (m)
dx	Horizontal measurement interval
dz	Vertical measurement interval
D	Diffusion coefficient (m^2s^{-1})
D_{n50}	Nominal armourstone diameter (m)
DV	Voltage difference between liquid and air voltage levels (V)
E	Wave energy per unit surface area (Jm^{-2})
E_b	Energy dissipation due to breaking (Jm^{-2})
E_i	Incident wave energy (Jm^{-2})
E_p	Potential energy of the bubble plume (J)
E_r	Reflected wave energy (Jm^{-2})
E_s	Potential energy of the splash-up (J)
E_t	Transmitted wave energy (Jm^{-2})
f	Wave frequency (Hz)
F	Gas flux (mol $m^{-2}s^{-1}$)
g	Acceleration due to gravity (ms^{-2})
h	Water depth (m); Height of water column (m); Parzen window width
Dh	Hold-up (m)
h_b	Water depth at breaking (m)
h_c	Water depth above reef crest (m)
H	Wave height (m); Henry's law constant
H_b	Breaking wave height (m)
H_i	Incident wave height (m)
H_o	Deepwater wave height (m)
H_s	Significant wave height (m)
H_t	Transmitted wave height (m)

Notation	Description
i	Horizontal position of the measurement point
j	Vertical position of the measurement point
$j_{50\%}$	Vertical position of the 50% void fraction contour
k	Wave number
k_L	Gas transfer velocity (ms^{-1})
K_r	Reflection coefficient
K_t	Wave height transmission coefficient
K_v	Turbulent diffusion coefficient (cm^2s^{-1})
l_b	Chord length (mm)
l_v	Vortex length (m)
L	Wavelength (m); Latency length (m)
L^*	Critical latency Length (m)
L_b	Turbulence lengthscale (m)
L_o	Deepwater wavelength (m)
m	Beach gradient; Slope of interface-velocity calibration curve
m^*	Orthogonal beach gradient
n	Phase average bin identifier; Bubble sample size; Refractive index
N	Number of moles of gas within a bubble
N_T	Total number of bubbles detected
P	Pressure (Nm^{-2})
P_A	Atmospheric pressure (Nm^{-2})
P_B	Pressure of gas within a bubble (Nm^{-2})
Q	Volume discharge per unit area across the bore (ms^{-1})
r	Bubble radius (mm)
r_H	Bubble radius at Hinze scale (mm)
R	Molar gas constant
R^2	Calibration coefficient
R_c	Relative reef crest height (m)
Re	Reynolds number
s	Phase indicator function
s_{ps}	Dual probe separation (m)
S	Scale factor
t	Time (seconds)
t_a	Air phase residence time (seconds)
t_A	Time at characteristic point A
t_b	Time at breaking
t_B	Time at characteristic point B
t_C	Time at characteristic point C
t_D	Time at characteristic point D
t_{fall}	Time for a water droplet to fall a distance Hb (seconds)
Dt_i	Time difference between bubble arrival times (seconds)
t_p	Time of bubble plume arrival at a probe
t_{po}	Cavity pinch off time (seconds)
t_{p0}	Time of maximum bubble penetration

Notation	Description
t_r	Optical probe signal rise time (seconds)
t_{rise}	Time for a bubble to rise a distance H_b (seconds)
T	Wave period (seconds); Temperature (°K)
T_t	Total sampling duration (seconds)
u^*	Air friction velocity (ms^{-1})
u_r	Bubble rise velocity (ms^{-1})
U_{10}	Wind speed at 10 m elevation (ms^{-1})
v_b	Differential velocity between a bubble and surrounding fluid (ms^{-1})
v_c	Critical jet velocity (ms^{-1})
v_i	Air-water interface velocity (ms^{-1})
v_j	Jet velocity (ms^{-1})
v_t	Jet translation speed (ms^{-1})
V_a	Volume of air (m^3)
V_A	Voltage level for characteristic point A (V)
V_{ap}	Total volume of the bubbles detected by a probe in time t (m^3)
V_b	Volume per unit width of entrained air in a bubble plume (m^2)
V_B	Voltage level for characteristic point B (V); Bubble volume (m^3)
V_C	Voltage level for characteristic point C (V)
V_D	Voltage level for characteristic point D (V)
V_G	Static air voltage level (V)
V_L	Static liquid voltage level (V)
V_s	Splash volume per unit width (m^2)
V_T	Total volume of fluid (m^3)
V_v	Vortex volume per unit width (m^2)
w	Number of waves measured
w_v	Vortex width (m)
x	Horizontal position
x_p	Horizontal position of the bubble plume centroid
x_s	Horizontal position of the splash centroid
z	Vertical position
$z_{0.5\%}$	Depth of the 0.5% void fraction contour below MWL (m)
$z_{1\%}$	Depth of the 1% void fraction contour below MWL (m)
$z_{50\%}$	Vertical distance from the measurement position to the 50% void fraction contour (m)
$z_{99\%}$	Height of the 99% void fraction contour above MWL
$z_{99.5\%}$	Height of the 99.5% void fraction contour above MWL
z_{max}	Maximum bubble penetration depth (m)
z_p	Vertical position of the bubble plume centroid
z_s	Vertical position of the splash centroid
α	Void fraction
$\bar{\alpha}$	Mean void fraction over a single wave period
α_g	Reference void fraction
α_m	Mean void fraction at a point during the time that the probe falls within the bubble plume

Notation	Description
α_p	Mean void fraction within a bubble plume
β	Wave age; Angle between the optical probe axis and the normal to the air-water interface (deg)
δ	Energy dissipation rate per unit surface area ($Jm^{-2}s^{-1}$); Phase difference
ε_l	Energy dissipation rate per unit crest length ($Jm^{-1}s^{-1}$)
Φ	Wave phase angle (deg)
Φ_1	Exponent of the power law scaling for the small bubble part of the bubble size spectrum
Φ_2	Exponent of the power law scaling for the large bubble part of the bubble size spectrum
γ	Direction of the bubble centre of mass (deg)
γ_b	Breaker depth index
λ	Bubble shape factor
λ_n	Distance between wave gauges (m)
η	Free surface elevation (m)
ρ_g	Gas density (kgm^{-3})
ρ_w	Density of water (kgm^{-3})
σ	Surface tension (Nm^{-1}); Standard deviation
θ	Angle between wave advance and normal to seabed contours (deg); Angle in inclination of breaking region (deg); Turbulence direction (deg)
ν_w	Kinematic viscosity of water (m^2s^{-1})
ν_g	Kinematic viscosity of gas (m^2s^{-1})
Ω_b	Breaker height index
ξ_o	Surf similarity parameter

CHAPTER 1 – INTRODUCTION

1.1 MOTIVATION

Wave breaking is a spectacular phenomenon that has long been a subject of fascination and importance within both the scientific and non-scientific communities. While the study of surface waves has a long tradition, current theory is unable fully to describe them as they become steep and overturn at breaking owing to the complex nature of the process. Consequently, a large amount of research using theoretical, numerical and experimental techniques continues to be conducted in order to gain a better understanding of the fundamental problem of wave breaking. Such studies are of great importance as breaking waves influence many ocean processes.

Wave breaking is the primary mechanism by which wave energy is dissipated in both shallow and deep water. Consequently it is responsible for limiting the height of surface waves in the ocean and is a primary driving force in many coastal processes. Observations of waves breaking at the coast and in high sea states offshore demonstrate that the process is associated with large quantities of turbulence, noise, air entrainment and splash, all of which contribute to the energy dissipated during the breaking event. While all of these factors are significant to the energy dissipation rate, we do not fully understand the details of each mechanism or their relative contributions to the total dissipation and so no comprehensive model of energy dissipation during breaking is currently available.

The breaking of surface waves is the primary source of air entrainment at the ocean surface. Many studies designed to investigate bubble entrainment have been completed as it is an obvious feature of wave breaking on almost all scales and has a considerable effect on many environmental processes. The presence of entrained air in the ocean can affect wave forces on coastal structures, produce marine aerosols, transfer energy to long waves in shallow water and enhance rates of air-sea gas transfer.

Of all of these processes, arguably the one that attracts the most attention is air-sea gas exchange due to current concern over the levels of atmospheric greenhouse gases,

particularly CO_2, which have a direct influence on the climate. It has been estimated that the oceans absorb between 18% and 40% of CO_2 emissions caused by human activities. Therefore in order to accurately predict the quantity of CO_2 and other anthropogenic gases in the atmosphere and their effect on the climate it is necessary to account for the transfer of gases across the air-sea boundary. A number of models have been developed in order to understand the ocean-atmosphere gas exchange across an unbroken surface during calms seas with low wind speeds (U<5 ms^{-1}). At higher wind speeds (U>10 ms^{-1}), a significant increase in the transfer velocity is observed which coincides with the onset of wave breaking and associated turbulence and bubble entrainment. This observed rise in the transfer velocity occurs due to the huge increase in the effective air-sea interface area available for exchange caused by the presence of air bubbles in the water and the pressurisation of bubbles at depth. Current models of bubble-mediated gas transfer generally use quasi-steady bubble population data obtained predominantly from acoustic measurements of oceanic bubble populations. However, this data generally represents the ambient bubble populations in the ocean, rather than the transient bubble plumes found in the immediate proximity of breaking waves. Immediately after breaking, a significant proportion of the entrained air volume is contained within larger bubbles (d>2 mm) which are generally broken up or rise to the surface within relatively short timescales of order one second, but can transfer their content of highly soluble gases such as CO_2 in a period comparable to this short residence time. Consequently, knowledge of these large transient bubble populations is essential if accurate estimates of oceanic gas transfer rates are to be made, but very little reliable data currently exists due to the difficulties involved in making suitable measurements. Detailed information about the two-phase flow in the region of breaking waves would also represent a major contribution towards a complete understanding of the process of wave breaking.

The goal of the current work was to investigate some fundamental aspects of wave breaking and provide high quality data that is essential to enable a better understanding of the process, but where existing information is currently lacking. The results are applicable to many different fields and across a range of scales, from providing a better understanding of the small scale flow properties of breaking waves through to global scale climate models.

The majority of the work presented in this study concentrates on air entrainment and the evolution of the dense bubble plumes generated by breaking waves. A series of novel measurements of the time-varying distribution of air below, and splash above the free surface in the region of breaking waves in both fresh and seawater are presented. In addition, the study describes measurements of the energy dissipated by waves breaking over a submerged reef structure and assesses the contribution of the air entrainment and splash mechanisms to the total energy dissipation.

1.2 OUTLINE OF THE THESIS STRUCTURE

The work presented in the current thesis is divided into eight chapters, the contents of which are briefly summarised below. A more detailed description of the structure of the thesis is presented in section 2.6.

Chapter 2 presents a review of the existing literature relating to wave breaking characteristics, air entrainment by violent free surface flows, splash generation by breaking waves and energy dissipation during wave breaking.

A description of the equipment used for the experiments described in chapters 4, 5, 6 and 7 is presented in chapter 3. The chapter provides a detailed description of the optical fibre phase detection probes and their use, as well as summarising a series of calibration exercises that were completed to ensure the accuracy of the techniques employed for the current work.

Chapter 4 outlines a series of experiments designed to examine the characteristics of waves breaking over a submerged reef. The work focuses on the energy dissipated during wave breaking and investigates how this value varies with the wave breaking intensity and amount of air entrainment.

Detailed measurements of the time-varying void fraction field, both above and below the free surface in the region of freshwater breaking waves made using optical fibre phase detection probes are presented in chapter 5. By taking moments of the void fraction field about the free surface, it is shown that the characteristics of the bubble

plumes and splashes generated by breaking waves are similar for varying breaker types and evolve as simple functions of time.

Optical fibre probe measurements of the bubble size distribution in the dense bubble plumes generated by freshwater breaking waves are presented in chapter 6. It is shown that optical fibre probes can be used to make reasonable estimates of bubble size in the violent aerated flow beneath breaking waves and that the measured bubble sizes vary with time and distance from the initial breaking event.

A series of measurements of the time-varying void fraction field within the bubble plumes generated in natural and artificial seawater are discussed in chapter 7 and are compared with the freshwater results presented in chapter 5. These measurements demonstrate that the air entrainment process and subsequent behaviour of the bubble plume is very similar in fresh and seawater and the implications of this result to physical model studies of breaking waves are discussed. In addition, the issue of scaling laboratory measurements of air entrainment processes to full scale is examined in detail.

The conclusions made on the basis of the research presented in chapters 2-7 are discussed in chapter 8 along with suggestions for future work.

CHAPTER 2 – LITERATURE REVIEW

2.1 INTRODUCTION

Wave breaking in the ocean is a common sight and influences many important physical processes. As such there exists a considerable body of research which examines many aspects of the wave breaking process in both shallow and deep water, including:

- post-breaking bores (for example Dally *et al.*, 1985),
- internal velocity field (Govender *et al.*, 2002),
- turbulence (Rapp & Melville, 1990),
- wave breaking criteria (Galvin, 1969),
- enhancement of air-sea gas transfer at the ocean surface (Keeling, 1993),
- generation of ambient sound (Loewen & Melville, 1991), and
- break-point sandbar formation (Wang *et al.*, 2003).

While many features of breaking waves have received attention from researchers, the review of existing literature presented here concentrates only on studies concerning the general characteristics of breaking waves, energy dissipation, air entrainment and splash generation as these are most relevant to the current study. Further information about other aspects of wave breaking can be found in the review articles of Peregrine (1983) and Battjes (1988) for shallow water waves and Melville (1996) and Banner & Peregrine (1993) for deep-water waves.

2.2 BREAKING WAVES

As noted in chapter 1, many theoretical, experimental and numerical studies have been completed on various aspects of the wave breaking process, however due to its complex nature, the mechanics of wave breaking are not fully understood and the topic remains one of the outstanding problems in the field of fluid mechanics.

While there remains no "wave breaking theory", understanding of breaking waves was improved in the late 1970's and early 1980's by the development of numerical models which allow the shape of breaking waves to be computed up to the point where the overturning jet strikes the free surface ahead of the wave at the "plunge point" (Longuet-Higgins & Cokelet, 1977; Vinje & Brevig, 1981; Peregrine *et al.*, 1980; New *et al.*, 1985; Cokelet, 1978 and others). In recent years, further progress, allowing computations of the flow field beyond the plunge point has been made using techniques such as Volume of Fluid (VOF) (Yasuda *et al.*, 1999; Abadie *et al.*, 1998; Chen *et al.*, 1999), Smoothed Particle Hydrodynamics (SPH) (Landrini *et al.*, 2005) and Large Eddy Simulation (LES) (Christensen & Deigaard (2001). However, while these advanced numerical techniques are useful tools for examining features of the flow in breaking waves, much of our knowledge of wave breaking including the mechanisms of air entrainment and splash generation comes from laboratory and field studies.

2.2.1 Wave Breaking Criteria

Many criteria have been suggested to describe the onset of wave breaking based on various properties of the flow at the break point. Probably the most common of these suggests that a wave breaks when the horizontal particle velocity at the wave crest becomes equal to the phase speed of the wave and the front face of the wave becomes unstable.

In order to provide a simple method to predict the location of wave breaking that can be applied universally without having to make complex calculations, many authors have suggested criteria that define breaking in terms of the wave's geometric properties. In shallow water, waves approach breaking as they shoal, increasing in height and steepness as the water depth decreases. Values of the limiting wave height to water depth ratio H/h_b for shallow water breaking waves have been published by McCowan (1891), Galvin (1969), Weggel (1972) and others. In deep water, waves may break as a result of wave-wave, wave-current or wind-wave interactions (Melville, 1996). Bonmarin (1989), Duncan (1983), Rapp & Melville (1990) and others have investigated deep-water wave breaking criteria based on the local wave steepness H/L.

2.2.2 Breaker Types

The common method for the description of breaker types on beaches was initially suggested by Iversen (1952) who divided breaking waves into 3 categories; spilling, plunging and surging, and found the breaker type to be governed by beach slope m and offshore wave steepness H_o/L_o. A further breaker type, the collapsing breaker was added by Galvin (1968) in the first detailed work on breaker classification. Peregrine (1983) gives the following descriptions of the four recognised breaker types (figure 2.1).

Spilling - White water appears at the wave crest and spills down the front face.

Plunging - Most of the wave's front face overturns and a prominent jet falls near the base of the wave, causing a large splash.

Collapsing - The lower portion of the front face overturns and behaves like a truncated plunging breaker.

Surging - No significant disturbance of the smooth wave profile occurs except near the moving shoreline.

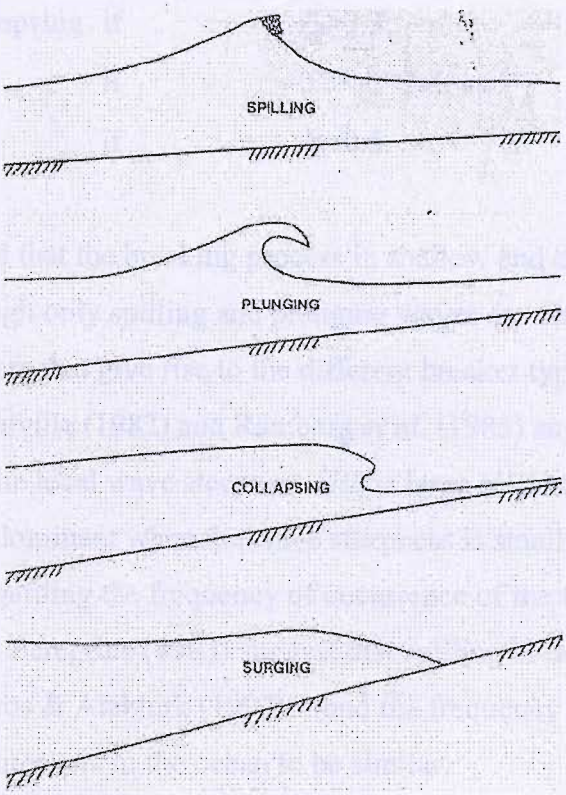

Figure 2.1 Breaker type classifications (after Galvin (1969), figure 2).

Galvin (1968) suggested that there is a continuous sequence of breaker types running in the order spilling, plunging, collapsing and surging with increasing beach slope or decreasing offshore wave steepness. Consequently intermediate breaker types are common and definition of breaker type is therefore rather subjective.

Battjes (1974) recognised the dependence of breaker type on beach slope and offshore wave steepness and extended the use of the Irribarren Number ξ_o (Irribarren & Nogales, 1949) to provide a surf similarity parameter to categorise the form of a breaking wave into the categories of Galvin (1968). The surf similarity parameter is defined as

$$\xi_o = \frac{m}{\sqrt{H_o / L_o}}, \tag{2.1}$$

where H_o is the offshore wave height, L_o the offshore wavelength and m represents the gradient of the beach.

The following approximate transition values were found:

surging or collapsing	if	$\xi_o > 3.3$,
plunging	if	$0.5 < \xi_o < 3.3$, and
spilling	if	$\xi_o < 0.5$.

Peregrine (1979) noted that the breaking process in shallow and deep water appears to be very similar, although only spilling and plunging waves are observed in deep water and the wave parameters that give rise to the different breaker types are less clear. Rapp & Melville (1990), Melville (1982) and Ramberg *et al.* (1985) suggest that plunging breakers occur when the local wave steepness H/L is large ($H/L > 0.11$ to 0.13), while spilling waves are predominant when the wave steepness is smaller. In addition there is some disagreement regarding the frequency of occurrence of the two breaker types in deep water. Banner & Peregrine (1993) suggest that spilling breakers are most common, while Katsaros & Atakturk (1992) found the frequency of occurrence of spilling and plunging breakers in the ocean to be similar.

2.2.3 General Description of Wave Breaking

While previous work has shown that four main breaker types exist in the ocean, this study will examine only spilling and plunging waves as these are most commonly observed forms in both deep and shallow water. Further work may go on to complete similar experiments to those described in this thesis to examine surging and collapsing waves in more detail.

Figure 2.2 summarises the typical large scale flow features of plunging waves which are characterised by the ejection of a well defined jet from the crest of the overturning wave as the front face becomes vertical. It is noted however that Basco (1985) suggests that the breaking of spilling waves is initiated by a small scale plunging motion close to the crest and thus the features presented in figure 2.2 are also true for spilling waves.

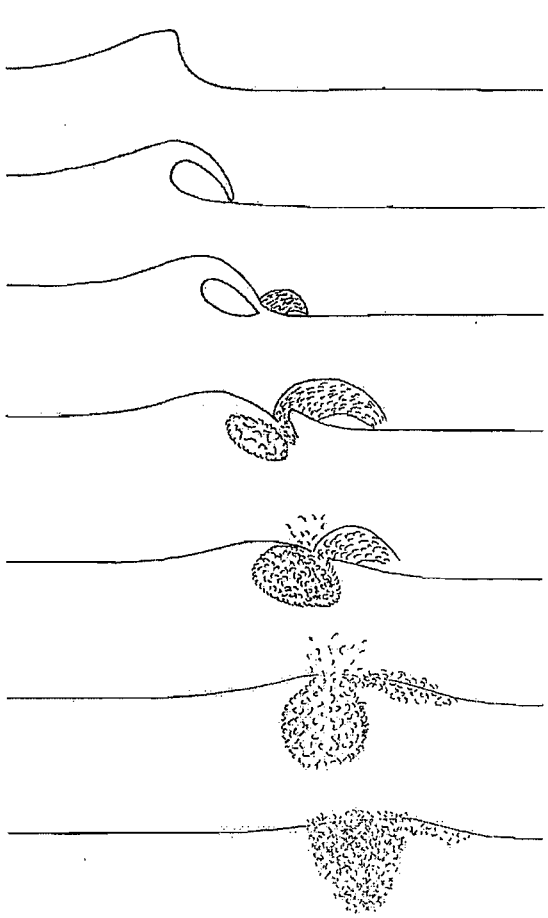

Figure 2.2 Evolution of a plunging breaker.

2.3 AIR ENTRAINMENT IN BREAKING WAVES

Breaking waves are associated with considerable air entrainment as the wave overturns and the jet formed at the wave crest impacts with the water in the preceding trough. This energetic process leads to the formation of a dense bubble plume over a short time scale which subsequently evolves under the influence of wave generated currents, turbulence, buoyancy, dissolution and bubble coalescence. Observations show that air entrainment occurs for waves of all breaker types but the level of entrainment varies with the scale of the overturning motion (Papanicolau & Raichlen, 1988; Yasuda *et al.*, 1999; Hwung *et al.*, 1992).

While many laboratory and field studies have been made, the details of the entrainment mechanisms and the spatial and temporal evolution of the bubble plume are not well understood and there is a large amount of conflicting data. This information is of great interest as entrainment of air at the ocean surface plays a role in many important environmental processes, some of which are summarised below.

- Transfer of energy to long waves in shallow water (for example Chanson *et al.*, 2002b).
- Behaviour of post-breaking waves in the surf zone (Cox & Shin, 2003).
- The individual and collective oscillations of the bubble plumes entrained by breaking waves are a significant source of sea-surface sound both in deep water (Knudsen *et al.*, 1948; Loewen & Melville, 1991) and the surf zone (Deane, 1997).
- The presence of entrained air in the water column increases the compressibility of the water and this affects the magnitude of wave impact pressures on coastal structures (Peregrine & Thais, 1996; Bullock *et al.*, 2001).
- Bubble bursting at the free surface leads to production of marine aerosols close to the air-sea interface (Blanchard, 1963; Cipriano & Blanchard, 1981).
- Bubbles rising through the water column can scavenge bacteria and other materials, leading to the enrichment of the surface layer and marine aerosol which may cause a health hazard to those living along the shore (Blanchard, 1989).

- Lamarre (1993) and Führböter (1970) showed that a significant proportion of the energy dissipated during wave breaking is expended in entraining dense bubble plumes immediately beneath breaking waves.
- The presence of bubbles in the ocean greatly increases the surface area available for the air-sea exchange of atmospheric gases and enhances the gas transfer rate (Melville, 1996).

2.3.1 Bubble Plume Evolution

Before reviewing the previous studies of air entrainment that have been completed to date, it is useful to describe briefly the large scale evolution of the air volume entrained by a breaking wave. De Leeuw & Leifer (2002) suggested that the life of a bubble plume generated by a breaking wave can be divided into four phases; formation, injection, rise and senescence and these are shown in figure 2.3. Formation takes place over a very short time scale of the order 0.1s as the wave overturns and entrains air in the form of large bubbles and cavities in an active entrainment region close to the intersection of the overturning jet and the free surface. During the injection phase the plume is rapidly driven down into the water column. Injection ends when the entrained bubbles reach their maximum penetration depth and is followed by the rise phase, where the plume disperses under the influence of buoyancy and dissolution. Finally the senescence phase consists of the smaller (mostly d<400 μm) plume remnants after the main plume has dispersed. The senescence phase corresponds to the background bubble population during which the majority of oceanic bubble measurements have been made.

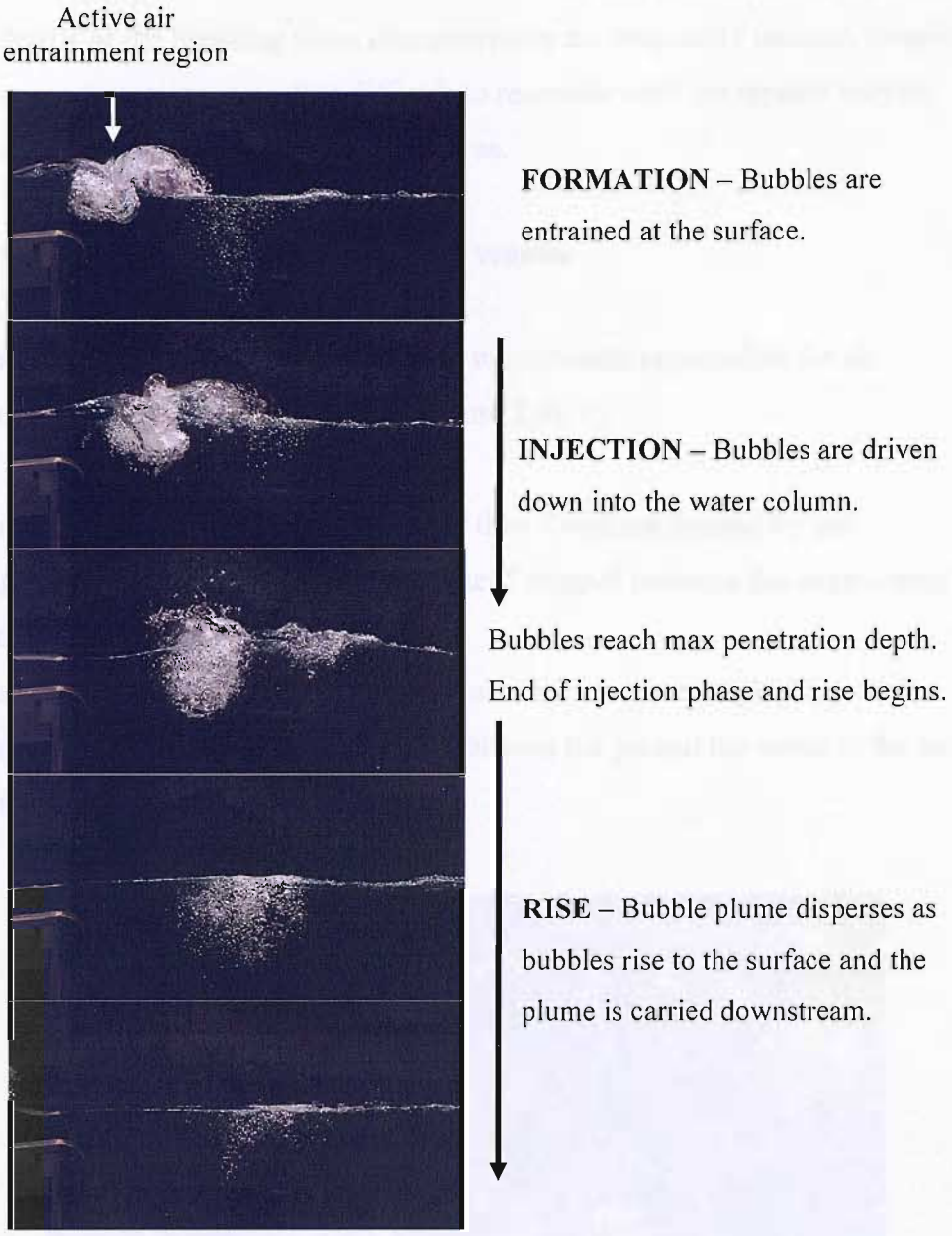

Figure 2.3 Stages of the bubble plume evolution based on the scheme of De Leeuw & Leifer (2002). The final phase is senescence which represents the ambient bubble population that remains after the majority of visible bubbles have dispersed.

A number of authors (Kalvoda, 2003; Papanicolau & Raichlen, 1988 &1992; Raichlen & Papanicolau, 1988) have examined the evolution of wave generated bubble plumes and shown that they are highly transient, making detailed quantitative information about them difficult to obtain. Many of the existing measurements of the bubble plumes entrained by breaking waves are made over long time periods or use large measurement volumes and as such features of the flow are lost through temporal and spatial

averaging. In addition the location of the measurement instrument relative to the break point and details of the breaking wave characteristics are frequently unclear, meaning that existing measurements are often difficult to reconcile with the rapidly varying bubble plumes observed beneath breaking waves.

2.3.2 Aeration mechanisms in breaking waves

Deane & Stokes (2002) observed two primary mechanisms responsible for air entrainment in laboratory breaking waves (figure 2.4).

1. Larger bubbles with a diameter greater than 2 mm are formed by the fragmentation of the air "tube" or "vortex" trapped between the overturning jet and the wave face as the wave breaks.
2. Smaller bubbles are formed by the impact and subsequent splashing of the overturning jet and in the shear layer between the jet and the water in the trough in front of the breaking wave.

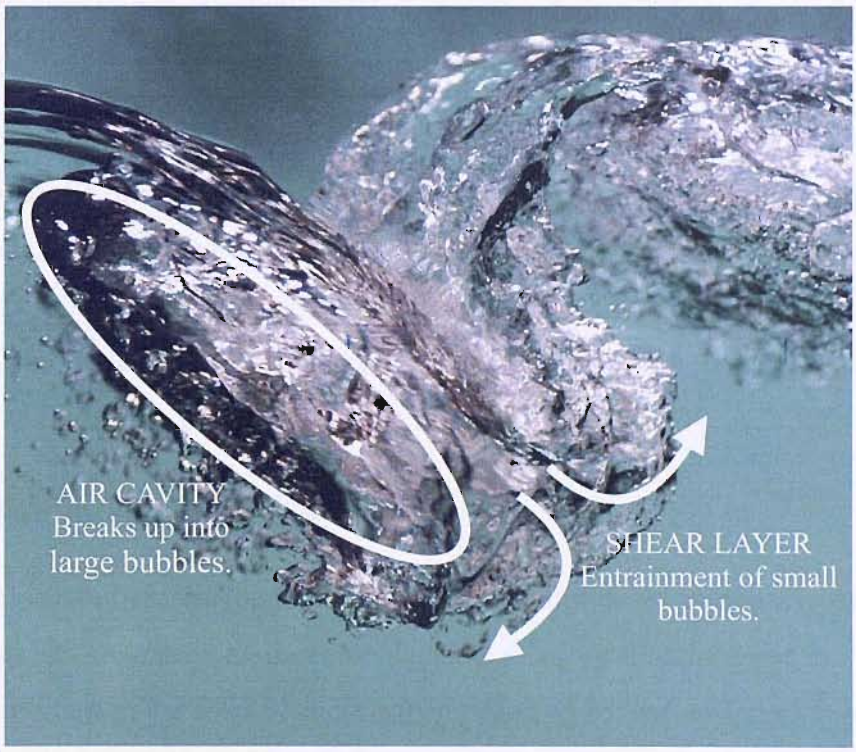

Figure 2.4 Primary air entrainment mechanisms in breaking waves, based on Deane & Stokes (2002).

This separation of the primary entrainment mechanisms was supported by photographic images and an analysis of the underwater sound radiated by laboratory breaking waves. A similar separation of the main entrainment mechanisms was also observed in the underwater photographs of Deane & Stokes (1999) and Watanabe *et al.* (2001) taken in oceanic surf zone waves. Secondary bubble entrainment mechanisms include the impact of the splash-up generated by the breaking process as it falls back down to the water surface under the influence of gravity (Lamarre, 1993), the detachment and re-entry of drops of water known as "spindrift" (Mackay & Shiu, 1984) and the secondary bubble burst mechanism discussed by Leifer *et al.* (2000).

Many of the existing studies of the process of air entrainment in breaking waves have concentrated on the second of the mechanisms described above by comparing the action of the overturning jet of the breaker to a steady plunging water jet (Cummings, 1996; Chirichella *et al.*, 2002; Cipriano & Blanchard, 1981; Chanson & Cummings, 1994; Chanson & Cummings, 1992; Chanson *et al.*, 2004; Koga, 1982; Asher & Farley, 1995). The results of some of this research, along with those of other investigations into the mechanism of air entrainment by a steady plunging jet are discussed in section 2.3.2.1.

While information about steady jets is readily available, it has been noted that the intermittent nature of breaking waves is poorly modelled by a steady plunging jet and consequently some recent studies have investigated aeration in unsteady, impacting jet flows (Ledesma, 2004; Koehr, 2002; Haines & Johnson, 1995; Chanson *et al.*, 2002b). A summary of the work of previous studies of air entrainment due to unsteady jets and droplets is given in section 2.3.2.2.

2.3.2.1 Steady Plunging Jet Flows

A large number of studies designed to investigate air entrainment in both circular and planar plunging jets have been made as the data has many applications and is particularly important in the field of chemical engineering for the design of gas-liquid reactors. The majority of this work has shown that air entrainment takes place at the interface between a vertical plunging jet and the free surface once the jet velocity exceeds a certain critical velocity v_c, which is dependent on the jet inflow conditions

(Ervine & Elsawy, 1985; Sene, 1988; Bin, 1988; Evans, 1990; Wood, 1991; Detsch *et al.*, 1992). In addition, many researchers have investigated the volume of air entrained by plunging jets and concluded that it is predominantly dependent on the jet velocity (Ervine & Elsawy, 1985; Van de Sande & Smith, 1975; Sene, 1988; Wood, 1991).

The air entrainment mechanisms at a plunging jet were summarised by Chanson (1997) in his review of the available literature. At low jet velocities (v_j<4 ms^{-1})[1], individual bubbles are entrained when the receiving fluid is unable to follow the undulations present on the surface of the jet. This leads to the creation of small pockets of air adjacent to the plunging jet which are subsequently driven down into the water column (figure 2.5(a)). At higher jet velocities (v_j = 4 to 12 ms^{-1}), the entrainment process is characterised by the creation of a thin air sheet or induction trumpet by the shear forces between the jet surface and the receiving flow as shown in figure 2.5(b). The length of this air sheet fluctuates due to the effect of jet turbulence and surface disturbances and is intermittently pinched off, entraining air in the form of elongated cavities which are subsequently broken up into bubbles. In addition, air can be introduced into the receiving fluid if the impinging flow is already aerated, this process is known as pre-entrainment.

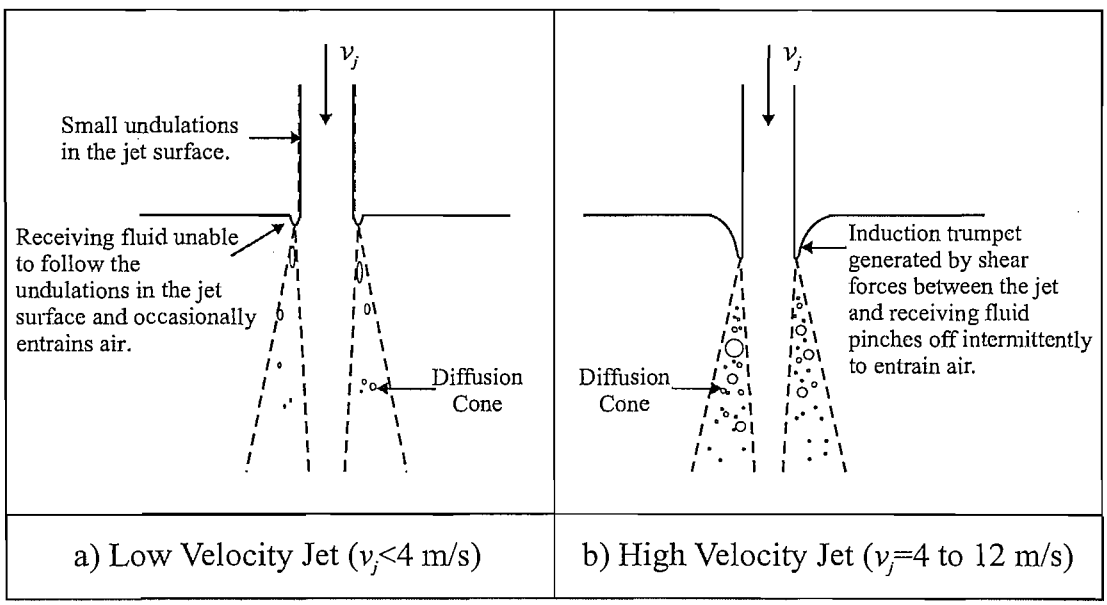

Figure 2.5 Air entrainment by a steady plunging jet as suggested by Chanson (1997).

[1] Note that values are given in terms of jet velocity rather than a dimensionless parameter such as Froude number because the critical inception velocity is independent of the scale of the jet. This method of presentation is consistent with existing literature, e.g. Bin (1993), Chanson (1997).

Despite the general agreement on the importance of jet velocity when modelling air entrainment in steady plunging jets, large discrepancies in the data of the different investigators were observed in a review article by Bin (1993). These inconsistencies were explained by Zhu *et al.* (2000) who showed that without any surface disturbances, a jet does not entrain air even at velocities exceeding the critical inception values reported by Bin (1993). Zhu *et al.* (2000) stated that unlike most previous authors, their jet nozzle was specially designed to minimise jet turbulence. They found that in order to entrain air it was necessary to introduce artificial disturbances on the jet surface and for a given jet velocity the volume of entrained air is approximately proportional to the size of the jet disturbance. Thus it was shown that the simple model of air entrainment when the jet velocity reaches a critical value is incorrect as this velocity is highly dependent on the jet turbulence and surface disturbances as suggested by Lin & Donnelly (1966) and Ervine *et al.* (1980).

Further work by Detsch & Sharma (1990) has demonstrated that air entrainment is also influenced by jet impact angle. Detsch & Sharma (1990) published an empirical expression for the critical inception angle as a function of surface tension, viscosity, density and jet velocity although no measurements of the jet turbulence levels were reported in their paper. Ledesma (2004) and Koga (1982) investigated inclined plunging jets as a model for a plunging breaking wave. Koga (1982) showed that at moderate jet velocities, bubbles are entrained at the tip of a wedge-shaped cavity on the upstream side of the inclined jet and that the size of this cavity and the entrained bubbles increases with decreasing injection angle.

Chirichella *et al.* (2002) and Ledesma (2004) took this simple model of a plunging wave further by investigating translating jets. They found that under conditions where a jet entrains no air when stationary, air entrainment can be induced by increasing the horizontal translation speed of the jet v_t to only a small fraction of the jet velocity v_j. When the jet is moved horizontally, a depression of the free surface is formed downstream of the jet. As the translation velocity of the jet is increased, the depth and length of this depression increase and a cusp forms at the bottom of its upstream edge from which air is entrained.

2.3.2.2 Unsteady Plunging Jet Flows

Recently, some investigators have recognised that the intermittent nature of breaking waves may be modelled more effectively by considering the transient impact of a water jet on a receiving pool than by comparing to a steady plunging jet. Although few studies on impacting jet flows have been completed, there is agreement that the mechanism of initial air entrainment is quite different to that for a continuously running jet. In the case of unsteady jets, the impact with the receiving fluid opens up a crater in the free surface surrounding the jet which is pinched off as the crater sides collapse inwards, entraining a large air cavity which subsequently breaks up into small bubbles in the shear flow generated by the jet. A similar mechanism was observed in plunging laboratory waves by Bonmarin (1989) who noted significant air entrainment in the cavity formed in the region between the overturning jet and the rear of the splash-up.

Ledesma (2004) completed an elegant series of experiments which examined the entrainment of air by translating unsteady two-dimensional jets with varying impact angles, and compared the results to a potential flow model similar to that of Oguz *et al.* (1995) with reasonable results. Flow visualisations showed that the inertia of the impacting jet created two open air craters at either side of the impact site. Initially these craters spread horizontally and deepen as the jet penetrates further into the receiving fluid. Following initial impact, hydrostatic pressure forces the crater walls to move towards the jet, eventually pinching off a large air cavity after time t_{po} at depth d_{po} (figure 2.6). The evolving shape of the underwater craters was observed to be significantly affected by the horizontal translation of the jet, with the values of t_{po} and d_{po} decreasing with increasing translation velocity.

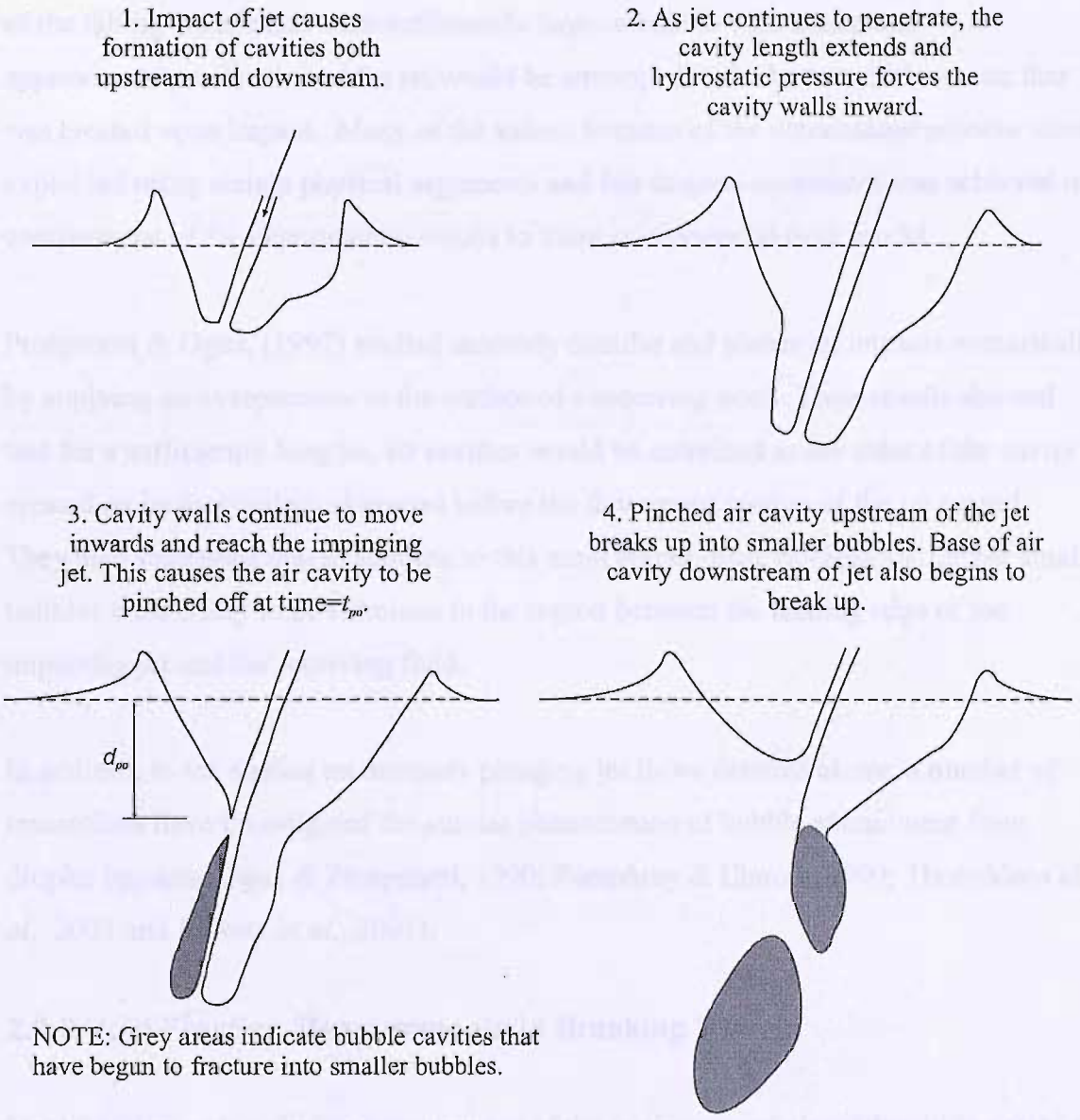

Figure 2.6 Process of air entrainment by an unsteady plunging jet based on the flow visualisations of Ledesma (2004).

Storr & Behnia (1999) completed a series of experiments to examine various features of the flow around impacting liquid jets using a range of different fluids. They concluded that the air entrainment process was dominated by the air carried into the pool by the initial impact. Consequently they found that the empirical equations developed by Bin (1993) to predict the penetration depth and volume of air in steady plunging jet systems were not applicable to impacting jets.

Oguz *et al.* (1995) studied the impact of an almost cylindrical water mass on a pool both experimentally and numerically. They found that when the aspect ratio and the energy

of the falling water mass were sufficiently large, a bubble with a diameter approximately twice that of the jet would be entrapped at the bottom of the crater that was created upon impact. Many of the salient features of the entrainment process were explained using simple physical arguments and fair to good agreement was achieved in comparisons of the experimental results to those of a potential flow model.

Prosperetti & Oguz, (1997) studied unsteady circular and planar jet impacts numerically by applying an overpressure to the surface of a receiving pool. Their results showed that for a sufficiently long jet, air cavities would be entrained as the sides of the cavity created on impact collapsed inward before the downward motion of the jet ceased. They also suggested that in addition to this main entrainment mechanism, further small bubbles were likely to be entrained in the region between the leading edge of the impacting jet and the receiving fluid.

In addition to the studies on unsteady plunging jet flows detailed above, a number of researchers have investigated the similar phenomenon of bubble entrainment from droplet impacts (Oguz & Prosperetti, 1990; Pumphrey & Elmore, 1990; Thoroddsen *et al.*, 2003 and Elmore *et al.*, 2001).

2.3.3 Void Fraction Measurements in Breaking Waves

Void fraction, α is a simple measurement of the percentage of air voids within a volume of fluid and is defined as

$$\alpha(\%) = \frac{V_a}{V_T} \times 100, \tag{2.2}$$

where V_a is the volume of air present in the water and V_T is the total volume of fluid including air voids.

Several researchers have made measurements of various aspects of the void fraction field around breaking waves in both the laboratory and field, and these are briefly summarised in table 2.1.

Table 2.1 Previously reported measurements of void fraction in breaking waves.

Author(s)	Study Type	Type of Waves	Measurement Technique	Summary
Waniewski *et al.* (2001)	Laboratory	Ship bow waves	Local conductivity probe	Contour plots produced. $0\%<\alpha<10\ \%$ Limited by free surface.
Kalvoda *et al.* (2003)	Laboratory	Wind waves	Photographic	Mean α in plume = 0.4%
Cox & Shin (2003)	Laboratory	Surf zone waves. Spilling and plunging	Local conductivity probe	$0\%<\alpha<24\%$ Decreasing α with depth.
Bullock *et al.* (2001)	Laboratory & Field	Regular & irregular waves against a breakwater	Global conductivity	Ambient α freshwater = 0.1 - 0.6% Ambient α in seawater = 1.4 - 3.9% Ambient α in field = 7.9 - 14.4%
Deane (1997)	Field	Surf zone waves	Photographic	α = 34% after breaking.
Vagle & Farmer (1998)	Field	Deepwater waves	Acoustic resonator Acoustic pulse propagation Backscatter sonar Global conductivity	Review of instruments. Ambient bubble population in deepwater. $10^{-6}\%<\alpha<10^{-3}\%$
Loewen et al. (1996)	Laboratory	Focussed, spilling waves	Photographic	Mean α in freshwater = 0.13-0.22% Mean α in seawater = 0.15-0.26%
Stanton & Thornton (2000)	Field	Surf zone waves	Global conductivity	Mean, near surface α = 0.05%
Hwung *et al.* (1992)	Laboratory	Surf zone waves Plunging and spilling	Laser blocking	Horizontal & vertical variation of α Plunging breaker, $0<\alpha<18\%$ Spilling breaker, $0<\alpha<12\%$ Vertical variation of α follows hyperbolic function.
Lamarre (1993)	Laboratory	2D Focussed plunging waves	Global conductivity	Contour plots produced. Instantaneous α varies rapidly. Mean $\alpha = 1\%<\alpha<21\ \%$
Lamarre (1993)	Laboratory	3D Focussed plunging waves	Global conductivity	Contour plots produced. Instantaneous α varies rapidly.
Lamarre (1993)	Field	Deepwater waves	Global conductivity	Max α = 24%
Hoque (2002)	Laboratory	Surf zone waves Plunging and spilling	Local conductivity probe	Horizontal and vertical variation of void fraction, α Plunging breaker, $0<\alpha<19\%$ Spilling breaker, $0<\alpha<16\%$

It is seen that there are significant differences between the various datasets and some of the reasons for these variations are listed below.

1. **Different measurement techniques.** A brief summary of the more common techniques for making void fraction and bubble size measurements in bubbly flows can be found in section 2.3.5.
2. **Wave characteristics.** It is seen in table 2.1 that there are differences in the methods of wave generation for the laboratory experiments and both spilling and plunging waves have been examined. In addition field measurements have been made in both surf zone and deep-water waves but detailed information on the type of wave breaking is not always available.
3. **Scaling problems.** The main issues in scaling air entrainment in breaking waves are discussed in detail in section 7.4.
4. **Measurement positions.** As will be shown in chapter 5, the void fraction field undergoes rapid spatial and temporal variation after a breaking event. Thus it is very difficult to compare two sets of measurements as the data is highly dependent on the location of the measurement position within the bubble plume generated by breaking.
5. **Definition of void fraction.** Both instantaneous and mean values of void fraction have been presented by previous investigators. While instantaneous measurements can sometimes be directly compared, it is often very difficult to directly compare mean void fraction measurements as the definition of the mean can vary widely from study to study.
6. **Salinity of the water.** Many authors have shown that there can be significant differences between aeration measurements in salt and freshwater. This will be discussed in section 2.3.6 and examined further in chapter 7.

This study will go on to examine in detail the temporal and spatial variation of the void fraction field in the dense bubble plumes generated immediately beneath breaking laboratory waves in both fresh and seawater. While it is seen that many studies have considered the void fraction field in breaking waves, the measurements most directly relevant to the present work are discussed below.

Undoubtedly the most comprehensive study of void fractions in breaking waves was completed by Lamarre (1993) and is also reported in Lamarre & Melville (1991, 1992 & 1994), Melville *et al.* (1993) and Melville *et al.* (1992). Lamarre (1993) used a global conductivity probe which infers the void fraction from the conductivity of the water to produce contour plots of the time-varying void fraction field beneath both 2D and 3D focussed laboratory waves as well as making some acoustic measurements in deep-water ocean waves. The results showed that the bubble plumes generated by breaking undergo rapid transformations and lose 95% of the initially entrained air volume during the first wave period. The measured void fraction results were used to calculate integral properties of the void fraction field such as the volume of entrained air, the area of the bubble plume and the mean void fraction. It was shown that these properties evolve as simple functions of time and scale reasonably well from small 2D laboratory waves to larger 3D breaking waves.

Hoque (2002) made measurements of the time-averaged void fraction field beneath 2D laboratory waves breaking on an emergent 1:9.5 slope using local conductivity probes. His measurements showed that the maximum mean void fractions were located close to the free surface and decayed approximately exponentially with depth, with plunging breakers entraining bubbles to a greater depth than spilling waves. Hoque & Aoki (2005) reanalysed the void fraction data and found that the vertical distributions of void fraction closely followed an analytical solution of the diffusion equation.

Hwung *et al.* (1992) measured the void fraction beneath spilling and plunging laboratory waves breaking on 1:15 emergent slope using a laser blocking technique. The experimental results suggested that the void fraction decays away from the point of air entrainment in both the vertical and horizontal directions.

2.3.4 Bubble Size Distribution

Breaking waves entrain air bubbles that generate ambient noise, enhance air-sea gas flux and collect biological surfactants as they rise through the water column that can then be released into the atmosphere upon bursting at the surface. The size distribution of the entrained bubbles is one of the most important factors controlling these processes and is an essential parameter in models of air-sea gas exchange. Consequently many

studies of the oceanic bubble size distribution, using a wide range of techniques have been undertaken and these are summarised in table 2.2.

It is seen that there are many discrepancies in the values reported by the previous investigations listed in table 2.2. The reason for this is that bubble plumes generated by breaking waves undergo rapid temporal and spatial changes after their generation and consequently the measurements are highly dependent on the position and time at which they were taken. Further variations may arise from the different measurement techniques and their range of validity, as well as differences in factors such as study location (laboratory or field), the salinity and composition of the water and the type of breaker. Despite these inconsistencies, there is general agreement in all studies that the bubble size distribution follows a power law scaling and there appears to be a change in the value of the spectral slope seperating the large and small bubble populations, although the values of the spectral slopes and the bubble diameter at which the slope transition occurs vary from study to study. As an example, the bubble size distribution of Deane & Stokes (2002) is shown in figure 2.7.

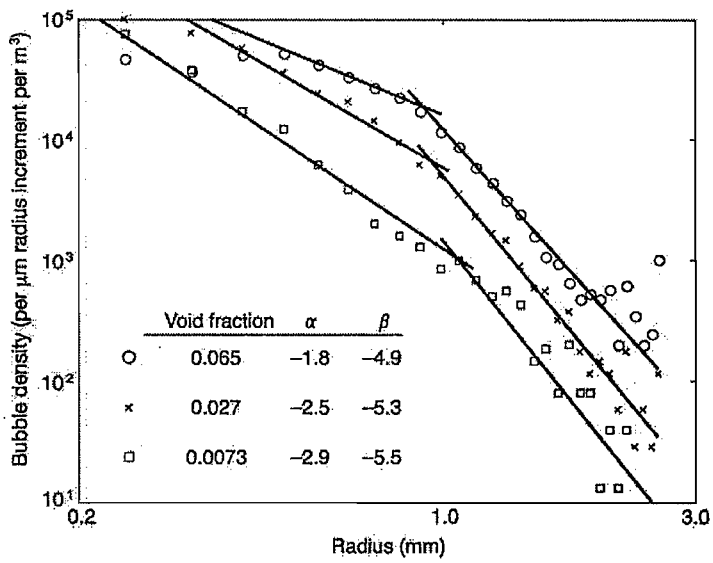

Figure 2.7 Example bubble size distribution (after Deane & Stokes (2002), figure 6).

Table 2.2 Previous measurements of bubble size distribution in breaking waves.

Author(s)	Technique	Study Area/Wave Type	Power Law Scaling	Peak d (μm)	No. bubbles at 200μm/m^3/μm	Approximate Plume State
Medwin (1970)	Acoustic	Coastal waters	d^{-4} d<160μm d^{-2} d >160μm	No peak	150	Senescence
Kolovayev (1976)	Bubble trap	Open sea	$d^{-3.5}$	140-160	350	Senescence
Medwin (1977)	Acoustic	Coastal waters	d^{-4} d <120μm d^{-2} d >120μm	No peak	250	Senescence
Walsh & Mulhearn (1987)	Photography	Wind waves at sea	d^{-4} d >200μm	136	300	Senescence
Johnson & Cooke (1979)	Photography	Coastal waters	d^{-4}	80-100	176	Senescence
Su *et al.* (1988)	Optical	30m Coastal waters	d^{3} d <60μm d^{-5} to d^{-6} d>400μm	80-100	1000	Senescence
Baldy (1988)	Laser	Laboratory wind waves	d^{-4} d <100μm $d^{-2.6}$ d >100μm	No peak	1000	All phases
Medwin & Breitz (1989)	Acoustic	Coastal waters spilling waves	d^{-4} d <120μm $d^{-2.5}$ d >120μm	No peak	2000	All phases
Vagle (1989)	Acoustic	Ocean 140m depth	d^{-4} to d^{-6}	16-140	200	All phases
Hwang *et al.* (1990)	Laser	Laboratory wind waves	$n(d) \sim d^{-k}$ k=2.8z/Hs+0.7	No peak	N/A	All phases
Vagle & Farmer (1992)	Acoustic	Ocean 140m depth	d^{-4} to d^{-7} for d <50μm	50	1000	All phases
Kalvoda (1992)	Video	Laboratory wind waves	$d^{-2.8}$	N/A	N/A	
Cartmill & Su (1993)	Acoustic	Laboratory focussed waves	d^{-3} 100< d <1200μm	No peak	1000 (salt water) 50 (fresh water)	All Phases
Loewen *et al.* (1996)	Photography	Small laboratory wind waves	$d^{-3.7}$ d >2 mm	1000	100	Injection & Rise
Deane (1997)	Photography	Surf zone	$d^{-2.5}$ d <2mm $d^{-4.5}$ d >2mm	No peak	10^6	Formation, Injection & Rise

Author(s)	Technique	Study Area/Wave Type	Power Law Scaling	Peak d (μm)	No. bubbles at 200μm/m3/μm	Approximate Plume State
Phelps *et al.* (1997)	Acoustic	Surf zone	N/A	N/A	10^5	Formation, Injection & Rise
Phelps & Leighton (1998)	Acoustic	Coastal waters 20m depth	N/A	40	1000	All phases
Deane & Stokes (1999)	Photography	Surf zone	N/A	No peak	N/A	Formation, Injection & Rise
Terrill *et al.* (2001a)	Acoustic	Offshore of surf zone	d^{-6} to d^{-8}	No peak	N/A	Senescence (bubbles advected from surf zone)
Terrill *et al.* (2001b)	Acoustic	Coastal waters	d^{-7} to d^{-4}	No peak	10^2 to 10^4 varies w. depth	Injection & Rise
Deane & Stokes (2002)	Photography	Laboratory plunging waves	$d^{-1.5}$ d <2mm $d^{-10/3}$ d >2mm	No peak	10^4	Formation
Kalvoda *et al.* (2003)	Photography	Laboratory wind waves	d^{-2} 1mm< d <5mm $d^{-3.7}$ 5mm< d <10mm	No peak	N/A	Injection & Rise
Leifer & de Leeuw (2002)	Photography	Laboratory wind waves	$d^{-0.5}$ to $d^{-1.9}$ d <300μm $d^{-2.2}$ to $d^{-3.6}$ d >300μm	No peak	N/A	Injection & Rise
De Leeuw & Leifer (2002)	Photography	Laboratory wind waves	$d^{-1.7}$ d <500μm $d^{-5.2}$ d >500μm	No peak	N/A	Senescence
Leifer *et al.* (2003)	Photography	Laboratory wind waves	$d^{-3.7}$ to $d^{-5.4}$ d >500μm Dependent on time	No peak	N/A	Injection & Rise
Terrill & Melville (2000)	Acoustic	Laboratory focussed waves	N/A	No peak	2000	Injection, Rise & Senescence
Bowyer (2001)	Photographic	Coastal waters, near surface	$d^{-2.1}$ to $d^{-4.7}$ Dependent on depth, proximity to breaking wave and salinity.	No peak	100 to 1000	All phases
Farmer *et al.* (1998)	Acoustic	Coastal waters	N/A	No peak	10 to 10^4 Depth dependent	Senescence

Table 2.2 (continued).

It is noted that many of the studies listed in table 2.2 have made measurements of the ambient oceanic bubble size distribution (senescence phase) and as noted in chapter 1, these datasets are often used in estimates of air-sea gas transfer. However this data typically omits the transient large bubble population that exists in the water column for a short period after wave breaking and has a significant effect on bubble-mediated gas transfer. Indeed, Keeling (1993) concluded that bubble-mediated gas transfer depends critically on the production rates of bubbles large than 1 mm in diameter, while Woolf (1993) demonstrated that shallow fluxes of large bubbles close to the ocean surface contribute significantly to bubble-induced gas exchange. For gas transfer studies Melville (1996) suggested that one would like to know the total volume and size distribution of bubbles entrained at the surface and be able to predict its subsequent evolution under the influence of bubble break-up, advection, dissolution and buoyancy. However, predominantly due to practical difficulties, relatively few detailed measurements have been made within the dense bubble plumes formed immediately after breaking. These plumes are optically and acoustically opaque and are characterised by high concentrations of large bubbles undergoing rapid changes. Deane & Stokes (1999) noted that both optical and acoustic radiation are scattered at the plume boundary, making studies of the plume using external instruments practically impossible.

The solution of Deane & Stokes (1999) and Stokes & Deane (1999) to this problem was to design a camera to operate within the interior of the dense bubble plumes generated by breaking surf zone waves in order to examine bubble formation mechanisms and produce bubble size distribution data during the early moments of the life of the bubble plume. Their results showed that total bubble concentration in the initial formation and injection phases of the plume is higher than at later times. In addition, there are a greater number of larger bubbles present in the initial phases of the plume development which are subsequently broken up into smaller bubbles or rapidly rise back to the surface. Similar temporal variation of the size distribution during the injection and rise phase of the bubble plume was measured by the laboratory studies of Deane & Stokes (2002), Leifer *et al.* (2003) and Leifer & De Leeuw (2002) using photographic techniques.

An increase in the number of large bubbles during the early stages of bubble plumes has also been observed by a number of researchers investigating the size distributions under simulated breaking waves such as water falls and tipping buckets (Monahan & Zietlow, 1969; Cipriano & Blanchard, 1981; Haines & Johnson, 1995).

The spatial variation of the bubble size distribution was investigated by Terrill & Melville (2000) whose laboratory measurements demonstrated a decrease in the large bubble population and the exponent of the power law scaling with horizontal distance from the active air entrainment region. Farmer *et al.* (1998), Bowyer (2001), Baldy (1988), Hwang *et al.* (1990), Cartmill & Su (1993) and others have demonstrated similar trends with increasing depth away from the free surface. Based on his laboratory measurements, Baldy (1988) suggested that the slope of the bubble size distribution follows a power law with an exponent of the order -2 in the "bubble generation layer" which remains close to the free surface and extends to a depth of approximately $0.5H_s$. Below this level there is a rapid drop off of the global bubble concentration and the slope of the bubble size spectrum approaches -4. This lower region was termed the "dispersion zone".

The difficulties of making measurements in dense bubble plumes were also noted by Serdula & Loewen (1998) who suggested that a technique employing optical fibre phase detection probes represented the most promising method for making accurate measurements of the transient bubble size distribution beneath breaking waves. Serdula & Loewen (1998) investigated the feasibility of making bubble size measurements using a single optical probe measurement technique which will be described in detail in section 3.4.4.2 but made no measurements in breaking waves.

2.3.5 Bubble Measurement Techniques in High Void Fraction Flows

As can be seen from tables 2.1 and 2.2, numerous different methods have been used for making measurements of the two-phase flow beneath breaking waves, including acoustic techniques (Medwin, 1970), laser blocking (Hwung *et al.*, 1992), photographic (Leifer *et al.*, 2003), bubble traps (Blanchard & Woodcock, 1957), phase doppler anemometry (Asher & Farley, 1995) and conductivity probes (Lamarre, 1993). However it was noted in section 2.3.3 that most of these methods are unsuitable for

making measurements in the dense bubble plumes formed in the active entrainment region of breaking waves. Laser techniques have problems when bubble masking occurs as multiple bubbles enter the beam and as such are unsuitable for use in very high void fractions. Similar bubble masking problems are observed in non-intrusive photographic techniques. Many different acoustic approaches are available, including resonance, pulse propagation and multi-frequency backscatter but the use of these are limited in high void fraction bubble plumes due to the acoustic opacity of the plume (Leifer *et al.*, 2003).

Some of the techniques that are considered most suitable for making measurements in dense two-phase flows are detailed in table 2.3.

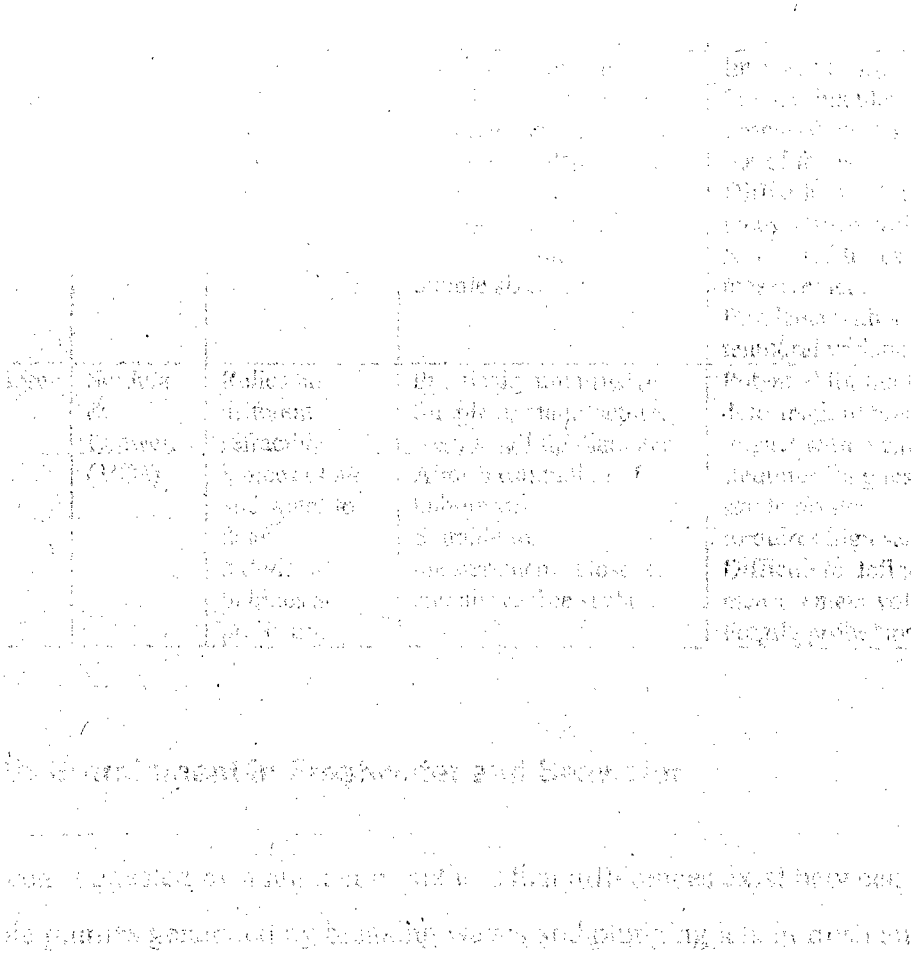

Table 2.3 Techniques suitable for making aeration measurements in high void fraction bubble plumes.

Technique	Example Author	Operation Principle	Advantages	Disadvantages
Global conductivity	Lamarre (1993)	Measures conductivity of the water and infers void fraction based on expression of Maxwell (1892).	Simple to make measurements of temporal evolution. Almost non-intrusive. Simple to manufacture and use. Low sample rate.	No bubble size measurements. Problematic close to free-surface. No information about individual bubbles. Potential for bubble deformation/ breakage upon impact with probe.
Local conductivity	Cox & Shin (2003)	Relies on different conductivity of air and water to detect individual bubbles at probe tip.	Almost non-intrusive. Simple to manufacture.	Potential for bubble deformation/ breakage upon impact with probe. Only provides bubble residence time and strike rate. Requires long tests to achieve stable results. Requires high sample rates. Larger tip diameter than optical fibre probe. Difficult to define measurement volume.
Intrusive photographic methods	Deane & Stokes (1999)	Camera designed to be used inside bubble plumes.	Provides excellent visualisation of bubble creation and dispersion. Provides a snapshot of the flow, no phase averaging required. Allows estimation of bubble size.	Intrusive technique. Smaller bubbles may be obscured by larger bubbles or out of focus. Difficult to define measurement volume. Not suited to real time measurement. Problems with assessing temporal variation.
Optical fibre probe	Serdula & Loewen (1998)	Relies on different refractive indices of air and water to detect individual bubbles at probe tip.	Practically unintrusive. Simple to manufacture. Very small tip diameter. Allows estimation of bubble size. Suitable for measurements close to and above free surface.	Potential for bubble deformation/ breakage upon impact with the probe. Requires long tests to achieve stable results. Requires high sample rates. Difficult to define measurement volume. Fragile probe tips.

2.3.6 Air Entrainment in Freshwater and Seawater

It has been suggested by a number of authors that differences exist between the nature of bubble plumes generated by breaking waves and plunging jets in fresh and seawater. This has a considerable influence on the applicability of laboratory results to field conditions as the vast majority of experiments designed to reproduce coastal processes are conducted in freshwater. However, while it is commonly agreed that differences

exist between fresh and seawater bubble plumes, there is much conflicting data regarding the nature of any variations.

The most commonly observed differences relate to the bubble size distribution and many previous investigators have completed experiments designed to examine the bubble sizes generated in fresh and seawater, however there is much disagreement in the published results.

Several researchers, including Haines & Johnson (1995), Monahan *et al.* (1994), Carey *et al.* (1993), Chanson *et al.* (2002a) and Monahan & Zeitlow (1969) present evidence which demonstrates that a greater number of small, sub-millimetric bubbles are present in salt/seawater than in freshwater. The common explanation for the observed variation of bubble sizes in the two solutions is that bubble coalescence in freshwater leads to a higher proportion of large bubbles, while biological surfactants and ions present in seawater somehow inhibit the process of coalescence. However Slauenwhite & Johnson (1999) suggested that the formation of bubbles is fundamentally different in fresh and seawater and differences in the initial "bubble shattering" cause variations in the eventual bubble size distribution in addition to the effects of coalescence. In order to investigate the "bubble shattering" mechanism, Slauenwhite & Johnson (1999) forced large bubbles with a volume of 5 μL to shatter into smaller bubbles as they passed into a water cell. In freshwater the number of bubbles produced by a shattering event was 50 or less, while in salt water more than 4 times as many bubbles were observed.

While the studies discussed above show a discrepancy between the bubble size distributions generated in fresh and salt/seawater, contradictory evidence is presented by Wu (2000) and Loewen *et al.* (1996) who suggest that no such difference exists.

Other investigations have examined the differences in the void fraction distribution and the total volume of air entrained by identical flows in fresh and salt/seawater, and again there is very little agreement between the various studies. Chanson *et al.* (2002a) made void fraction measurements in the bubble plumes generated by saltwater, seawater and freshwater plunging jets with identical inflow conditions and found that a significantly smaller volume of air was entrained in seawater than in freshwater. A contrasting result

was found by Wu (2000) who re-analysed the data of previous investigators including Cartmill & Su (1993) and suggested that considerably greater amounts of air are entrained by breaking waves in saltwater than freshwater. Still further confusion is introduced by Monahan *et al.* (1994) and Wang & Monahan (1995) who observed that the maximum void-fraction measured close to the surface immediately after bubble plume formation did not differ substantially between fresh and saltwater. Further support for this result was presented by Loewen *et al.* (1996) who reported that the bubble plumes created by laboratory wind waves behaved in a similar manner in both fresh and saltwater and presented data showing that the bubble size distribution and concentrations were very similar in both cases.

2.3.7 Air Entrainment Models

Due to the highly complex nature of wave breaking and lack of knowledge about the mechanisms of aeration, few models of air entrainment in breaking waves currently exist and those that have been developed concentrate only on parts of the process.

As discussed in section 2.3.2.2, Ledesma (2004) compared the air entrainment in plunging breaking waves to that from unsteady plunging jets and developed a potential flow model to describe the phenomenon that agreed well with experimental data.

Chanson & Cummings (1994) developed a simple model which predicts the sizes of entrained bubbles, the bubble interface area, maximum bubble penetration depth and the contribution to gas transfer based on empirical formulae for air entrainment by steady plunging jets which were assumed to be analogous to plunging breakers. The model was used to predict oxygen transfer during a storm and compared reasonably well with published results. However it has been shown that aeration in breaking waves is very different to that observed in steady jets and so the model is unlikely to perform well in all situations.

Garrett *et al.* (2000) used simple dimensional arguments to suggest that the air initially entrained by a breaking wave is rapidly broken up by turbulence, leading to an initial bubble size spectrum proportional to $d^{-10/3}$ before modification by buoyancy and dissolution. This result is in agreement with measurements made during the early stages

of bubble plume evolution by Deane & Stokes (2002). Garrett *et al.* (2000) also went on to demonstrate how the effects of buoyancy and dissolution would lead to changes in the bubble size distribution with time.

A number of authors have developed bubble tracking models which incorporate the main equations governing bubble dynamics, primarily to investigate bubble-mediated gas transfer in the ocean.

Thorpe (1984) presents a two-dimensional, Lagrangian, finite-difference bubble model that tracks the motion and size of individual bubbles as they are injected at the surface and incorporates the effects of bubble dissolution, buoyant rise, hydrostatic expansion and turbulence. The model was run until a steady state was reached and used to examine the bubble size distribution, gas fluxes and acoustic scattering cross-sections. It was found that the model correctly reproduced the variation of bubble numbers with depth but failed to describe the shape of the size distribution.

Woolf & Thorpe (1991) developed a model similar to that of Thorpe (1984) to incorporate the effect of Langmuir circulation on bubble populations in order to investigate the bubble-mediated transfer of nitrogen, oxygen, carbon dioxide and argon in the upper ocean. Woolf (1993) examined a surface flux of bubbles and demonstrated the importance of relatively large bubbles entrained close to the ocean surface which were shown to contribute the majority of the bubble-mediated transfer velocity.

Thorpe *et al.* (1992) used a model very similar to that of Thorpe (1984) to investigate factors affecting the size distributions of bubbles in the ocean. They found that the shape of the mean size distribution of ambient bubble populations in the ocean remained reasonably consistent, but the concentrations of bubbles were dependent on temperature, gas saturation levels and the presence of particulates in the water.

Other very similar bubble tracking models have been used in studies not focused on breaking waves, e.g. Thorpe *et al.* (2003) to investigate bubble bands produced by Langmuir circulation, Weber *et al.* (2005) to estimate the gas transfer rate from bubbles generated by a ship wake and Leifer & Patro (2002) who formulated a model to explore the bubble mediated transport of methane from the sea bed to the ocean surface.

2.4 SPLASH-UP FROM BREAKING WAVES

As well as entraining air, wave breaking on all scales leads to the generation of a splash-up which is projected out in front of the advancing wave crest when the overturning wave strikes the undisturbed water surface downstream. The splash-up from a breaking wave is perhaps the most impressive visual aspect of waves breaking on our coastlines, often reaching heights greater than that of the incident wave. However, despite their spectacular nature, very little is known about splashes from breaking waves and although many studies have commented on the phenomenon, there have been few detailed investigations.

Peregrine (1981) wrote an interesting discursive article on some fundamental aspects of splashes and presented a simple one-dimensional model of the splash-up process. Peregrine (1983) proposed 3 possible mechanisms for the origin of the water of the primary splash-up generated at the plunge point of a plunging wave and these are shown in figure 2.8. However, while many studies have drawn conclusions on which of these mechanisms is valid, there is much disagreement and no definitive answer has been achieved (table 2.4).

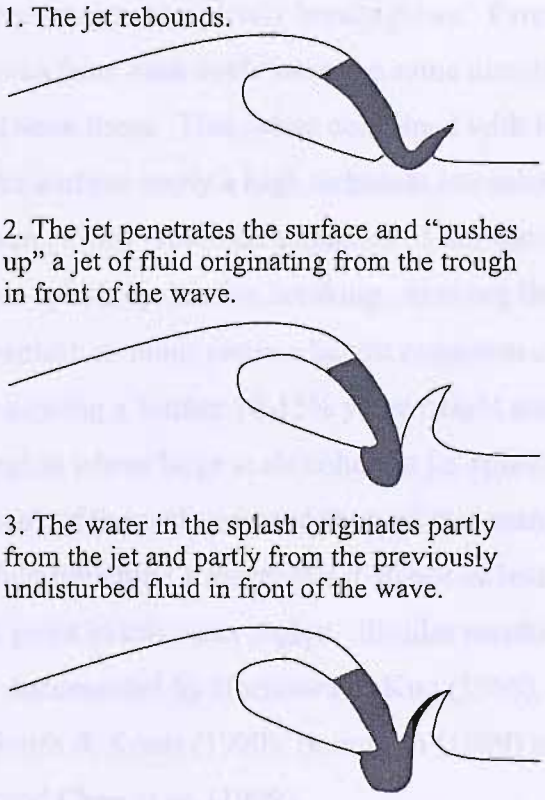

Figure 2.8 Splash-up mechanisms (based on Peregrine (1983), figure 4).

Table 2.4 Previous studies of the splash-up mechanism.

Author	Type of Model	Technique	Origin of Splash (Mechanism of Peregrine (1983), see figure 2.8)
Basco (1985)	Laboratory	Video, Photographic	Splash originates from trough (2)
Jansen (1986)	Laboratory	Video	Predominantly from the jet (1/3)
Bonmarin (1989)	Laboratory	Video	Initially from trough but later from jet also (2/3)
Tallent *et al.* (1990)	Laboratory	Video	'Spray' from jet and trough (3) 'Core' from the trough fluid (2)
Lin & Hwung (1992)	Laboratory	Photographic	Jet rebounds (1)
Abadie *et al.* (1998)	Numerical	VOF Method	Predominantly from trough (2/3)
Chen *et al.* (1999)	Numerical	VOF Method	Splash originates from trough (2)
Christensen & Deigaard (2001)	Numerical	Large Eddy Simulation	Jet rebounds (1)
Landrini *et al.* (2005)	Numerical	SPH Method	Combination of jet and trough (3)

It has been shown by many authors (Miller 1976; Jansen 1986; Nadaoka 1986; Nadaoka *et al.* 1989; Bonmarin, 1989; Tallent, 1990) that upon falling back to the water surface, the splash-up generated by the initial overturning motion pushes up a smaller secondary splash-up. This secondary splash-up is projected forward before falling back to the water surface where it creates strong vortex-like motions and generates another, smaller jet-splash cycle. Jansen (1986) showed that as many as 8 of these jet-splash cycles may occur before the organised motion completely breaks down. Peregrine (1983) noted that the vortex-like motions from each cycle have the same direction of rotation, leading to high rates of shear between them. This, when combined with the shear arising where each jet impacts the water surface imply a high turbulent intensity and high levels of energy dissipation. Jansen (1986) presented estimates of the wave height attenuation from each consecutive jet-splash cycle after breaking, showing that in a plunging breaker the first two jet-splash motions cause a height reduction of 20-25% each, with following motions each causing a further 10-15% wave height attenuation. Svendsen *et al.* (1978) defined the region where large scale coherent jet-splash motions take place as the "outer breaking region" of the surf zone and showed that many waves lose 50% of their breaking height while travelling a horizontal distance of less than 10 times the water depth at the break point in this outer region. Similar results of the initial wave height decay have been documented by Horikawa & Kuo (1966), Sawaragi & Iwata, (1974), Miller (1976), Smith & Kraus (1990), Bonmarin (1989) and Basco (1985), Iwata & Tomita (1992) and Chen *et al.* (1999).

Galvin (1969) made laboratory measurements of the horizontal distance between the "plunge point" of overturning waves and the touchdown point of the primary splash (figure 2.2). His measurements showed that the primary splash-up travels a horizontal distance between 2 and 6 times the breaking wave height and that this splash distance is approximately equal to the distance between the point of wave breaking and the "plunge point". Similar measurements were made by Smith & Kraus (1990) and Sawaragi & Iwata (1974) although their results were less conclusive than those of Galvin (1969).

Yasuda *et al.* (1999) made measurements of three types of laboratory waves breaking over a submerged reef structure. His results suggested that the amount of splash generated by a breaking wave increases with the size of the overturning jet formed at the wave crest. In addition, Yasuda *et al.* (1999) noted an approximately linear relationship between the wave height transmission coefficient and the dimensions of the primary splash-up.

Probably the most comprehensive investigation of splash-up was completed by Tallent *et al.* (1990) who completed an elegant flow visualisation study of laboratory waves breaking on an emergent slope. Tallent *et al.* report that the splash-up phenomenon typically commences as a fine fan-shaped "spray", followed by the eruption of a near vertical splash-up "core". The terms "spray" and "core" were selected according to observations of high and low air content respectively, although to this author's knowledge, no measurements of the void fraction in the splash-up from breaking waves have been made prior to the current study. Tallent *et al.* (1990) also made detailed measurements of the temporal evolution of the crest level of several consecutive jet-splash cycles similar to those of Bonmarin (1989) who found that the splash elevation decreases with each successive jet-splash cycle.

2.5 ENERGY DISSIPATION IN BREAKING WAVES

As noted in chapter 1, breaking is the predominant mechanism for the dissipation of wave energy in both shallow and deep water. Knowledge of the rate of energy dissipation in breaking waves is highly important as it has application in many areas, including the following.

- Surface wave energy is transferred to other processes such as generation of ocean currents and mixing of surface layers (for example, Agrawal *et al.* 1992).
- Models of post-breaking wave height in the surf zone (Thornton & Guza, 1983).
- Estimation of forces on coastal structures (U.S. Army Corps of Engineers, 2002).
- Limiting the height of ocean waves which is relevant to ocean wave models such as the WAM Model (WAMDI Group, 1988; Komen *et al.*, 1994).
- Design of submerged coastal structures such as submerged breakwaters or artificial surfing reefs (Black & Mead, 2001; Van der Meer & Angremond, 1992).

Consequently many researchers have commented on the energy dissipated by the wave breaking process although no complete model is currently available.

Svendsen *et al.* (1978) divided the area inshore of the break point in shallow water into two regions. The region immediately inshore of the break point is known as the "outer breaking region" and is characterised by large energy loss and rapid, large-scale variations of wave shape. As the wave propagates further, the large scale deterministic flow breaks up into smaller scale motions and the wave resembles a system of periodic bores. This is termed the "inner breaking region" and it extends to the shoreline where run-up begins. Many authors have modelled the post-breaking wave height decay using a steady state equation governing energy balance for waves advancing toward shore such that

$$\frac{\partial EC_g}{\partial x} = -\delta(x), \tag{2.3}$$

where δ is the energy dissipation rate per unit surface area, E represents the wave energy per unit surface area and C_g is the group velocity.

Many different approaches have been utilised to estimate δ, (Mizuguchi, 1980; Dally *et al.*, 1985; Tsai *et al.*, 2001) but the most common method, first suggested by Le

Mehaute (1962) is to approximate the broken wave as a propagating bore or hydraulic jump such that

$$\delta = \frac{\rho_w g}{4} \frac{(BH)^3}{h^2} Q, \tag{2.4}$$

where B is a breaking coefficient related to the fraction of the wave height covered by aerated water and Q is the volume discharge per unit area across the bore.

While this formulation is seen to perform well within the inner breaking region, agreement is less good in the outer breaking region where, as noted in section 2.4, waves can lose 50% of their breaking height while travelling a distance of less than ten times the water depth at breaking h_b (Svendsen *et al.*, 1978). Consequently a number of investigators have attempted to make measurements of the initial wave energy dissipation due to breaking in the outer breaking region and concluded that the initial wave decay is dependent on breaker type and is greater for plunging waves than spilling (Raichlen & Papanicolaou, 1988). A summary of the published values of initial energy dissipation due to breaking in shallow water is given in table 2.5.

Table 2.5 Previously reported estimates of energy dissipation in shallow water breaking waves.

Author	Method	Results
Svendsen *et al.* (1978)	Regular waves on laboratory beach	50% wave height decay over distance of approx $10h_b$.
Jansen (1986)	Regular waves on laboratory beach	50-60% wave height decay in outer region for plunging and spilling waves.
Svendsen (1984)	Theoretical model	35% wave height decay in outer region. Only 1/3 of this due to real dissipation, remainder due to redistribution of energy.
Chanson & Lee (1997)	Plunging waves on laboratory reef	Plunging breakers dissipate 20-60% of incident wave energy. Dissipation rate comparable to drop structure. Energy dissipation rate increases with bubble penetration depth.
Yuksel *et al.* (1999)	Plunging waves on laboratory reef	55-75% energy dissipation. Dissipation increases with decreasing H_o/L_o. Dissipation increases with bubble penetration depth.
Kapdasli & Turker (2002)	Regular waves on laboratory reef	70-85% energy dissipation in plunging breaker. 40% energy dissipation in spilling breaker.
Yuksel & Kapdasli (1994)	Regular waves on laboratory beach	60% of plunging wave energy dissipated at the plunge point

The energy dissipation rate in deep-water breaking waves is an essential parameter in wind-wave models and for modelling of air-sea interaction. Rapp & Melville (1990) suggested that a large fraction of the momentum flux from the atmosphere to the ocean is associated with wave generation, and the majority of this energy (around 95%) is dissipated by breaking within the generation region (Melville, 1994). While the input of wind energy to the wave field is well known, the rate of energy dissipation is uncertain. A number of approaches have been used to estimate the rate of energy dissipation and many different formulations have been suggested, some of these are summarised in table 2.6.

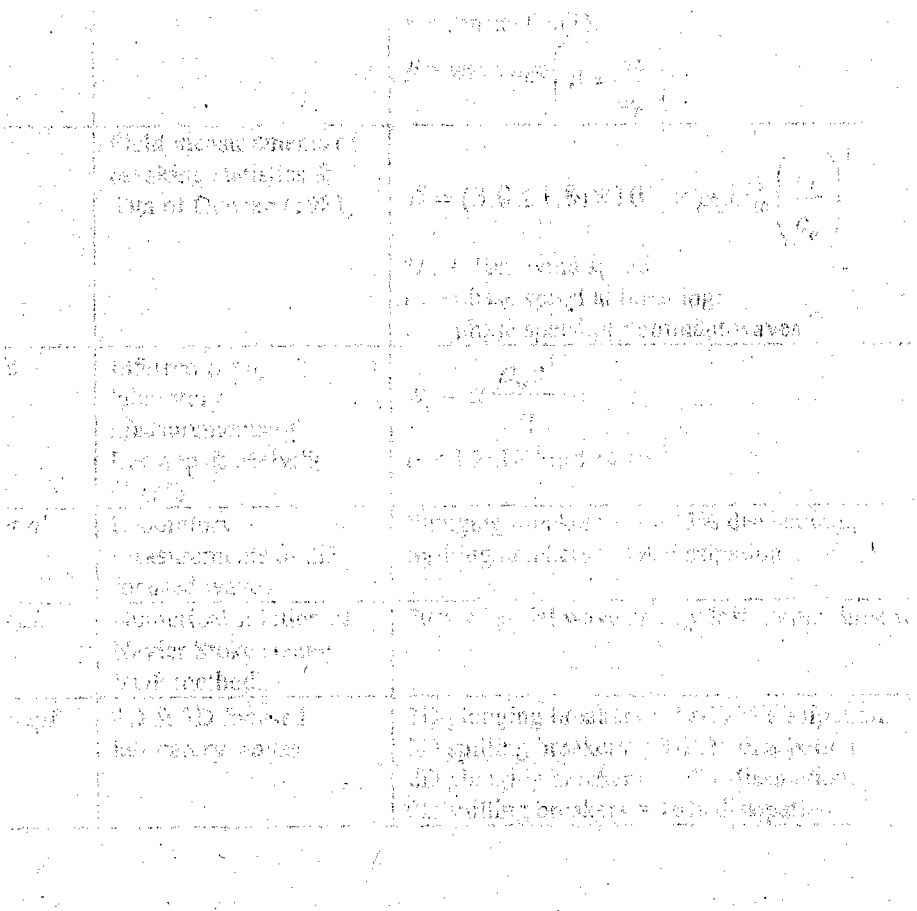

Table 2.6 Previously reported estimates of the energy dissipation rate in deepwater breaking waves.

Author	Method	Results
Hasselmann (1974)	Theoretical model	$\delta = 2.21\times10^{-3}\rho_w u_*^3$ (As presented by Zhao & Toba, 2001). δ = energy dissipation rate per unit surface area. u_* = air friction velocity.
Duncan (1981)	Quasi-steady laboratory wave	$\varepsilon_l = \frac{0.009\rho_w c^5}{g\sin\theta}$ for 10°<θ<15° ε_l = energy dissipation rate per unit crest length. c = phase speed of wave. θ = angle of inclination of breaking region.
Duncan (1983)	Quasi-steady laboratory wave	$\varepsilon_l = \frac{0.0075\rho_w c^5}{g\sin\theta}$ for 6.5°<θ<14°
Melville & Rapp (1985)	Laboratory measurements of focused waves.	Up to 40% of the incident wave energy lost through breaking.
Phillips (1985)	Equilibrium range theory.	$\delta \approx 2.36\times10^{-3}\rho_w u_*^3 \ln(r^{1/2}\beta)$ (As presented by Zhao & Toba, 2001). r = constant O(1). β = wave age $\left(\beta = \frac{gu_*}{\omega_p}\right)$.
Thorpe (1993)	Field measurements of breaking statistics & data of Duncan (1981)	$\delta = (3.0\pm1.8)\times10^{-5}\times\rho_w U_{10}^3\left(\frac{c_b}{c_o}\right)^5$ U_{10} = 10m wind speed. c_b = phase speed at breaking. c_o = phase speed of dominant waves.
Melville (1994)	Inferred from laboratory measurements of Loewen & Melville (1991)	$\varepsilon_l = \alpha\frac{\rho_w c^5}{g}$ $\alpha = 3.2\text{x}10^{-3}$ to $1.6\text{x}10^{-2}$
Kway *et al.* (1998)	Laboratory measurements of 2D focused waves.	Plunging breakers = 14-22% dissipation. Spilling breakers = 4% dissipation.
Chen *et al.* (1999)	Numerical solution of Navier Stokes using VOF method.	70% of initial wave energy lost within three wave periods.
Wu & Nepf (2002)	2D & 3D focused laboratory waves	3D plunging breakers = 18-32% dissipation. 3D spilling breakers = 9-12% dissipation. 2D plunging breakers = 16% dissipation. 2D spilling breakers = 10% dissipation.

2.5.1 Energy Dissipation Due To Air Entrainment

Führböter (1970) showed that the work done against buoyancy forces in order to entrain air into the water column must contribute significantly to the total energy dissipated during wave breaking. Führböter developed a very simple model for the energy dissipation due to air entrainment which assumed a uniform distribution of air bubbles throughout the water column. Flow bulking due to the addition of air voids raises the level of the free surface by Δh (figure 2.9). The energy required to raise the water level can be calculated and is taken to be equal to the potential energy of the entrained air volume

$$E_b = \rho_w g dx \left(\alpha \frac{h^2}{2} + \frac{(\alpha h)^2}{2(1-\alpha)} \right), \tag{2.5}$$

where α is the void fraction in the water column

$$\alpha = \frac{\Delta h}{h + \Delta h}. \tag{2.6}$$

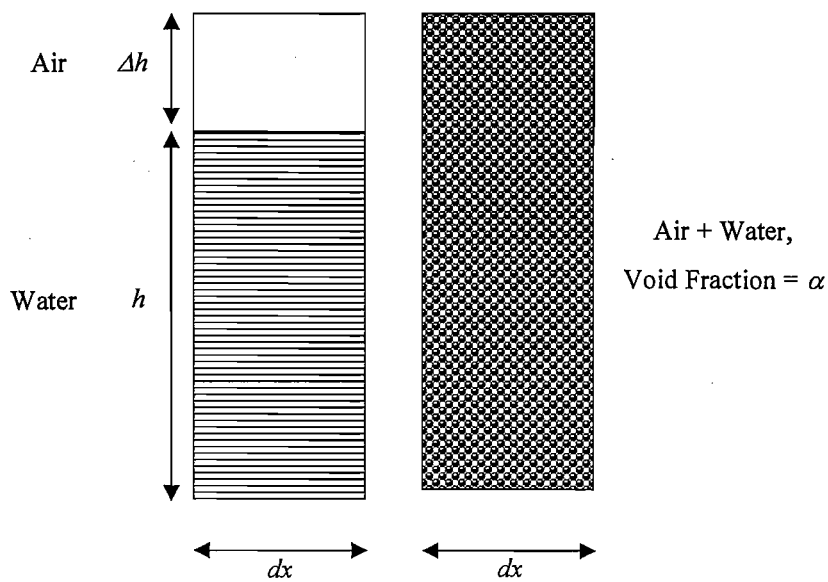

Figure 2.9 Definition sketch for the model of Führböter (1970) (after Führböter (1970), figure 1).

In reality, the situation is complicated by the fact that there is a non-uniform distribution of air bubbles and the distribution of air in the water column varies rapidly. However as

a first approximation, this simple model demonstrates the importance of air entrainment to the energy dissipation in both spilling and plunging breakers.

Lamarre (1993) calculated moments of his measured void fraction results in order to determine the work required to keep the air entrained against buoyancy. Lamarre's results showed that between 30% and 50% of the energy dissipated by breaking was expended in entraining air bubbles.

Hoque (2002) completed similar calculations in order to compare the variation in wave energy through the surf zone with the potential energy of the entrained bubbles, and estimated that air entrainment was responsible for approximately 20% of the total energy dissipated during breaking for both plunging and spilling waves.

Loewen *et al.* (1996) showed that the amount of energy required to submerge the bubbles they measured in spilling deep-water laboratory waves accounted for just 0.05 to 0.4% of the total energy dissipated in breaking. This result is considerably smaller than any other published data and the authors suggested that this discrepancy was due to the very gentle nature of the waves under examination.

Loewen & Melville (1994) presented a plot of the energy dissipated by breaking deep-water laboratory waves against the volume of air enclosed by the overturning jet of a plunging wave. Their results showed a strong correlation with the energy dissipation increasing approximately linearly as the volume of air increased. Based on this correlation, Loewen & Melville suggested that the amount of energy dissipated by breaking and the volume of entrained air are strongly related. Support for this conclusion is given by Yuksel *et al.* (1999) and Chanson & Lee (1997) who made measurements of the maximum bubble penetration depth and showed that it scales with the amount of energy dissipated by breaking.

2.5.2 Energy Dissipation Due To Splash-up

It was suggested by Peregrine (1983) that the strong vortex-like motions generated by consecutive jet-splash cycles are responsible for the generation of significant turbulence and high levels of energy dissipation. As noted in section 2.4, Jansen (1986) made

measurements of the wave height decay associated with each successive jet-splash cycle, however the dissipation measured by Jansen (1986) was associated with a large number of different mechanisms through the outer breaking region and was not entirely due to the generation of splash-up. The measurements of Yasuda *et al.* (1999) showed an approximately linear relationship between the wave height transmission coefficient and the height and width of the primary splash-up, suggesting that the generation of splash is important to the energy dissipated at breaking. However to this author's knowledge, no detailed measurements of the volume and distribution of the splash-up have been made to date and so direct estimates of the energy required to raise the potential energy of the splash generated by breaking waves are not currently available.

2.6 SUMMARY OF THE PRESENT STUDY

Due to its highly complex nature, the process of wave breaking is far from fully understood and there are many aspects where further elucidation can be gained from experimental study, though not all can fall within the scope of the current work. This chapter has given an outline of the current state of knowledge on the subjects of air entrainment, splash and energy dissipation in breaking waves. The work presented in the remainder of this thesis provides new data on these fundamental aspects of the wave breaking process which will be of use to future investigators in many fields.

The review of existing literature has identified a number of areas where there are gaps in the research that are relevant to the current study. These are summarised below and a brief description is given of how the work carried out for this thesis provides new information to address them.

The details of the apparatus and instrumentation used in the experiments presented in this thesis are described in chapter 3. The design of the optical fibre phase detection probes that are used to make the aeration measurements presented in later chapters are described in detail. In addition, a series of instrument calibrations that were completed to ensure the accuracy and applicability of the measurement techniques are presented.

It has been demonstrated by a number of previous authors that waves dissipate a significant amount of their incident energy during breaking by generating turbulence,

noise, air entrainment and splash, but at present there is no complete model that describes this process and the relative importance of each mechanism. Chapter 4 outlines a series of experiments which were designed to examine the energy dissipated by waves breaking over a submerged reef structure and investigates how this value varies with the wave breaking intensity. Further work presented in chapter 5 investigates the contribution of the air entrainment mechanism to the total energy dissipated during breaking and provides the first direct estimates of the energy expended in generating splashes.

It was noted in section 2.3.3 that while many studies on air entrainment in breaking waves have been completed, little detailed information about the very dense bubble plumes created immediately after wave breaking is available due to the practical difficulties of making such measurements and the limitations of previously used measurement techniques. The current study makes use of novel, optical fibre phase detection probes which detect the presence of air-water interfaces over extremely small areas at high frequencies to overcome these problems. Chapters 5 and 7 present measurements of the time-varying void fraction field in the dense bubble plumes entrained by breaking laboratory waves to a level of detail that has not been previously achieved and which allow various characteristics of the bubble plume to be examined. It is seen that the properties of the plume vary rapidly in space and time but behave in a broadly similar manner independent of the breaker characteristics. The optical fibre technique also allowed the first measurements of the temporal variation of the void fraction field in the splash-up generated by wave breaking to be made.

Chapter 6 goes on to present measurements of the bubble size distribution in dense, breaker generated bubble plumes, again using optical fibre phase detection probes. The results show that the distribution of bubble sizes varies rapidly with distance from the active air entrainment region of the breaking wave as the plume is carried downstream and evolves under the influence of buoyancy and dissolution.

A review of the existing knowledge of air entrainment in fresh and seawater showed that while the majority of authors agree that some differences should be expected in the characteristics of bubble plumes entrained in the two solutions, there is very little consensus about the nature of these differences. This knowledge is of great importance

as almost all laboratory studies of oceanic and coastal processes are completed in freshwater. Consequently it is essential that any differences in the entrainment of air by model scale breaking waves in freshwater and seawater are understood if we are to assess the validity of laboratory tests designed to reproduce oceanic processes. Chapter 7 of this thesis presents detailed measurements of the time-varying void fraction fields beneath breaking waves in artificial and natural seawater, to this author's knowledge for the first time, and compares them to the freshwater data detailed in chapter 5. It is seen that the bubble plumes behave in a very similar manner in all three water types confirming that freshwater measurements are reasonably valid at the current scale, although an additional population of very small bubbles which accumulate over several wave periods was observed in the seawater cases. Chapter 7 also discusses the issues involved in scaling laboratory data on air entrainment in breaking waves to field conditions and a numerical bubble model is developed to examine the evolution of breaker generated bubble plumes at different scales.

The conclusions made on the basis of the research presented in chapters 2-7 are discussed in chapter 8 along with suggestions for future work.

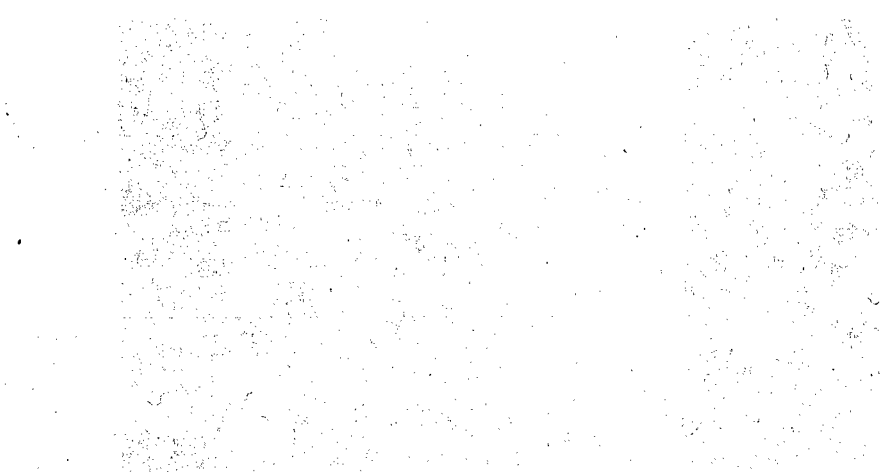

CHAPTER 3 – EXPERIMENTAL EQUIPMENT AND INSTRUMENT CALIBRATIONS

3.1 INTRODUCTION

The details of the experimental apparatus and instrumentation used in the experiments presented in this thesis are described in this chapter. The optical fibre phase detection probes that are used for the aeration measurements presented in chapters 5, 6 and 7 are described in detail and instrument calibrations are discussed in section 3.5.

3.2 APPARATUS DESCRIPTION

3.2.1 Wave Flume

The experiments presented in chapters 4, 5, 6 and 7 were conducted in a wave flume at the University of Southampton, School of Civil Engineering and the Environment. The flume is glass-walled, measures 17 m in length by 0.44 m wide and is filled with water to an optimum depth of 0.7 m (figure 3.1).

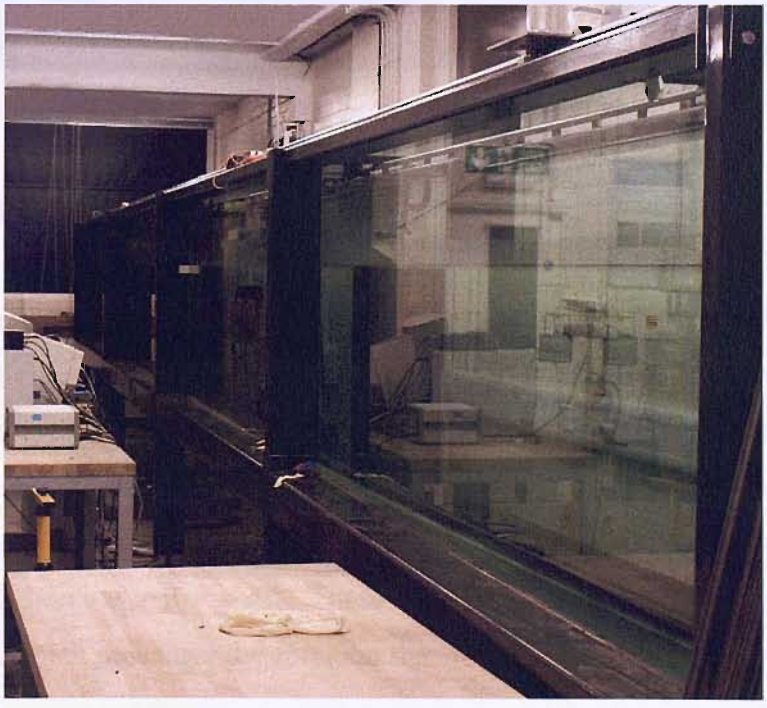

Figure 3.1 Photograph of the wave flume.

One end of the flume is equipped with a wave generator which is described in section 3.2.2. The opposite end of the wave flume is equipped with an absorbing beach designed to reduce the reflections present in the flume during tests and made using highly porous, wedge shaped foam blocks (figure 3.2). The efficiency of this beach was examined and found to be very good, with the reflection coefficient K_r varying from 2% to 13% (section 3.5.1).

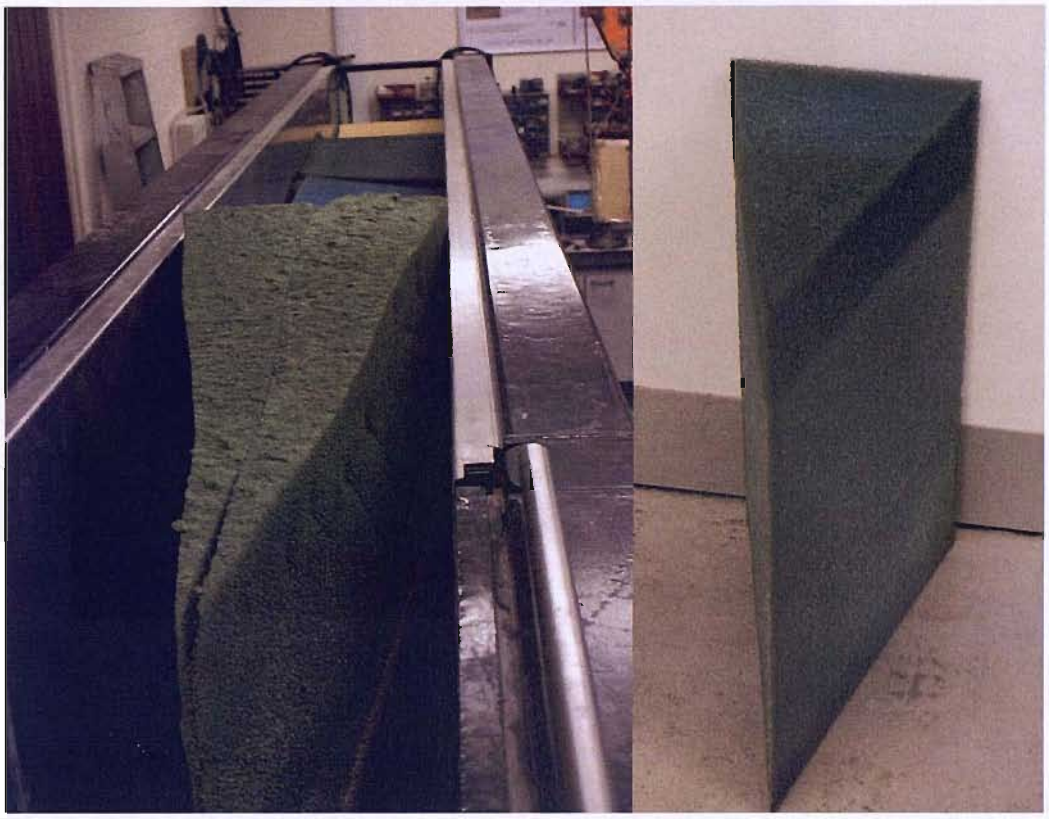

Figure 3.2 Photograph of the foam from the absorbing beach.

3.2.2 Wave Generation

The wave flume is equipped with a dry back, flap-type wavemaker manufactured by Edinburgh Designs. The wave paddle is driven by an electric servo-motor via a metal belt which runs over a curved guide on the top of the paddle. A piezo-electric transducer which senses the force acting on the front of the paddle is located between the curved guide and the paddle. The position of the wave paddle is sensed by an optical encoder mounted on the motor-shaft. These components form part of a force-feedback control system which measures the force on the wave paddle from any reflected waves

and corrects the motion of the paddle to absorb them, making the wave field predictable even with highly reflective models.

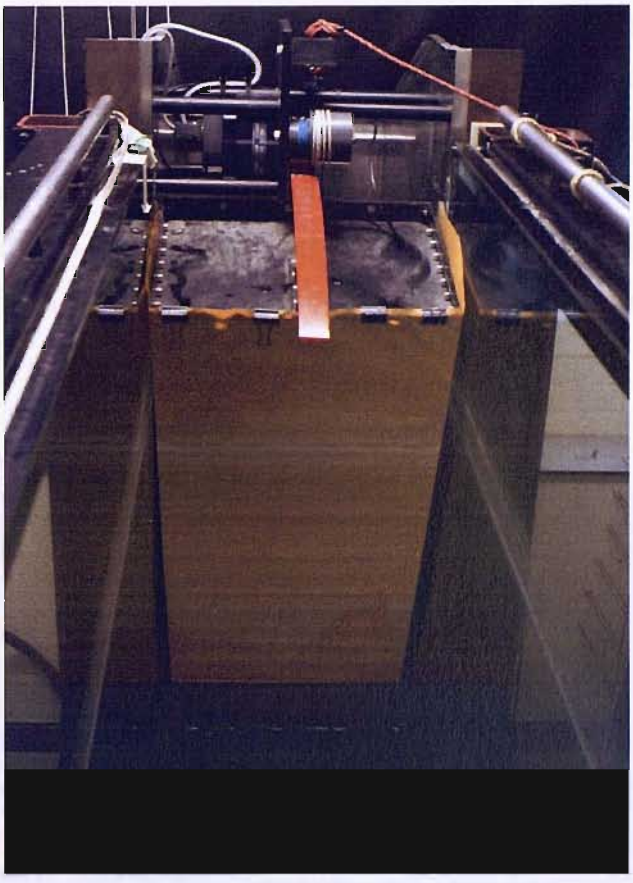

Figure 3.3 Photograph of the wavemaker.

The wavemaker motion is controlled by a sinusoidal command signal created using a PC equipped with a D/A card (section 3.3.1). A series of transfer functions to calculate the generated wave heights from the magnitude of the command signal were measured to ensure that the wave conditions were predictable for each test.

3.2.3 Reef Structure

For the tests described in this thesis, a submerged reef was constructed using grey high-density plastic with a thickness of 15 mm. The reef has a height of 618 mm and a front gradient of 1:10 which drops away vertically, immediately beyond the reef crest. Initially it was found that large uplift forces generated by waves passing over the reef lifted the structure from the bottom of the flume and caused the reef surface to flex considerably. To overcome this, the surface of the reef was heavily braced along its

underside and the structure was secured to the bottom of the flume using vacuum glass lifters (figure 3.4).

The reef was designed to have a zero crest width. This meant that by varying the water level and wave conditions, waves could be made to break at the top of the reef where they would plunge straight into deep water and immediately reform into a non-breaking wave, with no interaction between the bubble plume generated by the breaking wave and the flume bed. In this way the initial breaking process of the wave was isolated, with only a single jet-splash motion occurring before the wave reformed back into a non-breaking wave.

Figure 3.4 Photograph of the submerged reef structure.

3.3 INSTRUMENTATION

3.3.1 Data Acquisition

Two different data acquisition systems were used to drive equipment and collect data during the experiments described in chapters 4, 5, 6 and 7, and these are detailed below.

3.3.1.1 CED 1401

The experiment described in chapter 4 uses a CED 1401 data acquisition board installed in a personal computer. The 1401 is a 12 bit, 16 channel standalone data acquisition system which was controlled using custom written software.

3.3.1.2 Measurement Computing PCI-DAS6070

The experiments described in chapters 5, 6 and 7 used a Measurement Computing PCI-DAS6070 data acquisition card to control the wave paddle and sample the experimental data. The DAS6070 has a maximum sample rate of 1.25 MHz across 8 differential channels. The card was installed in a Novatech Personal Computer equipped with 1 Gb of RAM, a 2.6 MHz AMD processor and a 40 Gb hard drive. The Visual Basic based SoftWire 6.0 program was used to control the wavemaker and acquire data.

3.3.2 Free Surface Measurements

Measurements of the free surface elevation during the experiments described in chapters 4, 5 and 6 were made using double-wire, resistance-type wave gauges which were calibrated daily. These wave gauges were built at the University of Southampton and consist of two parallel Nichrome wires, 3.2 mm in diameter and 620 mm long with a separation of 20 mm. The wave gauges were connected to an array of wave monitors also constructed at the University of Southampton and sampled using the data acquisition hardware described in section 3.3.1.

3.3.3 Flow Visualisation Equipment

3.3.3.1 Digital Video Camera

A PULNIX TM-6710 monochrome digital video camera was used to record video footage of waves breaking over the crest of the submerged reef structure. The camera allows 8-9 seconds of footage at a frame speed of 120 fps and produces an image quality of 648(H) x 484(V) pixels. The camera was controlled by a Dell personal computer equipped with 512 Mb of RAM, an Intel Pentium 4 processor and an 18.5 Gb hard drive.

3.3.3.2 Digital Still Camera

A Nikon D100 digital camera with an image quality of 6.1 megapixels, equipped with a Nikon 28-105 mm telephoto lens was used to record still images of the experiments. The camera was also fitted with a Nikon MB-D100 Multi-Function Battery Pack which allowed the camera shutter to be controlled using the DAS6070 data acquisition system (section 3.3.1.2).

3.3.3.3 Lighting

In order to provide sufficient lighting to allow the use of the high shutter speeds necessary to obtain clear pictures of the wave breaking process and freeze the small-scale, high velocity motion, up to ten 500 W spotlights were used around the wave flume. A number of different lighting schemes and backgrounds were employed to ensure optimum conditions for the visualisation of different aspects of the flow.

3.3.4 Wave Detection Probe

A single tip conductivity probe based on the design of Chanson (1988) was constructed in order to measure the arrival time of waves at the break point. The probe makes use of the difference in the electrical conductivity of air and water to detect the arrival of the wave crest at the break point, the position of which was initially determined using video analysis (figure 5.2). The probe design is shown in figure 3.5. The inner electrode consists of an insulated nickel wire with a diameter of 0.25 mm, while the outer electrode is a stainless steel tube with an outer diameter of 1.1 mm.

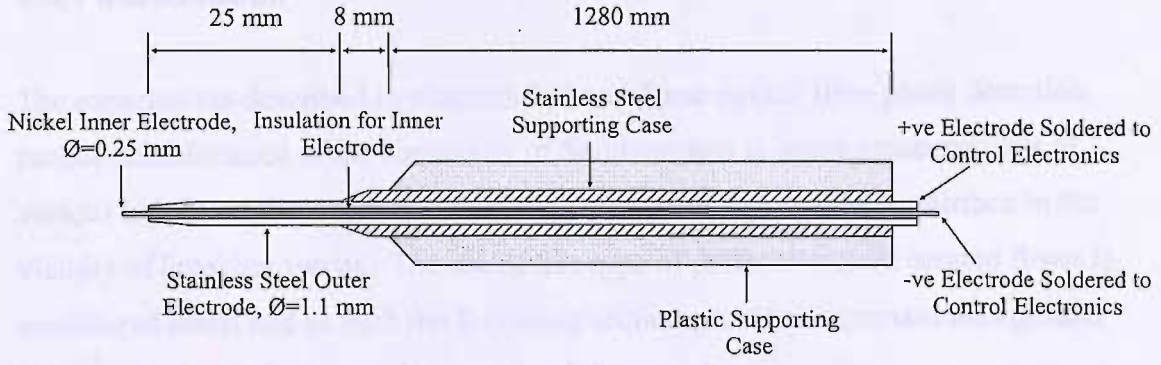

Figure 3.5 Conductivity wave detection probe.

3.3.5 Horizontal Traverse

A simple horizontal traverse (figure 3.6) was mounted on rails running along the top of the wave channel walls and used to accurately position the optical fibre phase detection probes used to make measurements of bubbly flow in chapters 5, 6 and 7. The traverse had a total horizontal travel of 150 mm and was equipped with a 6.0V stepper motor which could be controlled using the DAS6070 data acquisition board (section 3.3.1.2) to position the instruments with an accuracy of ±1 mm.

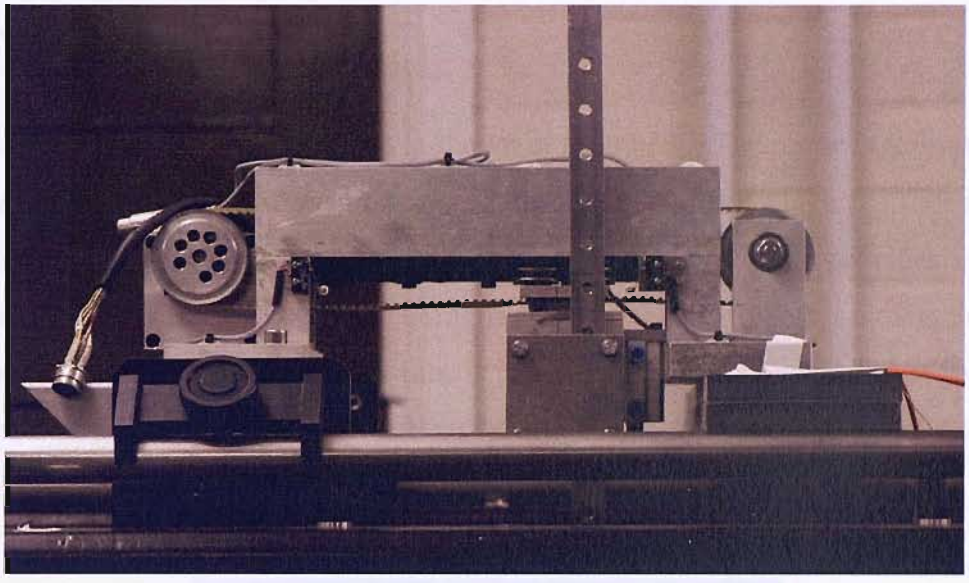

Figure 3.6 Photograph of the horizontal traverse.

3.4 OPTICAL FIBRE PHASE-DETECTION PROBES

3.4.1 Introduction

The experiments described in chapters 5, 6 and 7 use optical fibre phase detection probes manufactured at the University of Southampton to make measurements of various aspects of the two-phase flow both above and below the free surface in the vicinity of breaking waves. The use of this type of probe in violent aerated flows is considered novel and as such the following section provides important background information on the nature and operation of these probes.

3.4.2 Basic Description

Optical fibre probes are highly sensitive, practically un-intrusive instruments that detect the presence of air or water at their tip in a two-phase flow. Probes of this type have been used in the chemical industry for phase detection in many different, predominantly uni-directional two-phase flow conditions. Previous studies have examined flows such as air-bubble columns (Chabot, 1992), fixed bed reactors (Boyer *et al.*, 2002), hydraulic jumps (Murzyn *et al.*, 2004) and even liquid sprays (Hong *et al.*, 2004). Cartellier (2001) suggested that they have advantages over other types of phase detection probe because their intrinsic response time is much shorter than the typical time scales common in multiphase flows.

An example of a double tipped probe is shown in figure 3.7. The probe is a simple instrument, consisting of a shaped 62.5/125 μm multimode fibre which protrudes approximately 2 mm from a narrow aluminium tube arrangement that provides protection and structural support to the fragile fibre. The outer tube has a diameter of 3.2 mm and the diameter of the inner tube is just 1.1 mm. The exposed end of the fibre is shaped into a flattened conical profile by heating and then stretching the fibre to achieve a final tip diameter of approximately 20 μm as shown in figure 3.8.

Figure 3.7 Double-tipped optical fibre phase detection probe.

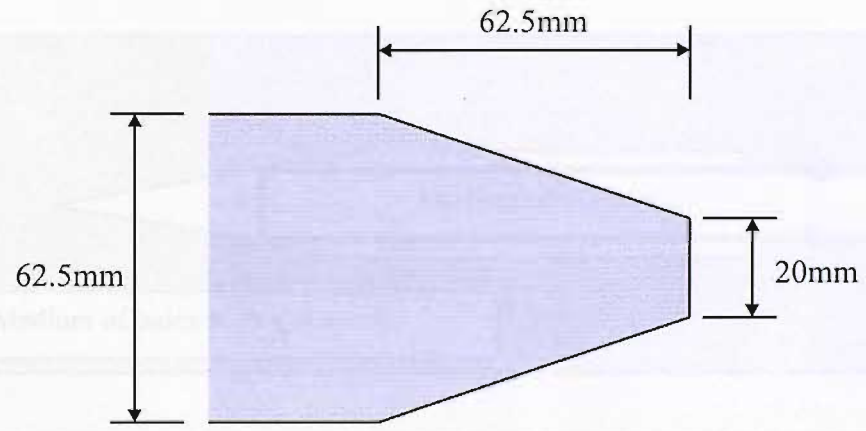

Figure 3.8 Probe tip geometry.

The unexposed end of the fibre is connected to an opto-electronic unit manufactured by the French company, RBI which essentially consists of a light source and an optical amplifier with a temporal resolution of 0.0033 μs. This high temporal resolution, along with the small size of the probe tip allows the successful detection of small, fast-moving bubbles.

In order to detect the medium in which the probe tip is placed, light is shone along the optical fibre from the opto-electronic unit to the sensitive conical tip of the probe which acts as a Descartes prism. When the probe tip is submerged in a medium with a low refractive index n_1 (i.e. air, n_1=1.003), much of the light from the opto-electronic unit is reflected by the walls of the prism back along the optical fibre (figure 3.9). Alternatively, when the probe is immersed in a medium with a relatively high refractive index n_2 (i.e. water, n_2=1.33), the incident light is diffracted into the external medium and little or no light is reflected back to the opto-electronic unit. Changes in the intensity of the light returning along the fibre are detected by the optical amplifier which produces a varying output voltage. This signal can be interpreted to provide a phase indicator function s which is high (s=1) when the probe is in air and low (s=0) when the probe is in water using a simple signal threshold technique (figure 3.10).

The probe can therefore be used to record a time series of phase indicator functions which indicate the nature of the medium in which the probe tip is located as it varies with time in a two-phase flow, and from this data various characteristics of the flow can be calculated.

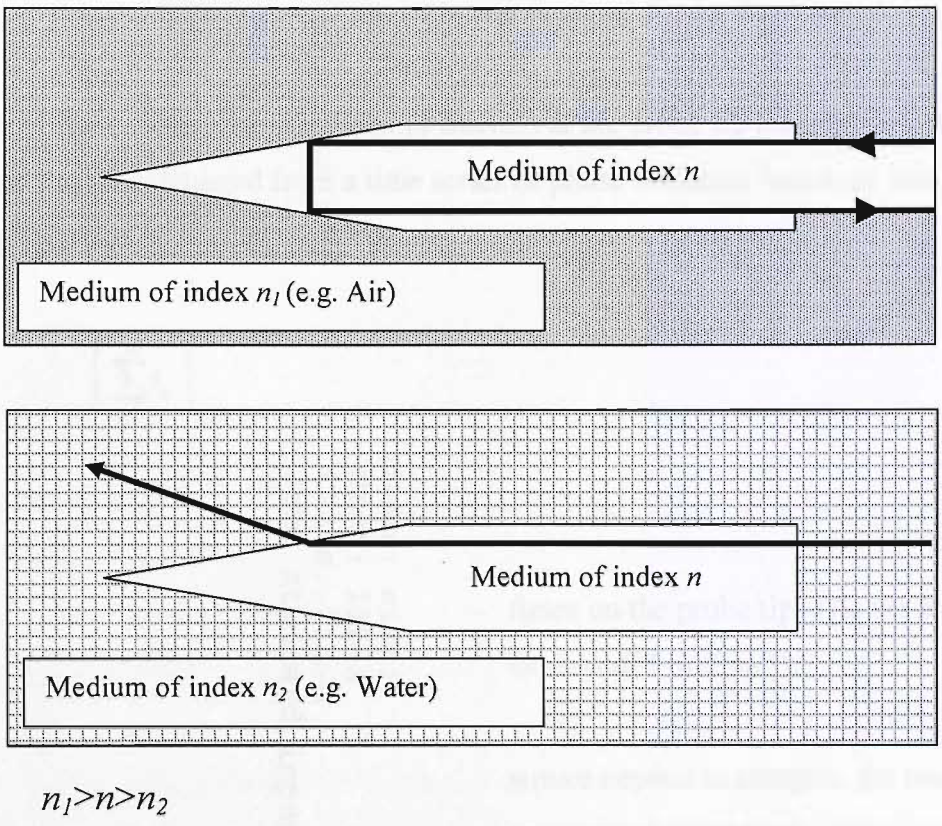

Figure 3.9 Operation principle of the optical fibre phase detection probes.

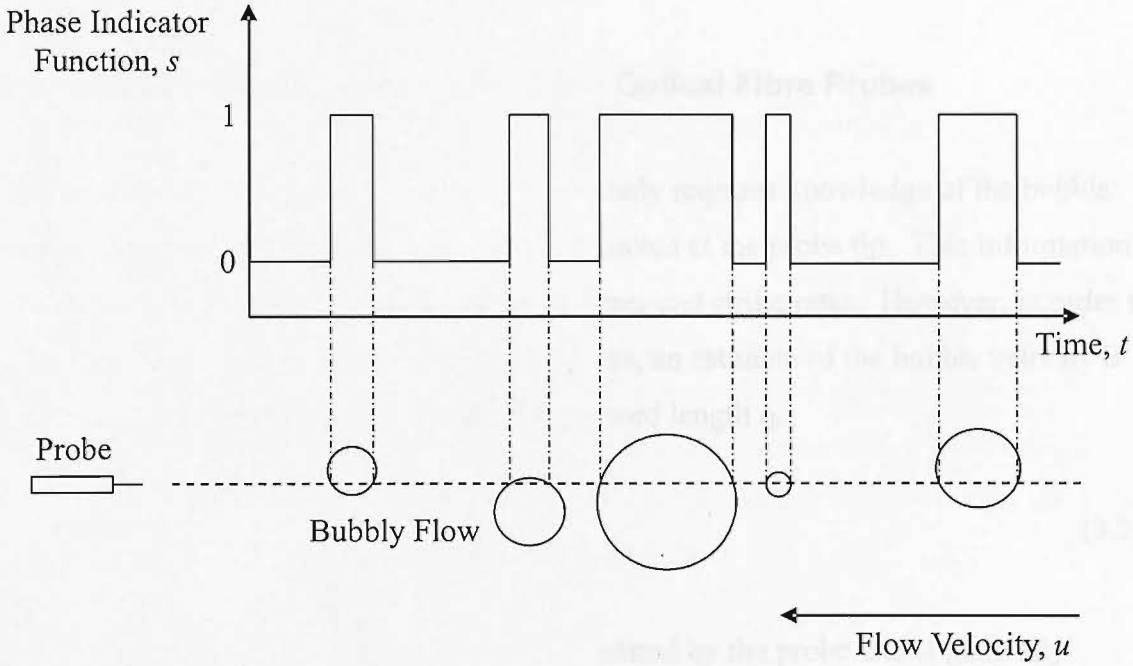

Figure 3.10 Idealised time series of phase indicator functions produced by an optical fibre probe in a uni-directional flow.

3.4.3 Void Fraction Measurements Using Optical Fibre Probes

Estimates of the time-averaged local void fraction at the probe tip location in a two-phase flow can be calculated from a time series of phase indicator functions using the following equation

$$\alpha(\%) = \left(\frac{\sum_{i=1}^{n} t_a}{T_t} \right) \times 100, \tag{3.1}$$

where t_a represents the individual air residence times on the probe tip, T_t is the total sampling duration and n is the number of bubbles recorded in time T_t.

To determine the time of bubble arrival and departure needed to compute the residence time of each bubble detected by the probe, it is necessary to process the time series of output voltages from the optical amplifier using a thresholding technique as described in section 3.4.5.

3.4.4 Bubble Size Measurements Using Optical Fibre Probes

The void fraction calculation discussed above only requires knowledge of the bubble arrival and departure times for each bubble detected at the probe tip. This information allows the computation of bubble residence times and strike rates. However, in order to obtain size information about individual bubbles, an estimate of the bubble velocity is required to allow a calculation of the bubble chord length l_b,

$$l_b = t_a v_i . \tag{3.2}$$

The chord length is the bubble dimension measured by the probe and is generally smaller than the actual bubble diameter (figure 3.11). Statistical corrections designed to convert chord length to bubble diameter probability distributions are discussed in 6.3.1.

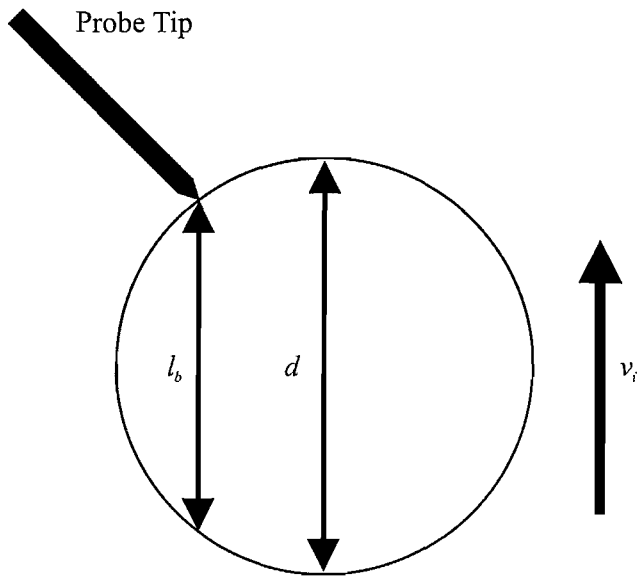

Figure 3.11 Definition of bubble chord length.

In some steady flows, chord length estimates have been computed by assuming that all bubbles travel at a velocity equal to the known flow velocity (Chanson *et al.*, 2004; Waniewski *et al.*, 2001). However in highly turbulent, unsteady flows such as that beneath breaking water waves where the speed and direction of bubbles is seen to vary on short time scales, it is necessary to obtain an estimate of the individual bubble velocity as it strikes the probe.

3.4.4.1 Interface Velocity Measurements – Dual Probe Technique

In some flow conditions, measurements of bubble velocity have commonly been made by measuring the time taken Δt_i for a bubble to pass between two optical fibre probes positioned a known distance s_{ps} apart (figure 3.12) as discussed by Barrau *et al.* (1999). The voltage time series from the optical amplifier is analysed on a bubble by bubble basis or using cross correlation analysis to compute the time taken for the leading edge of a bubble to travel between tip 1 and tip 2. This difference in bubble arrival times can then be used to assess the velocity of each bubble

$$v_i = \frac{s_{ps}}{\Delta t_i}. \tag{3.3}$$

It is noted however that while this method allows the interface velocity to be determined for each individual bubble rather than relying on a constant flow velocity, it requires bubbles to approach the probes perpendicular to the probe axis in the plane of the two probe tips to obtain valid measurements. If the direction of the bubble velocity is at an angle to the two probe tips, an overestimate of the bubble velocity would be calculated. Indeed, if a bubble approaches parallel to the probe axes, the leading edge of the bubble may strike the two probe tips simultaneously, leading to the calculation of an infinite bubble velocity. While this technique has been used successfully with both optical fibre and conductivity phase detection probes by Murzyn *et al.* (2004) and Chanson & Toombes (2002) in different flow conditions, the flow beneath breaking ocean waves is complex, unsteady and three-dimensional and as such the dual probe method is considered unsuitable for use in this environment.

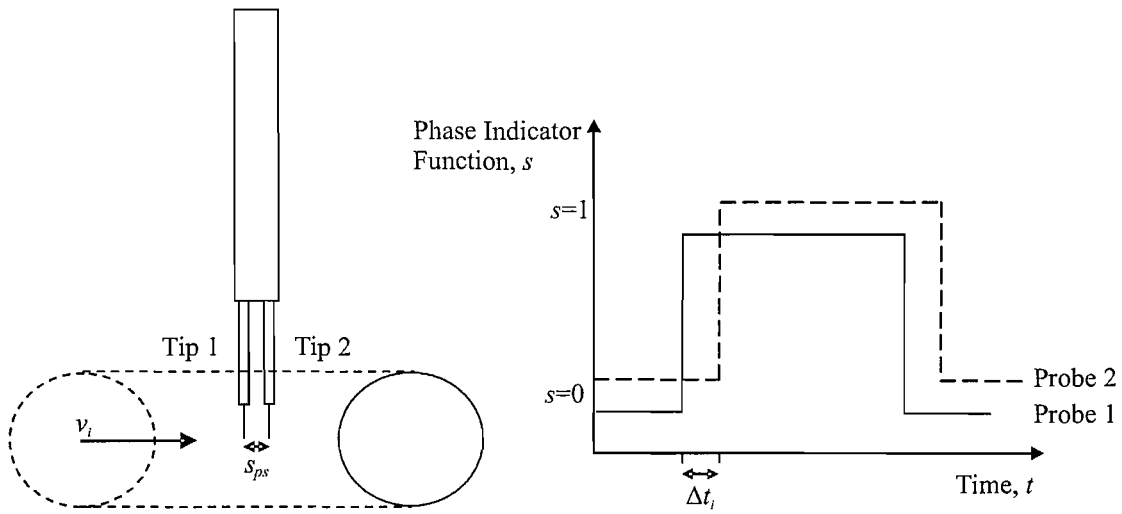

Figure 3.12 Dual probe method of bubble velocity measurement.

3.4.4.2 Interface Velocity Measurements – Single Probe Technique

An alternative method of obtaining bubble velocity estimates using a single optical fibre probe was demonstrated by Cartellier (1992) based on detailed analysis of the voltage output signals produced by the probe.

The detection of an air-water interface by an optical fibre probe does not generate an instantaneous change of the phase indicator function as suggested by figure 3.10, instead a transient exists between the two levels as shown in figure 3.13. This more gradual change of the phase indicator function when an air-water interface is detected

by a probe occurs due to the physical interaction between the shaped fibre tip and the interface. As discussed in section 3.4.2, when the probe moves from water to air the amount of light reflected from the tip increases significantly and this allows the nature of the medium in which the probe is immersed to be deduced. However the piercing of an air-water interface by the probe tip does not happen instantaneously due to the surface tension of the water. Consequently the amount of light reflected back from the probe tip increases gradually as the tip of the probe moves further into the air volume, leading to a steady increase in the value of the output voltage from the optical amplifier (figure 3.13). As the gradient of the signal transient is dependent on the physics of the piercing event, Cartellier (1992) showed that this information could be used to obtain an estimate of the interface velocity. The exact physical interaction between different probe tips and idealised air-water interfaces has been examined in detail by Cartellier (1990) and Cartellier & Barrau (1998).

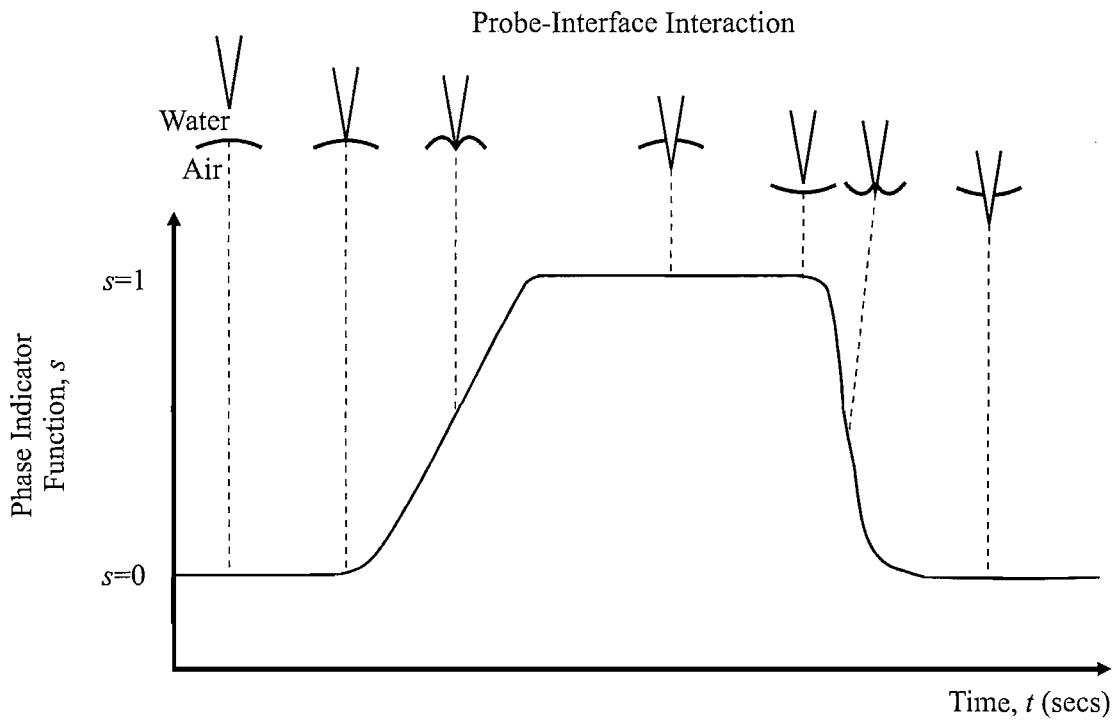

Figure 3.13 Variation of the phase indicator function during the piercing of an air-water interface (after Cartellier (1990)).

An example of a typical voltage signal output produced by the detection of a single bubble by an optical fibre probe is shown in figure 3.14 and is labelled with two characteristic points, A and B after Cartellier (1992). Cartellier showed that the

interface velocity v_i was related to the rise time of the signal t_r, which is defined as the time taken for the voltage level to rise from characteristic point A to point B. The positions of these characteristic points are defined according to two pre-selected threshold levels, V_A and V_B. Typically these thresholds are set at 10% and 90% of the total voltage difference between the static liquid and static air voltage levels DV. By measuring bubble velocity and signal rise time over a range of bubble velocities, a calibration curve can be produced. Cartelier (1992) and Serdula & Loewen (1998) found that when plotted on a log-log scale a power law could be fitted to the data.

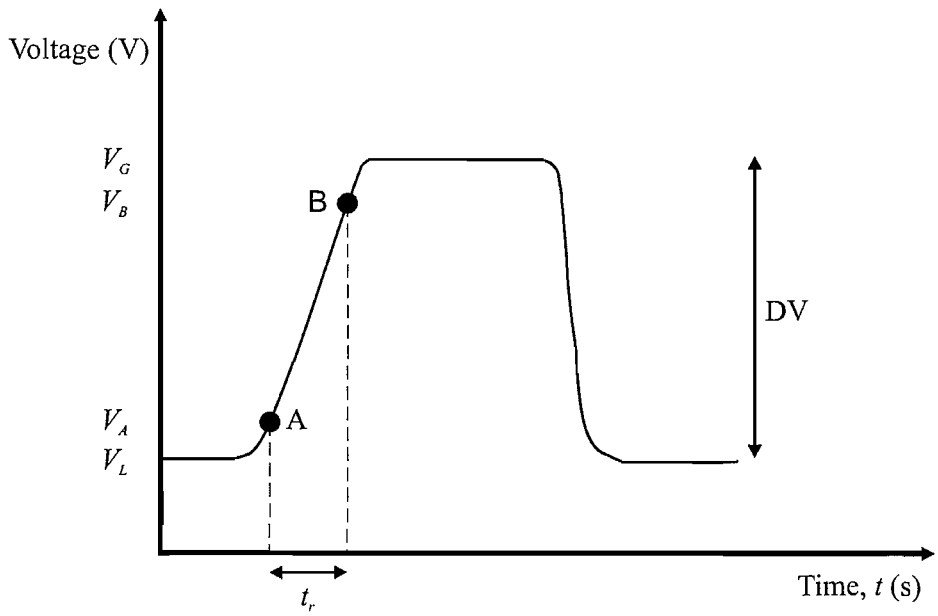

Figure 3.14 Typical voltage signal caused by the passage of a single bubble.

The applicability of this single probe technique for use in breaking waves was assessed by Serdula and Loewen (1998) who concluded that fibre optic probes represent the most promising method for making measurements of the bubble size distribution in the large transient bubble plumes entrained by breaking waves. Serdula and Loewen carried out calibration tests in a uni-directional flow at low void fraction with good results, although they suggested that the flow beneath breaking waves is significantly more complex and could limit the accuracy of the technique. Despite this potential limitation, they concluded that if optical fibre probes are able to provide estimates of the bubble size distribution inside the dense initial bubble plumes generated by breaking waves that are accurate to within a factor of 2 or 3 then this would be an improvement over previous techniques and would constitute a significant advance.

While it was concluded by Serdula & Loewen (1998) that the single probe technique is a feasible method of obtaining bubble size distributions in the dense bubble plumes formed by breaking waves, there are two drawbacks with the method. Firstly, the determination of the characteristic points requires fairly complex signal processing. This complex signal analysis, combined with the very high sample rate required to resolve the shape of the transient (generally>100 kHz), makes data processing computationally demanding.

The second drawback with the technique for use in complex breaking wave flows is that Cartellier (1990, 1992 & 1998), Cartellier & Barrau (1998) and Serdula & Loewen (1998) found that the signal response of the optical probe when a bubble is detected varies with both the orientation of the probe axis with respect to the normal of the bubble interface β and the direction of the bubble mass centre velocity γ (figure 3.15). Cartellier (1992) found the signal rise time increased by a factor of approximately 3 when β changed from 0° to 45°. The dependence of signal rise time on the probe orientation was found to be much less significant in the tests of Serdula and Loewen (1998), who found that changing the probe orientation from 90° to 0° led to a change of just 2%. This large difference between the two sets of results is probably due to differences in the tip designs of the probes under examination. A variety of different probe designs were examined by Cartellier & Barrau (1998) including conical tip, spherical tip, flat cleave, angled cleave and multiple-cone tips and it was seen that the geometry of the probe tip had a significant effect on both the latency length of the probe (section 3.5.4.3) and the sensitivity of the signal transient to β and γ. Thus to determine the feasibility of using the single probe technique to obtain estimates of bubble velocity in the current experiments it was necessary to complete a detailed calibration process using the available optical fibre probes and this is described in section 3.5.4.

Figure 3.8 showed a sketch of the probe geometry used for the current experiments and ten probes in total were made to this design. However, imperfections in the manufacturing process of such fine components and the sensitivity of the instruments to damage meant that the final shape and hence signal response of every probe was different. Consequently all probes underwent some initial investigation to find those

with the most suitable signal response characteristics for the void fraction and bubble size measurements. From the calibrations described in sections 3.5.3 and 3.5.4 it was found that probes with very fine conical tips produced the best response for void fraction measurements, while slightly flattened tips were more suitable for bubble size measurements as they showed less dependence on the probe-interface angle β.

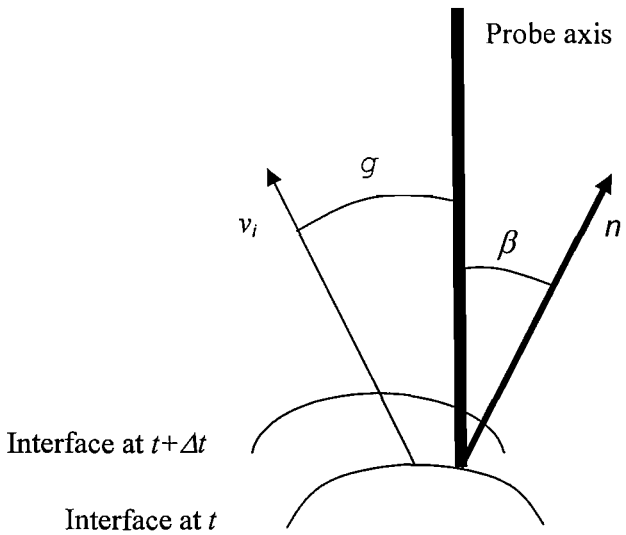

Figure 3.15 Parameters for the probe-interface interaction (after Cartellier (1992), figure 2).

A second technique for obtaining air-water interface velocity estimates using a single optical fibre probe has been proposed by Chang *et al.* (2003). This technique is based on the coherent mixing between the Fresnel reflection from the fibre-liquid interface and the scattered signal from an approaching air bubble. Lim & Chang (2004) suggested that this technique may be suitable for the measurement of bubble velocities and sizes in the two-phase flow beneath breaking waves, however it requires very high data acquisition rates of order 10 MHz and is highly sensitive to the approach direction of the air-water interface. Consequently, the method based on analysis of the signal transient discussed earlier in this section was chosen to measure bubble velocity and hence size in the experiments presented in chapter 6.

3.4.5 Signal Processing

To determine parameters such as the time of bubble arrival and the residence and rise times of bubbles detected by the probe tip, it is necessary to process the time series of

output voltages from the optical amplifier. This is done using a thresholding technique in order to produce a corresponding time series of phase indicator functions. A number of different thresholding methods have been suggested by previous authors, with the most common being the single and dual threshold methods which are detailed below and used in this study.

1. **Single Threshold Method.**

   A threshold level is set at a certain percentage of the difference between the static liquid and air voltage levels (say 30%). The time series of voltages is then processed assuming that any voltage above the chosen threshold level corresponds to the presence of air at the probe tip (s=1) and any voltage below this level represents water (s=0). Thus the arrival time of a bubble corresponds to the time at which the voltage first exceeds the pre-determined threshold level, while the bubble departure time corresponds to the next time that the voltage drops below the threshold level (figure 3.16).

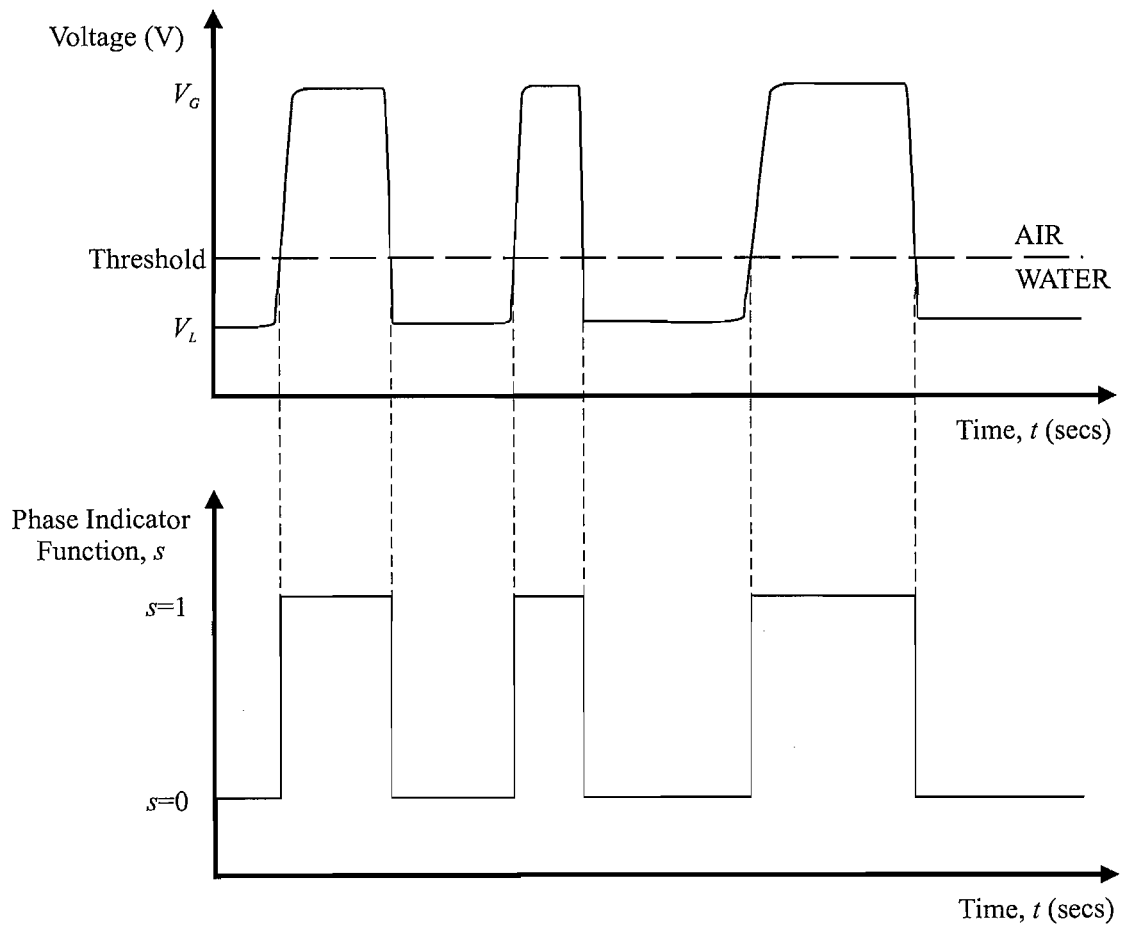

Figure 3.16 Bubble detection using a single threshold method.

2. **Dual Threshold Method.**

Upper and lower threshold levels are set at a fixed percentages of the difference between the static liquid and air voltage levels (say 90% and 10%) for detection of the bubble departure and arrival times respectively. The time series of voltages is then processed, and a bubble arrival time is taken to be the first point at which the voltage rises above the lower threshold limit and the phase indicator function s switches from 0 to 1. The phase indicator function then remains at 1 until the voltage falls below the upper threshold value, indicating a bubble departure (figure 3.17). It was suggested by Cartellier (1990) that the dual threshold detection method matches the physical behaviour of the probe-bubble interaction more accurately that the single threshold technique.

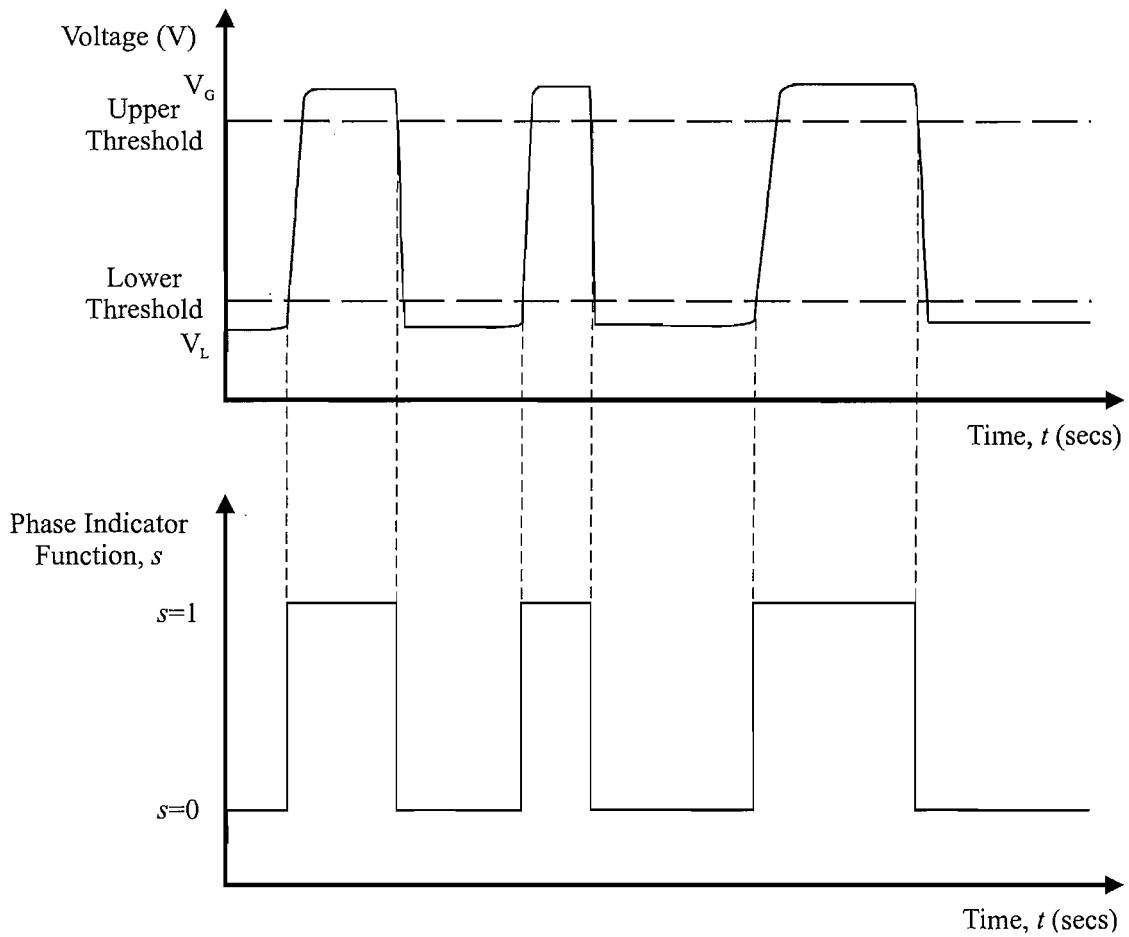

Figure 3.17 Bubble detection using a dual threshold method.

3.4.5.1 Signal Processing Software

In order to process the voltage time series from the optical fibre probes and identify the required information about the bubbles detected during each experimental run, signal

processing software was written using the FORTRAN 90 programming language which allowed rapid analysis of the large 0.5 to 1 Gb binary data files produced by the optical fibre probes.

Initially the software detects all bubbles using the single threshold technique, but can be easily adjusted to use the dual threshold technique and identify the signal rise time depending on the required output. Figure 3.18 shows a typical bubble signature marked with the characteristic points which are identified by the signal processing software in order to calculate bubble arrival, departure, residence and rise times.

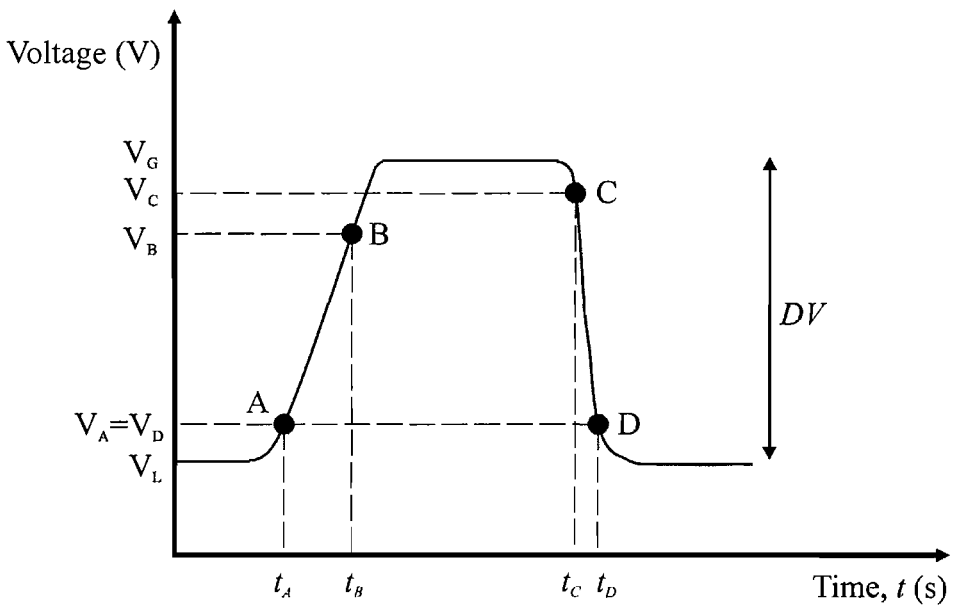

Figure 3.18 Characteristic points detected by the signal processing software.

In order to detect these characteristic points, the signal processing software goes through the following processes.

1. Determine the static air voltage level V_G visually by plotting a section of the data on the screen.
2. Determine the static liquid voltage V_L and the maximum noise amplitude from a section of data containing no bubbles at the start of the record.
3. The user inputs threshold values to allow calculation of the required threshold levels V_A, V_B and V_C. These values are commonly 10%, 60% and 90% of the

difference between the maximum noise at the static liquid level and the air voltage level.

4. Initial bubble arrival times t_A are determined as the first point at which the data exceeds V_A and initial bubble departure time t_D is identified as the next point in the record where the value of the output signal drops below V_A. In order to prevent bubbles being incorrectly detected due to noise about V_A, bubbles with a duration shorter than 5 time steps (approximately $3.3\text{x}10^{-5}$ seconds) are eliminated automatically.
5. The data between each of the valid bubble arrival and departure times is analysed in order to establish the maximum voltage level reached by each of the bubbles. A bubble is eliminated if this value is lower than a threshold set by the user. Commonly this threshold is set between 30% and 50% of the difference between the maximum noise at the static liquid level and the air voltage level. At this stage, the bubble arrival and departure times, t_A and t_D for the single threshold method are known.
6. To establish the bubble departure time for the dual threshold method, the program steps through the data between each valid value of t_A and t_D in order to establish the latest time at which the value of the output signal falls below V_C. This time is identified as the modified bubble departure time t_C. At this stage, the bubble arrival and departure times, t_A and t_C for the dual threshold method are known.
7. To calculate the time taken for each bubble signature to rise from V_A to V_B, the program steps through the data between each valid value of t_A and t_D in order to establish the earliest time at which the value of the output signal rises above V_B. This time is identified as t_B and the rise time t_r can be calculated simply as

$$t_r = t_B - t_A . \tag{3.4}$$

By going through the processes listed above, the signal processing software provides the bubble arrival and departure times for both the single and dual threshold methods as well as the time at which the signal reaches the upper threshold of the signal transient. These values can then be used to calculate various properties of the two-phase flow under investigation such as void fraction, bubble strike rate and bubble size distribution.

3.5 INSTRUMENT CALIBRATIONS

3.5.1 Foam Beach Efficiency

A simple experiment was carried out to investigate the efficiency of the foam beach for a range of wave heights (20 mm to 100 mm) and frequencies (0.5 Hz to 1.1 Hz). The reflection characteristics of the submerged reef are discussed in section 4.3.5.

For each wave condition, a series of regular waves was run in the flume for a period of 60 seconds. The instantaneous water surface displacements were recorded by three calibrated wave gauges located 6.8 m, 7.05 m and 7.45 m from the wavemaker. The wave gauges were sampled at a rate of 256 points per wave period for each wave condition using the CED1401 data acquisition system described in 3.3.1.1. A period of 5 minutes was allowed between each wave case to allow the water surface in the tank to return to a state of equilibrium. The experimental arrangements are shown in figure 3.19.

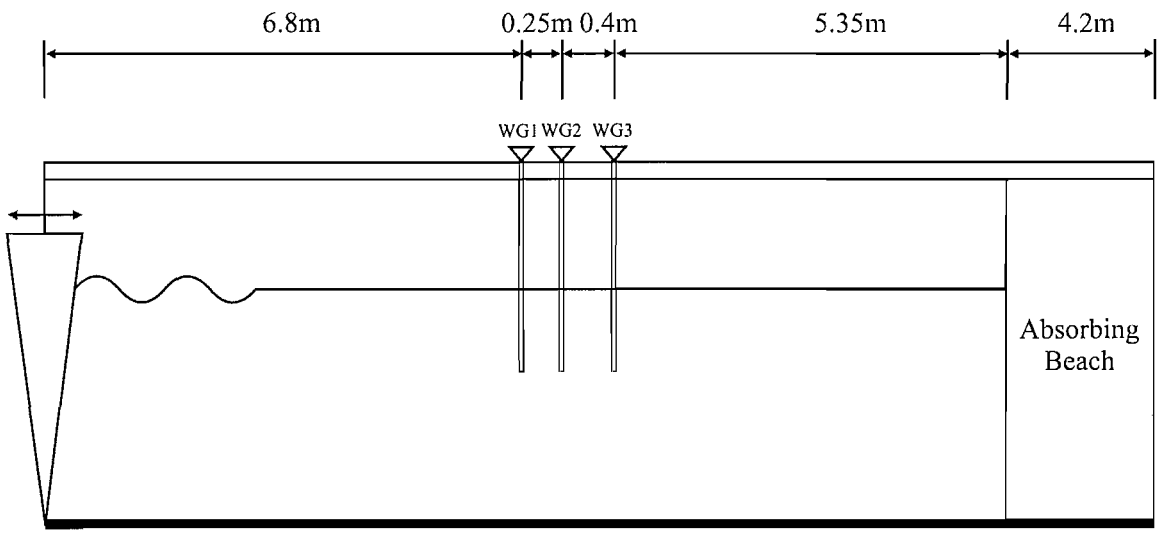

Figure 3.19 Apparatus for the beach efficiency test.

A Fast Fourier Transform was performed on the time series data to calculate the wave amplitude A and phase Φ at each of the wave gauges during a period of the wave record where reflections from the foam beach but no re-reflections from the wave paddle were present in the wave flume. This allowed the incident and reflected wave amplitudes a_i

and a_r at each wave gauge to be determined in order to calculate the reflection coefficient K_r using the two wave gauge method of Isaacson (1991) such that

$$K_r = \frac{a_r}{a_i} = \frac{H_r}{H_i}, \tag{3.5}$$

where

$$a_i = \frac{1}{2|\sin\Delta|}\sqrt{A_1^2 + A_2^2 - 2A_1A_2\cos(\Delta+\delta)}, \tag{3.6}$$

$$a_r = \frac{1}{2|\sin\Delta|}\sqrt{A_1^2 + A_2^2 - 2A_1A_2\cos(\Delta-\delta)}, \tag{3.7}$$

and

$$\delta = \Phi_2 - \Phi_1, \tag{3.8}$$

$$\Delta = k\lambda_n. \tag{3.9}$$

In these expressions λ_n is the distance between wave gauges, and k is the wave number.

To obtain consistent estimates of the reflection coefficient for each wave case, K_r was calculated initially using wave gauges 1 and 2, and then compared with the values calculated using wave gauges 2 and 3 with good agreement.

The values of K_r calculated using wave gauges 1 and 2 as a function of the incident wave height H_i are shown in figure 3.20. It is seen that for the range of wave frequency and amplitude examined in this experiment, the reflection coefficient lies in the range 2%-13%. However it is valuable to note that the highest values of the reflection coefficient are seen at low wave heights. For waves larger than 50 mm in height (which is comparable to the height of a typical transmitted wave in the experiments described in chapters 4, 5, 6 and 7), the value of the reflection coefficient remains approximately constant with a maximum value of 8.5% at low wave frequency (f=0.5 Hz).

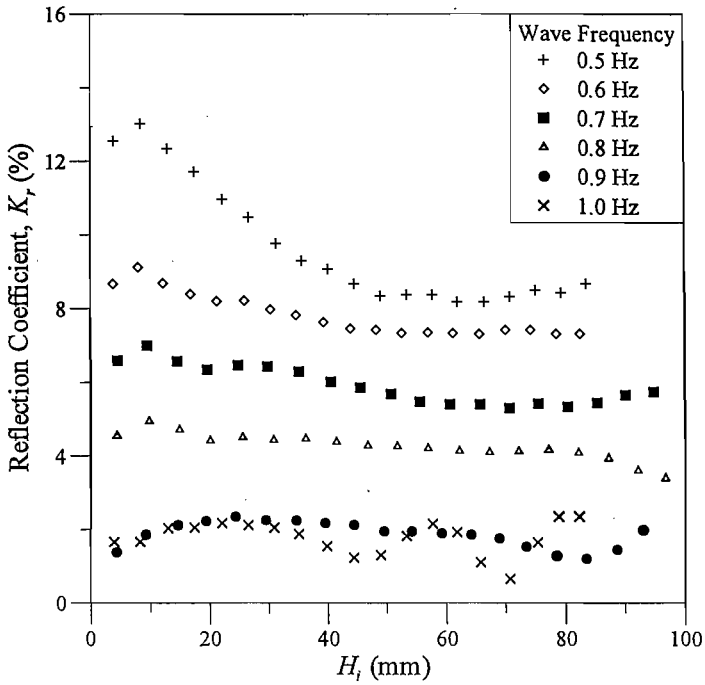

Figure 3.20 Measured reflection coefficients for the absorbing foam beach.

3.5.2 Repeatability of the Wave Profile

The submerged reef described in section 3.2.3 is used in chapters 5, 6 and 7 to generate long trains of repeatable breaking waves in order to allow a series of highly repetitive two-phase flow measurements to be made. To verify the repeatability of the generated wave profile and breaking wave form during long experimental runs, a simple experiment was completed.

To provide measurements of the incident waves soon after generation and as they travel up the reef slope, three wave gauges were installed at locations 1.5 m, 3 m and 4.5 m from the wave generator (figure 3.21). In addition, the PULNIX digital video camera described in section 3.3.3.1 was positioned adjacent to the flume to take video footage of the breakers to verify the repeatability of the breaking wave form. Three different wave cases, corresponding to those examined in chapter 5 were tested and 300 waves were run for each case. The details of the individual wave cases are listed in table 3.1.

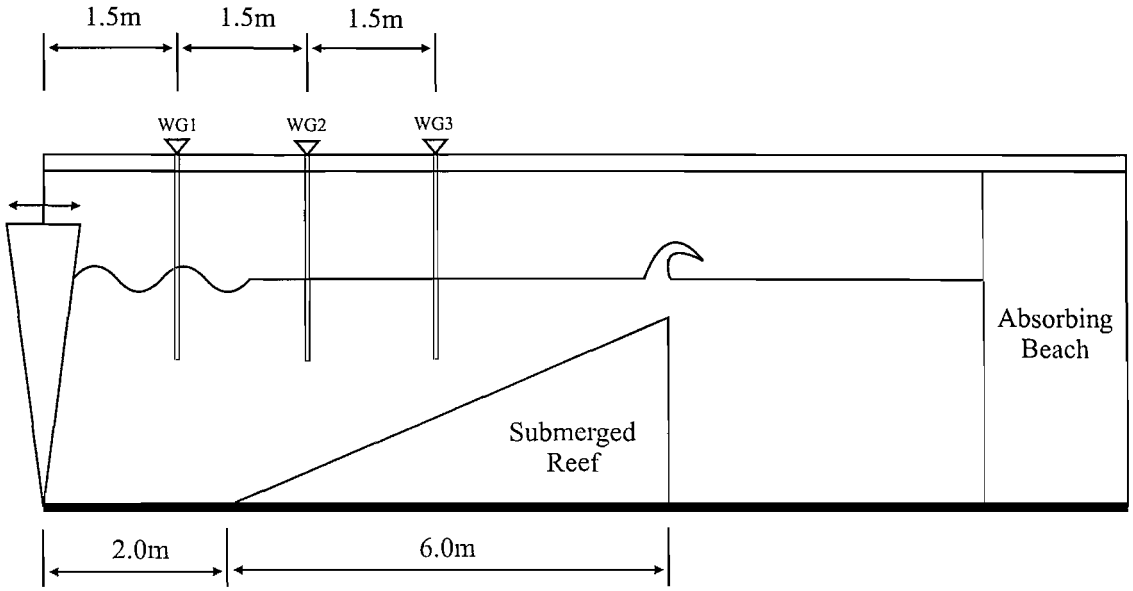

Figure 3.21 Experimental apparatus for the wave profile repeatability tests.

It was found that the generated wave profile for all three wave cases was highly regular after an initial period of approximately 25-30 seconds once the reflections present in the wave flume from both the submerged reef (see section 4.3.6) and the absorbing beach (section 3.5.1) had settled into a form of equilibrium. This is illustrated in figure 3.22 which shows the variation of the free surface elevation with time for wave case 1 at a distance 1.5 m from the wave generator. It is seen that during the initial part of the wave record there is some variation in the wave height but that after approximately 25 seconds, the wave profile becomes very regular at x=1.5 m. To further confirm the repeatability of the generated wave profile, table 3.1 shows the mean crest to trough wave height and standard deviation for the three wave cases at each of the wave gauges and it is seen that the standard deviation of the wave height is less than 1.1% for all cases.

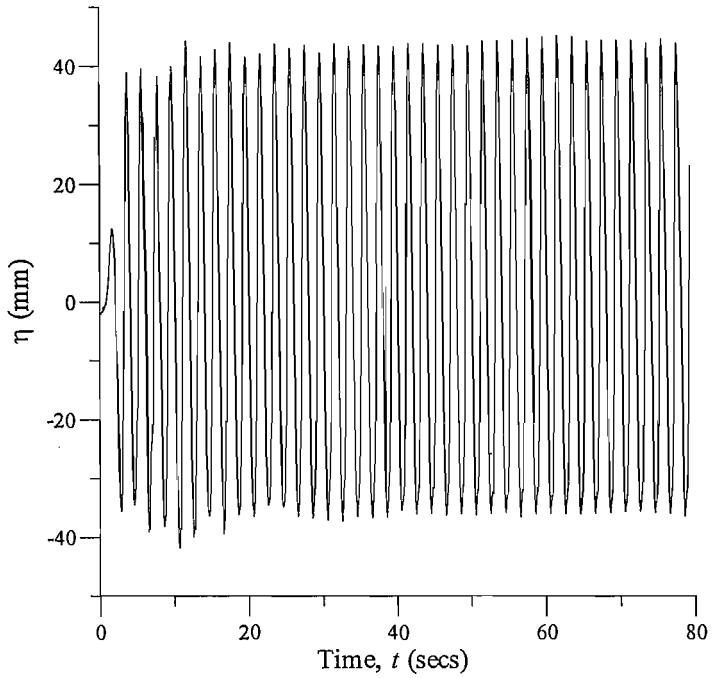

Figure 3.22 Variation of the free surface elevation with time for wave case 1, x=1.5 m.

Table 3.1 Results of the wave profile repeatability tests.

Wave Case	Frequency (Hz)	H_o (mm)	H_1 (mm)	σ_1	H_2 (mm)	σ_2	H_3 (mm)	σ_3
1	0.5	78.18	73.39	0.85%	78.90	0.62%	80.10	0.60%
2	0.7	97.19	86.21	0.88%	79.83	1.08%	78.71	1.07%
3	1	100.45	105.09	1.02%	103.51	0.92%	102.37	0.94%

The analysis described above has demonstrated that the generated waveform is highly repeatable during long experimental runs. It is noted however that despite careful control of the generated waveform, no two breaking events are identical, particularly in the dynamic region close to the overturning jet. While perfect repeatability is not possible, the experiments described in this thesis require consecutive breaking events to show good similarity. In order to assess the repeatability of the breaking wave form, the video images recorded during the calibration tests were examined and comparisons were made of the form of consecutive breaking waves. Figure 3.23 shows video captures of three consecutive breaking waves from wave case 1 at a time after the wave has overturned and begun to generate splash. To allow comparison of the three wave forms, the outlines of the upper water surface and the air cavity entrained beneath the surface were traced and these are presented in figure 3.24. It is observed that while there are some differences between the waveforms, the overall shape and position

relative to the reef of the three cases are very similar. It is suggested that a possible area for future work would be to develop a series of parameters that fully characterise the geometry of breaking waves. This would allow accurate comparison of different breaking events and enable the results from different datasets to be directly compared.

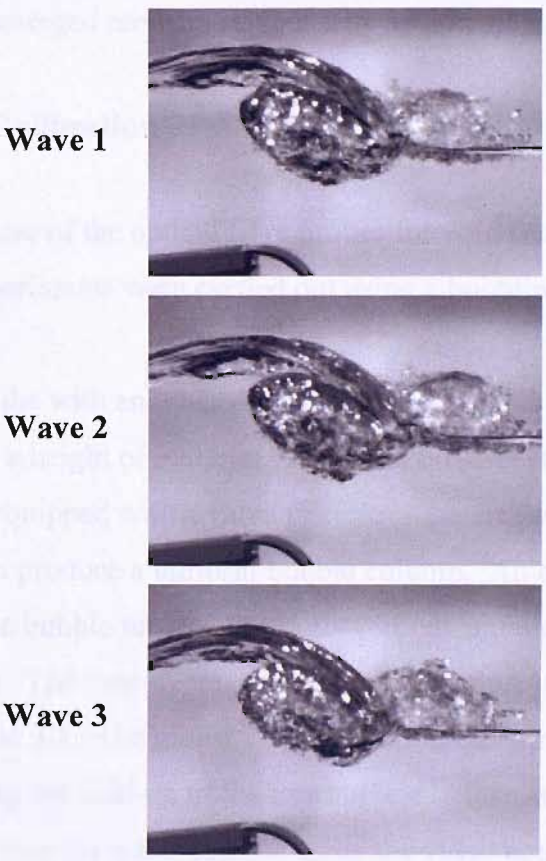

Figure 3.23 Video images of three consecutive waves for wave case 1.

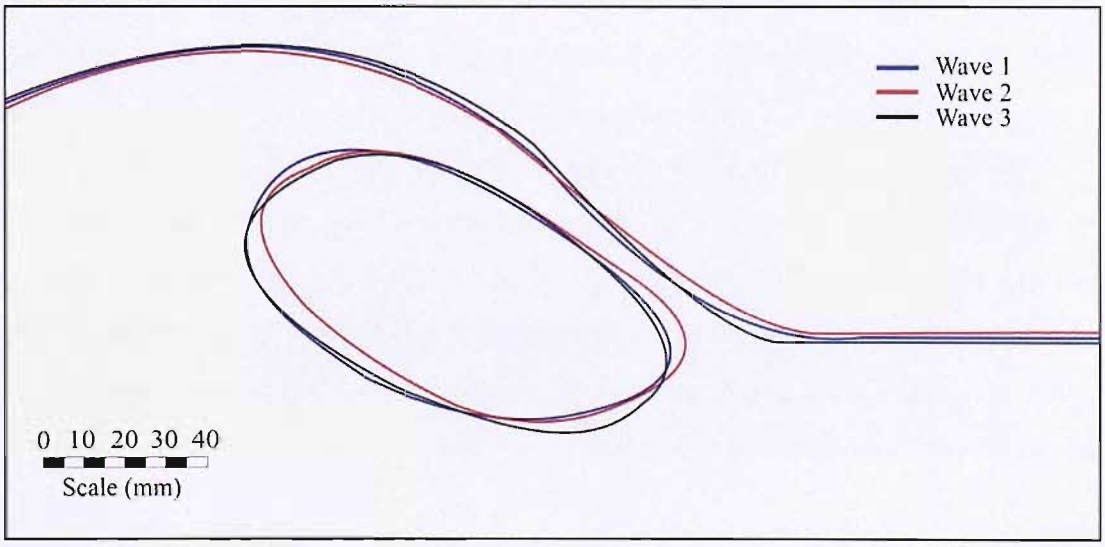

Figure 3.24 Surface traces of the three consecutive waves for wave case 1 presented in figure 3.23.

Based on the results presented in this section, it is concluded that the both the generated and breaking wave profile are sufficiently repeatable to allow ensemble averages of the bubble plume and splash-up properties to be made (see chapters 5, 6 and 7). It is suggested however that a settling time of 30 seconds should be allowed in each experimental run before measurements are taken at the reef crest. Further data on the reflections from the submerged reef can be found in section 4.3.5.

3.5.3 Void Fraction Calibration

In order to validate the use of the optical fibre probes for void fraction measurements, a series of calibration experiments were carried out using a bubbling water column.

A transparent perspex tube with an inner diameter of 95 mm and a height of 400 mm was filled with water to a height of 320 mm. A porous diffuser stone connected to a compressed air supply equipped with a valve to control the air flow rate was positioned at the base of the tube to produce a uniform bubble column. An optical fibre probe was placed into the top of the bubble tube with its axis vertical and the tip located 20 mm beneath the free surface. The time-averaged local void fraction at the probe tip was calculated using equation 3.1. The global void fraction in the bubble column was determined by measuring the hold-up of the free surface before and after the introduction of bubbles into the water column using the video equipment described in section 3.3.3.1 (figure 3.25).

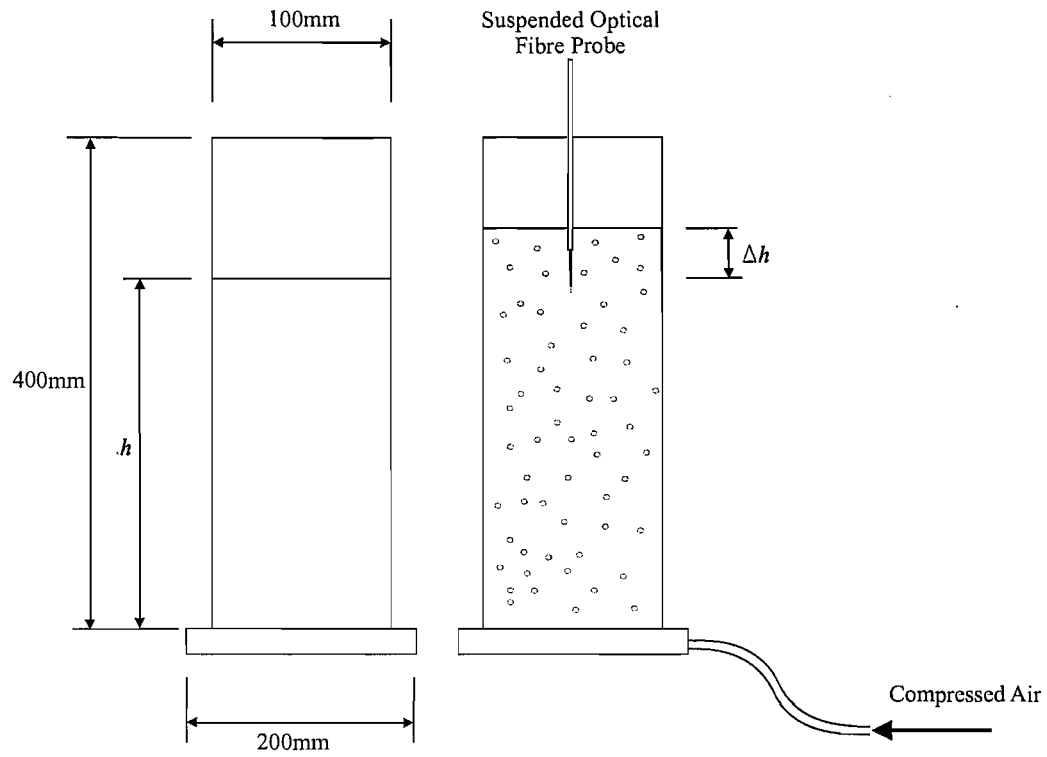

Figure 3.25 Apparatus for the void fraction calibration.

These measurements allowed a reference void ratio to be estimated using the following simple relationship,

$$\alpha_g(\%) = \left(\frac{\Delta h}{h + \Delta h}\right) * 100 . \tag{3.10}$$

Thirteen calibration tests were carried out to investigate the characteristics of two optical fibre probes in void fractions ranging from 0.6 to 17 %. Two probes were tested in order to ensure that they made comparable and repeatable measurements. For the purpose of this section these will be labelled probes 1 and 2. The two probes were constructed to the same design, however differences in the signal response of the probes are expected due to slight imperfections in the tip geometry. The probes were sampled at a fixed sample rate of 150 kHz for a test duration T_t of 60 seconds. Preliminary testing showed that a stable void fraction result could be obtained after approximately 20 seconds for void fractions of 3%, so a test duration of one minute was deemed to be adequate.

The time series of output voltages produced by the probes in the bubbly water column were analysed using both the single and dual thresholding techniques described in sections 3.4.5 in order to assess the most suitable method for void fraction determination in the tests described in chapters 5 and 7. It was suggested by Cartellier (1990) that the single threshold detection method poorly describes the physical behaviour of the probe-interface interaction. Cartellier and Barrau (1998) investigated the evolution of the probe signal with the position of the air-water interface in relation to the probe tip and found that a dual threshold technique was more physically intuitive. However the simpler single threshold method is less computationally expensive and has been used by previous researchers with some success (Hoque, 2002; Waniewski *et al.*, 2001). Thus it was decided to investigate the use of both single and double threshold techniques for the calculation of void fractions in the current experiments.

Initial analysis of the output signals showed that they were well behaved with very little noise around the static water voltage level. In order to examine the sensitivity of the void fraction measurements to threshold level, the single threshold value was varied between 10% and 80% at intervals of 10%. Only one set of dual threshold measurements were examined, with the upper and lower thresholds set at 90% and 10% of the difference between the static air and water voltage levels respectively.

The results of the calibrations using single threshold levels of 10% and 60% along with those using the dual threshold technique are shown in figure 3.26(a) and (b) for probes 1 and 2 respectively. It is seen that there is a clear linear relationship between the measured and actual values and there is very little difference between the results calculated with the three different threshold levels displayed on the plot. It is also observed that the optical fibre probes consistently underestimate the void fraction at all threshold levels but the magnitude of this underestimate is slightly lower for the 10% single threshold level. The following relationships can be used to convert the void fraction measured using a single threshold level of 10% α to the actual reference void fraction α_g,

$$\alpha_g(\%) = 0.839\alpha_1 \tag{3.11a}$$

$$\alpha_g(\%) = 0.906\alpha_2 . \tag{3.11b}$$

These relationships can be used to correct the void fraction measured using the optical probes in the range of void fractions investigated here. It is noted that the differences in the responses of the two probes is due to slight differences in the tip geometry.

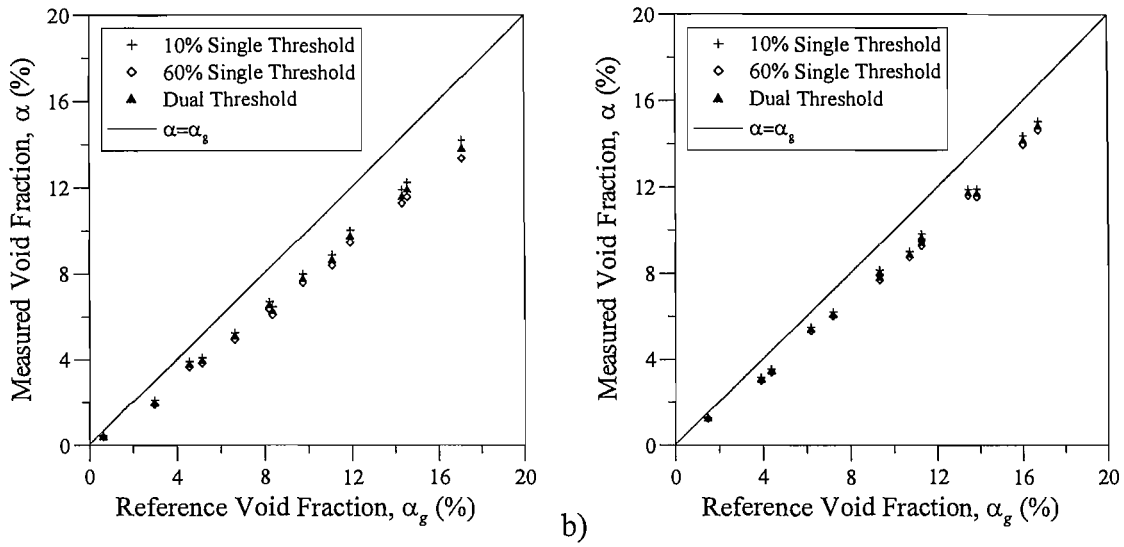

Figure 3.26 Void fraction calibration results for **(a)** probe 1 and **(b)** probe 2.

Figure 3.27 shows the difference between the reference void fraction and the value measured by the optical probes using a single threshold level of 10% as a function of the total number of air-water interfaces recorded during the experiment. While there is some scatter in the results, it is seen that the magnitude of the error increases approximately linearly with the number of interfaces detected. It is concluded therefore that the slightly low void fraction values obtained using the optical probes are due to a consistent underestimate of the residence time of each bubble detected by the probe. The magnitude of this underestimate is approximately 1.08 ms for probe 1 and 1.41 ms for probe 2. It is possible that the size of the discrepancy between the actual and measured void fraction will vary with the bubble velocity as the physical interaction between the air-water interface and the probe will change. However it is noted that increases in the bubble size and hence rise velocity with increasing air flow rate and void fraction were unavoidable in this calibration exercise.

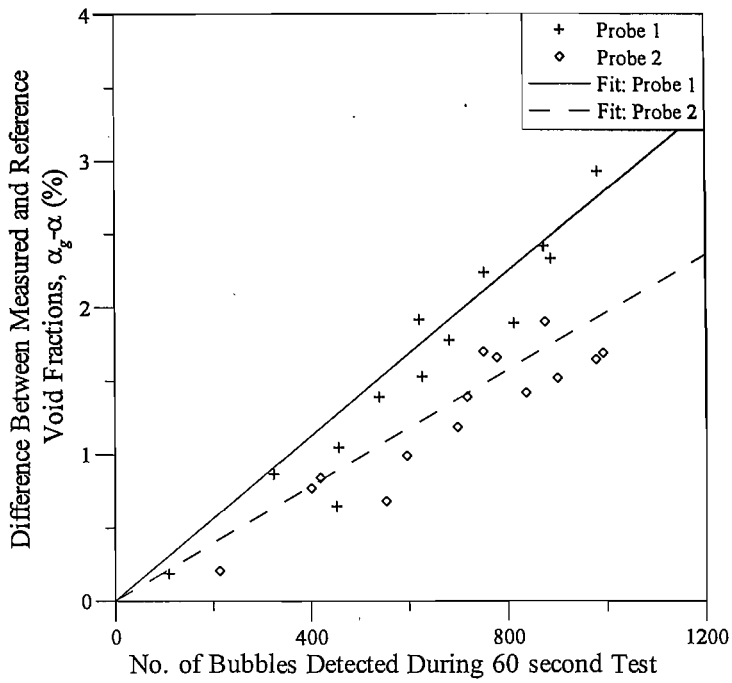

Figure 3.27 Error in the void fraction measurements made using a single threshold level of 10% as a function of the number of detected bubbles.

A similar result was found by Chang *et al.* (2003) who found that their optical fibre probes underestimated the bubble residence time by approximately 0.71 ms in a flow with a void fraction of approximately 13.3% and a mean bubble velocity of 0.170 ms^{-1}. Chang *et al.* (2003) suggested that this underestimate was due to the fact that the fibre tip experienced a short "drying time" when encountering an air bubble.

Barrau *et al.* (1999) reported relative underestimates on void fraction in the range 0.8% to 16%. They suggested that these underestimates were caused predominantly by the interaction of the probe with the air-water interface rather than a "drying time", citing the following mechanisms as potential contributing factors (figure 3.28).

1. **The blinding effect.** As the probe comes into contact with a bubble it may cause a slight deformation of the bubble shape. As the probe detects the position of the disturbed interface, this deformation will lead to an error in the detected bubble residence time on the probe (figure 3.28(a)).

2. **The drifting effect.** The trajectory of the bubble is altered by the presence of the probe, leading to either the detection of a smaller chord length or no detection at all (Figure 3.28(b)).

3. **The crawling effect.** The whole bubble can be decelerated or deformed during interaction with the probe. This category was proposed by Serizawa *et al.* (1984) in their study of bubble-wire interaction (figure 3.28(c)).

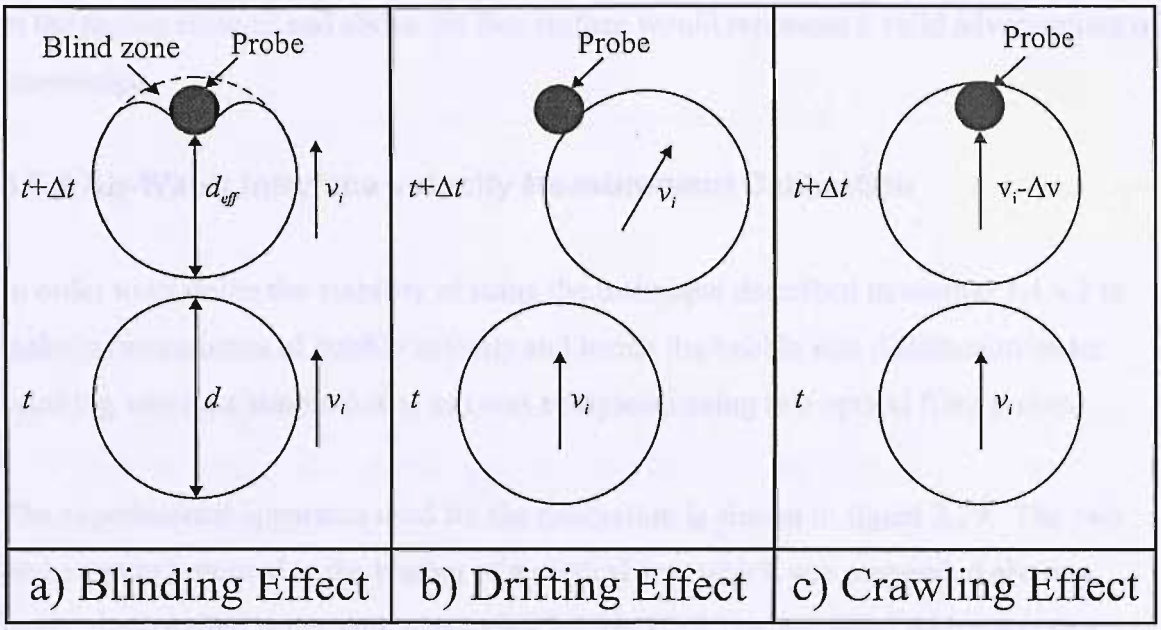

Figure 3.28 Possible mechanisms leading to an underestimate of the bubble residence time by an optical fibre probe.

A limitation of this calibration process is that it was only possible to carry out the calibration in the range $0.6\%<\alpha<17\%$ as it became too difficult to accurately measure the position of the disturbed free surface at higher void fractions. Chapter 5 presents measurements of void fraction both above and below the free surface in the region of breaking waves where the void fraction varies in the range 0% to 100% and thus is well outside the range of this calibration. While no satisfactory method was found to measure the performance of the probes at higher void fractions, the calibration process has shown that the probe performs satisfactorily at low void fractions ($\alpha<17\%$) and any errors are shown to be proportional to the number of air-water interfaces detected. This relationship between the error in void fraction and the number of interfaces can be used to adjust the measured void fraction over the full range of void fractions by simply

introducing a "drying time" correction to every air volume detected. It is suggested that further work to design a technique to calibrate void fractions in the range 0% to 100% would be highly beneficial for future studies of aeration in violent free-surface flows.

While it would have been preferable to calibrate the probes over the full range of void fractions from 0% to 100%, existing measurements of the time-varying void fraction field in breaking waves are limited, and to this author's knowledge are confined to the region below the free surface. Thus any reasonable estimate of the high void fractions in the region close to and above the free surface would represent a valid advancement of knowledge.

3.5.4 Air-Water Interface Velocity Measurement Calibration

In order to examine the viability of using the technique described in section 3.4.4.2 to make measurements of bubble velocity and hence the bubble size distribution under breaking waves, a simple initial test was completed using two optical fibre probes[1].

The experimental apparatus used for the calibration is shown in figure 3.29. The two probes were mounted at the bottom of a vertical arm which was suspended above a large, glass-walled water tank measuring 2.25 m x 2.25 m and filled with water to a depth of 400 mm. The vertical arm was mounted on a runner system which allowed it to be driven in a vertical plane at different velocities.

[1] Note that the probes used for this calibration and bubble size measurements presented in chapter 6 had a slightly flatter tip than those used for the void fraction measurements presented in section 3.5.3 and chapters 5 and 7.

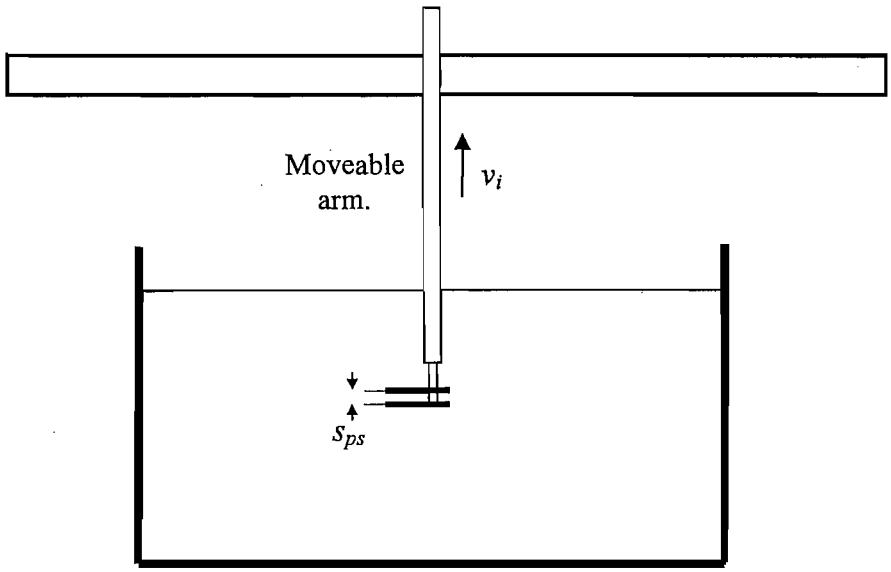

Figure 3.29 Experimental apparatus used for the air-water interface velocity detection calibration.

For this calibration, the probes were mounted at two different orientations on the moveable arm with a small vertical separation between the two probe tips. To examine the signal response of the optical probes to controlled air-water interfaces, the probes were submerged and then driven vertically through the water-air interface at velocities ranging from 0.15 to 3.37 ms^{-1}.

The output signal from the two probes was sampled at a rate of 400 kHz using a Measurement Computing PCI-DAS6070 A/D board connected to a personal computer described in section 3.3.1.2. The data from the probe was then analysed using the signal analysis software described in section 3.4.5.1 to identify the interface arrival time at each probe and the signal rise time t_r between characteristic points A and B (figure 3.14) in order to identify a relationship between interface velocity v_i and signal rise time.

The actual interface velocity was calculated using the known vertical separation of the two optical probes s_{ps} and the difference between the interface arrival time at each probe Δt_i

$$v_i = \frac{s_{ps}}{\Delta t_i}. \tag{3.12}$$

The relationship between the signal rise time t_r for each of the two probes and the known interface velocity v_i for both orientations was examined in a series of calibration curves.

3.5.4.1 Horizontal Probe Calibration

To examine relationship between the signal rise time and interface velocity with the probe axes aligned parallel to the free surface (β=90°, see figure 3.15), 195 test cases with velocities ranging from 0.15 to 2.25 ms^{-1} were completed. The lower threshold for characteristic point A (figure 3.14) was set at 10% of the difference between the steady water and air voltage levels, while the upper threshold for detection of point B was varied in the range 50-90% in order to obtain the best correlation between interface velocity and signal rise time. The calibration curves for probes 1 and 2 with the 60% upper threshold level are plotted on a log-log scale in figure 3.30.

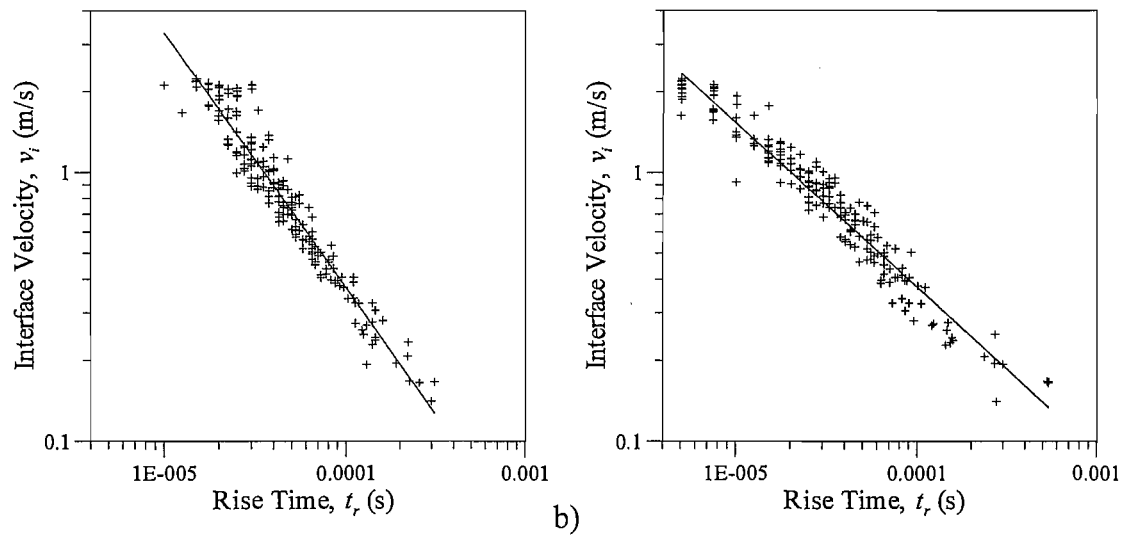

Figure 3.30 Horizontal interface velocity calibration curves for **(a)** probe 1 and **(b)** probe 2 using an upper threshold level of 60%.

Figure 3.30 shows that there is a clear relationship between the interface velocity and signal rise time for both probes, however the relationship is not the same for the two probes due to microscopic differences in the nature of the probe tips. A power law equation can be fitted to both sets of data in the form

$$v_i = 10^b t_r^m . \tag{3.13}$$

The coefficients m and b were calculated for each test and are shown along with the correlation coefficients in tables 3.2(a) and (b).

Table 3.2(a) Results of the horizontal interface velocity tests for probe 1.

Upper Threshold	m	b	R^2
50	-0.877	-4.046	0.949
55	-0.908	-4.097	0.941
60	-0.951	-4.222	0.958
65	-0.976	-4.301	0.905
70	-0.978	-4.222	0.847
80	-0.887	-3.699	0.629
90	-0.578	-2.398	0.266

Table 3.2(b) Results of the horizontal interface velocity tests for probe 2.

Upper Threshold	m	b	R^2
50	-0.606	-2.854	0.943
55	-0.612	-2.886	0.947
60	-0.612	-2.886	0.956
65	-0.618	-2.886	0.947
70	-0.625	-2.921	0.951
80	-0.630	-2.921	0.951
90	-0.662	-3.046	0.948

It is seen in tables 3.2(a) and (b) that the correlations between v_i and t_r are very good for both probes up to an upper threshold of 65%, with R^2 values of 0.9 or higher. Above an upper threshold of 65%, some of the signal transients from probe 1 cannot be correctly resolved by the signal processing software due to noise close to the steady air voltage level of the output signal and the correlation becomes weaker. Good correlations are obtained at all threshold levels for probe 2, although a value of 60% gives the highest value of R^2 for both probes. Consequently an upper threshold level of 60% was chosen to estimate the velocity of air-water interfaces in the present study. This is considerably lower than the level of 90% often suggested in literature (Cartellier, 1990; Serdula & Loewen, 1998; Cartellier & Barrau, 1998), however using a relatively low upper threshold level reduces the likelihood of errors being introduced due to noise close to the steady air voltage level of the output signal.

3.5.4.2 Angled Probe Tests

As discussed in section 3.4.4.2, previous researchers have found that the signal response of optical probes is sensitive to the angle between the probe axis and the normal to the air-water interface β (see figure 3.15). In order to examine the sensitivity of the optical probes to the interface impact angle, a second series of tests was completed with the probes orientated upwards at an angle of β=115°. 203 test cases with interface velocities ranging from 0.17 to 3.37 ms^{-1} were performed for this angled probe case. The calibration curves for probes 1 and 2 with the upper threshold for detection of characteristic point D set at 60% are shown in figure 3.31, along with the calibration curves from the horizontal test case.

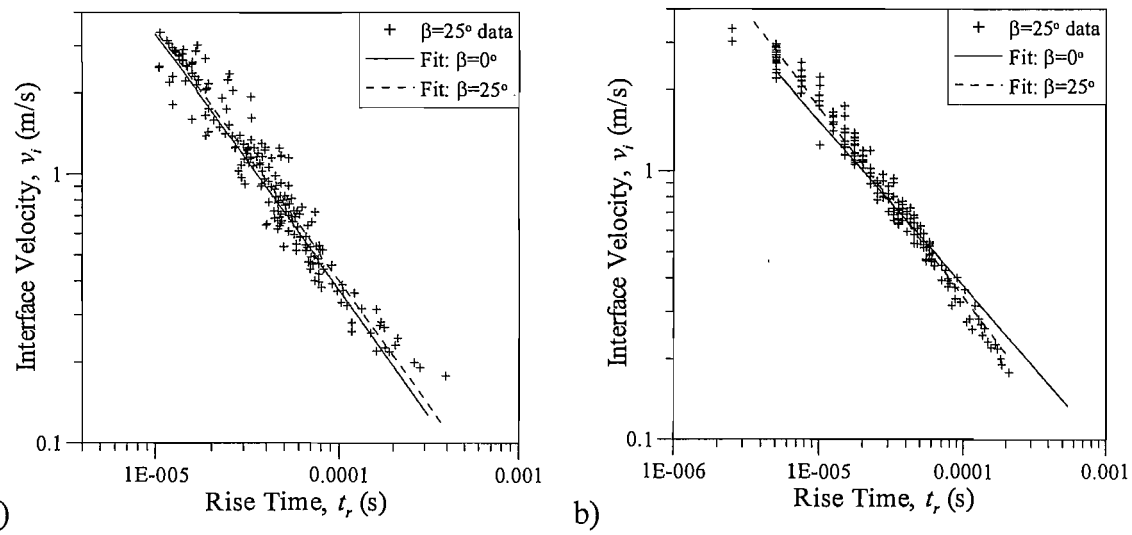

Figure 3.31 Angled interface velocity calibration curves for **(a)** probe 1 and **(b)** probe 2 using an upper threshold level of 60%.

Figure 3.31 shows that the results from the horizontal probe calibration are close to those for the angled probe tests and for the most part fall within the scatter of the angled test calibration data. The equations of the calibration curves for probes 1 and 2 at an angle of β=115° are

$$v_{i_1} = 10^{-4.097} t_{r_1}^{-0.932}, \tag{3.14a}$$

and

$$v_{i_2} = 10^{-3.301} t_{r_2}^{-0.705}. \tag{3.14b}$$

Thus it is concluded that within the range $90° < \beta < 115°$, there is relatively little dependence of the relationship between the signal rise time and the interface velocity on the angle of the probe to the interface.

Further test cases with the probes orientated vertically ($\beta=0°$) and at an angle of 65° were attempted in order to build a more complete picture of the angle dependence of the single probe velocity measurement technique. However it was found that when the probes were angled downwards, there was a tendency for water droplets to run down the probe and hang from the tip after it had been driven through the water surface, which made it impossible to obtain reasonable results. For the vertical probe tests, the existence of a pre-signal caused by reflections from the advancing air-water interface was detected and made it difficult to correctly resolve the signal transient (figure 3.32). The existence of pre-signals when air-water interfaces strike a probe at an angle close to $\beta=0°$ has been previously noted by Cartellier and Barrau (1998) and Chang *et al.* (2003), however no such signals were detected from the probes used in the void fraction tests described in chapters 5 and 7, so their presence here is surprising. It is thought however that this limitation is unlikely to reduce the effectiveness of the single probe bubble size measurement technique when used to detect bubble velocities in breaking waves, as bubble strikes outside of the range of calibration ($\beta>115°$) can be almost eliminated by careful orientation of the probes in the breaking wave tests (section 6.2.1).

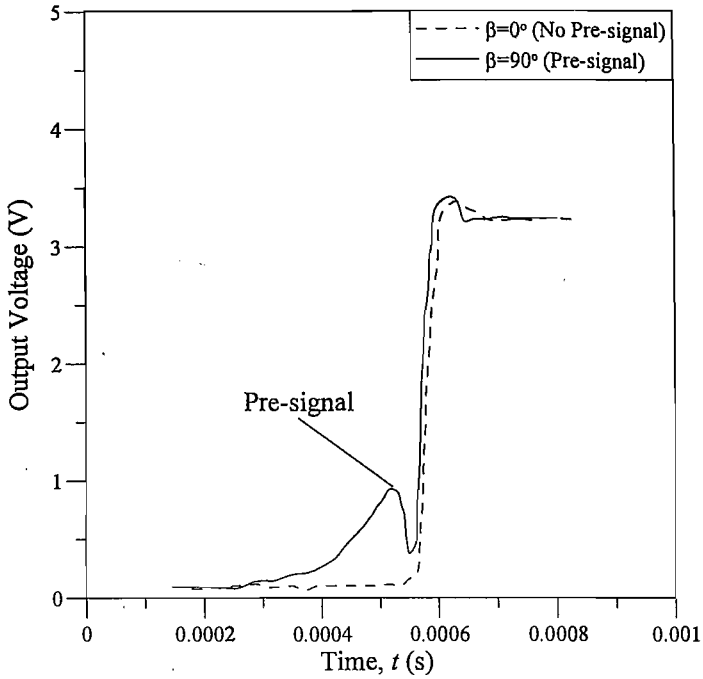

Figure 3.32 Example of a pre-signal detected when the probes used in the interface velocity calibration are oriented perpendicular to an air-water interface (β=0°).

The calibration process described in this section has shown that good estimates of the air-water interface velocity can be made using the single probe method, but that there are some limitations of this method of bubble velocity measurement in complex two-phase flows such as the observed small dependence of the signal response to the angle between the probe axis and the normal to the air-water interface. However, Serdula & Loewen (1998) suggested that as alternative techniques have been unable to provide accurate measurements of the bubble size distributions inside dense bubble plumes, estimates that are accurate to within a factor of two or three would provide a significant advance.

3.5.4.3 Latency Lengths

The idea of a latency length, L was introduced by Cartellier (1990) as an objective method of comparing the signal response of probes with different geometry. L has units of length and is defined as

$$L = t_r v_i \ . \tag{3.15}$$

The value of L is seen to decrease with increasing bubble velocity until a critical velocity v_c is reached. Above v_c, L remains constant and is termed L^* and thus the signal rise time is an inverse ratio of the interfacial velocity

$$t_r = \frac{L^*}{v_i}. \tag{3.16}$$

As well as providing an objective method of comparing the performance of different probes, L^* can be interpreted as the limit of applicability of an optical probe with respect to bubble velocity and size. Consider the residence time t_a of the probe inside a single bubble of diameter d and velocity v_i

$$t_a = \frac{d}{v_i}. \tag{3.17}$$

If the rise time of the signal t_r has a duration longer than t_a, complete dewetting of the probe would not be achieved before the probe passes back into liquid. Hence the bubble would not be fully detected, or at least the signal would not display a plateau at the static air level. Thus it can be seen that the latency length L^* provides an estimate of the range of applicability of the probe.

The latency lengths of the two probes investigated in these calibration tests were calculated for β=90° using an upper threshold of 60% of the difference between the water and air voltages and found to be 37 μm and 18 μm respectively. It is difficult to directly compare these values with those of other researchers shown in table 3.3 because an upper threshold of 90% has generally been used in previous studies. To obtain an approximate comparison it was assumed that the gradient of the signal transient remains constant between the 10% and 90% threshold levels which allows adjusted latency lengths of approximately 60 μm and 30 μm to be calculated for probes 1 and 2 respectively. This discrepancy in the measured latency lengths of the two probes can be attributed to small differences in the tip geometry caused by slight variations in manufacture.

Table 3.3 Characteristics of optical fibre probes examined by previous researchers.

Study	Probe Identifier	Latency Length (μm)	Probe Type	Comments
Serdula & Loewen (1998)	1	459	1 mm conical probe	Freshwater, Probe axis perpendicular to air-water interface
	2	513	1 mm conical probe	Freshwater, Probe axis perpendicular to air-water interface
	2	500	1 mm conical probe	Seawater, Probe axis perpendicular to air-water interface
	3	365	1 mm conical probe	Freshwater, Probe axis perpendicular to air-water interface
	3	373	1 mm conical probe	Freshwater, Probe axis parallel to air-water interface
Cartellier (1992)	2	44 +13/-11	51 μm conical probe	Probe axis perpendicular to air-water interface
	3	42.4 +17/-13	36 μm conical probe	Probe axis perpendicular to air-water interface
Cartellier (1990)	2	400	monofibre probe	Probe axis parallel to air-water interface
	3	400	monofibre probe	Probe axis parallel to air-water interface
	4	150	optoflow probe	Probe axis parallel to air-water interface
	4	130	optoflow probe	Probe axis perpendicular to air-water interface
	5	240	conical tipped	Probe axis perpendicular to air-water interface
	1	520	U-shaped probe	Probe axis perpendicular to air-water interface
Present Study	1	60	20 μm conical probe	Probe axis perpendicular to air-water interface
	2	30	20 μm conical probe	Probe axis perpendicular to air-water interface

It is seen that the probes used in this study have a smaller latency length than the majority of instruments used in previous studies. It is suspected that this relatively low latency length is predominantly due to the very small, 20 μm tip diameter of the current probes. As explained above, the latency length provides an estimate of the limit of applicability of the probe and so the calculation of L^* suggests that the minimum bubble chord length that can be successfully detected by the probes are of the order 60 μm for probe 1 and 30 μm for probe 2.

CHAPTER 4 – WAVE BREAKING CHARACTERISTICS AND ENERGY DISSIPATION

4.1 INTRODUCTION

This chapter presents measurements of the characteristics of waves breaking on a submerged reef. These measurements include breaker indices, the reflection properties of submerged reefs, breaking wave geometry and the energy dissipated during a breaking event.

Wave breaking is a violent phenomenon and is the predominant mechanism by which wave energy is dissipated in both deep and shallow water. Upon breaking, energy is dissipated by many processes including the generation of turbulence, splash and noise as well as the entrainment of large quantities of air. While all of these factors are significant to the energy dissipation rate, we do not fully understand the details of each mechanism or their relative contributions to the total dissipation and so no comprehensive model of energy dissipation during breaking is currently available.

Previous authors have suggested that plunging waves dissipate a greater amount of energy during the initial breaking event than spilling breakers because the increased violence of the overturning motion generates greater amounts of turbulence, splash and air entrainment (Govender *et al.*, 2002; Yasuda *et al.*, 1999; Lamarre, 1993). This observation suggests that the amount of energy dissipated at breaking is at least partially dependent on the intensity of the wave breaking event which was shown by Mead & Black (2001) to be defined by the wave geometry at breaking.

The focus of the work carried out in this chapter was to investigate the amount of energy dissipated during initial wave breaking and how this varies with the wave breaking intensity. In addition, some preliminary results indicating the importance of the air entrainment process to energy dissipation were obtained and this idea is developed further in later chapters. It is seen that the characteristics of waves breaking on a submerged reef are dependent not only on the offshore wave parameters and beach

slope as shown by previous studies on emergent, planar slopes, but are also highly sensitive to the water depth over the reef crest.

The data presented in the following chapter is of great interest in its own right as it has implications for studies of wave breaking on sandbars and nearshore reefs as well as in the design of submerged coastal structures such as submerged breakwaters and artificial surfing reefs. In addition, this work provides a good understanding of the characteristics of the experimental setup which is essential for the interpretation of the results presented in later chapters where the same reef structure was used to generate repeatable breaking waves to allow two-phase flow measurements to be made.

4.2 EXPERIMENTAL ARRANGEMENTS

The experiments described in this chapter were carried out in a wave flume at the University of Southampton equipped with a flap-type wavemaker, the specifications and operation of which have been described in sections 3.2.1 and 3.2.2. A submerged reef as described in section 3.2.3 was installed in the flume as shown in figure 4.1 to create repeatable breaking waves. The water depth in the flume was varied by ±20 mm around the optimum depth of 700 mm in order to adjust the water depth above the reef crest h_c.

The water surface elevation along the channel was measured using 7 double-wire resistance-type wave gauges as described in section 3.3.2. The wave gauges were calibrated daily and the output signals from these were logged to a PC via the 1401 D/A system (section 3.3.1.1) at a sample rate of 256 points per wave to allow analysis of the recorded data using a Fast Fourier Transform. The locations of the wave gauges along the centreline of the wave channel are shown in figure 4.1. The first two wave gauges were installed in front of the submerged reef structure in order to measure the incident waves. A further five wave gauges were installed beyond the reef crest to measure the transmitted waves which reform in the deep water section of the flume after breaking on the submerged reef. Wave gauge 6 was placed adjacent to gauge 5 with an offset of 0.2 m at a position 11.5 m from the wavemaker to investigate the existence of any cross-tank sloshing in the flume during the tests. It is noted that no significant cross or long-tank sloshing was measured during the experiments.

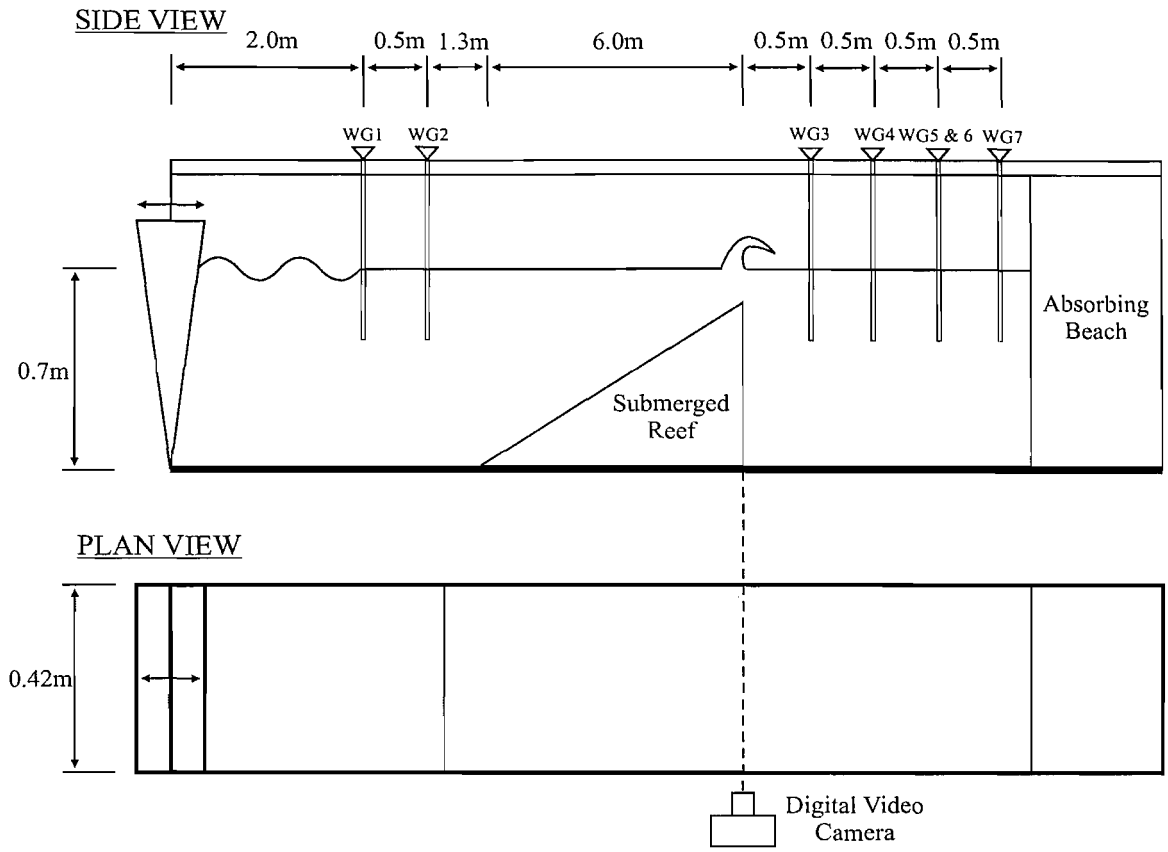

Figure 4.1 Experimental apparatus used for the measurements of wave breaking characteristics and energy dissipation.

A PULNIX TM-6710 monochrome digital video camera as described in section 3.3.3.1 was installed alongside the wave flume to record digital video images of waves breaking over the crest of the reef. These images were used to measure the aspects of the breaking wave geometry described in the section 4.3. The camera was positioned perpendicular to the wave flume and moved horizontally and vertically as the water level and breaker position varied in order to best capture the wave breaking process. To ensure clear pictures of the breaking waves and to freeze the small-scale, high velocity motion, four 500 W spotlights were installed on the far side of the flume opposite the camera position. The spotlights were shone through a semi-transparent screen fixed to the back wall of the wave flume to diffuse the high intensity light. It was found that this lighting set-up provided good flow visualisation and allowed the use of high shutter speeds of up to 1/32,000 seconds, which enabled well defined images of the wave breaking process to be recorded. A grid with 10 mm vertical intervals and 30 mm horizontal intervals was drawn on the glass on the nearside of the wave flume to provide a reference scale for the analysis of the video images.

4.3 RESULTS

4.3.1 Breaker Indices

The breaker height and breaker depth indices are important parameters in coastal science and engineering as they allow simple calculation of different aspects of breaking waves based only on the beach gradient and the offshore wave properties. To clarify the characteristics of the breaking waves in the experimental setup used for the tests described in this thesis and provide new information about wave breaking over submerged reefs it is interesting to examine the values of these indices for a range of incident waves.

4.3.1.1 Breaker Depth Index

The breaker depth index γ_b is used to determine the break point in nearshore wave models and is important for the calculation of forces on coastal structures in shallow areas. The index is defined as

$$\gamma_b = \frac{H_b}{h_b}, \tag{4.1}$$

where H_b and h_b are the wave height and water depth at the break point respectively as shown in figure 4.2.

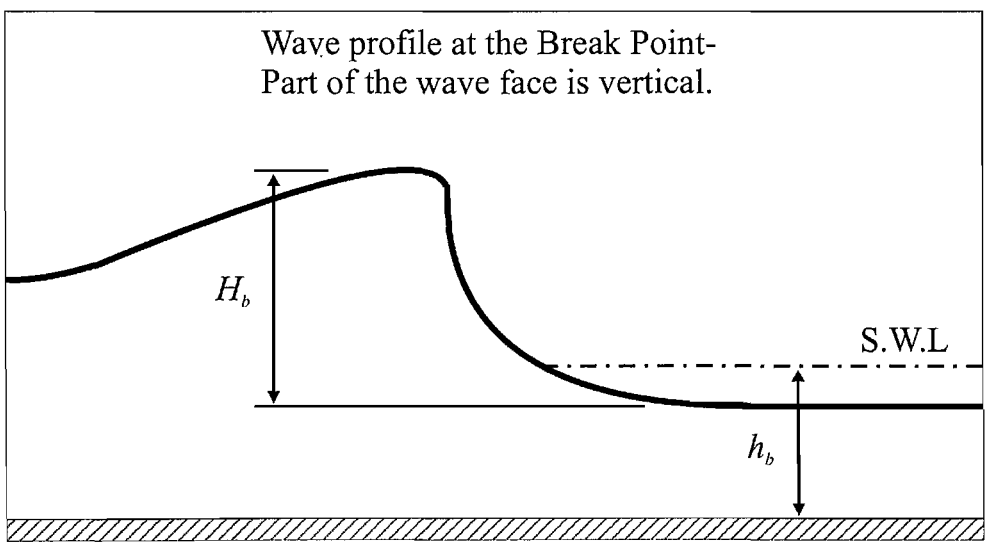

Figure 4.2 Definition of the wave profile at the break point.

A large number of studies (Munk, 1949; Collins & Weir, 1969; Singamsetti & Wind, 1980; Sunamura, 1981; Komar & Gaughan, 1973; Galvin, 1969; Weggel, 1972) have been completed to determine the magnitude of the breaker depth index on plane slopes, however to this author's knowledge only Smith & Kraus (1990, 1991) have examined γ_b for waves breaking over submerged reefs.

For the breaker index tests, the total water depth in the wave flume was kept constant at 0.7 m, and 48 different wave cases with frequencies ranging from 0.4 Hz to 1.0 Hz and offshore wave heights H_o in the range 40 mm to 105 mm were examined. The position of the break point and the magnitude of H_b and h_b were determined through analysis of digital video images of wave breaking for each case. The break point was defined according to the description of Iversen (1952) as the point where any portion of the forward face of the wave first becomes vertical (figure 4.2). This definition is consistent with the majority of breaking wave studies.

It should be noted that wave breaking is a highly unstable process which can be sensitive to small variations in factors such as the water level or the presence of reflected waves. In addition, the measurement of the wave geometry at breaking and determination of the break point involves a degree of subjectivity and this tends to introduce scatter into the results. In an attempt to reduce the level of scatter, at least 5 waves were measured for each test case to define an average value for each quantity.

The measured breaker depth indices are shown in figure 4.3 as a function of deepwater wave steepness H_o/L_o. It is seen that while there is some scatter in the present results, γ_b maintains an approximately constant value of 0.85 over the range of deepwater steepnesses under examination. This suggests that despite the relatively steep gradient of the front face of the reef, breaking occurs by depth limited conditions and the breaker depth index appears to be insensitive to deepwater wave parameters. It was observed that in the cases where the value of γ_b is less than 0.8, the wave almost remained unbroken as it passed over the reef but eventually broke right at the crest of the reef in a relatively weak manner.

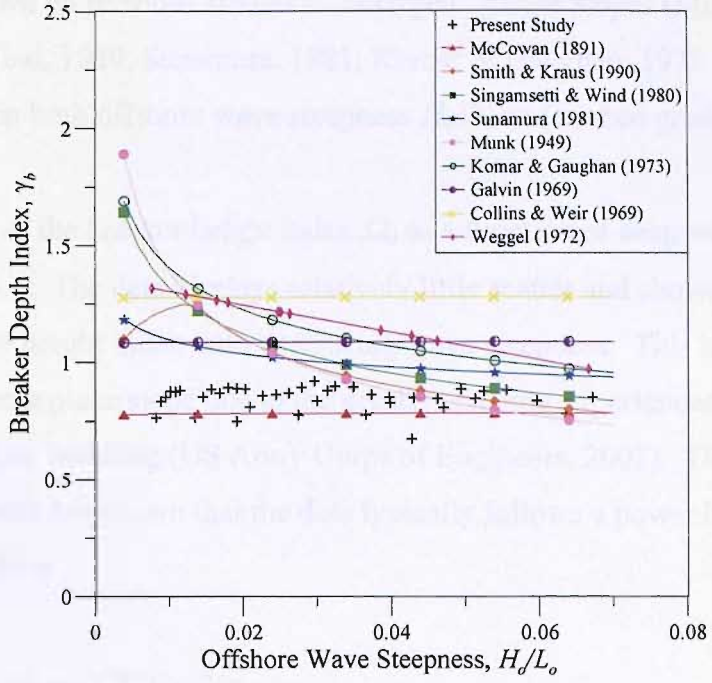

Figure 4.3 Measured breaker depth index as a function of deepwater wave steepness. All except for the present data and those from Smith & Kraus are for emergent plane slopes.

The results obtained in this study are compared with those of previous authors in figure 4.3 and are seen mostly to fall within the ranges obtained in existing studies. However, unlike many previous experimental results, the values of γ_b obtained in the present tests shows no obvious dependence on the deepwater wave steepness and agrees most closely with the commonly used breaker criterion of McCowan (1891), γ_b=0.78. Surprisingly, the measured breaker depth indices in the current tests differed considerably from those of Smith & Kraus (1990, 1991) who examined waves breaking on a similar reef structure.

4.3.1.2 Breaker Height Index

The breaker height index is defined as

$$\Omega_b = \frac{H_b}{H_0}, \tag{4.2}$$

and has been shown by previous studies on emergent, planar slopes (Munk, 1949; Singamsetti & Wind, 1980; Sunamura, 1981; Komar & Gaughan, 1973; Weggel, 1972) to be dependent on both offshore wave steepness H_o/L_o and seabed gradient m.

Measured values of the breaker height index Ω_b as a function of deepwater steepness are shown in figure 4.4. The data displays relatively little scatter and shows a clear trend of increasing breaker height index with decreasing wave steepness. This trend is typical of waves breaking on a plane slope due to the greater shoaling experienced by the longer period waves before breaking (US Army Corps of Engineers, 2002). The work of previous researchers has shown that the data typically follows a power law and can be expressed in the form

$$\Omega_b = C(m)\left(\frac{H_0}{L_0}\right)^{-n(m)} . \tag{4.3}$$

However as only one reef gradient is examined in the present study, the values of $C(m)$ and $n(m)$ are constant and the expression for the breaker height index Ω_b is reduced to

$$\Omega_b = 0.4982\left(\frac{H_o}{L_o}\right)^{-0.2058} . \tag{4.4}$$

The results obtained by previous authors of the breaker height index are also shown on figure 4.4 for comparison with the current data. It is seen that most of the results fall within the range of values obtained in previous studies. It is encouraging that the results presented in figure 4.4 compare most favourably with the data of Smith & Kraus (1990) as this is the only other dataset that was obtained from waves breaking on submerged reefs rather than emergent planar slopes. Smith & Kraus (1990) noted that the presence of an offshore current produced by the high velocity backwash from a preceding wave on an emergent slope would act to increase wave heights at breaking. Because mass can be transported over the reef crest in the case of a submerged reef, the velocity of the backwash is expected to be lower and the effect on the breaking event is reduced, leading to lower values of Ω_b as seen in figure 4.4.

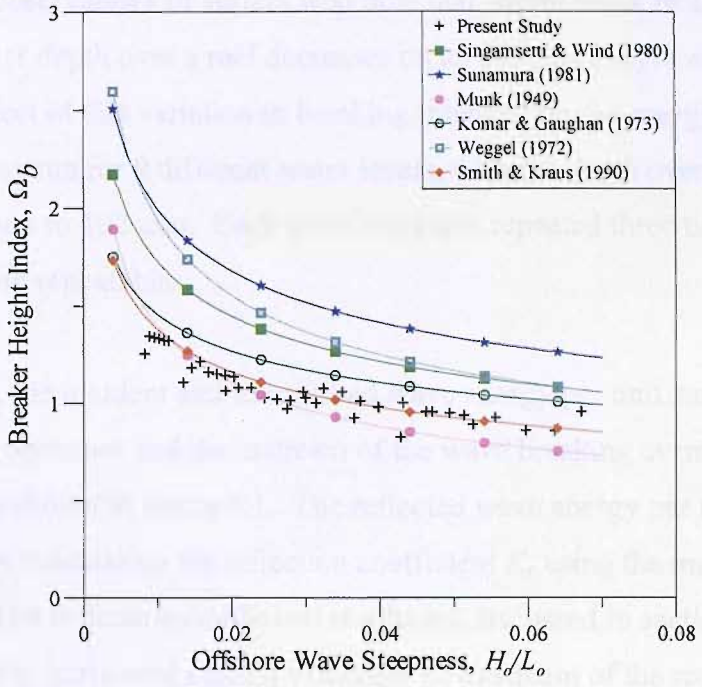

Figure 4.4 Measured breaker height index as a function of deepwater wave steepness. All except for the present data and Smith & Kraus (1990) are for emergent plane slopes.

4.3.2 Energy Dissipation due to Wave Breaking

The primary goal of this chapter is to provide information about the amount of energy dissipated during wave breaking and how it varies with the breaker characteristics. The experiments described in this section were designed to investigate the proportion of the incident wave energy dissipated as waves broke over a submerged reef structure.

As explained in section 3.2.3, the presence of the submerged reef structure caused waves to shoal and break close to the reef crest where they would plunge over the back of the reef and quickly reform into an unbroken wave with only a single jet-splash motion. Thus the experimental setup isolated the initial breaking event and estimates of energy dissipation were made by measuring the incident and transmitted wave fields.

In these tests, 16 different wave cases were run with the deepwater wave steepness H_o/L_o varying in the range $0.0055<H_o/L_o<0.0691$. Preliminary testing showed that the characteristics of the breaking wave varied not only with the deepwater steepness as shown by previous authors (section 2.2.2), but also with the water depth over the reef, with the wave becoming more plunging as the water level was reduced. This trend is

supported by the observations of surfers who note that waves break in a more plunging manner as the water depth over a reef decreases on an ebb tide (Sayce *et al.*, 1999). To investigate the effect of this variation in breaking intensity on the energy dissipation, each wave case was run for 9 different water levels, with the depth over the reef crest h_c ranging from 62 mm to 102 mm. Each set of tests was repeated three times to ensure that the results were repeatable.

For each test case, the incident and transmitted wave energy per unit surface area, E_i and E_t were measured upstream and downstream of the wave breaking event using a series of wave gauges as shown in figure 4.1. The reflected wave energy per unit surface area E_r was obtained by calculating the reflection coefficient K_r using the method presented in section 3.5.1. The reflection coefficient results are discussed in section 4.3.5. LDV measurements of the horizontal current velocities downstream of the reef suggested that the energy associated with large-scale circulation in the deepwater area behind the reef was minimal. The measured values of E_i, E_t and E_r were used to calculate the total wave energy loss due to the breaking event E_b for each wave condition at the 9 different water levels, where

$$E_b(\%) = \left(\frac{E_i - E_t - E_r}{E_i} \right) \times 100 . \tag{4.5}$$

Figure 4.5 (a) and (b) present the energy loss due to breaking E_b as a function of the water depth above the reef crest h_c normalised by the offshore wave height H_o and the breaking wave height H_b respectively. These figures show that the proportion of the incident wave energy that is dissipated during breaking varies in the range 17 to 86 % and is highly dependent on the water depth over the reef, with the value of E_b increasing as the depth reduces.

These results are of the same order as those of Kapdasli & Turker (2002), Chanson & Lee (1997) and Yuksel *et al.* (1999) who measured the proportion of energy dissipated by waves breaking over reefs to be in the range 20% to 80% and suggested that more energy was dissipated in plunging waves than spilling waves. However these authors

do not appear to have taken the water depth over the reef into consideration and this may explain the large amount of scatter observed in their results.

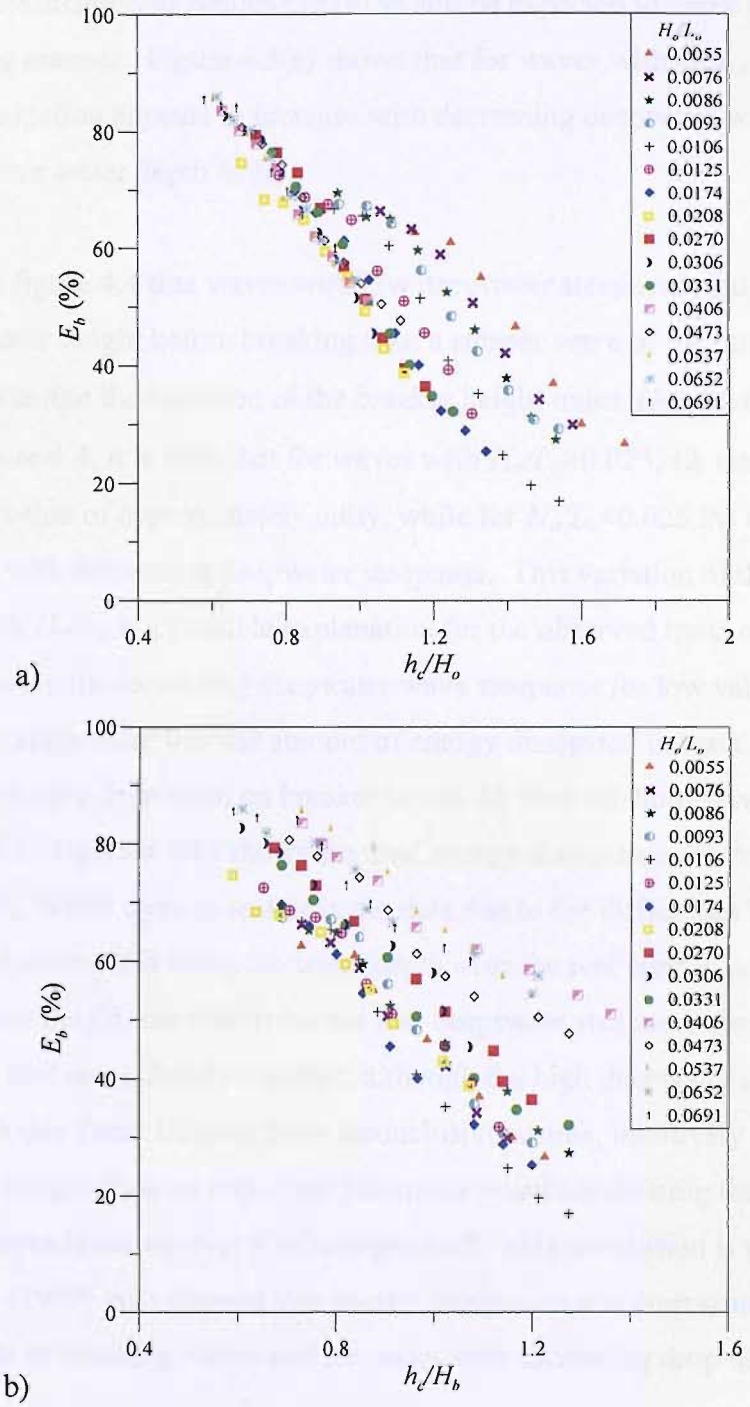

Figure 4.5 Wave energy dissipation as a function of **(a)** h_c/H_o, and **(b)** h_c/H_b.

It is seen in figure 4.5(a) that the results for waves with relatively high values of deepwater steepness ($0.0174 \leq H_o/L_o \leq 0.0691$) collapse approximately onto a single line, suggesting that for a constant reef gradient the energy dissipation from a breaking wave

event is dependent only on the offshore wave height and the water depth over the reef crest, and is not affected by the deepwater wave parameters. However, this trend does not hold true for waves with lower deepwater steepness (H_o/L_o<0.0174), which according to classification of Battjes (1974) would be expected to break in a more intense plunging manner. Figure 4.5(a) shows that for waves with H_o/L_o<0.0174, the total energy dissipation appears to increase with decreasing deepwater wave steepness for a given relative water depth h_c/H_o.

It was shown in figure 4.4 that waves with low deepwater steepness tend to shoal over the reef to a greater height before breaking than a steeper wave of the same initial height. If we examine the variation of the breaker height index Ω_b with deepwater wave steepness in figure 4.4, it is seen that for waves with H_o/L_o>0.025, Ω_b remains fairly constant with a value of approximately unity, while for H_o/L_o<0.025 the breaker height index increases with decreasing deepwater steepness. This variation of the breaker height index with H_o/L_o is a possible explanation for the observed trend of increasing energy dissipation with decreasing deepwater wave steepness for low values of H_o/L_o (H_o/L_o<0.0174), suggesting that the amount of energy dissipated in wave breaking is perhaps more strongly dependent on breaker height H_b than offshore wave height H_o. To investigate this, figure 4.5(b) shows the total energy dissipation due to breaking as a function of h_c/H_b. While there is scatter in the data due to the difficulties in measuring H_b, figure 4.5(b) shows that when the water depth over the reef crest is normalised by the breaking wave height, the results for the low deepwater steepness cases (H_o/L_o<0.0406) plot more closely together, although the high deepwater steepness cases tend to lie above this data. Despite these inconclusive results, intuitively it seems likely that the breaker height H_b is an important parameter when considering the energy dissipated by waves breaking over a submerged reef. This conclusion is supported by Chanson & Lee (1997) who showed that energy dissipation at a drop structure is analogous to that in breaking waves and increases with increasing drop height.

4.3.3 Breaking Intensity and Vortex Size

The previous section has shown that the energy dissipated by wave breaking over a submerged reef increases as the water level over the reef crest is reduced. It was also observed that there was a corresponding increase in the intensity of the breaking event,

with the wave becoming more plunging as the water level decreased. This result is not entirely surprising as previous authors have suggested that as a breaking wave becomes more plunging in nature, there is a corresponding increase in the amount of turbulence, splash and air entrainment associated with the breaking event, (Govender *et al.*, 2002; Yasuda *et al.*, 1999; Lamarre, 1993) all of which contribute to the energy dissipated during breaking. The following section describes measurements designed to investigate this apparent relationship between wave breaking intensity and energy dissipation.

While the term "breaking intensity" is frequently used in the literature as a description of the violence of wave breaking and it is generally understood that a wave with high breaking intensity breaks in a strong plunging manner, very few quantitative definitions of the term exist. Here we examine the use of a definition based on the vortex parameters of Mead & Black (2001) as a quantitative measure of the intensity of breaking waves.

Mead & Black found that the standard definition of breaking intensity using the surf similarity parameter of Battjes (1974) was insufficient for the description of surfing waves. Consequently they defined the breaking intensity of a surfing wave based on the experience of surfers that a wave with a more open "tube" or "vortex" formed between the underside of the overturning jet and the wave face will break in a more violent manner. Mead & Black made use of the work of Longuet-Higgins (1982) whose parametric solution of the equations of motion gives a good description of the forward face of a plunging wave as the jet strikes the trough in front of the wave (figure 4.6). By analysing crest parallel photographs of breaking waves at 23 international surfing breaks, they found that waves breaking on steep reef slopes broke with greater intensity and that there was a linear relationship between the length to width ratio of the vortex l_v/w_v and the orthogonal reef gradient m^*. In this study, the tube of air created between the overturning jet and the wave face in a plunging wave will be termed the vortex after Mead & Black (2001).

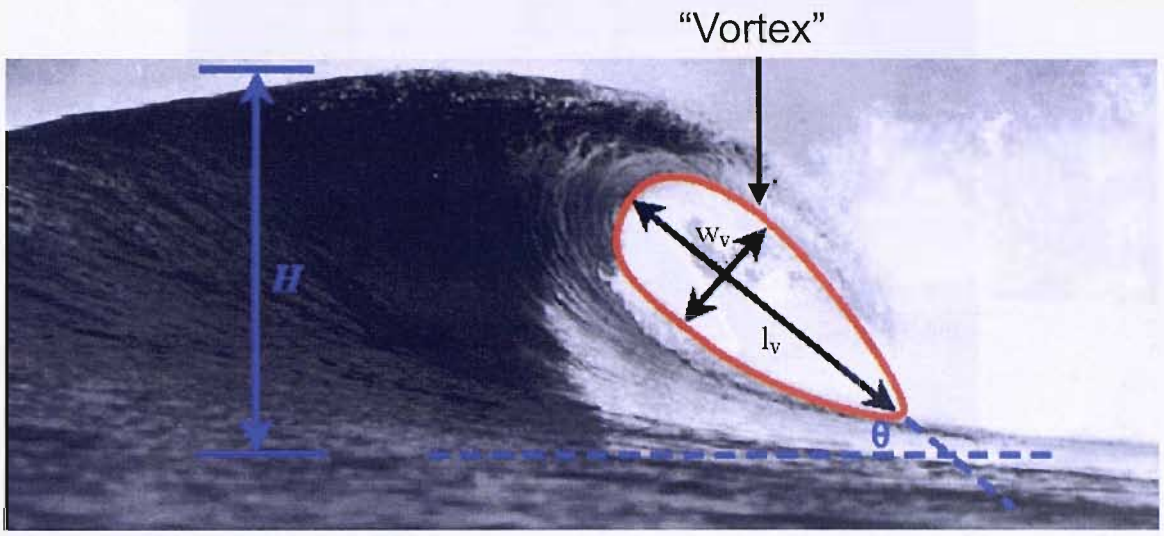

Figure 4.6 Cubic curve fitting to images of breaking waves (after Mead & Black (2001), figure 6.1).

In order to assess the viability of using vortex parameters as a quantitative measure of breaking intensity in the current tests, 7 different plunging wave cases with the value of deepwater wave steepness in the range $0.0055<H_o/L_o<0.0331$ were run for 9 different water levels, with the water depth over the crest, h_c ranging from 62 mm to 102 mm. The vortex length and width were measured by digitising points on scaled digital images of waves at the plunge point, where the leading edge of the overturning jet initially strikes the water surface in front of the wave (figure 4.7). In the majority of cases some water entrainment was evident within the vortex of the breaking wave, a problem also encountered by Couriel *et al.* (1998). This occurred principally due to friction between the high velocity plunging jet and the side walls of the flume and often made determination of the vortex dimensions difficult. However by using high contrast and brightness levels when analysing the images it was possible to determine the predominant vortex shape in the majority of cases, with an accuracy on length of approximately ±10%. To ensure that consistent results were obtained, an average of the measurements from 5 waves for each test case was taken.

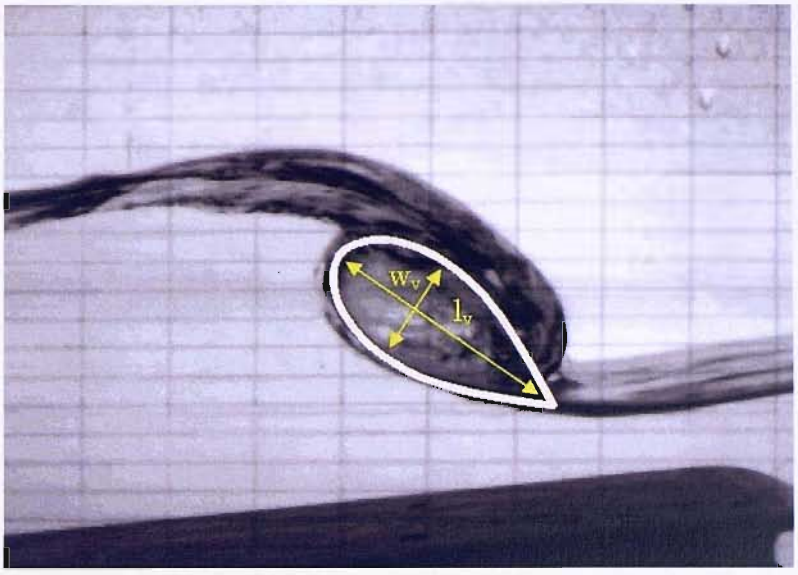

Figure 4.7 Photograph of a laboratory wave at the plunge point with a cubic curve fitted to the vortex shape (f=0.6 Hz, H_o=80 mm).

Following the findings of Mead & Black (2001), figure 4.8 shows the measured vortex length to width ratio as a function of the relative crest depth h_c/H_b. The results suggest that there is little dependence of the vortex ratio on the water depth over the reef crest as the value of l_v/w_v varies in a non-systematic manner between 1.46 and 2.28 for all tested values of deepwater wave steepness and water depth. The mean of all the measured vortex ratios is 1.76 which is reasonably consistent with the value of 1.47 calculated using the expression given by Mead & Black (2001) which relates the vortex ratio to the orthogonal seabed gradient, independent of the incoming wave parameters

$$\frac{l_v}{w_v} = 6.5m^* + 0.821, \tag{4.6}$$

where m^* is the orthogonal seabed gradient which is the actual seabed gradient that waves encounter as they refract onto a reef. The parameter m^* is defined by Couriel *et al.* (1998) as

$$m^* = m\cos\theta, \tag{4.7}$$

where θ is the angle between the direction of wave advance and the normal to the bed contours, which in this case is 0°.

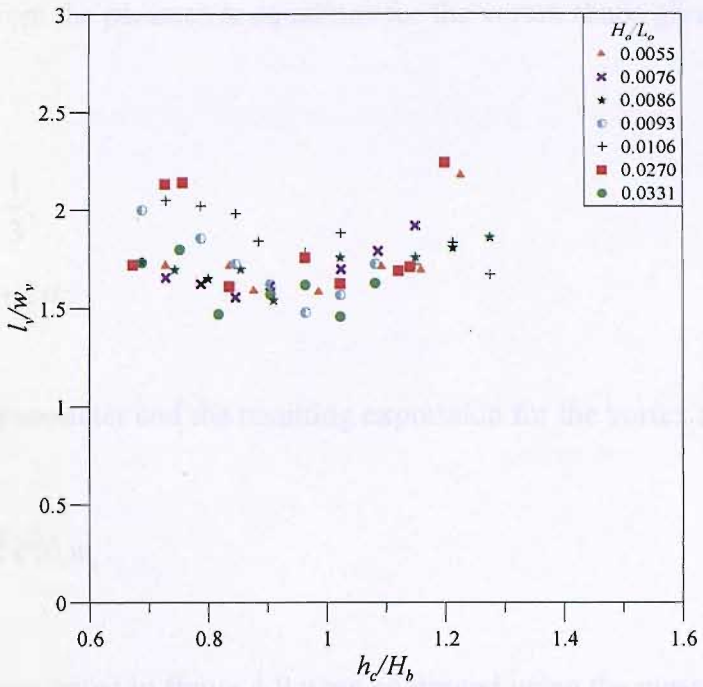

Figure 4.8 Measured vortex length to width ratio as a function of relative water depth over the reef crest.

It is interesting to note that the measured vortex ratios are within the range of values previously observed by Mead & Black (2001) and Sayce *et al.* (1999) in the field and by Couriel *et al.* (1998) in the laboratory, shown in table 4.1. The mean measured vortex ratio of 1.76 is also very close to the value of 1.73 computed by New (1983) for the aspect ratio of an elliptical solution of the shape of the front face of plunging wave, but is considerably lower than the theoretical result of 2.76 for all wave conditions and seabed geometries given by Longuet-Higgins (1982).

Table 4.1 Measured values of the breaking wave vortex length to width ratios.

Study	Type of Study	Max l_v/w_v	Min l_v/w_v
Sayce *et al.* (1999)	Field	4.01	1.79
Couriel *et al.* (1998)	Laboratory	3.4	1.5
Mead & Black (2001)	Field	3.43	1.42
Present Study	Laboratory	2.29	1.46

While no systematic relationship between the vortex length to width ratio and water level could be established from the current data, a better correlation was found by plotting the vortex area A_v normalised by the square of the breaker height H_b as a

function of the relative water depth over the reef crest (figure 4.9). An expression for A_v can be obtained from the parametric equations for the vortex shape given by Mead & Black (2001)

$$l_v = 3\mu^2 - \frac{1}{3}, \tag{4.8a}$$

$$w_v = -\mu^3 + 2\mu, \tag{4.8b}$$

where μ is a free parameter and the resulting expression for the vortex area is

$$A_v = \frac{1}{5}\sqrt{2}\sqrt{6} l_v w_v . \tag{4.9}$$

The vortex areas presented in figure 4.9 were computed using the measured values of l_v and w_v for each test case. The error on the presented values of A_v/H_b^2 is estimated to be approximately ±20%.

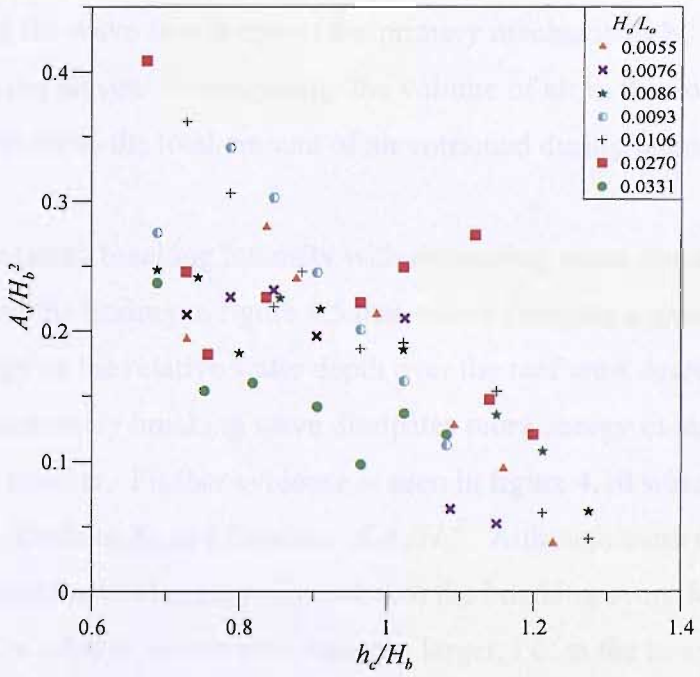

Figure 4.9 Measured vortex area as a function of relative water depth over the reef crest.

Although there is some scatter, figure 4.9 suggests that for each of the wave cases under examination it is clear that the area of the vortex increases in relation to the square of

the breaking wave height as the relative water depth over the reef crest decreases. There does not appear to be any strong correlation between the normalised vortex area and the offshore wave steepness H_o/L_o. This is surprising as the surf similarity parameter (Battjes, 1974) implies that waves break in a more intense manner as the deepwater wave steepness decreases.

The available data shows that while the shape of the vortex remains reasonably consistent for all wave cases and water depths, the absolute dimensions of the vortex increase as the relative water depth over the reef crest decreases. These results suggest therefore that the vortex area normalised by the breaking wave height may be more suitable than the vortex length to width ratio as a quantitative measure of the breaking intensity, and this value increases as the relative water depth over the crest of the submerged reef reduces.

In addition, knowledge of the size of the vortex is essential for studies of air entrainment in breaking waves as it was suggested by Deane & Stokes (2002) that submergence and breakup of the air volume enclosed between the underside of the overturning jet and the wave face is one of the primary mechanisms by which air is entrained by breaking waves. Consequently the volume of air in the vortex will contribute significantly to the total amount of air entrained during breaking.

If the result of increasing breaking intensity with decreasing water depth is considered in combination with the finding in figure 4.5 that waves dissipate a greater proportion of their incident energy as the relative water depth over the reef crest decreases, it appears to confirm that an intensely breaking wave dissipates more energy in initial breaking than a less intense breaker. Further evidence is seen in figure 4.10 which displays the energy loss due to breaking E_b as a function of A_v/H_b^2. Although there is some scatter, this figure shows that the total energy dissipated in the breaking event for each wave case increases as the relative vortex area becomes larger, i.e. as the intensity of breaking increases. These results are in agreement with those of Loewen & Melville (1994) and Lamarre (1993), who found a similar strong correlation between the area of the vortex A_v and the energy dissipated at breaking. As entrainment of air is one of the mechanisms by which breaking waves dissipate energy, this result may be partly explained by considering that as the area of the vortex increases, more air will be

entrained and thus a greater proportion of the incident wave energy will be dissipated by this mechanism.

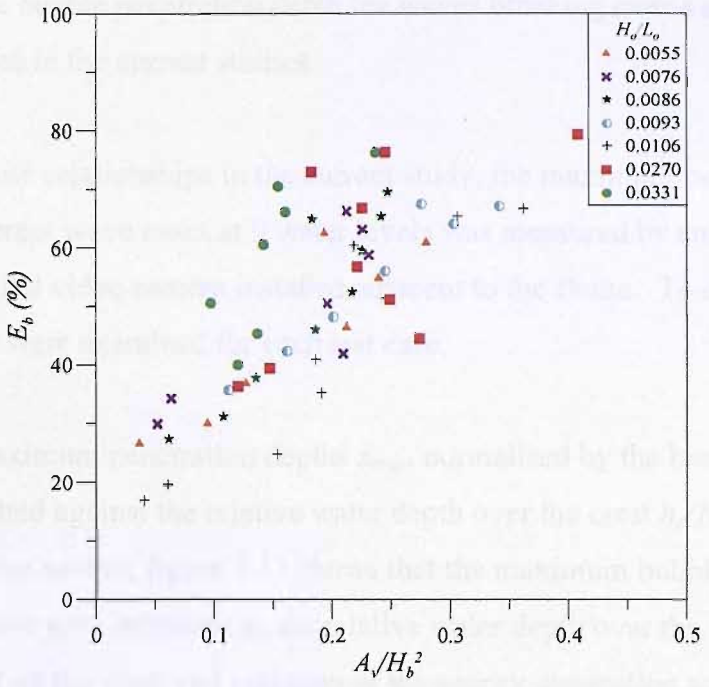

Figure 4.10 Wave energy dissipation as a function of relative vortex area.

4.3.4 Energy Dissipation due to Air Entrainment

Breaking waves are associated with large quantities of air entrainment, which has been shown by previous authors to contribute to the energy dissipated during wave breaking (section 2.5.1). In addition, the results in section 4.3.3 demonstrate that the amount of energy dissipated by a breaking wave increases with the size of the vortex of air enclosed between the underside of the overturning jet and the wave face and it was suggested that energy lost in entraining this air volume may partially explain this relationship.

A more detailed investigation of the contribution of air entrainment to the total energy dissipated by a breaking event is presented in chapter 5. However it is initially informative to examine the relationship between the bubble plume penetration depth and the energy dissipated during wave breaking for waves with various breaking intensities. Hwung *et al.* (1992) and Hoque (2002) noted that plunging breakers entrain air to a greater depth than lower intensity spilling breakers of an equivalent height,

implying that more energy is expended in entraining air against buoyancy in a high intensity plunging wave. Support for this conclusion is provided by Yuksel *et al.* (1999) and Chanson & Lee (1997) who showed that the energy dissipated at breaking increases with the bubble penetration depth for waves breaking over a submerged reef similar to that used in the current studies.

To investigate these relationships in the current study, the maximum bubble penetration depth for 16 different wave cases at 9 water levels was measured by analysing images obtained by a digital video camera installed adjacent to the flume. To obtain consistent results, 10 waves were examined for each test case.

The measured maximum penetration depths z_{max}, normalised by the breaking wave height H_b are plotted against the relative water depth over the crest h_c/H_b in figure 4.11. While there is some scatter, figure 4.11 shows that the maximum bubble penetration depth for each wave case increases as the relative water depth over the reef crest decreases. Based on the observed variation of the energy dissipation and breaking intensity with water depth presented in sections 3.3.2 and 3.3.3, this suggests that the bubble penetration depth becomes greater as the breaking intensity increases and more energy is dissipated during wave breaking. Support for this is shown in figure 4.12 where a clear relationship is seen between the depth of bubble penetration normalised by the offshore wave height H_o (for consistency with Chanson & Lee (1997) and Yuksel *et al.* (1999)) and the total energy dissipated by breaking for each wave case, although again there is some scatter in the data. Best fits to the results of Yuksel *et al.* (1999) and Chanson & Lee (1997) are also plotted on figure 4.12 and it is seen that while there are differences between the three sets of results, they are of the same order of magnitude and there is a consistent trend of increasing energy dissipation with bubble penetration depth.

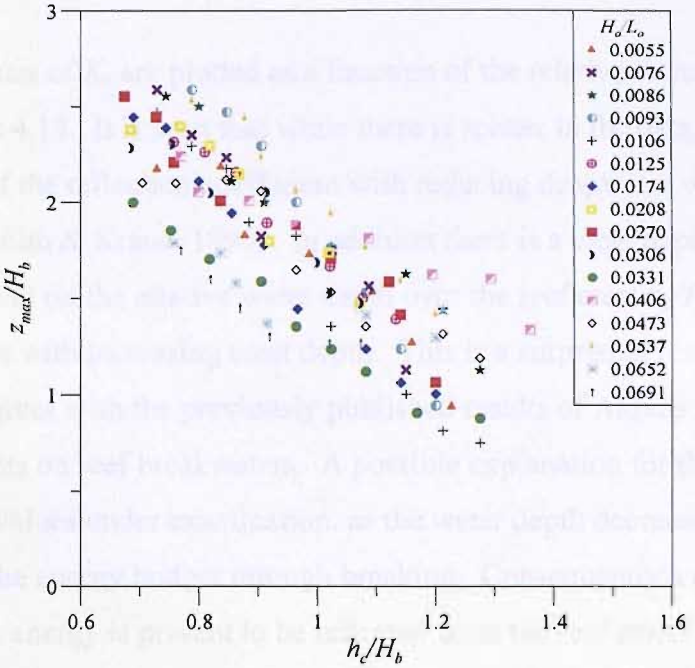

Figure 4.11 Bubble penetration depth as a function of relative water depth over the reef crest.

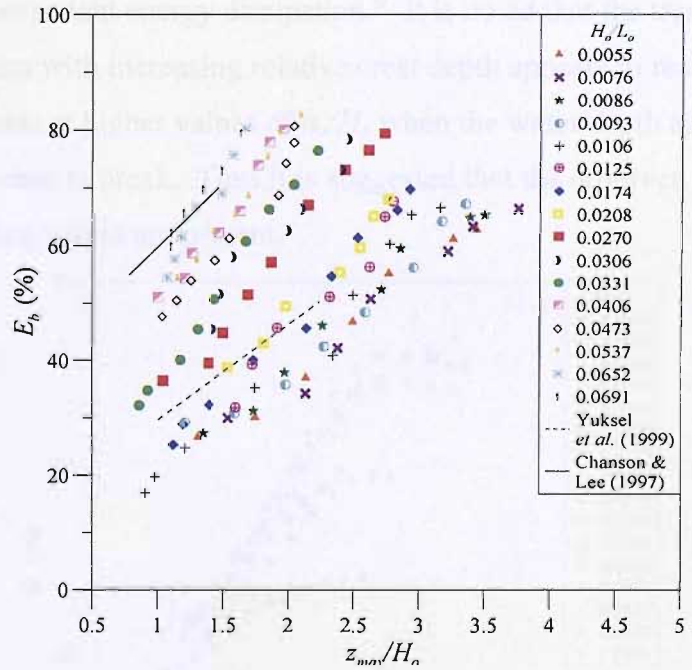

Figure 4.12 Wave energy dissipation as a function of bubble penetration depth.

4.3.5 Reflection Characteristics of the Submerged Reef

In order to estimate the reflected wave energy E_r used in equation 4.5, and also to provide information about the experimental setup used for the tests presented in this thesis, the value of the reflection coefficient K_r was calculated for each of the wave cases examined in section 4.3.2.

The measured values of K_r are plotted as a function of the relative water depth over the reef crest in figure 4.13. It is seen that while there is scatter in the data, there is a general increase of the reflection coefficient with reducing deepwater wave steepness in agreement with Smith & Kraus (1990). In addition there is a clear dependence of the reflection coefficient on the relative water depth over the reef crest h_c/H_o with the value of K_r getting larger with increasing crest depth. This is a surprising result as it is non-intuitive and disagrees with the previously published results of Ahrens (1987) who made measurements on reef breakwaters. A possible explanation for this result is that over the range of values under examination, as the water depth decreases, more energy is removed from the energy budget through breaking. Consequently a smaller amount of organised wave energy is present to be reflected from the reef structure. This conclusion is supported by Battjes (1974) who suggested that the "relative amount of wave energy that can be reflected off a slope is intimately dependent on the breaking processes and the attendant energy dissipation." It is noted that the trend of increasing reflection coefficient with increasing relative crest depth appears to reach a maximum and begin to decrease at higher values of h_c/H_o when the water depth approaches a level where the waves cease to break. Thus it is suggested that the observed trend is only valid where breaking waves are present.

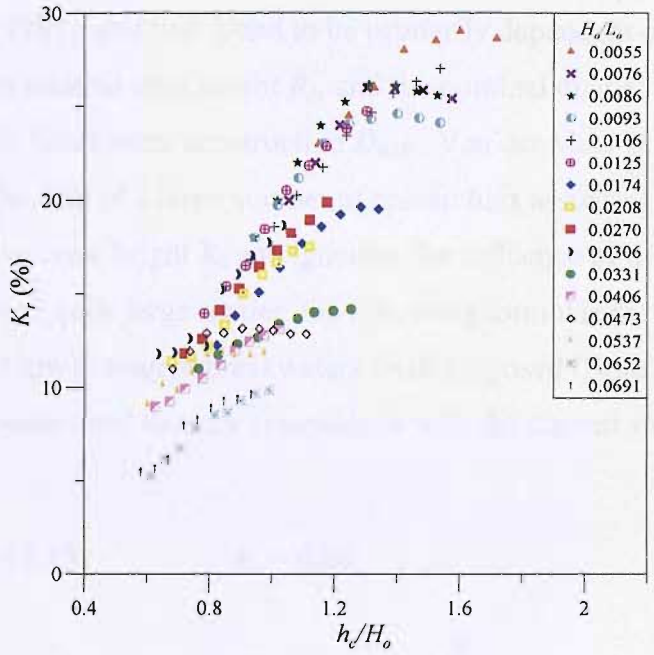

Figure 4.13 Measured reflection coefficients as a function of relative water depth over the reef crest.

4.3.6 Coastal Protection Reefs

The measurements of the amount of energy dissipated by waves breaking over a submerged reef presented in figure 4.5 are also of interest to the designers of submerged reefs and breakwaters for coastal protection as they provide information about wave transmission past low gradient submerged structures.

The results presented in figure 4.5 display the percentage of the incident wave energy lost due to wave breaking over the reef. For design of coastal structures such as breakwaters, it is more common to examine the wave energy dissipation over a structure in terms of a wave height transmission coefficient K_t which is defined as

$$K_t = \frac{H_t}{H_i} = \left(\frac{E_t}{E_i}\right)^{1/2}, \tag{4.10}$$

where H_t and H_i are the transmitted and incident wave heights respectively.

Wave height transmission past both submerged and low emergent breakwaters has been examined by many researchers including Ahrens (1987), Seelig (1980), Van der Meer (1990) and Allsop (1983), and was found to be primarily dependent on the incident wave conditions, the relative crest height R_c, and the nominal diameter of the armourstone used for breakwater construction D_{n50}. Van der Meer & Angremond (1992) reanalysed the data of a large number of researchers assuming that K_t depends largely on the relative crest height R_c and ignoring the influence of the armour size. While the data showed quite large scatter, the following formulae for wave transmission over submerged and low emergent breakwaters were proposed (Note that R_c is positive for emergent breakwaters and thus for comparison with the current study R_c=-h_c);

for $-2.0 < \frac{R_c}{H_i} < 1.13$ $\qquad K_t = 0.80,$ (4.11a)

for $-1.13 < \frac{R_c}{H_i} < 1.2$ $\qquad K_t = 0.46 - 0.3\frac{R_c}{H_i},$ (4.11b)

for $1.2 < \frac{R_c}{H_i} < 2.0$ $K_t = 0.10.$ (4.11c)

The data from the current study is plotted in figure 4.14 and compared to the formulae of Van der Meer & Angremond (1992). It should be noted that all of the data analysed by Van der Meer & Angremond (1992) was taken from irregular wave studies, while the current work examines the breaking of regular waves. It is seen that the measured transmission coefficients for waves breaking on the submerged reef are predominantly lower than the values derived from submerged breakwater studies, particularly as the relative water depth over the reef crest decreases. This suggests that a submerged reef with a relatively low seaward gradient is more efficient at dissipating wave energy through wave breaking than a steep sided breakwater. A likely explanation for this is that the relatively low gradient submerged reef examined in this study allows waves to shoal and break by depth limited conditions. By contrast, a wave breaking on a submerged rubble mound structure with a seaward gradient typically of the order 1:2 will have no opportunity to shoal prior to breaking and tends to surge up over the breakwater and break with a modified breaker type such as the two-step breaker or the drop-type breaker (Takikawa *et al.* 1997).

A further point of interest is that the data of Van der Meer (1990) suggests that for a constant value of R_c/H_i on a submerged breakwater, a longer period wave will yield a larger value of K_t. This is in contrast to the data from the current tests where it is seen that waves with a low offshore steepness tend to yield lower transmission coefficients, particularly for higher values of relative crest height. A possible explanation for this has been discussed earlier where it was suggested that the amount of energy dissipated by breaking is at least partially dependent on the height of the wave at breaking. As seen in figure 4.4, waves with lower deepwater steepness have a higher breaker height index and thus shoal to a relatively greater height, dissipating a greater proportion of their incident wave energy on breaking, leading to a lower value of K_t.

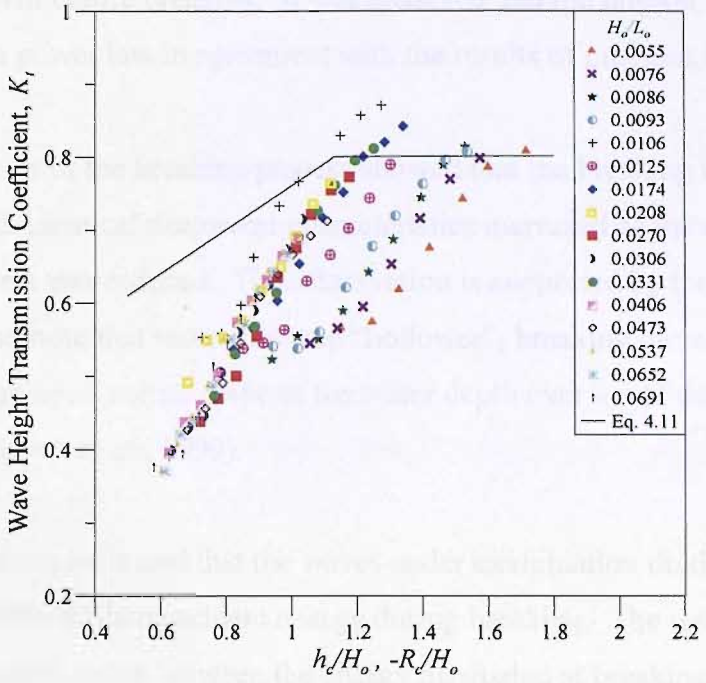

Figure 4.14 Measured wave height transmission coefficients as a function of the water depth over the reef crest.

4.4 DISCUSSION AND SUMMARY

The experiments presented in this chapter have examined various properties of waves breaking over a submerged reef structure, focussing on the intensity of wave breaking and the associated energy dissipation. The results obtained in these tests supply new information on the nature of waves breaking over submerged reefs which are of interest to the coastal science and engineering community as a whole, as well as providing specific knowledge about the current experimental set-up which is essential for the proper interpretation of the work presented in chapters 5, 6 and 7.

The main findings of the work described in this chapter are listed below.

1. The breaker depth index γ_b for waves breaking on a submerged reef with an offshore gradient of 1:10 was found to be approximately constant for all measured values of deepwater wave steepness H_o/L_o, with a mean value of γ_b=0.85H_b. The measured breaker height index Ω_b was observed to increase with decreasing deepwater wave steepness due to the increased shoaling of longer

period waves before breaking. It was observed that the breaker height index followed a power law in agreement with the results of previous researchers.

2. Observations of the breaking process showed that the breaking intensity of waves with identical deepwater characteristics increased as the water level over the reef crest was reduced. This observation is supported by the observations of surfers who note that waves become "hollower", breaking more intensely and with a more open vortex shape as the water depth over a reef decreases on an ebb tide (Sayce *et al.*, 1999).

3. Measurements indicated that the waves under examination dissipated between 17% and 86% of their incident energy during breaking. The results showed that there is a relationship between the energy dissipated at breaking and the relative water depth over the reef crest (h_c/H_o or h_c/H_b), with the amount of energy dissipation increasing as the water depth was reduced and the wave became more violently plunging in nature.

4. The use of vortex parameters to provide a quantitative measure of the breaking intensity of breaking waves was investigated. It was found that the relative area of the vortex of a breaking wave provided the most successful measure of the intensity of waves breaking over a submerged reef. Measurements showed that the value of the relative vortex area A_v/H_b^2 increased systematically as the relative water depth over the reef crest h_c/H_b was reduced, supporting the conclusion suggested above that waves become more violently plunging in nature as the water depth decreases. No obvious dependence of the relative vortex area on the deepwater wave parameters was observed.

5. The results showed that the energy dissipated during wave breaking increased with the area of the vortex, i.e. as the breaking intensity became greater in agreement with the results of Lamarre (1993) and Loewen & Melville (1994). It is suggested that a partial explanation for this is that as the area of the vortex increases, more air will be entrained and thus a greater proportion of the incident wave energy will be dissipated by this mechanism. In addition, it is suggested

that a more intensely breaking wave will also generate more turbulence, noise and splash, all of which will contribute to the increased dissipation.

6. The maximum bubble penetration depth was observed to increase as the breaking intensity of each wave case and the amount of energy dissipated by wave breaking increased in agreement with the results of Yuksel *et al.* (1999) and Chanson & Lee (1997). This result provides further support that the energy required to entrain air against buoyancy during wave breaking contributes to the total wave breaking energy dissipation and this will be examined in greater detail in chapter 5.

7. When examined together, the results presented in this chapter suggest that for each wave case, the total energy dissipated during breaking and the associated air entrainment increase as the water depth over the reef crest is reduced and the breaking wave becomes more plunging in nature. The results suggest that air entrainment contributes to the total energy dissipated during wave breaking and that the magnitude of this contribution increases as the breaking intensity of the wave increases.

8. The reflection coefficient K_r measured upstream of the submerged reef was seen to increase with decreasing deepwater wave steepness, supporting the results of Smith & Kraus (1990). In addition a clear dependence of the reflection coefficient on the relative water depth over the reef crest h_c/H_b was observed, with the value of K_r increasing with increasing water depth. This result is thought to be explained by the observed increase in energy dissipated at breaking as the water level is reduced, i.e. as the water depth is reduced, more energy is removed from the total energy budget through wave breaking and consequently less energy is available to be reflected from the reef structure.

9. The relevance of the measurements presented in this chapter to the design of submerged coastal protection structures was discussed. It was seen that in general the value of the transmission coefficients K_t measured over the submerged reef used in the current experiments was lower than those measured by previous investigators for steep sided submerged breakwater structures,

particularly at low water levels. Therefore the results suggest that a relatively low gradient reef structure such as that used in these tests is more efficient at dissipating wave energy than a standard, steep sided submerged breakwater.

CHAPTER 5 – VOID FRACTION MEASUREMENTS

5.1 INTRODUCTION

Of the energy dissipation that takes place in violent breaking waves, part can be accounted for by work done against the buoyancy of bubbles and also by generating splashes that may rise to elevations far above the wave crest. In deep water the probability of encountering air in the vicinity of breaking waves varies from close to zero at large submergence to almost unity at high elevations. Between these extremes in regular long-crested waves, there exists a two-dimensional continuum of time-dependent, ensemble-averaged void fractions. A detailed knowledge of this distribution would represent a major contribution to a better understanding of the process of wave breaking and have application in many scientific fields as discussed in section 2.3. However, despite much interest in the subject, existing measurements of the void fraction field in breaking waves other than those of Lamarre (1993) are relatively limited. This is mostly due to the difficulties involved in making accurate measurements in the dense bubble plumes generated at breaking which undergo rapid spatial and temporal variations in the period after their creation. Previous studies of air entrainment beneath breaking waves have made use of a variety of techniques including local conductivity probes (Cox & Shin, 2003; Hoque 2002), global conductivity probes (Lamarre & Melville, 1994), acoustic techniques (Vagle & Farmer, 1998) and laser methods (Hwung *et al.*, 1992). However as discussed in section 2.3.5 many of these have shortcomings such as large measurement volumes, limited sensitivity at either end of the range of void fractions, or probes that are significantly intrusive.

This chapter presents detailed measurements of the time-varying void fraction field in the region of breaking laboratory waves. The measurements were made using a novel optical fibre phase detection probe that detects individual air-water interfaces over extremely small areas at high frequency. This technique allowed the distribution of void fractions to be measured, not only in the bubble plume generated beneath the free surface, but also, for the first time in the splash-up created by the impact of the overturning jet.

5.2 EXPERIMENTAL ARRANGEMENTS

5.2.1 Description of Apparatus

The experiments described in this chapter were carried out in a wave flume at the University of Southampton equipped with a flap-type wavemaker, the specifications and operation of which have been described in sections 3.2.1 and 3.2.2. A submerged reef as described in section 3.2.3 was installed in the flume with the crest of the reef located 8 m from the wave generator (Figure 5.1). The flume was filled to a depth of 0.7 m with fresh water.

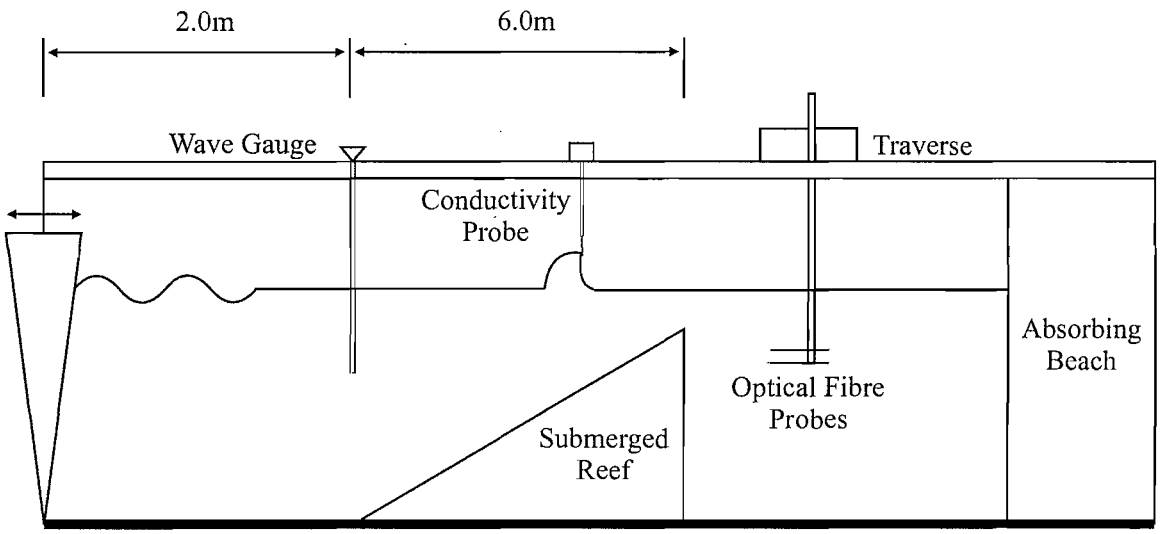

Figure 5.1 Experimental apparatus for the void fraction measurements.

In the experiments described in this chapter and in chapters 6 and 7, the submerged reef was used to generate long trains of repeatable breaking waves (section 3.5.2) in order to allow highly repetitive two-phase flow measurements to be made. The presence of the reef forces waves to break by depth limited conditions at the crest, plunging into the deepwater area behind the reef where they generate splash and entrain air before reforming into an unbroken wave. By causing waves to plunge over the back of the reef into deep water, there is no interaction between the bubble plume generated by the breaking wave and the flume bed as shown in the photographs presented in figure 5.7 and Appendix A, and this allows the plume to become fully developed. As the bubble plume generated by breaking is allowed to fully evolve, the measurements presented here are more closely comparable to the deep water wave measurements of Lamarre

(1993) than to those of Hoque (2002) or Cox & Shin (2003) which were carried out on an emergent beach structure and where interactions between the bubble plume and the flume bed would be expected.

To make measurements of the incident waves before they broke, a single wave gauge as described in section 3.3.2 was installed at the toe of the reef, a distance of 2 m from the wave generator. In addition, a conductivity probe of the type described in section 3.3.4 was positioned at the breakpoint for each of the wave cases under examination. This probe was used to detect the time of breaking for each wave in a test run to be used as a reference time. The probe was positioned such that it was triggered by the crest of each wave in a test run as the face of the wave became vertical. A photograph of the probe position at the break point is shown in figure 5.2.

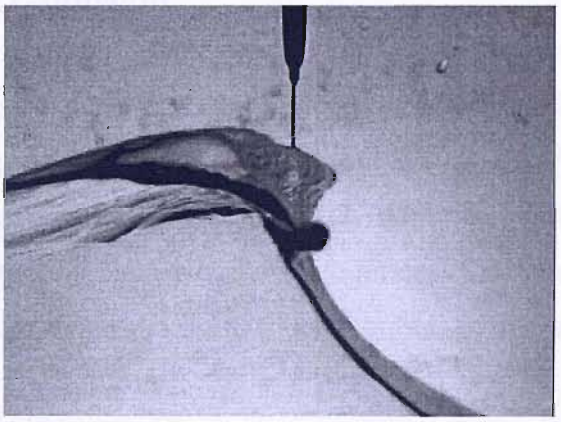

Figure 5.2 Photograph of a wave at the break point triggering the wave detection probe.

Measurements of the air void fraction in both the bubble plume and the splash generated by wave breaking were made using two optical fibre phase detection probes mounted horizontally on an arm suspended from the traverse system. The two probes were arranged such that the tip of the upper probe was positioned directly over the lower probe with a vertical separation of 60 mm. The probes were orientated with their axes aligned with the longitudinal axis of the wave flume (figure 5.3) to maximise the number of bubbles striking them approximately parallel to their axes (β=90°). A detailed description of the principles and operation of the optical fibre probes is given in section 3.4.

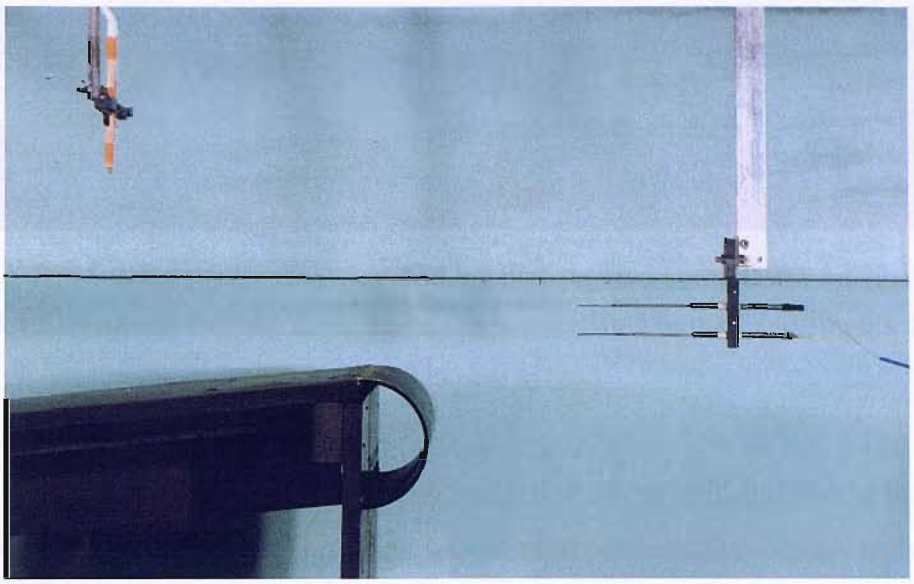

Figure 5.3 Side view of the wave probe and optical fibre probe setup.

5.2.2 Measurement Campaign

The output from the wave gauge and the conductivity and optical probes was sampled at a rate of 150 kHz using a Measurement Computing DAC6070 A/D board connected to a personal computer as described in section 3.3.1.2. A purpose written FORTRAN program described in section 3.4.5.1 was used to process the data from the experiment and detect the arrival and departure times of each bubble at the probe using a single threshold technique.

Three different wave cases were examined, ranging from a strongly plunging breaker to a spilling wave close to the spilling/plunging boundary which demonstrated a small initial overturning motion and then continued to break in a spilling manner. The details of the wave cases examined in this chapter are shown in table 5.1 and photographs of the three breaking waves are presented in figure 5.4.

Table 5.1 Test cases for the void fraction measurements.

Case No.	f (Hz)	H_o (mm)	H_b (mm)	E_i (J/m)	E_b (J/m)	A_v (mm^2)	A_v/H_b^2	Breaker Type
1	0.5	78.2	95	30.58	17.15	2987	0.331	Strongly Plunging
2	0.7	97.2	100	29.46	19.54	2770	0.277	Plunging
3	1.0	100.5	95	19.08	13.14	1697	0.188	Spilling/Plunging

E_i and E_b represent the incident wave energy and energy dissipated during wave breaking based on the results presented in chapter 4. A_v is the cross-sectional area of the vortex enclosed beneath the underside of the plunging jet.

Wave Case 1 **Wave Case 2** **Wave Case 3**

Figure 5.4 Photographs of the three wave cases examined in the experiments described in chapter 5.

In order to examine the spatial and temporal variation of the void fraction in the bubble plume and splash-up created by breaking waves, phase-averaged measurements were taken using the optical fibre probes at between 770 and 970 positions on a 20 mm x 20 mm grid. The origin of the grid was located at the still water level, directly above the reef crest. The size of the measurement grid was determined by the extent of the bubble plume and splash for each wave case, and the limits along each vertical or horizontal transect were taken as the point where two consecutive time-averaged void fraction measurements were either 0% beneath the surface or 100% in the air above the surface. Consequently the size of the measurement grid varied slightly for each wave case, but extended approximately from x=-140 mm, z=120 mm in the top left hand corner to x=840 mm, z=-200 mm in the bottom right corner (figure 5.5).

At each measurement location, a long series of between 200 and 400 regular waves were generated by the wavemaker, where the total number of waves was varied to ensure a stable measurement of the time-varying void fraction at each point in the grid. The repeatability of the void fraction measurements at different points within the measurement grid was confirmed by completing multiple runs at more than 5 locations for each wave case, with the chosen locations distributed throughout the measurement area. The repeatability of the generated and breaking waveforms were examined in section 3.5.2 and shown to be consistent over long periods despite the existence of some reflected waves within the flume. The tests carried out in section 3.5.2 showed that the form of the breaking wave was highly regular once the reflections in the flume had settled into a form of equilibrium which generally occurred at the reef crest after a period of approximately 30 seconds had elapsed since starting the wavemaker. Measurements using the conductivity probe at the break point showed that the time

between successive breaking events was very regular, varying by no more than 0.85% of the average wave period from wave to wave after an initial settling period of 30 seconds. Based on these observations, void fraction measurements for all three wave cases were commenced from the time of the first breaking event after this 30 second settling period had elapsed.

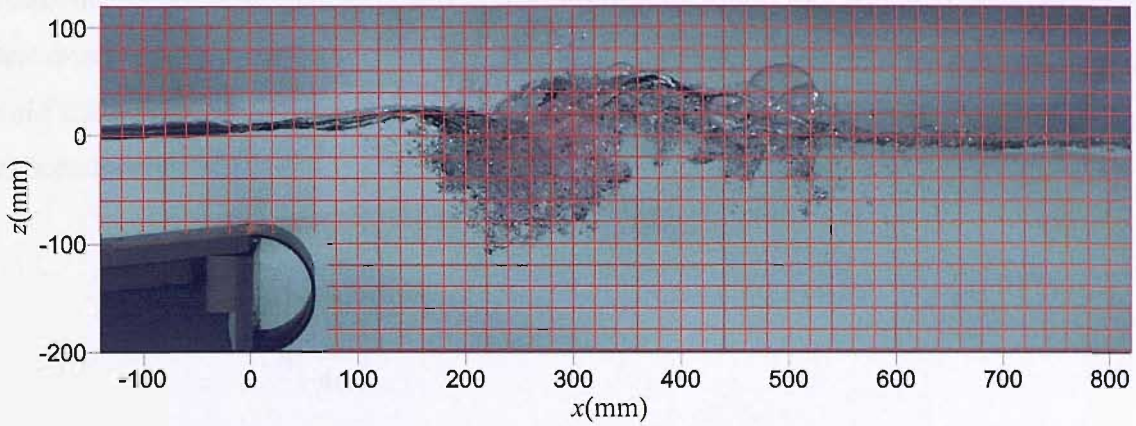

Figure 5.5 Typical measurement grid for the void fraction measurements.

5.2.3 Data Processing

The arrival and departure times of the individual air volumes detected by the optical fibre probes were determined using the purpose written software described in section 3.4.5.1 to compute a residence time t_a for each detection. Note that because the optical fibre probe allows measurements to be taken of both the bubbly flow beneath the free surface and the splash-up above it, an air volume may correspond to either an entrained bubble or a region where no splash exists above the free surface.

In steady flows, the void fraction α at a point corresponds to the proportion of the test duration that the probe tip is in air, and consequently can be computed using a simple data processing method. However, due to the intermittent nature of wave breaking, the air void fraction in the region both above and below the free surface in breaking waves is a function of both time and position. Therefore it is not sufficient to simply record the overall void fraction at each measurement location as this provides no information about the rapidly varying void fractions in the bubble plume and splash-up as the wave breaks.

To examine the temporal evolution of the void fraction at each position within the measurement region, each wave period was divided into 40 phase average time bins of equal length where the time origin of the first bin corresponds to the time of wave breaking as recorded by the conductivity probe. To illustrate this, figure 5.6 shows the raw probe data collected during 5 consecutive waves from wave case 2 where the tick marks along the x-axis represent the size of each phase average bin. The recorded air residence times were then assigned to the appropriate bin(s) and summed over the entire test duration to produce a total air time for each phase average bin. This then allowed a void fraction to be calculated at each position and for each time bin using the following expression

$$\alpha(i,j,n) = \frac{\sum t_a(i,j,n)}{w\left(\frac{T}{40}\right)}, \tag{5.1}$$

where

i = horizontal position of the measurement point,

j = vertical position of the measurement point,

n = phase average bin,

w = number of waves in the experimental run,

T = wave period, and

t_a = individual air residence times.

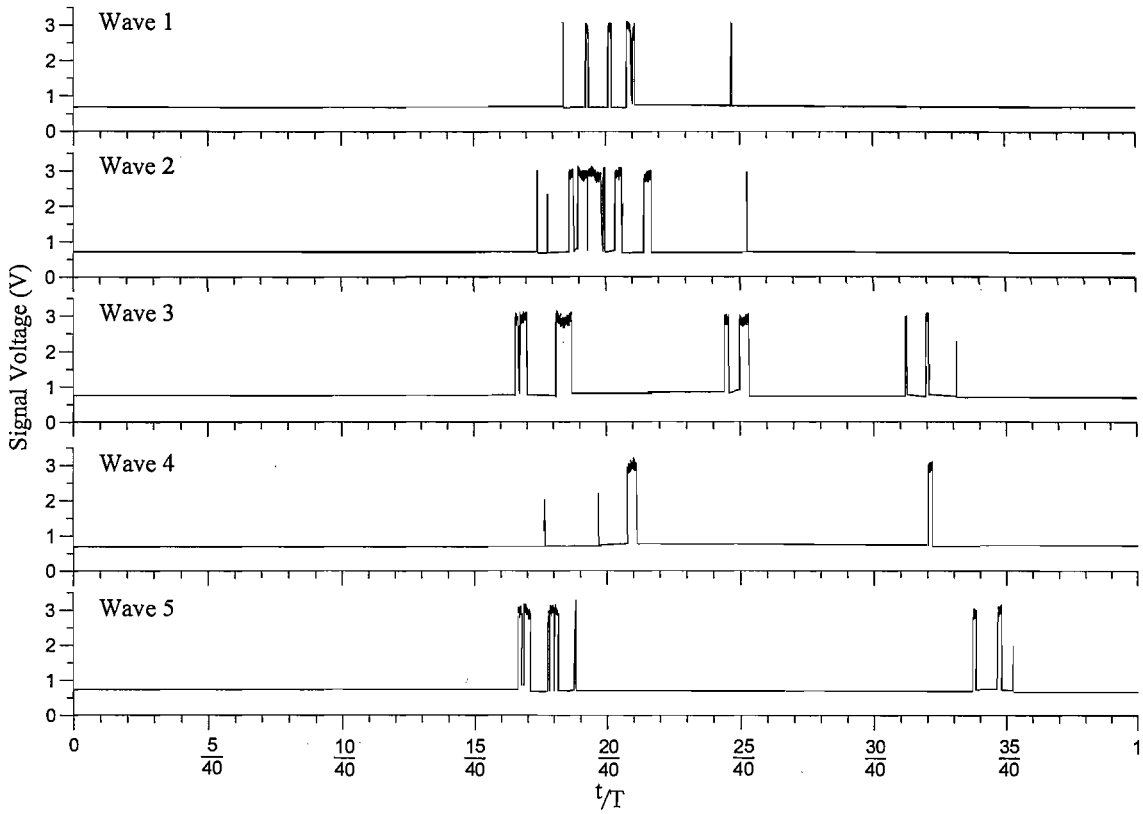

Figure 5.6 Raw data from an optical fibre probe at position x=280 mm, z=-80 mm recorded from 5 consecutive waves during the plunging wave test (wave case 2).

5.3 EXPERIMENTAL RESULTS

5.3.1 Time-varying Void Fraction Distributions

The results from the current experiments were used to create coloured contour plots of the time-varying void fraction field in the region of the wave breaking event. A sequence of plots for wave case 2 is shown in figure 5.7 alongside photographs of the wave profile at the corresponding time. The first plot represents the void fraction distribution at time $t=T/40$ and the time interval between each pair of images is $T/20$. As it is difficult to accurately define the free surface in a turbulent, aerated flow, the 50% void fraction contour was used to approximate the position of the free surface and this is marked with a yellow line in all plots.

It should be noted that the void fraction colour scale in figure 5.7 is non-linear in order that the variations in the void fraction at the upper and lower extremes are captured in the plots. It is also noted that the ensemble averaging process means that the detection

of a single air-water interface over 200 to 400 waves will be visible on the plots. This can make the features of the flow appear more extensive in the contour plots when compared to the corresponding photograph but has the purpose of demonstrating the envelope within which bubbles or splashes were detected during the experiments.

A limitation of the phase averaging process is that the time bins have a length of $T/40$ seconds which is not a sufficiently short period to completely freeze the motion of the rapidly varying wave form at breaking. In addition, despite careful control of the generated waveform and the good measured repeatability of the incident waves, no two breaking events are identical, particularly in the highly dynamic region of the plunging jet. Consequently the flow features evident in the contour plots are often less clearly defined than in the corresponding photograph.

Despite these limitations, it is clear from figure 5.7 that the measurement technique appears to capture the primary features of the two-phase flow generated by wave breaking. The figures show that in the region of breaking waves there is a continuum of time-varying void fractions which varies from 0% at large depths beneath the free surface to 100% at high elevations, with strong gradients in the void fraction distribution close to the free surface and the breaking event. The value of void fraction at a point in the flow is seen to vary rapidly and there is a continuous evolution of the size and position of the bubble plume and splash-up.

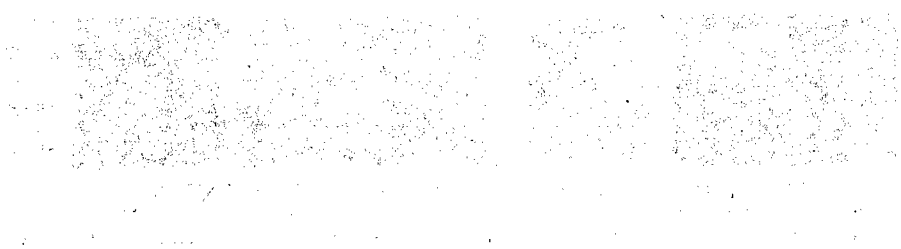

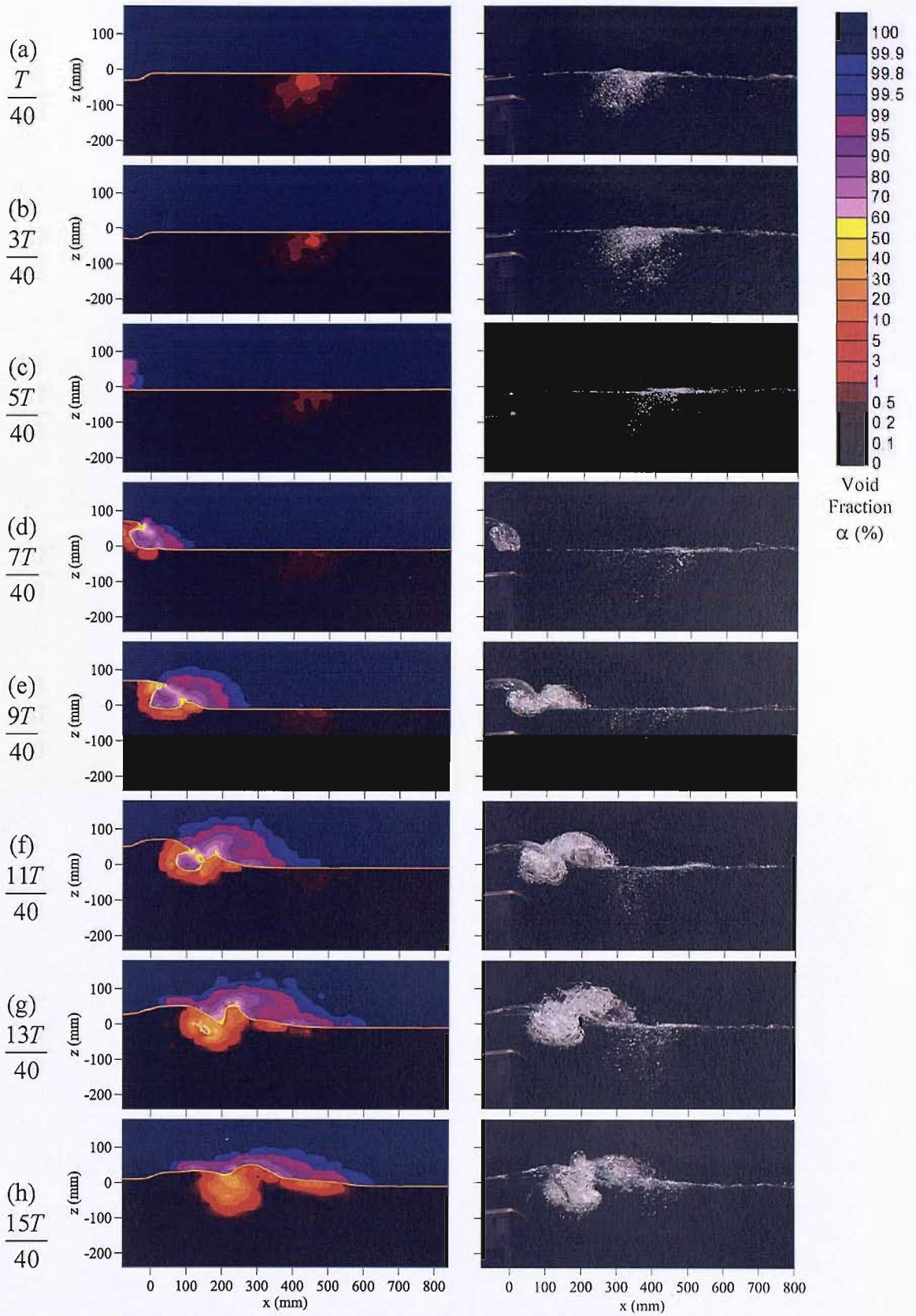

Figure 5.7 Time-varying void fraction distributions for wave case 2. The distributions presented here are calculated at intervals of $T/20$, starting at time, $t=T/40$.

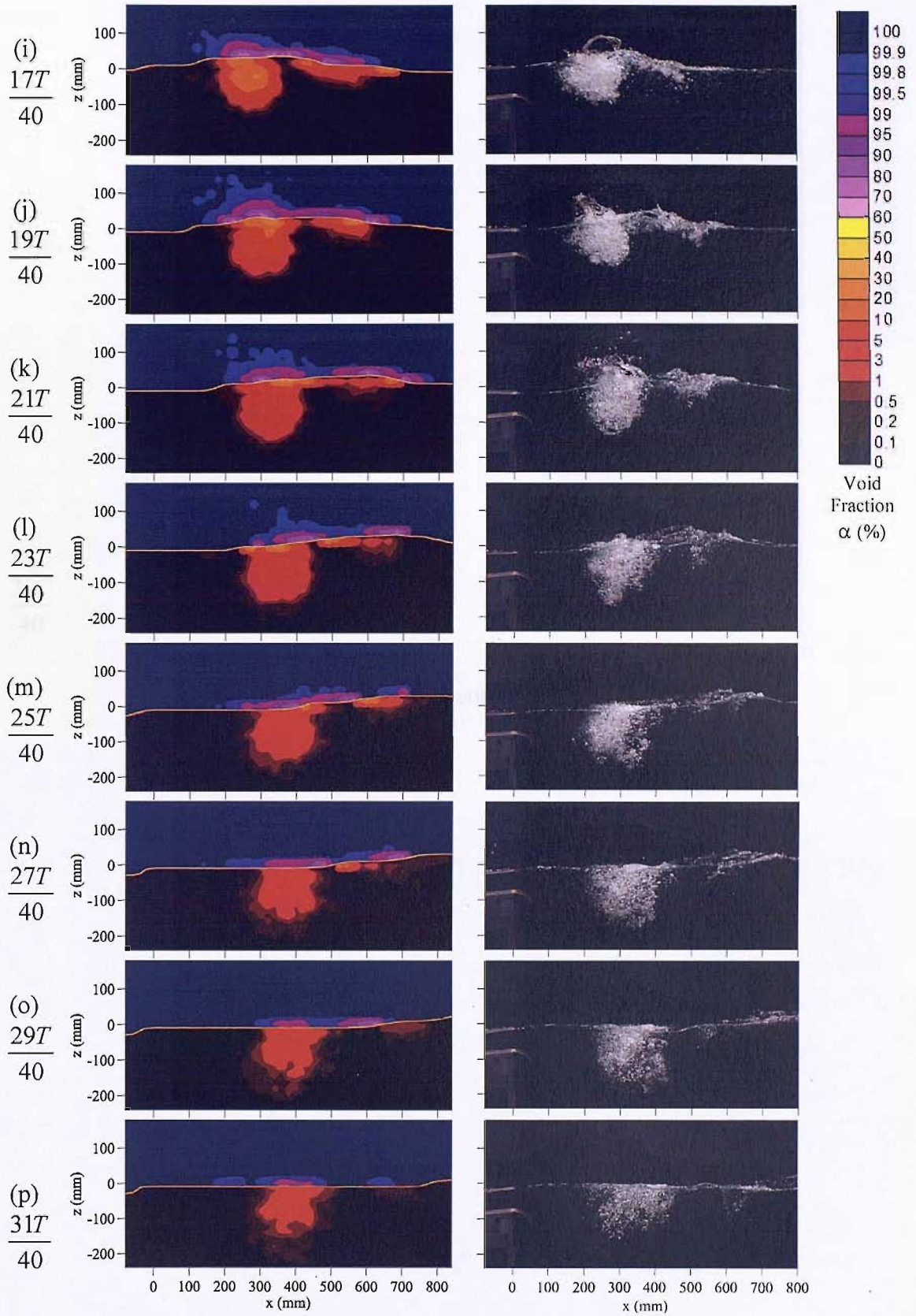

Figure 5.7 (continued).

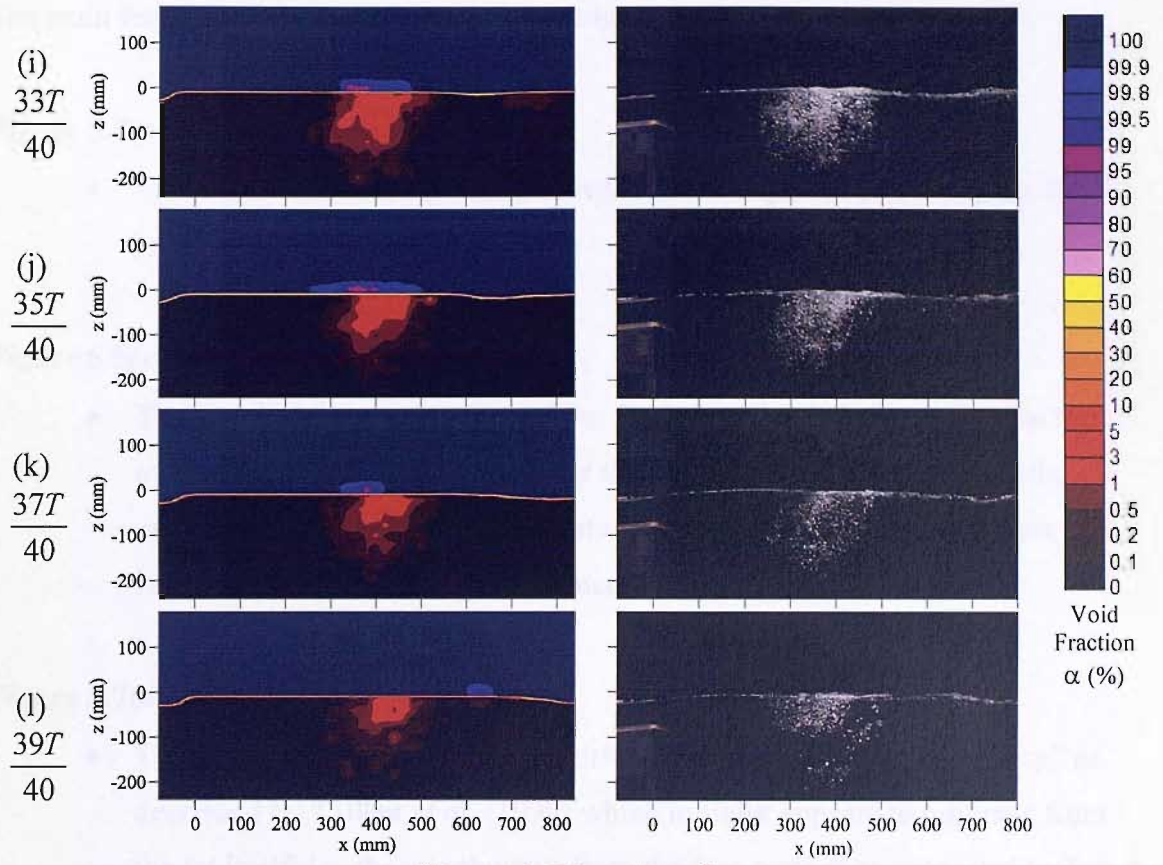

Figure 5.7 (continued).

The main features of the flow that are evident in figure 5.7 are described below:

Figure 5.7(a) to (b) (t=T/40 to 3T/40)

- There is evidence of the remnants of the bubble plume left over from the previous breaking event.

Figure 5.5(c) to (d) (t=5T/40 to 7T/40)

- The new breaking wave enters from the left of the domain and begins to overturn. The shape of the crest as the wave begins to overturn and the water entrainment in the vortex between the plunging jet and the wave face are well captured by the measurements in figure 5.7(d).

Figure 5.7(e) (t=9T/40)

- The plunging jet strikes the free surface and begins to generate "spray" as described by Tallent *et al.* (1990) which initially appears to originate from the jet itself, i.e. the jet rebounds from the free surface as suggested by Lin & Hwung (1992) and Christensen & Deigaard (2001).

Figure 5.7(f) to (g) (t=11T/40 to 13T/40)

- The majority of air entrainment takes place between figures 5.7(f) and (h).
- As the overturning motion continues, the air volume trapped in the vortex between the overturning jet and the wave face is driven down into the water column creating a region of high void fraction beneath the free surface. At this stage, the bubble plume is very dense and consists predominantly of large air cavities rather than small, defined bubbles.
- At the same time, the plunging jet penetrates the free surface and pushes up a triangle of un-aerated water in front of the wave as described by Basco (1985), forming an air cavity between the upper surface of the jet and the distorted free-surface in a similar manner to that seen by Ledesma (2004) and Prosperetti & Oguz (1997) for an unsteady plunging jet.
- The initial "spray" described above develops into a "core" of splash as described by Tallent (1990) which is ejected out in front of the wave from the region between the overturning jet and the green water triangle. This

region can be clearly seen in figure 5.7(g), where the 50% contour line has been distorted into a v-shape.

- The splash is ejected to a height greater than that of the breaking wave and its leading edge is projected a horizontal distance of over 100 mm in front of the wave.
- The origin of the water in this splash core is unclear, however it seems to come partly from the overturning jet and is partly pushed up from the water in the wave trough in front of the breaking wave as suggested by Basco (1985) and Chen *et al.* (1999).

Figure 5.7(h) (t=15T/40)

- The v-shape in the 50% contour becomes less well defined as the overturning motion ceases and the free surface moves back toward an equilibrium position, partially enclosing the air cavity created between the upper surface of the plunging jet and the triangle of un-aerated water.

Figure 5.7(i) to (k) (t=17T/40 to 21T/40)

- This period corresponds to the injection phase of De Leeuw & Leifer (2002) where the air cavities entrained during the formation phase are driven down into the water column and broken up into smaller bubbles as the wave completes its overturning motion, reaching a maximum penetration depth in figure 5.7(l).
- During this period, the free surface moves back to an equilibrium position and the high void fraction bubble plume is compressed, forcing air and water up through the free surface. This creates a vertical spray of small droplets which can reach elevations of up to $5H_b$. This vertical spray can be clearly seen in the photographs and is also well captured in the void fraction measurements. A similar vertical spray was observed by Miller (1976).
- Between figures 5.7(h) and (i), the water forming the primary splash-up falls back to the water surface, generating small amounts of spray close to the free surface and a secondary bubble plume downstream of the main plume. This secondary bubble plume remains close to the free surface and disperses as it is carried downstream by the reformed wave.

- There is no evidence of a significant secondary splash-up generated by the impact of the primary splash-up on the water surface as observed by numerous previous investigators (see section 2.4). It is thought that the lack of additional splash-up cycles is a consequence of the experimental setup, where the wave breaks by depth limited conditions at the reef crest but then rapidly reforms into a non-breaking wave in the deep water area behind the reef.

Figure 5.7(l) to (t) (t=23T/40 to T)

- This long period corresponds to the rise phase of De Leeuw & Leifer (2002) or the "quiescent phase" described by Deane & Stokes (2002). During this period, the primary bubble plume slowly disperses as bubbles rise back to the surface under the influence of buoyancy and the plume spreads horizontally as it is carried downstream by the motion of the reformed wave.
- Small amounts of spray are seen in the void fraction measurements close to the free surface during this period. It is thought that this spray originates predominantly from bubbles bursting at the surface, although it is likely that there is also some unresolved interaction with the free surface.

A sequence showing the results for all 40 time-averaged void fraction plots is found in Appendix A along with the results from the other two wave cases listed in table 5.1. The other sequences show the same general characteristics, although it is observed that in the spilling/plunging case the overturning motion is less violent and there is a less defined active entrainment region. Also, rather than the rapid entrainment and subsequent break up of large air cavities as observed in the plunging wave case shown in figure 5.7, air appears to be entrained steadily over a wider region as the wave gradually overturns in the spilling/plunging wave case.

5.3.2 Integral Properties of the Bubble Plume and Splash-Up

To examine some of the characteristics of the bubble plume and splash-up, various moments of the void fraction field were calculated using a similar method to Lamarre (1993) who presented integral properties of the bubble plumes generated by focussed laboratory waves.

5.3.2.1 Volume per Unit Width of Air and Splash

The total volume of air entrained beneath the approximate free surface (50% void fraction contour) per unit width for each of the 40 phase average bins was computed using the expression

$$V_b(n) = \sum_{i=1}^{i=I} \sum_{j=1}^{j=j_{50}} \alpha_{i,j,n} \delta z \delta x \,, \tag{5.2}$$

where

n = phase average bin,

i = horizontal position of the measurement point,

j = vertical position of the measurement point,

j_{50} = vertical position of the 50% void fraction contour,

δx = horizontal measurement interval, and

δz = vertical measurement interval.

The total volume of splash-up per unit width measured above the approximate free surface was calculated as

$$V_s(n) = \sum_{i=1}^{i=I} \sum_{j=j_{50}}^{j=J} (1 - \alpha_{i,j,n}) \delta z \delta x \,. \tag{5.3}$$

The volume per unit width of the bubble plume and splash-up for each of the 40 phase averages is shown as a function of time in figure 5.8 for the three wave cases detailed in table 5.1. To be consistent with Lamarre (1993), the volumes of air and splash are normalised by the volume per unit width of the vortex of air enclosed between the underside of the plunging jet and the wave face V_v calculated using the measured values of the vortex area A_v presented in table 5.1.

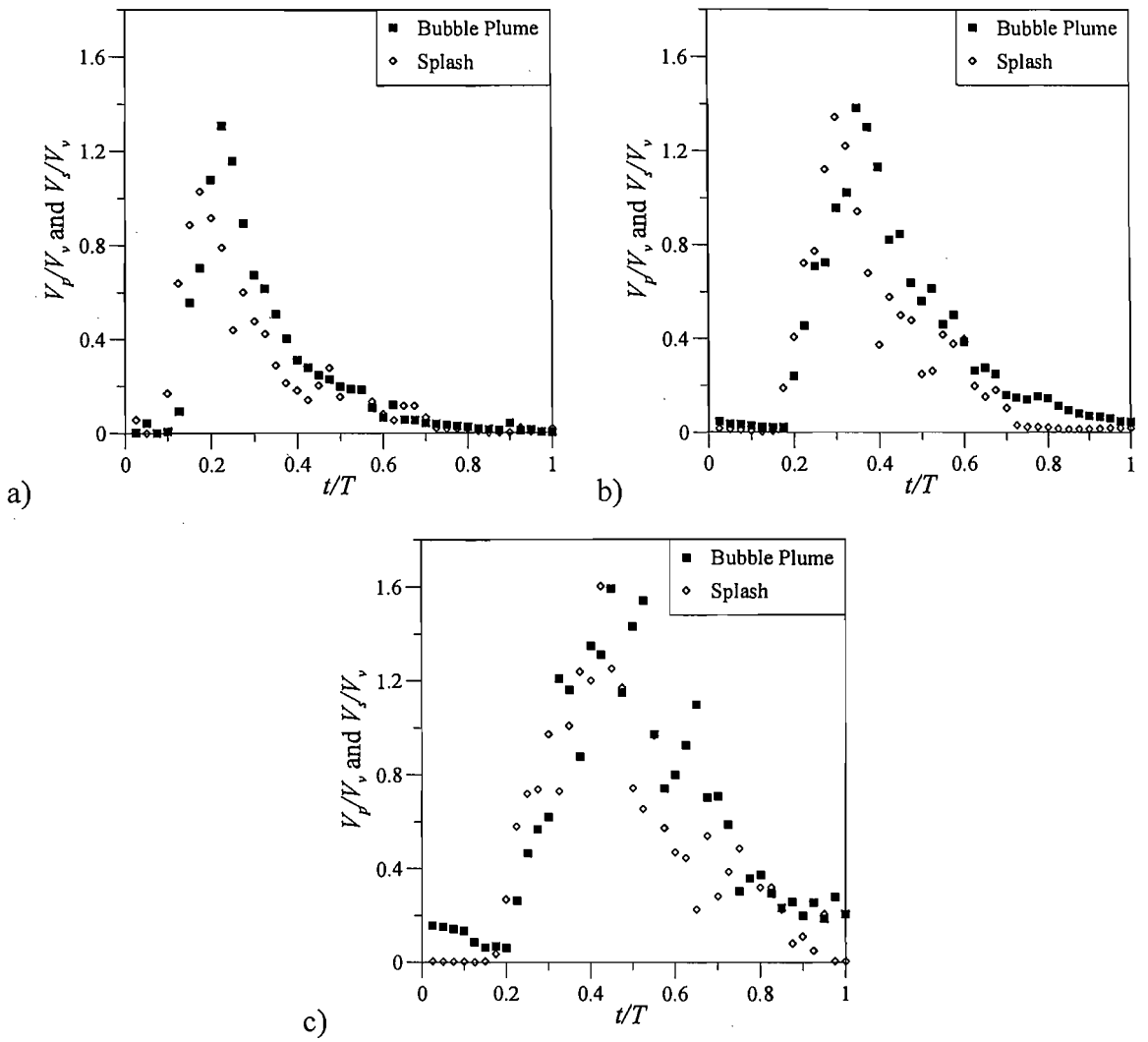

Figure 5.8 Plots of normalised air and splash volume per unit width as a function of time for the **(a)** strongly plunging wave (case 1), **(b)** plunging wave (case 2) and **(c)** spilling wave (case 3).

Figure 5.8 shows that the peak volume of entrained air V_p/V_v varies from 1.3 for the strongly plunging wave, which has the largest vortex volume, to 1.6 in the spilling case where the vortex volume is smallest. These values are higher than those reported by Lamarre (1993) who measured a maximum value of $V_p/V_v \approx 1$ in his experiments. This discrepancy with previous results is thought to be explained by the greater sensitivity of the current measurement technique, the ability of the optical probes to measure void fractions right up to the free surface and possibly differences in the nature of the breaking waves in the two experiments. The plots also show that the maximum splash volume is of the same order as the volume of entrained air in each test case and a phase difference is evident between the start of splash generation and bubble entrainment.

This phase difference can be observed in the images shown in figure 5.7, where splash begins to be generated in figure 5.7(e) but no significant air entrainment is observed until figure 5.7(f).

As noted in section 2.3.2, Deane & Stokes (2002) indicated that air in breaking waves is entrained by two predominant mechanisms:

1. breakup of the vortex of air enclosed between the underside of the overturning jet and the wave face, and
2. entrainment of air in the shear layer generated between the overturning jet and the receiving fluid in the preceding wave trough.

If it is assumed that the entire volume of air enclosed in the vortex is subsequently entrained in the water column, the peak values of V_p/V_v presented in figure 5.8 imply that the vortex accounts for approximately 74% of the total entrained air volume in the strongly plunging case and 62% in the spilling case where the volume of the vortex is relatively small (table 5.1). Thus, the current results suggest that the breakup of the vortex contributes significantly to the total volume of air entrained by breaking waves. It also appears that this air entrainment mechanism becomes more important as the size of the vortex and hence breaking intensity increases in agreement with the suggestion made in section 4.3.3.

In figure 5.8, the time scale on the x-axis is normalised by the wave period in order to be consistent with the results of Lamarre (1993), Kalvoda *et al.* (2003) and others, who found that the time-dependent properties of the bubble plume scaled well with the wave period. It is clear from examination of figure 5.8 that this method of scaling is incorrect for the current study as there is an obvious shift in the position of the peak of the distributions for the three wave cases (a similar shift can be seen in the mean void fraction results of Cox & Shin (2003)). This is not surprising because once they have been generated, there is no significant physical dependence of the bubble plume and splash-up on the wave properties and so there is no reason why they would be expected to evolve on the same time scale.

It seems more reasonable that the characteristic time scale of the bubble plume evolution, at least during the rise phase is the bubble rise time as suggested by Chanson *et al.* (2002b). To examine the validity of this alternative time scale, figure 5.9 presents the volume of bubbles per unit width as a function of time normalised by the time taken for a bubble with a diameter of 2.5 mm to rise a distance equal to the wave breaking height

$$t_{rise} = \frac{H_b}{u_r}, \tag{5.4}$$

where u_r is the bubble rise velocity.

The rise velocity of the bubble, u_r was calculated using the expression of Leifer & Patro (2002) given in equation 7.18. A 2.5 mm diameter bubble was chosen based on the mean bubble diameter results presented in section 6.4.1 and observations of the typical bubble diameters in the laboratory bubble plumes. It is clear from figure 5.9 that this alternative method of scaling the bubble plume parameters is more suitable than that used in figure 5.8, with all three distributions collapsing reasonably well onto a single curve and the total volume of entrained air decaying as an exponential in agreement with the results of Lamarre (1993). It is noted that there is no strong physical dependence of the timescale of the formation and injection phases on the bubble rise time and the fact that the data collapses onto a single curve is partially because these processes occurred on a similar timescale in all three cases and the bubble rise time is almost constant for the three cases.

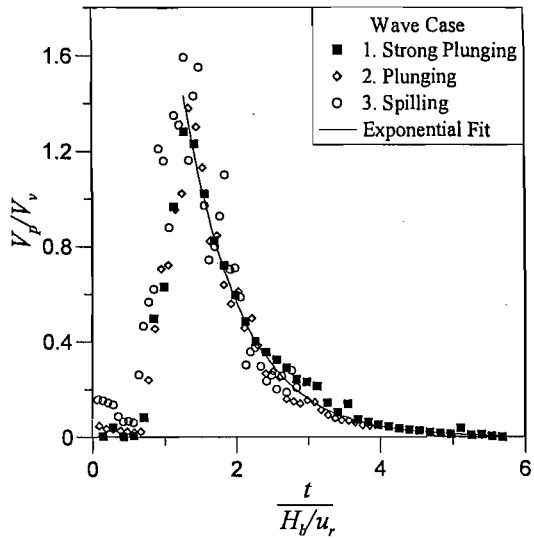

Figure 5.9 Volume per unit width of entrained air bubbles as a function of time for all three wave cases.

The use of this alternative time scale means that it is not possible to quantitatively compare the integral properties of the bubble plume in the current study with those presented by Lamarre (1993), because insufficient data is available to correctly convert his results to the current time scale. It is possible however to compare the trends displayed by Lamarre's results to the current data and this is done where appropriate.

Figure 5.10 presents the volume of the spray in the splash-up per unit width as a function of time normalised by the time for a splash droplet to fall a distance equal to the breaking wave height

$$t_{fall} = \sqrt{\frac{2H_b}{g}}. \tag{5.5}$$

Although a slight shift in the position of the peak values of the distributions is evident, figure 5.10 suggests that this alternative method of scaling the temporal evolution of the splash-up properties is more suitable than that used in figure 5.8 and will be used in subsequent plots.

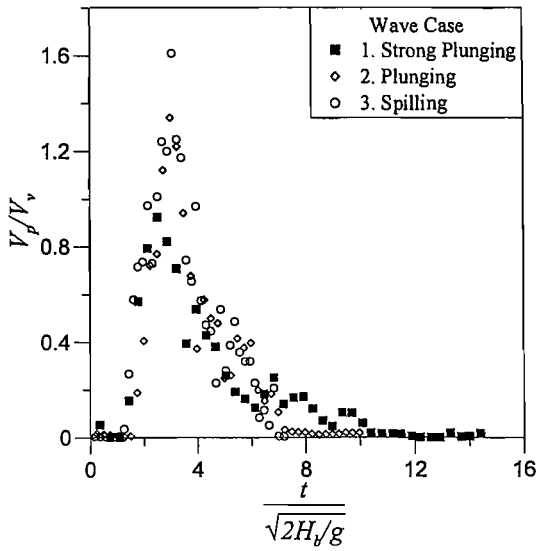

Figure 5.10 Volume per unit width of the splash-up as a function of time for all three wave cases.

5.3.2.2 Horizontal Movement of the Bubble Plume and Splash Centroids

Plots showing the positions of the horizontal centroid of the bubble plume and splash volume as functions of time for the three different wave cases are presented in figure 5.11. Also included on the plots is the shallow water wave speed at the reef crest calculated using linear theory. In all three wave cases, the bubble plume and splash volume centroids move at a velocity approximately equal to the shallow water wave speed during the period immediately after breaking when active bubble entrainment and splash generation are taking place. Once the bubble plume moves into the rise phase, its horizontal velocity slows considerably as it disperses, in agreement with the results of Lamarre (1993). A similar reduction in the splash velocity is observed as the primary splash-up initially generated by the plunging jet falls back to the water surface.

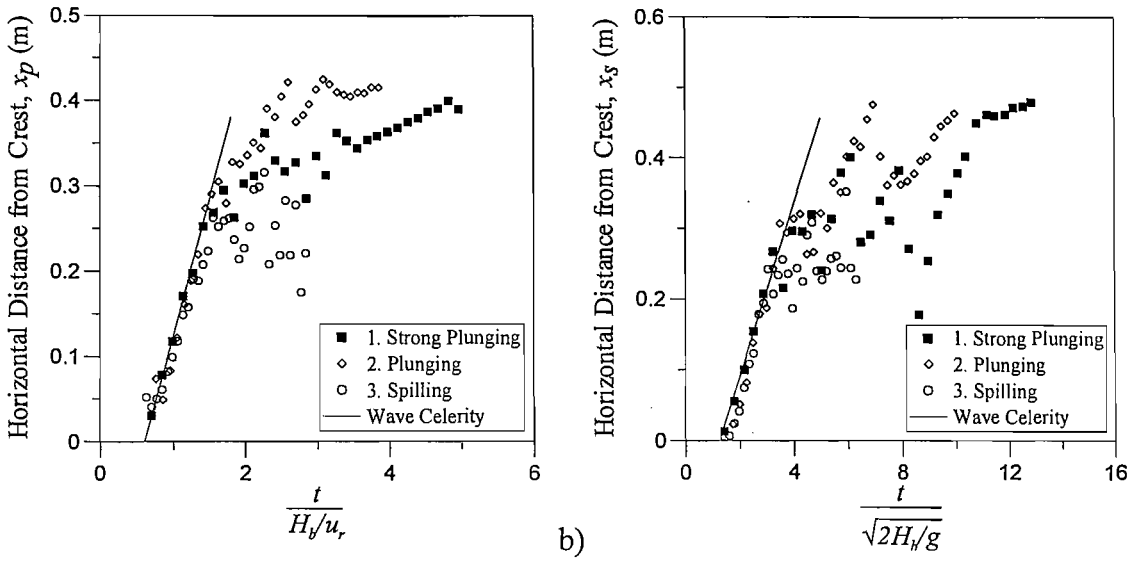

Figure 5.11 (a) Horizontal movement of the bubble plume centroid, and **(b)** horizontal movement of the splash-up centroid as a function of time.

5.3.2.3 Vertical Movement of the Bubble Plume and Splash Centroids

The movements of the vertical centroid of the bubble plume and splash volume with time are shown in figure 5.12. In all cases the elevation of the vertical centroid relative to the undisturbed free surface for the both the bubble plume and splash is normalised by the breaking wave height H_b. Figure 5.12(a) shows that for all three wave cases, before the incoming wave first breaks the centroid of the bubble plume is below the level of the undisturbed free surface due to bubbles left over from the previous wave. The level of the centroid then moves quickly up to the free surface as large numbers of bubbles are introduced at the water surface by the incoming breaker. In the two plunging wave cases, the entrained bubbles are driven rapidly downwards to a depth of around $0.75H_b$ in the currents generated by the overturning wave. Once the bubble plume centroid has reached its maximum depth it begins to slowly rise as the bubble plume disperses and the bubbles rise back to the free surface. The movement of the vertical centroid of the bubble plume in the spilling case is similar and is seen to take place over approximately the same time scale as the two plunging cases, however the depth of penetration in this less violent breaker is smaller, reaching a maximum depth of about $0.55H_b$. The movement of a typical single bubble with a diameter of 2.5 mm as it rises through a water column is also plotted on figure 5.12(a). It is seen that the bubble plume centroid rises more slowly than the individual bubbles contained within it. The reason for this is that the formation and injection phases of the bubble plume evolution

do not take place instantaneously and so the position of the bubbles within the plume is not constant, but changes as newer bubbles are entrained and driven down into the water column while bubbles generated earlier have begun to rise. As the bubble plume centroid does not represent a single bubble but a constantly changing plume, it does not behave as an individual bubble.

The vertical movement of the splash volume shows similar behaviour in all three cases, rising to a height of approximately z_s/H_b=0.4 after breaking and then falling back to the free surface under the influence of gravity. It is seen however that in the spilling case, the splash returns to the free surface more quickly than in the two plunging cases. An explanation for this result is that the period of splash generation is longer in the plunging wave cases and thus the splash centroid remains close to the peak elevation for a longer time as splash continues to be generated by the overturning wave. In the spilling wave case, the overturning motion is only sufficiently violent to generate splash for a relatively short period and consequently the period that the splash is in the air is reduced. Figure 5.12(b) also displays the movement of a single water droplet which is introduced at the highest point of the splash centroid and falls under the influence of gravity. It is clear that the centroid of the splash-up falls more slowly than the individual water droplets contained within it. As with the movement of the bubble plume centroid, the reason for this is that the total splash volume is not generated instantaneously. Consequently the water droplets making up the splash volume are not constant, with newly generated splash rising as earlier splash has reached the top of its trajectory and begun to fall. As the splash centroid does not represent a single splash droplet but a larger water volume which changes with time, it does not fall as an individual projectile.

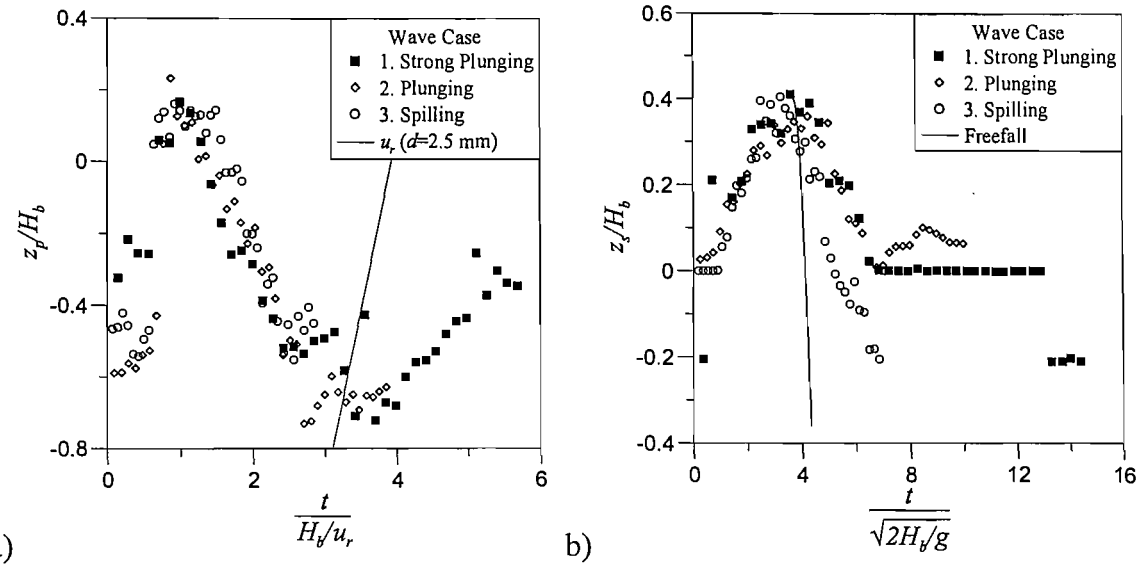

a) b)

Figure 5.12 Vertical movement of **(a)** the bubble plume centroid and **(b)** the splash-up centroid as a function of time.

5.3.2.4 Mean Void Fraction in the Bubble Plume

Previous authors have frequently published values of the maximum void fraction in the bubble plume generated by breaking waves (table 2.1). However such values have little meaning as it has been seen that the free surface is difficult to define in the highly aerated region close to the breaking event and void fractions from 0% to 100% have been measured in the region of breaking waves in the current tests.

It is informative however to examine the temporal variation of the mean void fraction within the bubble plume boundaries shown in figure 5.13 because this demonstrates the rapid evolution of the concentration of air in the plume. For this purpose, the boundaries of the bubble plume were taken to be the 50% and 0.3% void fraction contours to be consistent with Lamarre (1993).

The value of the mean void fraction is initially around 1% due to the remnants of the bubble plume from the previous wave. It then increases rapidly to a peak over a period of approximately 0.15 seconds as the wave overturns and air is entrained. The peak value of the mean void fraction for the two plunging cases is approximately 17.5%, while for the less violent spilling wave case it is just 13%. The probable reason for this difference is that the vortex breakup mechanism of air entrainment is more dominant in the plunging wave cases, leading to a very concentrated initial bubble plume consisting

predominantly of large air cavities. In the spilling case, the vortex breakup mechanism is less important and a larger proportion of the air volume is entrained more gradually in the jet-trough shear layer (see section 2.3.2), leading to a less concentrated initial plume. After the peak has been reached, the mean void fraction in all three wave cases decays according to a power law in agreement with Lamarre (1993).

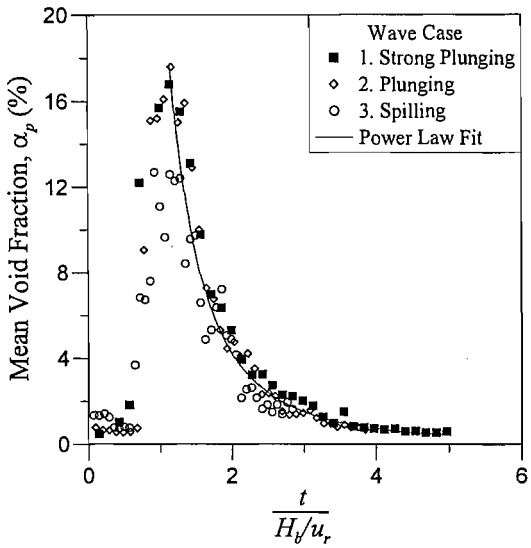

Figure 5.13 Variation of the mean void fraction in the bubble plume as a function of time.

5.3.2.5 Cross-Sectional Area of the Bubble Plume and Splash-Up

The cross-sectional area of the bubble plume for each wave case was taken to be the area enclosed between the 0.3% and 50% void fraction contours for consistency with Lamarre (1993). Plots showing the variation of the area of the bubble plume and splash-up normalised by the vortex area A_v as a function of time for each wave case are presented in figure 5.14, where the splash-up area is defined as the area enclosed by the 50% and 99.7% void fraction contours.

Figure 5.14 shows that the normalised area of the bubble plume is initially greatest in the spilling case and smallest in the strongly plunging case. This is because the experiment was conducted using regular waves and the shorter wave period used to generate the spilling breaker means that a larger proportion of the plume remains after a single wave period. When the new breaker arrives, the plot shows that the bubble plume area increases relatively slowly compared to the mean void fraction (figure 5.13),

suggesting that when the plume is originally entrained it is small and concentrated but then gradually increases in size as it is driven into the water column and begins to disperse. The bubble plume area reaches a peak value approximately 0.3 seconds after the peak of the mean void fraction and then gradually decreases as the void fraction at the plume boundaries falls below 0.3%. It is noted that the peak value of the normalised plume area is greatest in the spilling case ($A_p/A_v \approx 16$) and smallest for the strongly plunging case ($A_p/A_v \approx 12$) and these results are of the same order as those of Lamarre (1993) who reports peak values of A_p/A_v of between 9 and 13.

The results presented in figure 5.14(a) display a similar variation with time as the previously published values of Lamarre (1993), Papanicolau & Raichlen (1988) and Kalvoda *et al.* (2003), however no exact comparison has been made owing to the different time scale used in the present work.

The variation of the splash-up area with time (figure 5.14(b)) is similar for all three wave cases. The splash is generated as the plunging jet strikes the free surface and its area quickly increases to a maximum which varies in the range $8.2 < A_s/A_v < 11.8$. Once the peak value has been reached, the area of the splash-up reduces very quickly as the spray falls back to the water surface. The large differences in the values of the maximum splash area in the plot are predominantly caused by the variation in the vortex area A_v for the three wave cases (see table 5.1) which was used to normalise the results. It may be more suitable to normalise the plume area by an alternative parameter such as H_b^2, however A_v was used in this case to allow direct comparison with the bubble plume data.

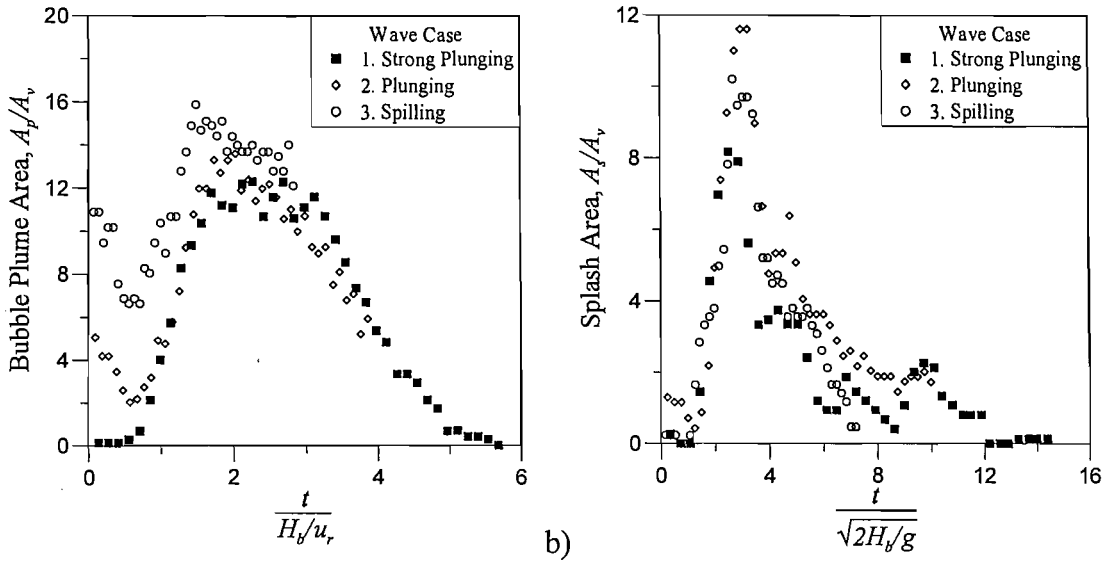

Figure 5.14 Variation of **(a)** the bubble plume area and **(b)** the splash-up area as a function of time.

5.3.2.6 Bubble Penetration Depth

The maximum depth of the 0.5% and 1% void fraction contours normalised by the breaking wave height are presented in figure 5.15. At first the bubble plume remains close to the free surface because the bubbles initially present are remnants of the bubble plume from a previous wave. These bubbles rise slowly until the arrival of the breaking wave when a new bubble plume is generated and the bubble depth increases with time as the plume is driven into the water column during the formation and injection phases which last approximately 0.4 seconds in the current experiments. It is seen that the maximum penetration depth is greater for the two plunging wave cases than for the spilling wave in agreement with the results presented in section 4.3.4. After the maximum penetration depth has been reached, the depth of the bubble plume gradually decreases as the plume disperses and the bubbles rise back to the surface. It is seen that the base of the bubble plume rises at a speed close to that of a single bubble with a diameter of 2.5 mm once the injection phase has ceased and it is no longer being refreshed with newly entrained bubbles.

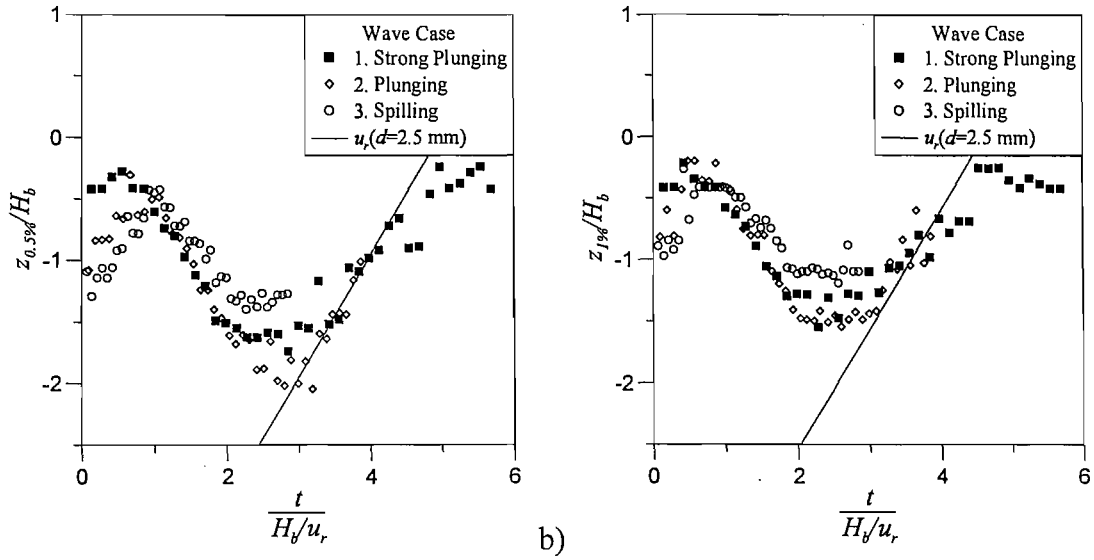

Figure 5.15 Variation of the maximum depth of **(a)** the 0.5% void fraction contour and **(b)** the 1% void fraction contour as a function of time.

5.3.2.7 Splash Height

The maximum heights of the 99% and 99.5% void fraction contour lines normalised by the breaking wave height as a function of time are presented in figure 5.16 for the three wave cases under investigation. The elevation of both the 99% and 99.5% contours lines is well behaved and displays a trend of increasing splash height during the period of splash generation after the impact of the overturning jet. The levels of the 99% and 99.5% contours reach a peak approximately 0.25 seconds after the beginning of splash generation and then fall quickly back down to the free surface. It is noted that the recorded splash height falls more slowly than an individual droplet in freefall. The reason for this is that the measurements do not follow the movements of individual droplets in the primary splash, and at later times when the primary splash has predominantly fallen back to the free surface, the maximum height of the 99% and 99.5% contours are confused by the presence of surface waves and small secondary splashes.

In both of the plunging wave cases, the maximum height of the 99.5% contour line is approximately $1.2H_b$, while the corresponding value for the spilling wave case is just $1.0H_b$, in line with the observation of Yasuda *et al.* (1999) that more violent plunging waves produce greater splash heights. The highest elevation at which splashes were detected by the optical fibre probes was approximately $2H_b$ for all cases, but individual

droplets were observed to be thrown up to approximately $5H_b$ above the still water level during the vertical splash phase discussed in section 5.3.1 and shown in figure 5.7(i) to (k). Note that in the plunging and spilling cases, the splash height does not return to the still water level due to the presence of waves in the measurement domain at all time steps.

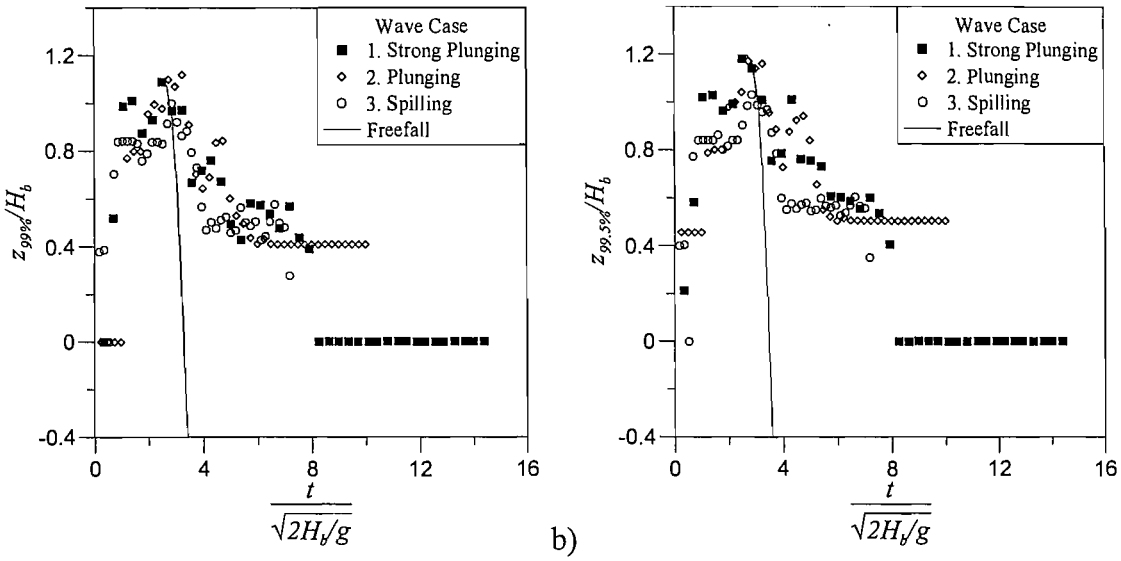

Figure 5.16 Variation of the maximum height of **(a)** the 99.5% void fraction contour and **(b)** the 99% void fraction contour as a function of time.

5.3.2.8 Potential Energy of Air and Splash Volumes

Fürhböter (1970) showed that the process of air entrainment must contribute to the initial energy dissipation during wave breaking (section 2.5.1). He suggested that much of the wave energy lost during the breaking process is initially transferred to the potential energy of the bubbles in the bubble plume as they are driven into the water column. These bubbles then rise back to the surface, losing potential energy (and incurring smaller losses through the generation of turbulence and heat). Upon reaching the surface, the bubbles burst, producing small droplets as described by Blanchard (1989) and generating very small, high frequency waves which are visible at the free surface but do not contribute to the wave reformed after breaking.

It is informative to investigate the contribution of air entrainment to the total energy dissipated by wave breaking. The work per unit width required to keep air bubbles entrained against their buoyancy for each phase average bin is

$$E_p(n) = \rho g \sum_{i=1}^{i=I} \sum_{j=1}^{j=j_{50}} \alpha_{i,j,n} z_{50\%} \delta z \delta x, \qquad (5.6)$$

where $z_{50\%}$ is the elevation of the measurement position measured from the 50% void fraction contour.

It is noted that additional viscous energy losses will occur as the bubbles move through the water column, however such losses are very small compared to the work required to entrain air against buoyancy.

Chanson *et al.* (2002b) suggested that flow bulking caused by the volume of air entrained by a breaking wave leads to a rise in the elevation of the free surface above the bubble plume which subsequently propagates in the flume as a surge wave. A similar rise in the level of the free surface above a region of entrained bubbles was observed by Friedl & Fanneløp (2000) in their study of the interaction of bubble plumes with the free surface. No obvious surge waves were observed in the present experiments and it is assumed that none of the energy required to submerge bubbles against the force of buoyancy is transferred back to the organised wave motion after the bubbles return to the surface, however the complexity of the flow around the breaking waves would make such features difficult to observe.

As well as entraining air, we have observed that the wave breaking process generates a significant amount of splash-up. As the plunging jet strikes the free surface, energy is transferred to raise the potential and kinetic energy of the splash volume and it is suggested that this must also contribute to the total energy dissipated during the wave breaking process. The kinetic energy of the splash could not be reliably estimated from the present measurements, but a measure of the potential energy per unit width of the splash-up is

$$E_s(n) = \rho g \sum_{i=1}^{i=I} \sum_{j=1}^{j=j_{50}} (1 - \alpha_{i,j,n}) z_{50\%} \delta z \delta x. \qquad (5.7)$$

Plots of the potential energies of the bubble plume and splash volume normalised by the incident wave energy E_i as a function of time are presented in figure 5.17.

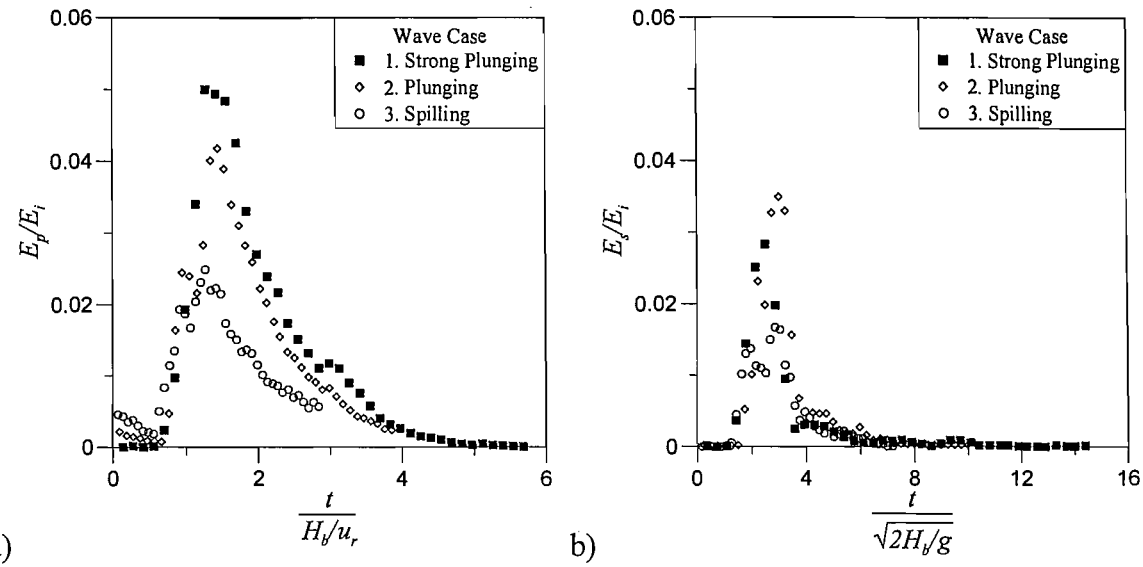

Figure 5.17 Potential energy of **(a)** the entrained bubble plume and **(b)** splash-up volume normalised by the incident wave energy as a function of time.

It should be noted that the values displayed in figure 5.17 represent the potential energy of the bubble plume and splash-up for each of the 40 phase averages. As the air/splash is generated over a finite period of time and remains present for a period that is greater than a single time-step, none of the values in figure 5.17 represent the total energy transferred to the potential energy of the air/splash, because the same bubbles/droplets can be measured more than once at different times and positions. Consequently, the plots cannot be used to estimate the total contribution of the air entrainment and splash generation processes to the energy dissipated at breaking. Despite this, the peak values of the distributions can be used as an estimate of the minimum amount of energy dissipated by the generation of air and splash as these values represent the maximum potential energy of the air/splash at any one time, thus the cumulative energy expended in entraining air and generating splash must be at least this amount.

Based on this assumption, figure 5.17(a) shows that in the current experiments a minimum of between 2.5% and 5% of the incident wave energy is dissipated through entrainment of air during wave breaking and the amount of energy dissipated increases with the intensity of the breaking event. Using estimates of the total energy dissipation

presented in table 5.1, the energy expended in entraining air bubbles against buoyancy accounts for a minimum of 4%, 6% and 9% of the total amount of energy dissipated during wave breaking for the spilling, plunging and strongly plunging wave cases respectively. These values are considerably smaller than those of previous authors who estimated that air entrainment was responsible for between 20% (Hoque, 2002) and 30% to 50% (Lamarre, 1993) of the energy dissipated at breaking. This large difference between the current results and those previously published is surprising as it was noted in section 5.3.2.1 that the total volume of entrained air detected in the current experiment was greater than that measured by Lamarre (1993). There is no definite explanation for the observed discrepancy, however it may be partly explained by the differences in the method of creating breaking waves (focussed waves (Lamarre, 1993), emergent beach (Hoque, 2002)), or the intensity of wave breaking. It is also noted that the current results are greater than those presented by Loewen *et al.* (1996) who suggested that entrainment of air in their experiments contributed just 0.05% to 0.4% to the total dissipation during breaking, although these measurements were made in very gently spilling laboratory wind waves and so a smaller amount of dissipation would be expected.

It is interesting to note that figure 5.17(a) demonstrates that the energy expended in entraining air into the water column during breaking accounts for a greater proportion of the total incident wave energy as the breaker type changes from spilling to strongly plunging. This is in agreement with the suggestions made in section 4.3.3 that as the size of the vortex enclosed beneath the overturning jet increases with the breaking intensity, the amount of energy dissipated by the air entrainment mechanism will increase.

It is seen in figure 5.17 that the peak values of the potential energy of the bubble plume are greater than those of the splash volume for all three wave cases, but that the results suggest that the splash generation mechanism also contributes significantly to the total energy dissipation. Figure 5.17(b) shows that the work required to raise the potential energy of the primary splash-up generated at breaking accounts for a minimum of approximately 3.5% of the incident wave energy for both of the plunging wave cases under examination, and 1.7% for the spilling wave case. These values correspond to 2.5% of the total energy dissipated during breaking for the spilling wave case and 5%

for the two plunging waves. To this author's knowledge, these are the first estimates of the contribution of splash generation to the total energy dissipated during wave breaking and suggest that the dissipation due to splash becomes more significant as the breaking intensity of the wave increases.

In summary, the results presented in this section suggest that air entrainment and splash generation combined account for a minimum of 6.5% to 14% of the total energy dissipated during breaking in the current experiments. It is also noted that the air entrainment process contributes more to the total energy dissipation than splash generation and that these mechanisms become more significant as the breaking intensity of the wave increases. However, as the dissipation due to air entrainment and splash measured in the present experiments accounts for less than 20% of the total dissipation during breaking, it is clear that these are not the dominant mechanisms of dissipation and further work should examine the contributions of other processes in detail, in particular the generation of turbulence.

5.4 DISCUSSION AND SUMMARY

This chapter describes possibly the most comprehensive measurements of the rapidly varying void fraction field in the region of breaking laboratory waves to date. The results presented here were made using a novel optical fibre phase detection probe which allowed measurements of the two-phase flow both in the dense bubble plume generated beneath breaking waves but also in the splash region above the free surface, to this author's knowledge, for the first time.

The primary conclusions that can be drawn from the work presented in this chapter are listed below.

1. The optical fibre phase detection probes used in this chapter proved to be highly suitable for making measurements of the rapidly varying void fraction field in the region of breaking laboratory waves and the results appear to capture the spatial and temporal variations of the two-phase flow.

2. Previous authors have assumed that the temporal evolution of the bubble plume would scale with the wave period, but this was found not to be the case. Once entrained, the properties of the bubble plume had little or no dependence on the surface wave motion. Instead, an alternative scaling using the characteristic time of bubble detrainment was found to be more satisfactory, although this timescale is thought to be only physically significant during the rise phase of the bubble plume.

3. The peak volume of entrained air normalised by the volume of the vortex enclosed between the underside of the plunging jet and the wave face V_p/V_v varied between 1.3 and 1.6, which is greater than the result of $V_p/V_v=1$ presented by Lamarre (1993). The maximum values of the splash volume were of the same order as the peak volumes of entrained air in all cases.

4. Measurements showed that the breakup of the vortex enclosed beneath the overturning jet contributes significantly to the total volume of air entrained during wave breaking. In addition it was shown that this mechanism of air entrainment becomes more important as the breaking intensity increases, in agreement with the conclusions presented in section 4.3.3.

5. Measurements of the maximum depth of the 0.5% and 1% void fraction contours and vertical centroid of the bubble plume suggest that bubbles are entrained to a greater depth as the breaking intensity increases, in agreement with the results presented in section 4.3.4.

6. The maximum value of the mean void fraction in a plunging wave is greater than that for a spilling wave, with values of 17.5% and 13% respectively. This is due to the fact that in plunging waves, the bubble plume is initially very concentrated, consisting predominantly of large air cavities formed by the breakup of the vortex enclosed between the plunging jet and the wave face. In the spilling case, the vortex breakup mechanism is less significant and a larger proportion of the air volume is entrained more gradually in the jet-trough shear layer, leading to a less concentrated initial plume.

7. Measurements of the variation of the splash height suggest that the splash-up produced by the action of violent plunging waves rises to a greater height than that from spilling waves, supporting the conclusions of Yasuda *et al.* (1999).

8. It was shown that a minimum of between 2.5% and 5% of the incident wave energy is dissipated through entrainment of air during wave breaking and this accounts for a minimum of 4% to 9% of the total dissipation in the current tests. This is significantly less than the previously reported values of Lamarre (1993) and Hoque (2002) who found that air entrainment accounted for between 20% and 50% of the energy dissipation. It was also seen that the energy expended in entraining air into the water column during breaking accounts for a greater proportion of the total incident wave energy as the breaker type changes from spilling/plunging to strongly plunging in agreement with the conclusions presented in chapter 4.

9. Estimates of the work required to raise the potential energy of the primary splash-up produced at breaking showed that between 1.7% and 3.5% of the incident wave energy was dissipated by this mechanism, and this corresponds to a minimum of 2.5% to 5% of the total energy dissipated at breaking for spilling and plunging breakers respectively. To this author's knowledge these are the first estimates of the contribution of splash-up generation to the total energy dissipated by a breaking wave.

10. The measurements discussed above suggest that while entrainment of air and the generation of splash contribute to the total energy dissipated during wave breaking, it is clear that these are not the dominant mechanisms of dissipation for the wave cases examined in this study and further work should investigate the contributions of other processes in detail, in particular the generation of turbulence.

CHAPTER 6 – BUBBLE SIZE DISTRIBUTION MEASUREMENTS IN FRESHWATER

6.1 INTRODUCTION

As discussed in section 2.3.4, the bubble size distribution in the ocean is an important parameter for models that examine the enhancement of air-sea gas exchange due to the presence of bubbles in the ocean. Melville (1996) suggested that for gas transfer studies, we would ideally like to know the total volume of air and the size distribution of air bubbles entrained at the surface and be able to predict its subsequent evolution. Detailed measurements of the void fraction field beneath breaking waves were presented in the previous chapter and these allow us to make estimates of the total volume of air entrained at the surface. This chapter goes on to examine the temporal and spatial variation of the distribution of bubble sizes in the dense bubble plumes formed beneath breaking waves in a laboratory wave flume.

Previous investigations of the bubble size distributions produced by breaking waves have often been restricted to the ambient bubble populations in the ocean measured some time after the actual breaking event. Much less information is available within the dense bubble plumes entrained immediately beneath breaking waves due to the restrictions of the available measurement techniques. Consequently models of bubble-mediated gas transfer tend to be based on ambient bubble populations and often neglect the effect of the large bubbles which are present immediately after breaking and have been shown to contribute significantly to bubble-induced gas exchange (Woolf, 1993; Keeling, 1993).

The current study develops the work of Serdula & Loewen (1998) who suggested that optical fibre probes represent the most promising technique for making measurements of the bubble size distribution in the transient bubble plumes generated immediately beneath breaking waves. The measurements presented here allow the validity of this technique to be assessed and demonstrate the variation of the bubble size distribution in dense breaker generated bubble plumes.

6.2 EXPERIMENTAL ARRANGEMENTS

6.2.1 Experimental Set-up and Methods

The experiments were carried out in a wave flume at the University of Southampton equipped with a flap-type wavemaker, the specifications and operation of which have been described in sections 3.2.1 and 3.2.2. A submerged reef as described in section 3.2.3 was installed in the flume with the crest of the reef located 8 m from the wave generator (figure 6.1). The flume was filled with freshwater to a depth of 0.7 m.

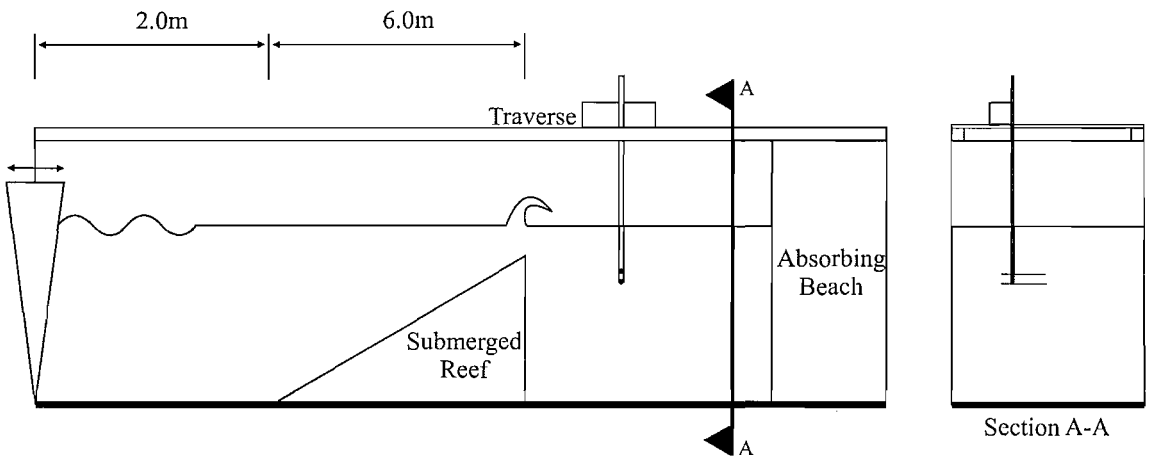

Figure 6.1 Experimental apparatus for the bubble size distribution measurements.

Bubble size measurements were made at two points in the flow during each experimental run using two optical fibre probes mounted horizontally on the traverse system. The probes were arranged such that the tip of the upper probe was positioned directly over the lower probe with a vertical separation of 20 mm. The probes were connected to the opto-electronic unit described in section 3.4.2 and the output from this was sampled at a rate of 400 kHz using a Measurement Computing PCI-DAS6070 A/D board installed in a personal computer as described in section 3.3.1.2.

The bubble chord lengths detected by the probes were calculated using the single probe technique described in section 3.4.4.2. The calibration experiment described in section 3.5.4 showed that it was difficult to correctly resolve the probe response to air-water interfaces that approached the tip parallel to the probe axis due to the existence of a pre-signal (figure 3.32). In order to minimise the number of these parallel bubble strikes,

the probes were orientated across the flume, pointing at the far wall with the two probe tips positioned in line with the flume centreline (figure 6.1). Assuming that bubbles entrained by the breaking waves predominantly travel parallel to the flume walls, this arrangement maximises the number of bubble strikes where the angle between the normal to the air-water interface and the probe axis β is in the range 90° to 115° over which it was shown in section 3.5.4 that the measured calibration curves remain valid.

A purpose written FORTRAN program described in section 3.4.5.1 was used to process the data from the experiment to determine the times of bubble arrival and departure, and the rise time between characteristic points A and B (figure 3.14) in order to calculate the bubble residence time t_a and the interface velocity v_i using the calibration results presented in section 3.5.4. This data could then be used to calculate the chord lengths of the bubbles detected by the probes during each experimental run using equation 3.2. The lower threshold for detection of point A was set at 10% of the difference between the air and water voltage levels, while the upper threshold to detect point B was maintained at 60%, consistent with the results presented in section 3.5.4.

Table 6.1 Test cases for the bubble size measurements.

Case No.	Frequency, f (Hz)	Wave Height, H_o (mm)	Breaker Height, H_b (mm)	Breaker Type
1	0.5	78.2	95	Strongly Plunging
3	1.0	100.5	95	Spilling/Plunging

Two different wave cases were examined, a strongly plunging case and a spilling wave close to the spilling/plunging boundary, the details of which are shown in table 6.1. As explained in section 5.2.1, the submerged reef causes the waves in the flume to break in a repeatable manner and at a constant location for long test durations such that there is no interaction between the bubble plume and the flume bed. In order to examine the spatial and temporal variation of the bubble sizes in the bubble plumes generated by breaking waves, measurements of the bubble chord lengths were taken using the optical fibre probes at 20 mm vertical intervals along four vertical transects behind the reef for each wave case. The locations of the vertical transects are shown in figure 6.2 and were chosen to ensure a good distribution of data throughout the bubble plume, including measurements close to the region of most active air entrainment. To obtain stable

bubble size distributions, at least 800 bubbles were sampled at each measurement location. The high sample rate of 400 kHz meant that the tests could only be run for 300 seconds and thus at most positions it was necessary to build up stable size distributions from a series of several 300 second runs.

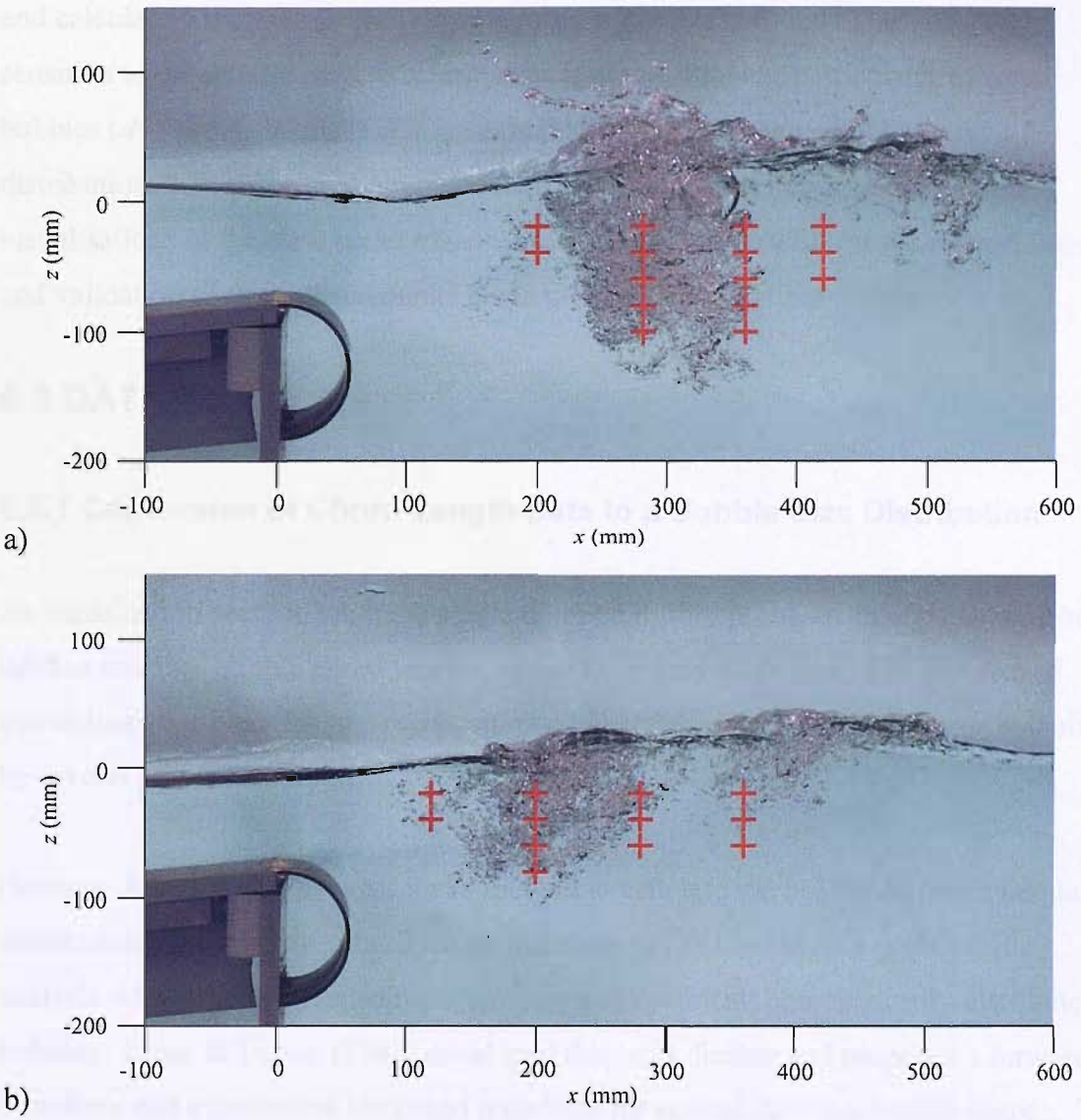

Figure 6.2 Transect positions for the bubble size measurements for **(a)** the strongly plunging wave case and **(b)** the spilling case.

To provide some validation for the measurements of bubble size made using the optical fibre probe technique during the tests described in this chapter, a series of close-up photographs at intervals of $T/40$ throughout the life of the bubble plume were taken by synchronising the Nikon D100 camera described in section 3.3.3.2 with the wave generator using the Measurement Computing D/A hardware.

Some attempts were made to produce bubble size distributions from the digital images in the low void fraction areas of the bubble plume for direct comparison with the optical probe measurements. Bubble sizes were obtained by digitising the outline of any bubbles falling into the camera focus using the surface mapping software, SURFER 7.0 and calculating their diameter. However this method was found to be extremely sensitive to the criteria used to select valid, in-focus bubbles, particularly for small bubbles (d<1 mm). While it was not possible to obtain accurate bubble size distributions using this photographic technique, the images obtained provide good visualisations of the flow under examination and are very useful for the interpretation and validation of the measurements made using the optical fibre probes.

6.3 DATA ANALYSIS

6.3.1 Conversion of Chord Length Data to a Bubble Size Distribution

As explained in section 3.4.4, the single tip optical fibre probe technique can only be used to measure bubble chord lengths, rather than their diameters. The problem of converting chord lengths to a representative bubble size distribution has been examined by several previous authors.

Herringe & Davis (1976) presented a method to estimate the bubble diameter frequency distribution $P(d)$ from the chord length distribution $P(l_b)$ based on a probabilistic analysis which assumed uni-directional flow and spherical, homogenously distributed bubbles. Clark & Turton (1988) developed this work further and proposed a forward transform and a numerical backward transform for several different bubble shapes. The forward transform describes the relationship between the chord lengths and bubble diameters while the backward transform allows the interpretation of measured chord length data. Liu & Clark (1995) presented an analytical solution as well as a non-parametric backward transform to allow direct conversion of measured chord length data to a bubble size distribution. Liu *et al.* (1996) noted instability problems with the numerical backward transform presented by Liu & Clark (1995) and developed a method to overcome this by transforming the measured chord length data to a bubble size distribution directly using a Parzen window function.

The method of Liu *et al.* (1996) is particularly suitable for the direct conversion of discrete chord length measurements to a bubble size distribution and will be examined further here. Liu *et al.* (1996) show that the probability density function of the bubble diameter, $P_p(d)$ is

$$P_p(d)=\frac{\lambda}{nh\sqrt{2\pi}}\sum_{i=1}^{n}e^{-(\lambda d-l_{bi})^2/2h^2}+\frac{\lambda^2 d}{nh^3\sqrt{2\pi}}\sum_{i=1}^{n}(\lambda d-l_{bi})e^{-(\lambda d-l_{bi})^2/2h^2}, \tag{6.1}$$

where λ is a bubble shape factor (in this case, bubbles were assumed to be spherical), $d=l_b/\lambda$, n is the sample size and h is the Parzen window width. Liu (1995) suggested that an estimate for the best value of h is

$$h=\frac{\sqrt{mean(l_b)\times stdev(l_b)}}{\sqrt[5]{n}}. \tag{6.2}$$

The probabilistic methods discussed above are designed to represent the physical interaction between the tip of a phase detection probe and a rising bubbly flow, however they require a number of assumptions which are not valid in breaking wave flows. For example the method of Liu *et al.* (1996) assumes bubbles with a constant shape are distributed homogenously in a uni-directional flow. The assumptions of homogeneity and uni-directional flow are clearly invalid in breaking wave flows. In addition, bubbles in breaker generated plumes are not necessarily spherical as freely rising air bubbles in water have shapes which vary from spherical for small (d<1mm) bubbles to ellipsoidal or spherical cap bubbles as the equivalent bubble diameter increases. Visualisation of the bubbles entrained by breaking waves in the current experiments demonstrates that bubbles exist over a large size range and confirms that the bubbles are not of constant shape as can be seen in the photograph presented in figure 6.11.

Due to the uncertainties in the shape of larger bubbles (d>1mm) and the local flow direction at the probe tip, an alternative conversion method was also considered. Serdula & Loewen (1998) suggested that for a sufficiently large dataset, chord length data can be multiplied by a correction factor of 3/2 to obtain an estimate of the bubble

size distribution. This simple correction factor is based on the probability of a chord length l_b being measured across a bubble with diameter d in a rising flow (for a full derivation see Saberi *et al.* (1995)) and has been previously used by Serdula & Loewen (1998), Liu & Bankoff (1993) and Saberi *et al.* (1995). In order to compare this method to that of Liu *et al.* (1996), figure 6.3 shows the bubble diameter probability density functions calculated using the two different techniques at the position x=360 mm, z=-60 mm for the strongly plunging wave case.

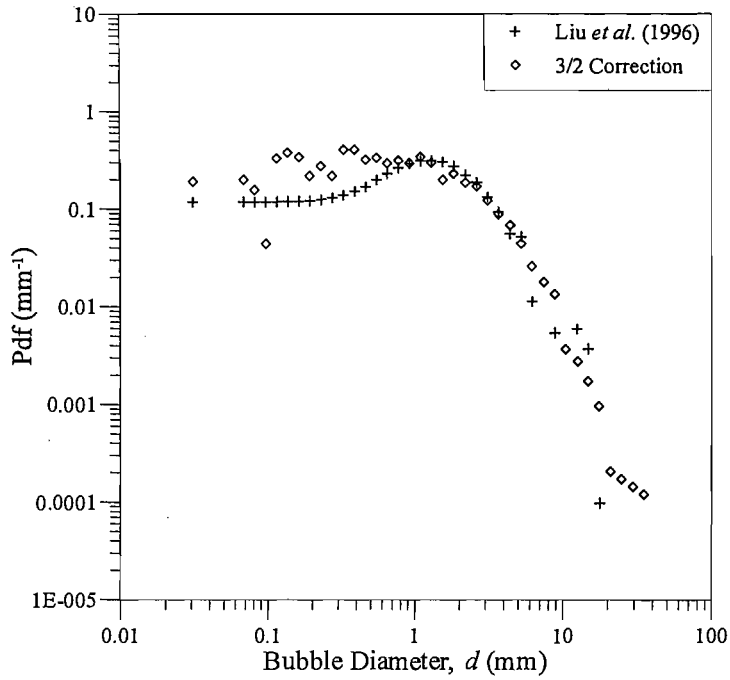

Figure 6.3 Sample bubble size distribution using the method of Liu *et al.* (1996) and the simple 3/2 correction suggested by Serdula & Loewen (1998).

It is seen that in the range 1 mm<d<5 mm, the two distributions are very similar. Both distributions display a power law scaling over larger bubble sizes (d>2.4 mm) consistent with the results of previous authors (section 2.3.4), and the value of the power law is approximately equal for both distributions. The distribution calculated using the method of Liu *et al.* (1996) shows an obvious peak at a diameter of approximately 1.5 mm which is in contradiction to the majority of published bubble size distributions which generally display no peak. It is also noted that while this distribution is very well behaved in the small bubble range, it becomes unstable for bubble diameters larger than 5 mm. The size distribution calculated using the simple 3/2 correction factor suggested

by Serdula & Loewen (1998) is reasonably well behaved throughout the full range of bubble sizes although some scatter is evident in the range of small bubble sizes.

The measurements presented in this chapter are novel in that they provide information about the bubble size distribution in the dense bubble plumes present immediately after wave breaking, which are characterised by the presence of numerous large bubbles. Due to the lack of stability of the method of Liu *et al.* (1996) at large bubble sizes it was decided to employ the simple 3/2 correction method to estimate the bubble size distributions presented in section 6.4.

6.3.2 Presentation of Data

Bubble size spectra generated by breaking waves are usually presented in terms of bubble concentration (bubbles per m^3 per μm radius increment) as shown in figure 2.7. In the present tests however, the measurement volume is unknown making it difficult to obtain valid concentration estimates and so the bubble size measurements shown in section 6.4 are plotted simply as a function of the probability density function.

An indirect calculation of bubble concentration at each diameter increment can be carried out for the point measurements made using the optical probes by simply multiplying the probability density function by a constant

$$C = \frac{N_T}{\left(V_{ap} / \overline{\alpha} \right)}, \tag{6.3}$$

where N_T is the total number of bubbles detected across all size bins and $V_{ap}/\overline{\alpha}$ is an equivalent measurement volume based on the total volume of air detected V_{ap} at the measurement position and the mean void fraction over a full wave period at the measurement location $\overline{\alpha}$.

It should be noted however that this method is problematic because it is very sensitive to the total detected bubble volume V_{ap} and this cannot be estimated with sufficient accuracy due to uncertainties in the exact size and shape of the detected bubbles.

Consequently, rather than presenting potentially misleading concentration data it was decided to present the measured bubble size distributions in terms of the probability density function. It is noted that previous authors who have made point measurements of bubble sizes using optical or conductivity probes have also avoided presenting their results in terms of concentration. Instead, bubble diameters or chord lengths have been plotted as functions of bubble strike rate (Waniewski *et al.*, 2001), probability (Cummings, 1996) or probability density function (Chanson & Toombes, 2002).

While no value of the bubble concentration at each measurement location can be obtained directly from the bubble size distributions presented in section 6.4, the graphs display the same slopes as the equivalent concentration plots and so the power laws observed in the current data can be compared directly with those presented by previous authors listed in table 2.2.

6.3.3 Spatial and Temporal Variation of Bubble Sizes – Interpretation of Point Measurements

Bubble size distributions measured using the single optical fibre probe technique are built up from point measurements taken over a long time scale, with each value being averaged over several 300 second test runs. The results presented in chapter 5 demonstrate that the bubble plumes generated by breaking waves evolve rapidly in time and space. Consequently the point measurements presented in section 6.4.1 represent the bubble size distribution throughout the formation, injection and rise phases of the bubble plume evolution at a single point in the flow as the bubble plume moves past. While these measurements are taken at a fixed location, they cannot be said to represent the bubble size distribution at a specific point within the bubble plume as the plume continuously evolves in space while the measurements are being taken. Equally it is not possible to take a snapshot in time of the bubble size distribution to allow easy comparison with instantaneous, spatially averaged photographic results using the present technique because the method relies on the residence time of bubbles on the probe in order to estimate their size. However some estimates of the temporal evolution of bubble sizes are made in section 6.4.2 by dividing the detected bubble sizes into phase average bins in a similar manner to that used to examine the void fraction data in the previous chapter.

While the optical fibre measurement technique does not allow the spatial and temporal evolution of the bubble size distribution to be completely resolved, similar or more significant restrictions exist for any of the alternative bubble size measurement techniques when used in such dense bubble plumes. While there are some limitations, the results presented in this chapter provide some of the most detailed measurements to date of the time-averaged bubble size distribution during the early stages of the bubble plume, and give some information about the temporal evolution of bubble sizes within a single wave period.

6.3.4 Assumptions for the Bubble Size Measurements

The flow beneath breaking waves is unsteady, turbulent and three dimensional and so the interactions between bubbles entrained in this flow and the optical fibre probe are complex. Consequently it is necessary to make a number of assumptions about the nature of the flow and the measurement technique. The main assumptions for the use of the optical fibre probes to estimate the size of bubbles beneath breaking laboratory waves are listed below.

1. *The bubble size is not affected by its interaction with the optical fibre probe.* This is a reasonable assumption as the flow velocities are generally high and the dimensions of the probe tip are very small.

2. *Bubble velocity is unaffected by the probe tip and remains constant while a bubble is in contact with the optical fibre probe.* The high fluid velocities and small probe dimensions should ensure that the bubble velocity is not significantly affected by the probe, however it is possible that some of the larger bubbles may change direction or speed while they are in contact with the probe due to the high pressure gradients in the region of breaking waves or turbulence in the flow.

3. *Bubbles entrained by the breaking waves move predominantly along streamlines which are parallel to the sidewalls of the wave flume.* Based on visual

observations of the bubble plume evolution in the wave flume during the current experiments, this assumption is considered to be reasonably valid.

4. *The probe orientation ensures that the angle between the probe axis and the majority of detected bubble interfaces is in the range $90° < \beta < 115°$, which was the range of the calibration tests described in section 3.5.4.* As described in section 6.2.1, the orientation of the optical probes in the flume was designed to maximise the number of bubble strikes within this range.

5. *Bubbles are assumed to be spherical throughout the complete range of bubble sizes detected by the optical probe.* As discussed in section 6.3.1, bubble hydrodynamics theory and analysis of still images of the bubble plume show that this is not the case and there is significant variability in the bubble shape and orientation (figure 6.11). However due to the currently unresolved complexities of modelling bubbles with varying shape and orientation, no suitable alternatives are available.

6. *The calibration curves obtained using well controlled air-water interfaces in section 3.5.4 remain valid in the complex flow beneath breaking wave.*

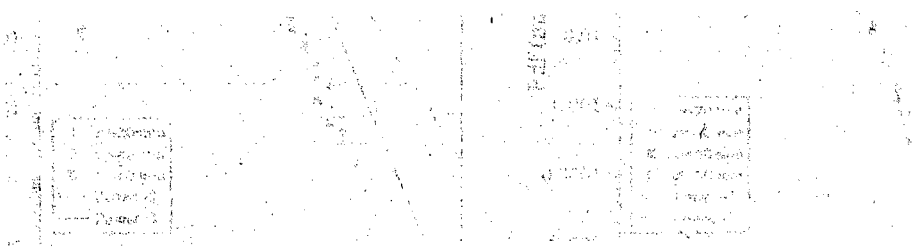

6.4 EXPERIMENTAL RESULTS

6.4.1 Spatial Variation of Bubble Sizes

Plots of the bubble diameter probability density function measured along two of the vertical transects shown in figure 6.2 are presented on a log-log scale in figures 6.4 and 6.5 for the strongly plunging and spilling wave cases respectively. Additional plots that display the bubble size distribution data measured along the vertical transects not presented here can be found in Appendix B.

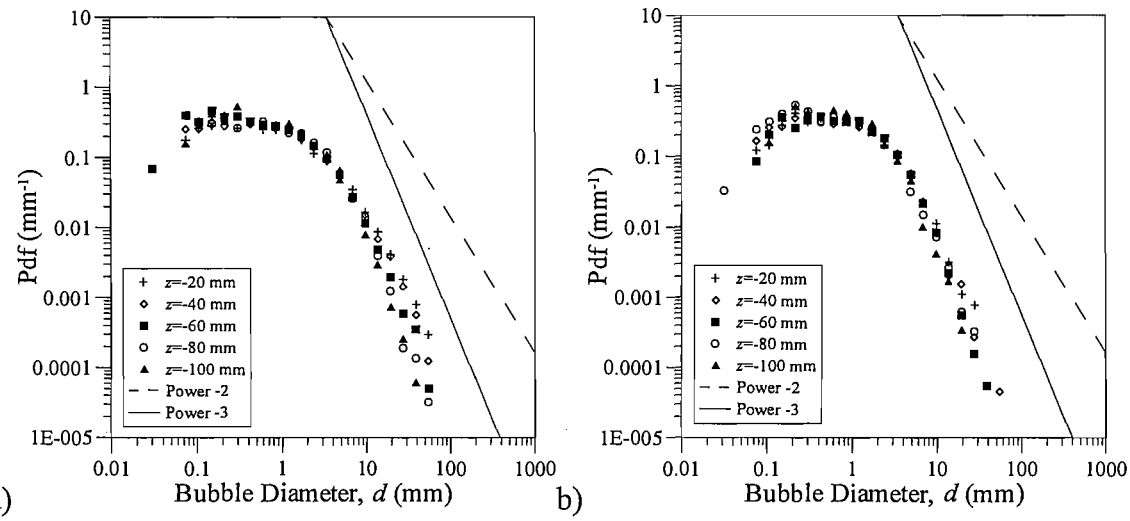

Figure 6.4 Bubble size distributions for the strongly plunging wave case along vertical transects at **(a)** x=280 mm and **(b)** x=360 mm.

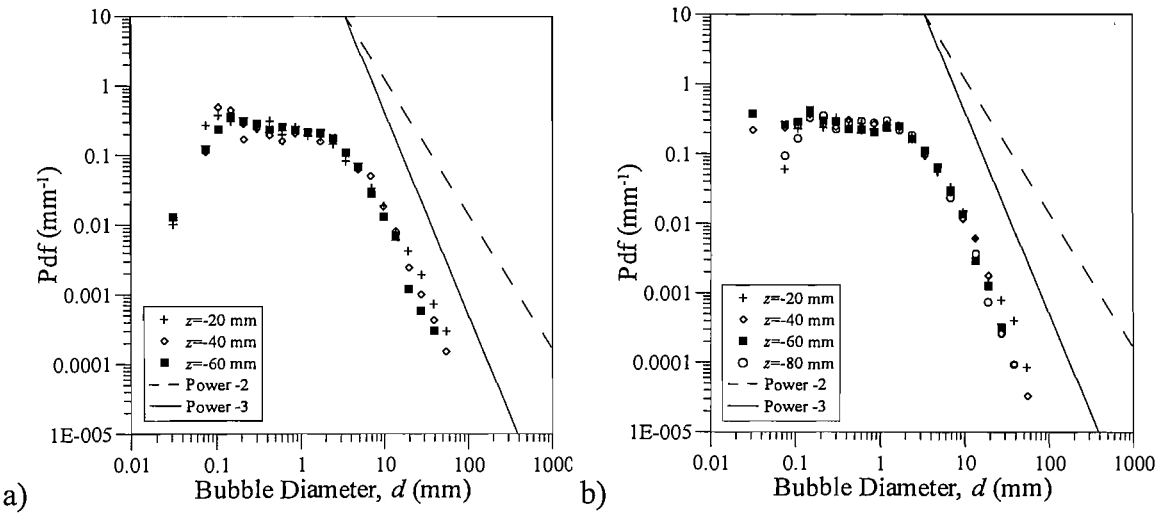

Figure 6.5 Bubble size distributions for the spilling wave case along vertical transects at **(a)** x=200 mm and **(b)** x=280 mm.

An obvious feature of figures 6.4 and 6.5 is that some very large bubbles with diameters in the range 20 mm<d<64 mm were detected in both wave cases, particularly at high elevations close to the free surface. Such large bubbles have not generally been recorded by previous investigators who usually report bubble diameters in laboratory waves no larger than 10-20 mm (Kalvoda *et al.*, 2003; Leifer *et al.*, 2003; Deane & Stokes, 2002; Loewen *et al.*, 1996). However, it is noted that Cummings (1996) measured bubble diameters of up to 60 mm in his experiments on plunging jets, while Waniewski *et al.* (2001) and Cummings & Chanson (1997) measured bubble chord lengths of up to 30 mm in their experiments on bow waves and plunging jets respectively, so such large bubble sizes are not unheard of in violent two-phase flows. In order to confirm the existence of the very large bubbles detected by the optical probe measurements, photographs taken during the experiment were examined and two of these are presented in figure 6.6. Figure 6.6(a) shows a very large bubble with a maximum dimension of approximately 60 mm entrained close to the free surface but away from the active entrainment region where the wave initially breaks and the majority of air entrainment takes place, suggesting that bubbles as large as those detected by the optical probes do indeed exist. Figure 6.6(b) demonstrates that some of these large bubbles can be entrained to significant depths by showing evidence of a bubble with a maximum dimension of approximately 35 mm at a depth of 100 mm.

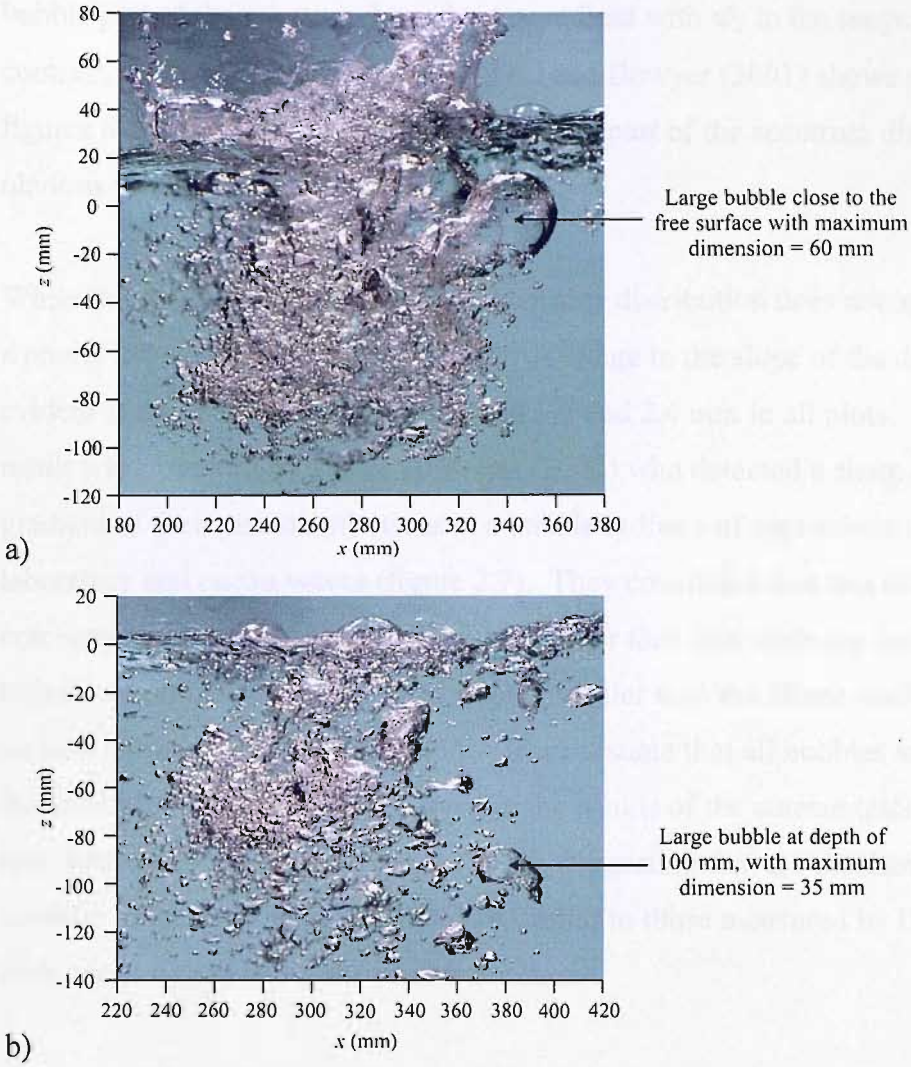

Figure 6.6 Photographs showing the presence of large bubbles in the bubble plumes generated by breaking waves in the current experiments, **(a)** close to the free surface and **(b)** at a depth of 100 mm.

The bubble size distribution data presented in figures 6.4 and 6.5 shows two obvious trends. In the large diameter range, there is an obvious power law dependence of the probability density function on the bubble diameter. This observation is consistent with the results presented by previous researchers (section 2.3.4) and will be discussed in greater detail below. For smaller bubble sizes, the distribution flattens off, showing no obvious power law scaling. There is some inconsistency in the existing literature regarding the shape of the size distribution for small bubbles. Some researchers, such as Leifer *et al.* (2003), Deane & Stokes (2002), Deane (1997) and De Leeuw & Leifer (2002) present bi-modal distributions where the large bubble part of the distribution follows a power law scaling with an exponent Φ_2 between -10/3 and -6.4 while the small

bubble part of the spectrum has a lower gradient with Φ_1 in the range 0.4 to -3.7. By contrast, the data of Loewen *et al.* (1996) and Bowyer (2001) shows a similar trend to figures 6.4 and 6.5 with only the large bubble part of the spectrum displaying an obvious power law scaling.

While the small bubble part of the bubble size distribution does not appear to adhere to a power law scaling in the current data, a change in the slope of the distributions is evident at a bubble diameter of between 1.7 and 2.4 mm in all plots. A very similar result was observed by Deane & Stokes (2002) who detected a sharp change in the gradient of their size distributions at a bubble radius r of approximately 1 mm for both laboratory and ocean waves (figure 2.7). They concluded that this change in gradient corresponds to the Hinze scale. Bubbles larger than this scale are fragmented by turbulence and shear flow, while bubbles smaller than the Hinze scale are stabilised by surface tension forces (Hinze, 1955). If we assume that all bubbles are spherical such that $d=2r$, the slope change observed in the results of the current tests is consistent with that measured by Deane & Stokes (2002), suggesting that the mechanisms of bubble breakup in the tests described here are similar to those measured by Deane & Stokes in both ocean waves and a seawater wave flume.

It is evident from figures 6.4 and 6.5 that the slope of the large bubble part of the bubble size distribution becomes steeper with depth. This observation is confirmed by figure 6.7(a) and (b) which show the variation of the exponent of the power law scaling Φ_2 in the range 2.4 mm$<d<$64 mm with depth for the strongly plunging and spilling wave cases respectively. These plots demonstrate that the value of Φ_2 measured in the strongly plunging wave case ranges from -1.4 close to the free surface at the point of active air entrainment to -3.15 at depth, while the values in the spilling case vary in the range $-2.1<\Phi_2<-2.9$.

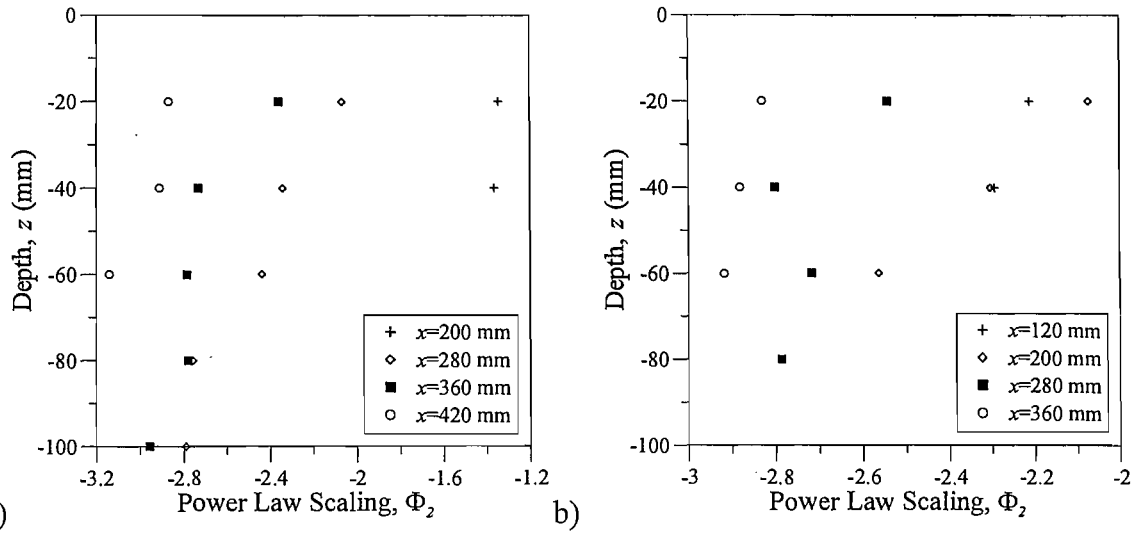

Figure 6.7 Variation of the exponent of the power law scaling Φ_2 in the range 2.4 mm<d<64 mm with depth for **(a)** the strongly plunging, and **(b)** spilling wave cases.

A similar change in the slope of the bubble size spectrum with depth has been observed by previous authors, including Farmer *et al.* (1998), Terrill *et al.* (2001), Hwang *et al.* (1990) and Boywer (2001). This occurs because the majority of the larger bubbles initially entrained in the plume will remain close to the surface and rise quickly out of the water column due to their high buoyant rise velocities, or be broken up by strong differential forces acting on their surface as they are driven deeper, leading to a greater proportion of small bubbles in the bubble plume at depth.

Garrett *et al.* (2000) used simple dimensional arguments to suggest that the air initially entrained by breaking waves is rapidly broken up by turbulent pressure fluctuations, leading to an initial bubble size spectrum proportional to $d^{-10/3}$ before modification by buoyancy and dissolution. Some confirmation of this analysis was given by Deane & Stokes (2002) who found that the large bubble part of the bubble size distribution measured in a seawater flume followed a power law scaling with an exponent of approximately -10/3. It is encouraging that in both of the wave cases examined in the current experiments, the exponent of the power law scaling Φ_2 approaches -10/3 at the maximum measurement depths.

A prominent feature of figure 6.7(a) are the two very high values of $\Phi_2 \approx -1.4$ at x=200 mm. These high values occur because the locations where these values were measured are very close to the most active air entrainment region where large air cavities formed

by the submergence of the vortex of air enclosed beneath the overturning jet are present before they are broken into smaller bubbles by the action of turbulence and shear flows as observed by Deane & Stokes (2002) and shown in figure 6.8. Consequently many large bubbles and air cavities in the range 2.4 mm<d<64 mm were detected at these measurement locations leading to a flattening of the bubble size distribution over the large diameter range. It was suggested by Deane & Stokes (2002) that the smaller bubbles (d<2 mm) detected during the early stages of air entrainment are predominantly entrained in the shear flow between the plunging jet and the wave trough as the jet penetrates the surface.

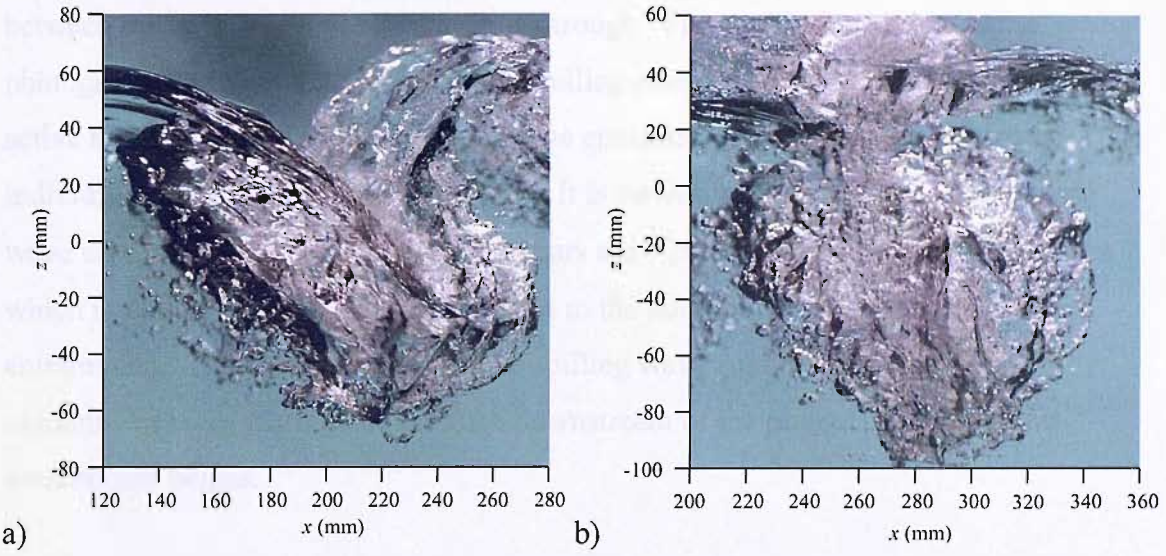

Figure 6.8 (a) Large air cavity entrained by the overturning wave, at this stage few small, defined bubbles are present (t=9T/40). **(b)** The air cavity begins to break up into smaller bubbles under the influence of turbulence and shear flows (t=11T/40).

Figure 6.7(a) also shows that the exponent of the power law scaling in the strongly plunging wave case becomes increasingly negative as the measurement location moves downstream from the active entrainment region at x=200 mm. Thus it is seen that the shape of the size distribution becomes steeper not only with depth, but with horizontal distance away from the active air entrainment region in agreement with the measurements of Terrill & Melville (2000). This result is expected because many of the large bubbles that are initially entrained will rise out of the water column before the plume moves a significant distance away from the active entrainment region, leading to

a larger proportion of small bubbles at greater distances from the location of the breaking event.

A similar variation of the power law scaling with the horizontal measurement location is seen for the spilling case in figure 6.7(b) although in this case Φ_2 varies over a smaller range, with a maximum value of just -2.1. A probable reason for this smaller maximum value of Φ_2 is that as shown in section 5.3.2.1, the submergence and breakup of the vortex, which is the origin of the majority of large bubbles becomes less significant in lower intensity, spilling waves and a greater proportion of the total air volume is likely to be entrained in the form of smaller bubbles in the shear layer which develops between the overturning jet and the wave trough. Figure 6.9 shows close-up photographs of the bubble plume in the spilling case at two times during the period of active air entrainment and it is seen that the entrained air is primarily in the form of individual bubbles and small air cavities. It is interesting to note that in the spilling wave case, the maximum value of Φ_2 occurs at x=200 mm, rather than at x=120 mm which is the measurement position closest to the point of initial overturning and air entrainment. Thus it appears that in the spilling wave case, the most active air entrainment takes place some distance downstream of the plunge point where air entrainment begins.

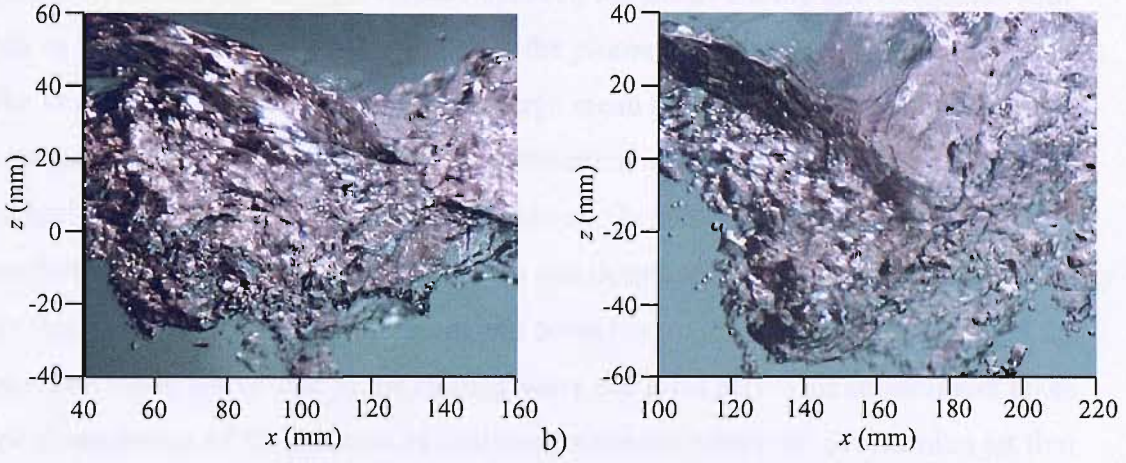

Figure 6.9 Photographs of the bubble plume entrained in the spilling wave case at times **(a)** t=5T/40, and **(b)** t=9T/40. Air is entrained predominantly in the form of individual bubbles and small air cavities in this wave case.

It was noted above that the proportion of small bubbles in the bubble plume increases with vertical or horizontal distance away from the active air entrainment region as the larger bubbles rise more rapidly back to the surface or break up as the plume is driven into the water column and carried downstream. This trend is illustrated in figure 6.10 which shows the variation of the mean bubble diameter with depth for the strongly plunging and spilling wave cases.

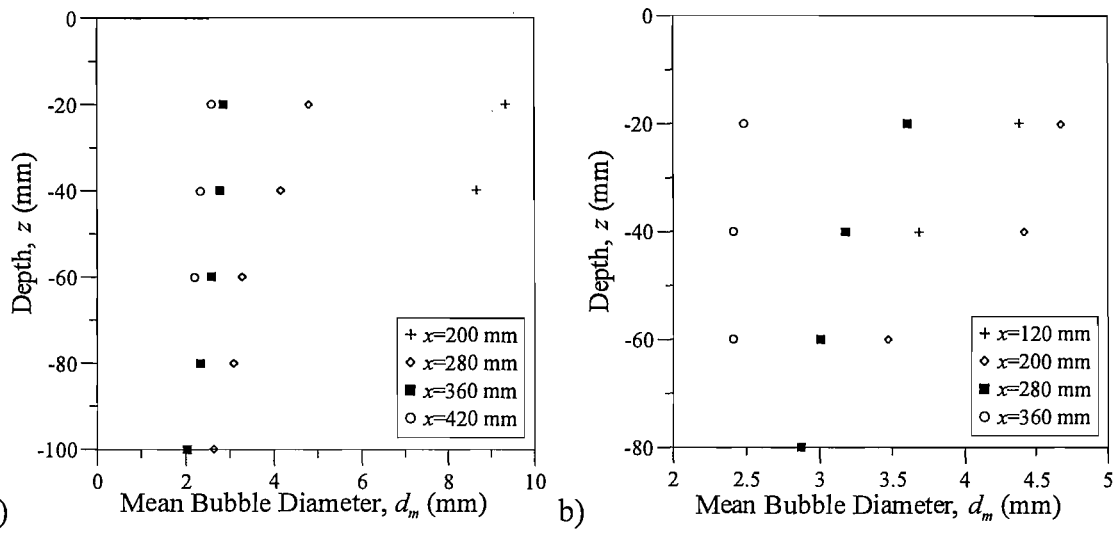

Figure 6.10 Variation of the mean bubble diameter with depth for **(a)** the strongly plunging and **(b)** spilling wave cases.

Figure 6.10 shows that along a vertical transect, the mean bubble size decreases with depth as the proportion of large bubbles in the plume decreases. It is also observed that in the strongly plunging wave case, very large mean bubble sizes are recorded close to the surface in the region of most active entrainment at x=200 mm and then decrease with horizontal distance away from this location. In the spilling case, the maximum mean bubble size also occurs at x=200 mm and decreases with horizontal distance away from this position in both the upstream and downstream directions. This supports the suggestion made above that in the spilling wave the most active air entrainment takes place downstream of the location of initial entrainment where the overturning jet first strikes the water surface. In both wave cases, the mean bubble diameter varies in the range 2 mm$<d_m<$5 mm outside of the active entrainment region. These results agree reasonably well with visual estimates of the bubble sizes made during the injection and rise phases of the plumes. Figure 6.11 shows a close up view of part of a typical bubble plume in the strongly plunging wave case at time t=17T/40 when the plume has just

reached its maximum penetration depth. It is seen that the typical bubble diameters are between 1 and 5 mm providing some confirmation that the optical probe measurements are of the correct order of magnitude. To this author's knowledge there are no existing measurements of mean bubble diameter in the plumes generated by laboratory breaking waves, however the current measurements compare reasonably well with those made by Wang & Monahan (1995) and Chanson *et al.* (2002a & 2004) in steady jets.

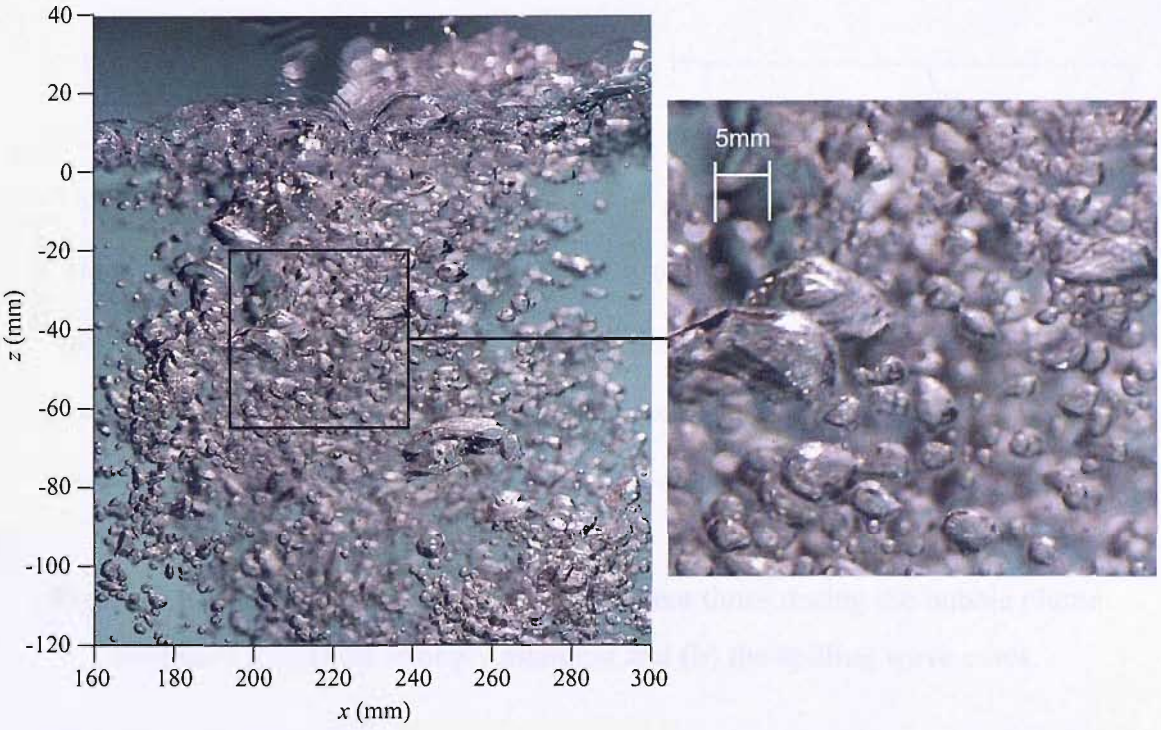

Figure 6.11 Typical bubble sizes in a fully developed bubble plume at the start of the rise phase.

6.4.2 Temporal Variation of Bubble Sizes

In order to examine the temporal evolution of the bubble size distribution at a point in the flow, repeated tests were run at a single location for each wave case detailed in table 6.1 ensuring that at least 2000 bubbles were recorded at each position. Measurements were take at x=360 mm, z=-20 mm for the strongly plunging wave case and x=280 mm, z=-20 mm in the spilling case. Each wave period was divided into a series of phase average bins of duration 0.2 seconds, and the individual bubble size measurements were assigned to the appropriate bin in a similar manner to that described in section 5.2.3 for the void fraction measurements. As with the void fraction estimates presented in

chapter 5, these measurements were critically dependent on the repeatability of the breaking event which was discussed in section 3.5.2.

Figure 6.12 shows the bubble size distributions at various intervals for the strongly plunging and spilling wave cases. Note that there was insufficient data to compile a stable distribution for all time bins due to the low number of bubble detections toward the end of the rise phase.

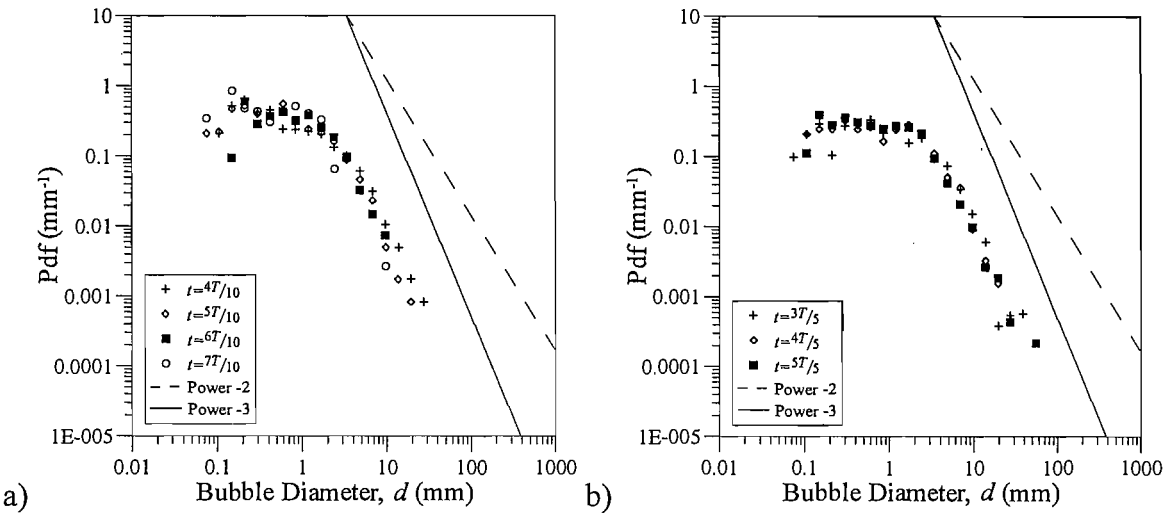

Figure 6.12 Bubble size distributions at different times during the bubble plume evolution for **(a)** the strongly plunging and **(b)** the spilling wave cases.

The data presented in figure 6.12 demonstrate that the bubble size distributions measured here display the same trends as those shown in figures 6.4 and 6.5, with the large bubble part of the spectrum (d>2.4 mm) adhering to a power law scaling. In addition a noticeable change in the slope of the distribution is evident at a bubble diameter between 1.7 and 2.4 mm. While the scatter in the data makes it difficult to calculate stable values of Φ_2 for all of the bubble size spectra presented in figure 6.12, the plots show that there is an apparent increase in the gradient of the distributions in the large bubble range with time. This result is in agreement with Garrett *et al.* (2000) who demonstrated theoretically that the gradient of a bubble size distribution at constant depth increases with time as the bubbles are influenced by buoyancy and dissolution.

As explained above, the scatter in the bubble size distributions made accurate estimates of the variation of Φ_2 with time difficult. However, the cause of the observed change in

the gradient of the bubble size distributions is an increase in the proportion of small bubbles detected by the probe with time as the bubble plume evolves and moves through the measurement location. In order to illustrate this trend, figure 6.13 displays the proportion of detected bubbles with a diameter smaller than 2.4 mm as a function of time. In these plots t_p refers to the arrival time of the bubble plume at the measurement location. The plot shows a steady increase in the proportion of small diameter bubbles with time for both wave cases as the large bubbles which are initially entrained in the bubble plume break up and rise to the surface.

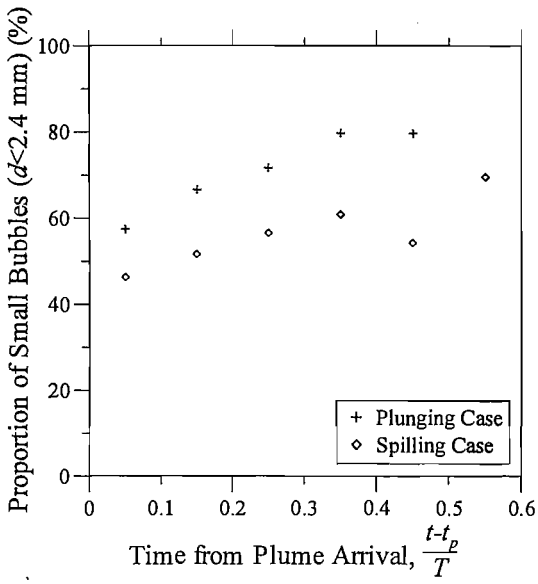

Figure 6.13 Variation of the proportion of small bubbles (d<2.4 mm) as a function of time for the strongly plunging and spilling wave cases.

Further information about the variation of the measured bubble sizes with time is presented in figure 6.14 which shows the variation of the mean bubble diameter as a function of time. As expected, a general decrease in the mean bubble size with time since the arrival of the bubble plume is observed for both wave cases, with the average bubble size reducing from approximately 4.5 mm to 1.5 mm in the spilling wave case and from 3.2 mm to about 1 mm in the plunging example. Note that in this case it is not appropriate to directly compare the bubble sizes in the strongly plunging and spilling waves as they were taken at different locations in the flow field, figure 6.14 simply shows the overall tendency of decreasing mean bubble size with time as the number of large bubbles present in the bubble plume decreases.

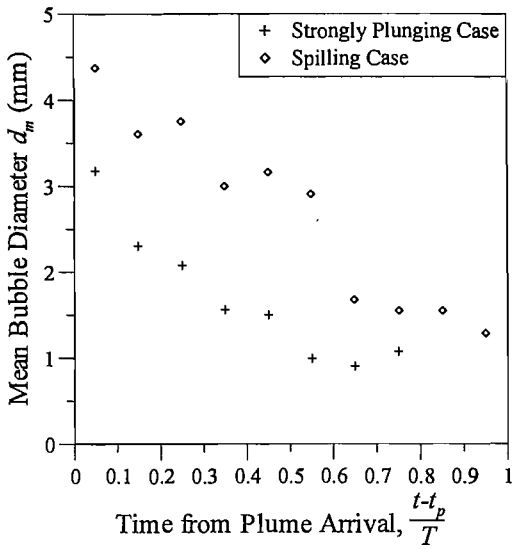

Figure 6.14 Variation of the mean bubble diameter with time for the strongly plunging and spilling wave cases.

6.4.3 Variation of Bubble Size Distribution with "Plume Age"

One of the most important features of the results presented in section 6.4.1 and 6.4.2 is that the proportion of large bubbles in the bubble plume decreases as the plume evolves in space and time away from the active entrainment region causing a change in the slope of the bubble size distribution. In order to better understand these changes it is informative to think of variations in the position of the plume or the time since plume generation in terms of "plume age", where plume age increases with distance away from the active entrainment region and with time since the period of active entrainment. A number of factors make it difficult to make an accurate physical measurement of the plume age and relate it to bubble sizes. Firstly it is difficult to define the exact location of the active entrainment region in time and space as the air entrainment process is not instantaneous or stationary. Secondly, the bubble size measurements presented in section 6.4.1 were made at a single point but averaged over a full wave period and thus represent a range of plume ages.

Deane and Stokes (2002) used the local void fraction to approximate plume age based on the premise that the void fraction would be at a maximum at the point of most active entrainment and decrease away from this position as plume age increases. Support for this assumption can be drawn from the void fraction results presented in chapter 5. Deane and Stokes (2002) found a systematic increase in the gradient of the large bubble

part of the bubble size distribution with decreasing void fraction (i.e. increasing plume age) in their measurements of ocean waves. The results of Deane & Stokes (2002) are presented in figure 2.7.

The graph in figure 6.15 shows the variation of the exponent of the power law scaling Φ_2 with the mean void fraction at the measurement point α_m presented on a log-normal scale, where the void fraction is used to approximate the plume age. In these plots α_m is defined as the mean void fraction at the measurement location during the time that the probe falls within the bubble plume, where the plume boundary is taken to be the 0.3% void fraction contour. The results show that the exponent of the power law scaling increases with increasing void fraction in agreement with the results of Deane & Stokes (2002). For the results obtained during the current experiments, it was found that Φ_2 is proportional to $0.546\ln\alpha_m$.

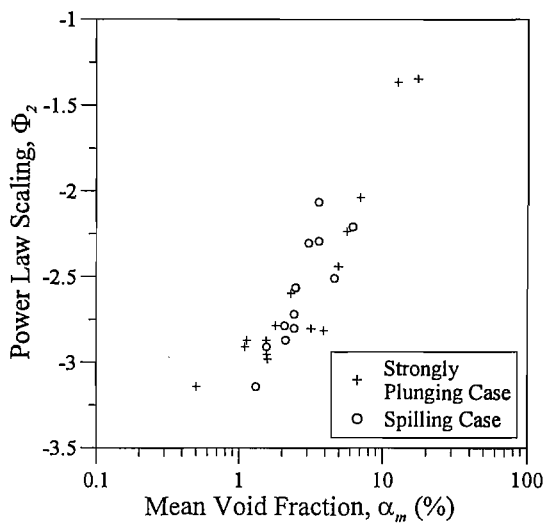

Figure 6.15 Variation of the power law scaling for the large bubble part of the bubble size distribution (d>2.4 mm) with the mean void fraction in the bubble plume.

It is encouraging that the data for both the spilling and plunging wave cases collapse together reasonably well onto a single line in figure 6.15, suggesting that the relationship between power law scaling and mean void fraction in the bubble plume is not dependent on breaker type. Therefore it may be possible to use the mean plume void fraction to estimate the slope of the local bubble size distribution for all wave types.

6.5 DISCUSSION AND SUMMARY

In this chapter, a series of time-averaged bubble size spectra measured at various locations throughout the dense bubble plumes generated by two different breaker types have been presented. These measurements allow a detailed examination of the spatial variation of the bubble size distribution in the dense two-phase flow close to the point of active air entrainment at the free surface. In addition, some limited measurements of the temporal variation of bubble sizes were presented. This data provides new information about the large bubble population that is initially entrained in breaking waves and has been shown to have a significant effect on bubble-mediated air-sea gas transfer.

The main findings from the work presented in this chapter are summarised below.

1. The optical fibre probes were found to perform well and produced reasonable estimates of bubble size which agreed well with flow visualisations of the breaking process. This represents a significant advance because the point measurements made by the probe allow the bubble size distribution in the very dense initial bubble plume to be examined in detail. Such measurements are not possible using alternative techniques due to the acoustic and optical opacity of the bubble plume during its early stages.

2. It was found that the bubble size distribution in the large bubble range (d>2.4 mm) followed a power law scaling in agreement with the results of previous investigators.

3. The exponent of the power law scaling was seen to decrease with distance from the active entrainment region and varied in the range $-1.4<\Phi_2<-3.15$ for the strongly plunging wave case and $-2.1<\Phi_2<-2.9$ for the spilling wave. The low gradient of the distribution close to the active entrainment region occurs because at this point the entrained air exists predominantly in the form of large bubbles and air cavities. Further away from the region of active entrainment, the value of the power law scaling decreases as the larger bubbles break up or rise back to

the surface and Φ_2 approaches the theoretical value of -10/3 presented by Garrett *et al.* (2000).

4. A distinct change in the slope of the measured bubble size distributions was observed at a bubble diameter of between 1.7 and 2.4 mm. A similar result was found by Deane & Stokes (2002) who concluded that the change in gradient corresponds to the Hinze scale. This will be discussed further in chapter 7.

5. A series of results demonstrating the variation of the bubble size spectrum with time were presented in section 6.4.2. These results showed that the proportion of small bubbles present in the plume increases with time as larger bubbles break up or rise back to the surface. This temporal variation of bubbles sizes leads to a gradual increase in the gradient of the bubble size distribution with time, in agreement with the theoretical model of Garrett *et al.* (2000).

6. In an attempt to bring together the observed temporal and spatial variations in the bubble size distribution, the concept of "plume age" was introduced where the plume age increases with distance and/or time away from the point of active air entrainment. An exact measure of plume age is difficult to make due to the rapid evolution of the bubble plume and the instability in the location of the active entrainment region, consequently the mean void fraction in the bubble plume was used to approximate the plume age. A systematic increase in the exponent of the power law scaling Φ_2 with increasing void fraction was observed as the measurement location moved closer to the point of active air entrainment. The data from both the strongly plunging and spilling wave cases were seen to collapse reasonably well onto a single curve, suggesting that void fraction provides a good approximate of the plume age, independent of breaker type.

CHAPTER 7 – AIR ENTRAINMENT IN FRESHWATER AND SEAWATER

7.1 INTRODUCTION

This chapter describes a series of detailed measurements of the time-varying void fraction field in the bubbly flow generated by laboratory breaking waves in natural and artificial seawater and compares them with the freshwater results presented in chapter 5.

The results of this work are of interest to the scientific and engineering community for a number of reasons. The experiment provides new fundamental information about the volume and distribution of entrained air beneath laboratory scale breaking waves in seawater. While a number of previous authors have commented on the differences in the properties of bubble plumes entrained in fresh and seawater there is very little consensus about the exact nature of these differences (section 2.3.6). It is noted also that the majority of previous studies have been based on simple plunging jet or tipping bucket flows, primarily due to the difficulty of making measurements in breaking waves. To this author's knowledge, while work exists that examines the differences in the bubble size distributions beneath breaking laboratory waves (Cartmill & Su, 1993; Loewen *et al.*, 1996) there have been no previous studies that have compared the distribution of void fractions and the bubble plume evolution beneath breaking waves in fresh and seawater.

As well as providing fundamental information about air entrainment in breaking waves, the results of this chapter also have direct application to physical model studies of oceanic processes. Most physical tests designed to examine flow properties of interest to coastal scientists and engineers are carried out at small scale, and virtually all use freshwater to model oceanic phenomena on the assumption that the properties of seawater and freshwater are very similar. Initially, this assumption would appear reasonable as seawater is typically only about 2.5% more dense, 7.5% more viscous and has only 1% higher surface tension than freshwater at 20°C. However, as noted above,

previous authors have commented on differences between bubble plumes generated in freshwater and seawater. Air entrainment in breaking waves has been shown to affect a number of physical processes (section 2.3), for example the presence of air alters the compressibility of the water column which can affect wave impact pressures (Bullock *et al.*, 2001) and it was shown in chapter 5 that entrainment of air can account for part of the total energy dissipated during wave breaking. It is important therefore that any differences in the entrainment of air by laboratory scale breaking waves in freshwater and seawater are understood if we are to assess the validity of small scale laboratory tests designed to reproduce oceanic processes. The issues involved in scaling model scale tests of air entrainment in breaking waves to field conditions are also discussed and a numerical bubble model is developed to examine the evolution of breaker generated bubble plumes at different scales.

7.2 EXPERIMENTAL ARRANGEMENTS

7.2.1 Description of Apparatus

The experimental apparatus used for this experiment was very similar to that used in the tests described in chapter 5. The experiments were carried out in a wave flume at the University of Southampton equipped with a flap-type wavemaker, the specifications and operation of which have been described in sections 3.2.1 and 3.2.2. A submerged reef detailed in section 3.2.3 was installed in the flume with the crest of the reef located 8 m from the wave generator (figure 5.1). The flume was filled to a depth of 0.7 m with artificial and natural seawater.

As with the experiments described in chapter 5, a conductivity probe of the type described in section 3.3.4 was positioned at the breakpoint for each of the wave cases examined. This probe was used to detect the time of breaking for each wave in a test run, to be used as a time origin for the examination of the temporal evolution of the void fraction field. The probe was positioned such that the crest of each wave in the test triggered the probe as the wave face became vertical at the break point.

In order to make measurements of void fraction in the bubble plume generated by wave breaking, two optical fibre phase detection probes were mounted horizontally on an arm suspended from the traverse system described in section 3.3.5 and aligned with the longitudinal axis of the wave flume as shown in figure 5.3.

The only significant difference between the experimental setup for the experiments described in this chapter and those in chapter 5 was that the resistivity type wave gauge used to make measurements of the wave field before breaking was replaced with a capacitance wave gauge at the same position. It was necessary to use a different type of wave gauge because the conductivity of seawater is approximately 570 times greater than that of freshwater. Consequently no valid measurements can be made in seawater using a resistivity wave gauge which relies on the conductivity of the water being low. It was found that the capacitance gauges did not perform as well as the resistivity gauges used in chapter 5. A significant amount of noise was often present and the probe responded poorly during the high accelerations of the free surface at the wave crest and trough. Despite these limitations, the probes were found to be adequate for the purpose of checking the consistency of the generated wave form in the current tests.

7.2.2 Measurement Campaign

The methodology used to make void fraction measurements during the experiments outlined here was the same as that described in section 5.2.2, however the measurement campaign was less extensive. Due to the corrosive nature of seawater and the potential risk to the laboratory equipment, each test case was run for only 5 days, after which the water was disposed of. Because of the relatively short time available to make measurements for each of the water types, only wave case 2 (table 5.1) was examined and the size of the measurement region was reduced, concentrating on the area beneath the free surface and downstream of the plunge point where the overturning jet strikes the free surface. In order to obtain comprehensive measurements of the time-varying void fraction field in the bubble plumes generated by breaking waves in artificial and natural seawater, measurements were taken using two optical fibre probes at 330 positions on a 20 mm x 20 mm grid. The origin of the grid was located at the still water level, directly above the reef crest and measurements were made in the most active areas of the bubble plume as shown in figure 7.1.

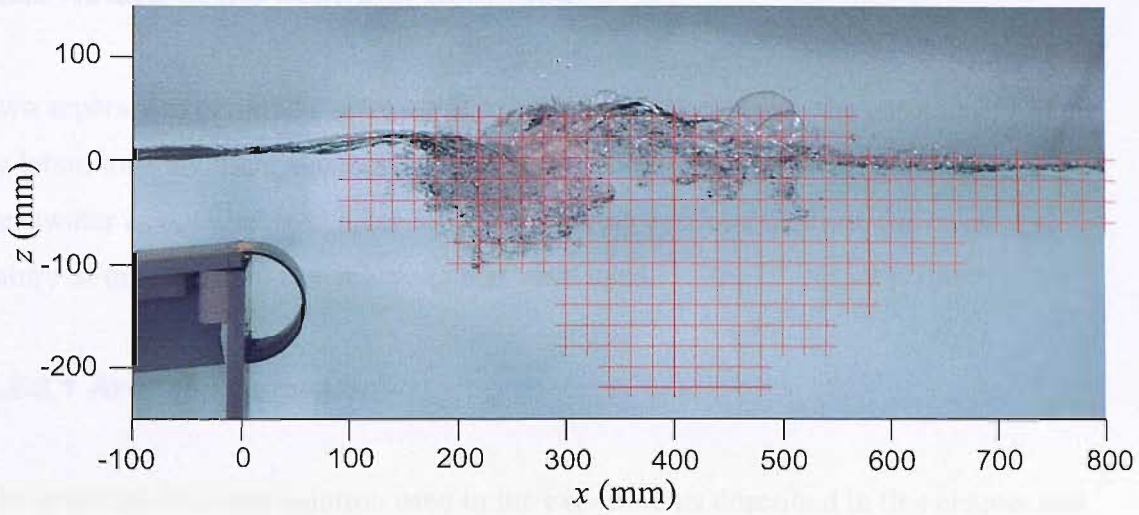

Figure 7.1 Measurement grid for the void fraction measurements in natural and artificial seawater.

At each measurement location, stable phase-averaged void fraction measurements were obtained over a long series of at least 200 regular waves. The stability of the void fraction measurements was confirmed by completing multiple runs for at least 5 locations for each test case, with the chosen positions distributed throughout the measurement area. As in chapter 5 it was observed that at the start of an experimental run, the form of the breaking wave was quite variable but appeared to settle into a form of equilibrium after a period of approximately 30 seconds had elapsed since starting the wavemaker. Consequently, measurements of the void fraction during the current tests were commenced from the time of the first breaking event after an initial settling period of 30 seconds.

In order to obtain detailed information about the spatial and temporal variation of the void fraction in the bubble plumes generated by breaking waves in the current experiments, the time series of air volume detections obtained from the optical probes at each measurement point was used to compute a value for the void fraction for each of 40 phase averaged time bins per wave period using the same method as described in section 5.2.3.

7.2.3 Nature of the Seawater Solutions

Two seperate experiments were carried out in order to compare the entrainment of air by laboratory breaking waves in natural and artificial seawater with that observed in freshwater as detailed in chapter 5. The following sections describe the origin and nature of the two seawater solutions that were used.

7.2.3.1 Artificial Seawater

The artificial seawater solution used in the experiments described in this chapter was produced using a commercial sea salt purchased from Dryden Aqua Ltd which contains the five main constituents that make up typical seawater (table 7.1). A total of 157.5 kg of sea salt was dissolved in freshwater in the wave flume to create artificial seawater with a salinity of 32 ppt.

Table 7.1 Chemical constituents of the artificial seawater.

Constituents (Ions)	Concentration (g/kg)	Weight Percent (%)
Chloride (Cl^-)	18.9799	1.9
Sodium (Na^+)	10.5561	1.1
Sulphate (SO_4^{2-})	2.6486	0.3
Magnesium (Mg^{2+})	1.2720	0.1
Calcium (Ca^{2+})	0.4001	0.04

7.2.3.2 Natural Seawater

Natural seawater was obtained from Calshot boat ramp, located at the mouth of the Solent Estuary (figure 7.2). The seawater was pumped into a 2000 litre water bowser supplied by Finclean Ltd, taking care to minimise the amount of large sediment and seaweed that was taken into the pump inlet (figure 7.3). The water was then transported to the university campus and pumped into the wave flume. Immediately after being pumped into the wave flume the water appeared very murky due to the presence of fine suspended sediments, however this sediment quickly settled to the base of the flume leaving the seawater to appear almost clear. No large sediment or debris was observed in the wave flume.

Figure 7.2 Map of the Solent showing the location of Calshot.

Figure 7.3 Pumping seawater into the water bowser at Calshot boat ramp.

A chemical analysis of the seawater was completed using a DIONEX 500 Ion Chromatograph using ion suppression (D. Smallman pers. comm.), the results of which are listed in table 7.2.

Table 7.2 Chemical constituents of the natural seawater sample.

Constituents (Ions)	Concentration (g/kg)	Weight Percent (%)
Chloride (Cl^-)	14.9806	1.50
Sodium (Na^+)	8.3318	0.83
Sulphate (SO_4^{2-})	2.0905	0.21
Magnesium (Mg^{2+})	1.00397	0.10
Calcium (Ca^{2+})	0.3158	0.03

It has been noted by previous authors (Slauenwhite & Johnson, 1999) that the biological content of seawater can have an effect on air entrainment, therefore it is suggested that future experiments using seawater should include an assessment of the biological activity such as a Biochemical Oxygen Demand (BOD) or Chemical Oxygen Demand (COD) test in addition to a chemical analysis.

7.2.4 Consistency of the Wave Field in Freshwater and Seawater

Before commencing the void fraction tests, measurements of the wave field both upstream and downstream of the reef crest were made using a pair of capacitance wave gauges. The wave gauges were installed at distances of 2 m and 10 m from the wavemaker and measurements were made in both freshwater and artificial saltwater in order to make comparisons of the wave form in the two liquids[1] for 16 different wave cases.

It was found that while there were some difficulties with the capacitance wave probes as noted in section 7.2.1, the measurements provided reasonable confirmation that both the incident waves and those transmitted beyond the reef crest after breaking were very similar in fresh and seawater (figure 7.4). This is an interesting result as the effect of the water type on energy dissipation during wave breaking has been identified as an important factor when applying small scale laboratory measurements, which are generally made in freshwater to field conditions (G. Müller, pers. comm.). While not conclusive, the results from this test suggest that the waves transmitted downstream of

[1] Unfortunately measurements were not taken in natural seawater due to limited time and problems with the wave gauges.

the reef crest after wave breaking are very similar in fresh and artificial seawater and there is no significant difference in the amount of energy dissipated during breaking in the two liquids at this scale.

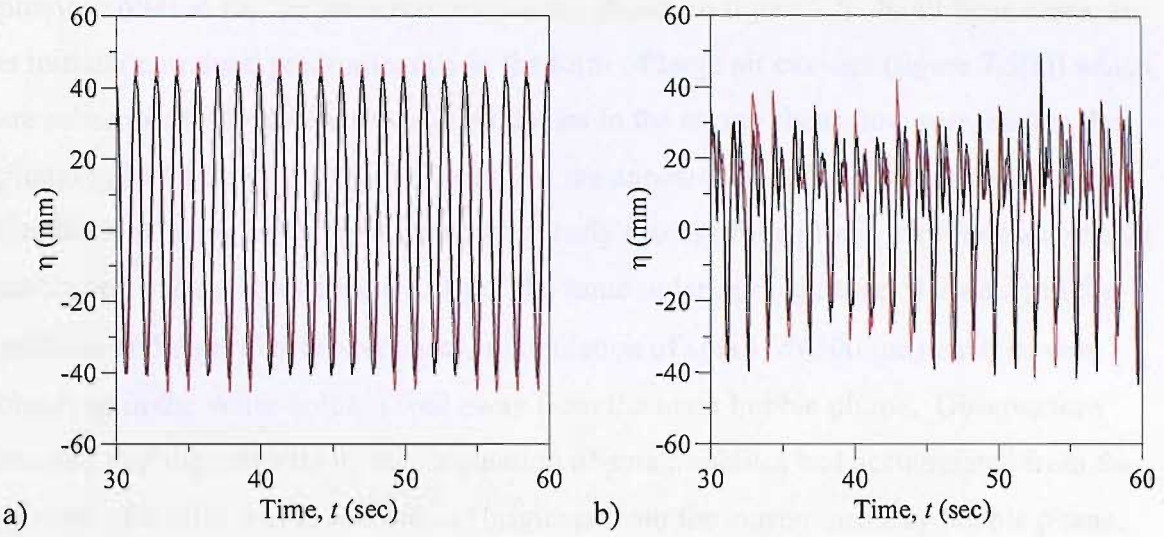

Figure 7.4 Comparison of measured waveforms in freshwater (black) and artificial seawater (red) for **(a)** the generated waves measured 2m downstream of the wavemaker and **(b)** transmitted waves measured 2m downstream of the reef crest.

7.3 EXPERIMENTAL RESULTS

7.3.1 Observations of Air Entrainment and Bubble Plume Evolution

Observations of the bubble plumes generated by laboratory breakers in natural and artificial seawater in the current experiments suggest that the process of air entrainment, the distribution of entrained air and the temporal and spatial evolution of the bubble plume is very similar to that in freshwater. These observations are in agreement with those of Loewen *et al.* (1996) who found that the bubble plumes generated by laboratory wind waves behaved in a similar manner in both fresh and saltwater. This is an interesting result because, as detailed in section 2.3.6 other studies have suggested that significant differences should be observed.

While the overall behaviour of the bubble plumes in artificial and natural seawater is generally very similar to that in freshwater, some differences do exist, particularly in the later stages of the bubble plume evolution and these are described below. It is

interesting to note that the appearance of the bubble plumes in natural and artificial seawater were almost identical at all times.

A series of photographs taken during the formation and injection phases of bubble plume evolution for the three water types are shown in figure 7.5. In all three cases, air is initially entrained predominantly in the form of large air cavities (figure 7.5(a)) which are subsequently broken into smaller bubbles in the strong shear flow surrounding the plunging jet (figure 7.5 (c)). It is seen that the appearance of the bubble plume is very similar in all three cases throughout these early stages of the plume evolution and the air cavity and bubble sizes appear to be of the same order of magnitude. However in the artificial and natural seawater cases, a population of small (d<300 μm) bubbles were observed in the water column well away from the main bubble plume. Observations showed that the majority of this population of small bubbles had accumulated from the passage of earlier waves and did not originate from the current primary bubble plume, although it is possible that the large air bubbles and air cavities present in the plume mask a significant population of very small bubbles. The photographs presented in figure 7.5 also suggest that the volume of entrained air is of the same order in all three cases and this is confirmed in section 7.3.3.1 below.

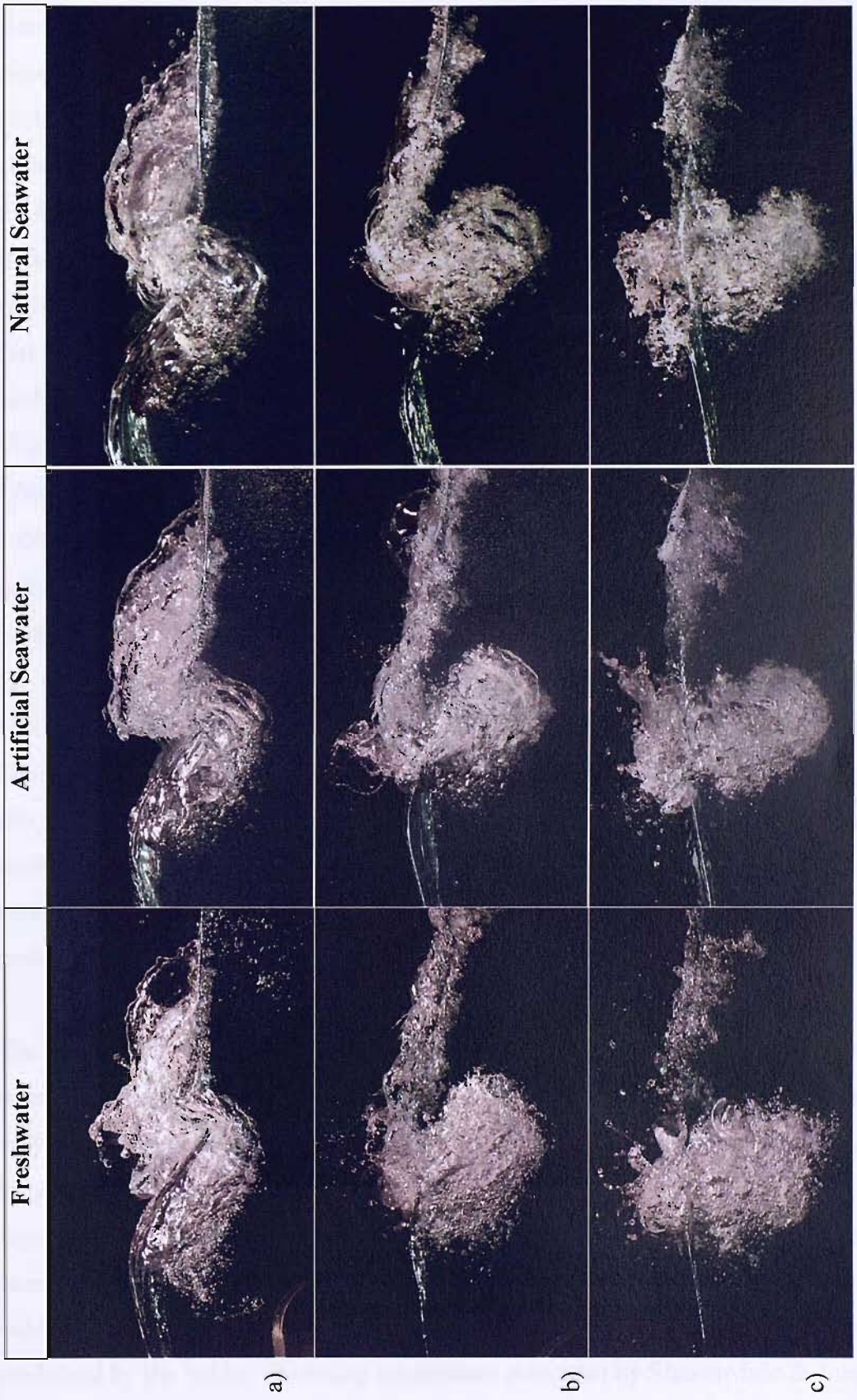

Figure 7.5 Photographs of the bubble plume at three times during the formation and injection phases of bubble plume evolution.

Once the rapid formation and injection phases of the bubble plume evolution have taken place, the bubbles in the plume begin to rise back to the surface and the plume disperses. Photographs of the bubble plume at three stages during the rise phase of the bubble plume evolution are presented in figure 7.6. Figure 7.6(a) shows the bubble plumes at their point of maximum penetration and it is seen that they appear to be very similar for all three water types. However, as the plume begins to rise some small differences become evident. In figures 7.6(b) and (c), a population of small, sub-millimetric bubbles is observed around the plume boundaries in the two seawater cases that are not seen in freshwater. These bubbles become evident after most of the larger bubbles have risen out of that part of the water column, leaving the smaller bubbles which rise at a lower velocity. Eventually, all of the larger bubbles observed in figure 7.6(c) rise to the water surface, leaving a disperse, senescent population of very small bubbles (d<300 μm) which is spread throughout the wave breaking region. The rise velocity of bubbles with a diameter smaller than approximately 300 μm is so small (u_r<0.1 ms^{-1}) that it takes many of them longer than a single wave period for them to rise to the water surface, consequently this leads to an accumulation of small bubbles over repeated wave breaking events and this is discussed further in section 7.4.3.1. Chanson *et al.* (2002a) also noted a similar accumulation in their study of plunging jets and suggested that it can give a misleading impression of the total number of fine bubbles entrained during a single entrainment event which may explain the widely varying small bubble populations described by some previous authors in fresh and seawater (section 2.3.6).

The source of the additional population of small bubbles observed in the seawater cases is unclear. However as it was seen in figure 7.5 that the initial stages of entrainment are very similar in all three cases, it appears that the entrainment mechanisms are the same for all water types and lead to approximately the same initial bubble sizes. It is suggested therefore that the subsequent bubble breakup process differs in the seawater cases and leads to an increased production of smaller bubbles. The difference in the bubble sizes caused by the breakup of the initial bubble population in seawater may be explained by the bubble shattering mechanism presented by Slauenwhite & Johnson (1999) who showed that bubbles broke up into 4-5 times more small bubbles in seawater than in freshwater.

It is concluded that the bubbles generated in the main bubble plume in freshwater and natural and artificial seawater are of a similar size and relatively large bubbles with diameters of the order of 1 mm or greater are visually predominant. However, additional populations of fine bubbles are observed in the two seawater solutions and the slow rise velocity of these small bubbles leads to an accumulation of fine bubbles in the region of breaking waves at the current scale. Thus the experiments described here agree in part with previous authors such as Haines & Johnson (1995), Monahan *et al.* (1994), Carey *et al.* (1993) and Monahan & Zeitlow (1969) who suggest that more small bubbles are entrained in seawater than in freshwater, but it appears that the presence of this population of small bubbles is not as significant as previously proposed and that the accumulation of small bubbles over time gives a misleading impression of the number of fine bubbles that are produced.

While the accumulation of small bubbles will tend to give a misleading impression of the number of fine bubbles generated by a breaking event, it appears that they are not present in sufficient numbers to contribute significantly to the distribution of void fraction, and this is confirmed in section 7.3.2. Nevertheless, the presence of even a small senescent population of air after the passage of a breaking wave significantly affects the compressibility of the water column. Bullock *et al.* (2001) found that an increase of void fraction from zero to just 0.01% caused an increase in the bulk modulus of elasticity of up to 65%, and this influences a number of processes of interest to coastal and marine engineers including pressure propagation in cracks (Muller *et al.*, 2003), wave impact forces (Bullock *et al.*, 2005; Peregrine, 2003) and ship slam (G. Müller, pers. comm.).

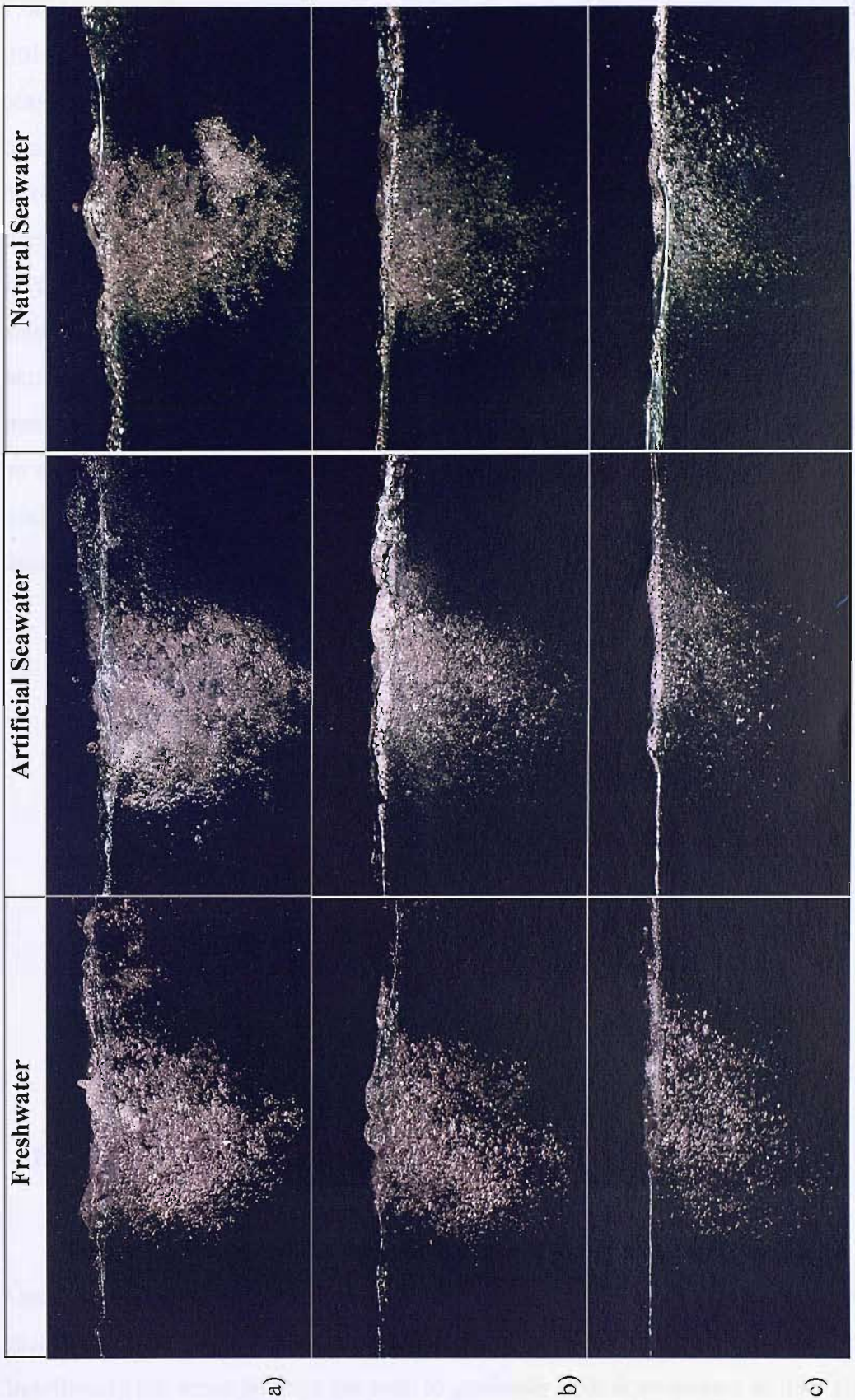

Figure 7.6 Photographs of the bubble plume at three times during the rise phase of bubble plume evolution.

In addition to the differences in the production of small bubbles discussed above, figure 7.6(b) and (c) shows the presence of surface foam in the two seawater cases while very little foam is observed in freshwater. The increased presence of foam at the surface in seawater and saltwater breaking waves was explained by Scott (1975) who demonstrated that bubbles in seawater are stabilised by the presence of salt once they have reached the surface and thus can persist for long periods, while freshwater bubbles burst rapidly upon reaching the surface. A photograph of the foam present on the free surface for the artificial seawater case taken from overhead is shown in figure 7.7 and shows that the surface foam is patchy and not confined to the region directly above the active bubble plume, but persists as surface currents carry it downstream. It was also noted that the generation of foam and the bursting of bubbles at the free surface caused an almost continuous fizzing noise to be heard during the seawater experiments that was not noticeable in the freshwater case and this is a phenomenon that can be heard in the ocean after a large wave has broken in the surf zone.

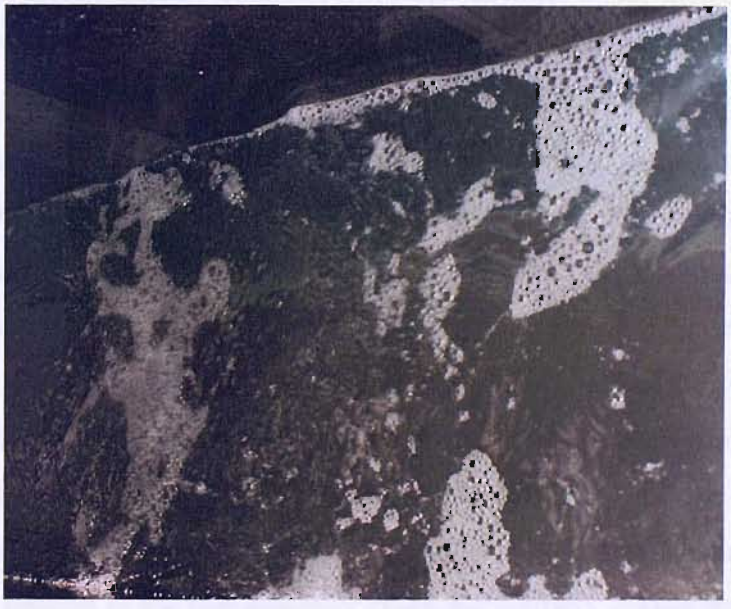

Figure 7.7 Overhead view of the surface foam observed in the artificial and natural seawater cases.

One further point of interest is that while the observed accumulation of small bubbles predominantly occurs close to the breaker location, not all remain in that region indefinitely but some bubbles are seen to gradually drift downstream as they slowly rise to the surface, predominantly confined in a layer within the upper 100 mm of the water column. These bubbles are observed up to 2.5 m downstream of the reef crest and can

be seen in figure 7.8 (a) and (b) at distances of 1m and 1.4 m from the reef crest respectively.

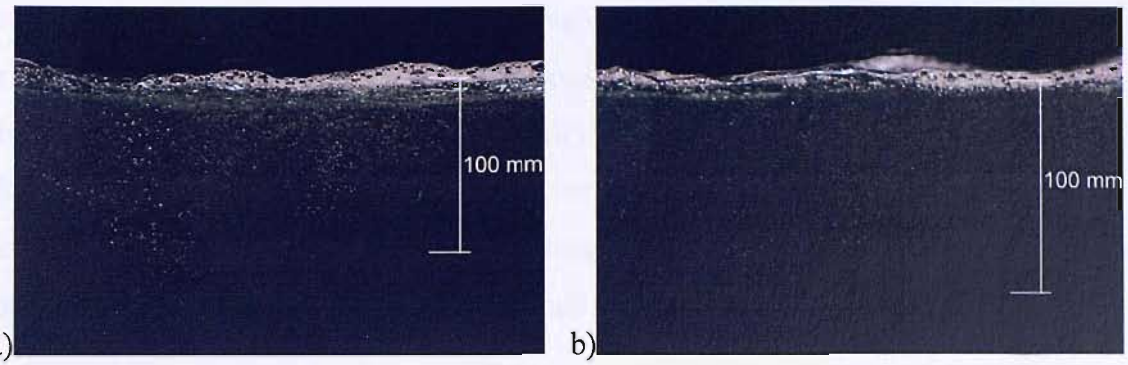

Figure 7.8 Drifting senescent bubble population observed downstream of the main bubble plume at **(a)** 1 m from the reef crest and **(b)** 1.4 m from the reef crest.

7.3.2 Time Varying Void Fraction Distributions

The void fraction measurements obtained from the seawater experiments described above were used to create coloured contour plots of the time-varying void fraction field similar to those discussed in section 5.3.1. A sequence of plots showing the corresponding results for the freshwater, artificial seawater and natural seawater cases are shown in figure 7.9. These plots support the observations made in the previous section that there are no major differences in the distribution of entrained air and the temporal and spatial evolution of the bubble plume for the three test cases. The three sequences show very similar characteristics although there are some differences as the wave overturns due to the difficulties involved in capturing this very rapid motion. The similarity between the three sets of void fraction distributions at all time steps supports the suggestion made in the previous section that while an additional population of very small bubbles is present in the two seawater cases, particularly during the later phases of the plume evolution these fine bubbles are not sufficiently numerous to be significant to the total volume of entrained air or the distribution of void fractions within the plume. It is interesting to note that the number of bubbles detected by the probes was on average 27% greater in artificial seawater and 15% greater in natural seawater than in the freshwater case, and the majority of these additional bubble strikes occur during the rise phase of the bubble plume evolution. This provides some evidence of the existence of a larger number of small bubbles within the bubble plume in seawater.

It was noted that a population of small bubbles accumulated over several wave periods and was distributed over the entire wave breaking region. However they were not very numerous and so small that the probability of detection by the optical probes was very low, consequently their contribution to the void fraction in regions away from the primary bubble plume is not known. It is possible that some of the small bubbles observed in the water column were too small to be detected by the optical probes, although the calibration process detailed in section 3.5.4 indicated that the minimum detectable bubble diameter was between 30 and 60 μm and this is sufficient to detect the smallest bubbles found by most previous studies of bubble sizes in breaking waves.

The only obvious consistent difference in the plots is that in the two seawater cases, the bubble plume is consistently slightly further downstream than in the freshwater case. No obvious explanation can be given for this as the measurements of the incident wave field presented in figure 7.4 demonstrate that the waves generated by the wavemaker do not vary significantly between freshwater and seawater. In addition, observational evidence suggested that there were no obvious differences in the breaking event, although a slightly smaller amount of splash was observed in the two seawater cases. A sequence showing all 40 phase-averaged void fraction plots for the artificial and natural seawater cases is found in Appendix C.

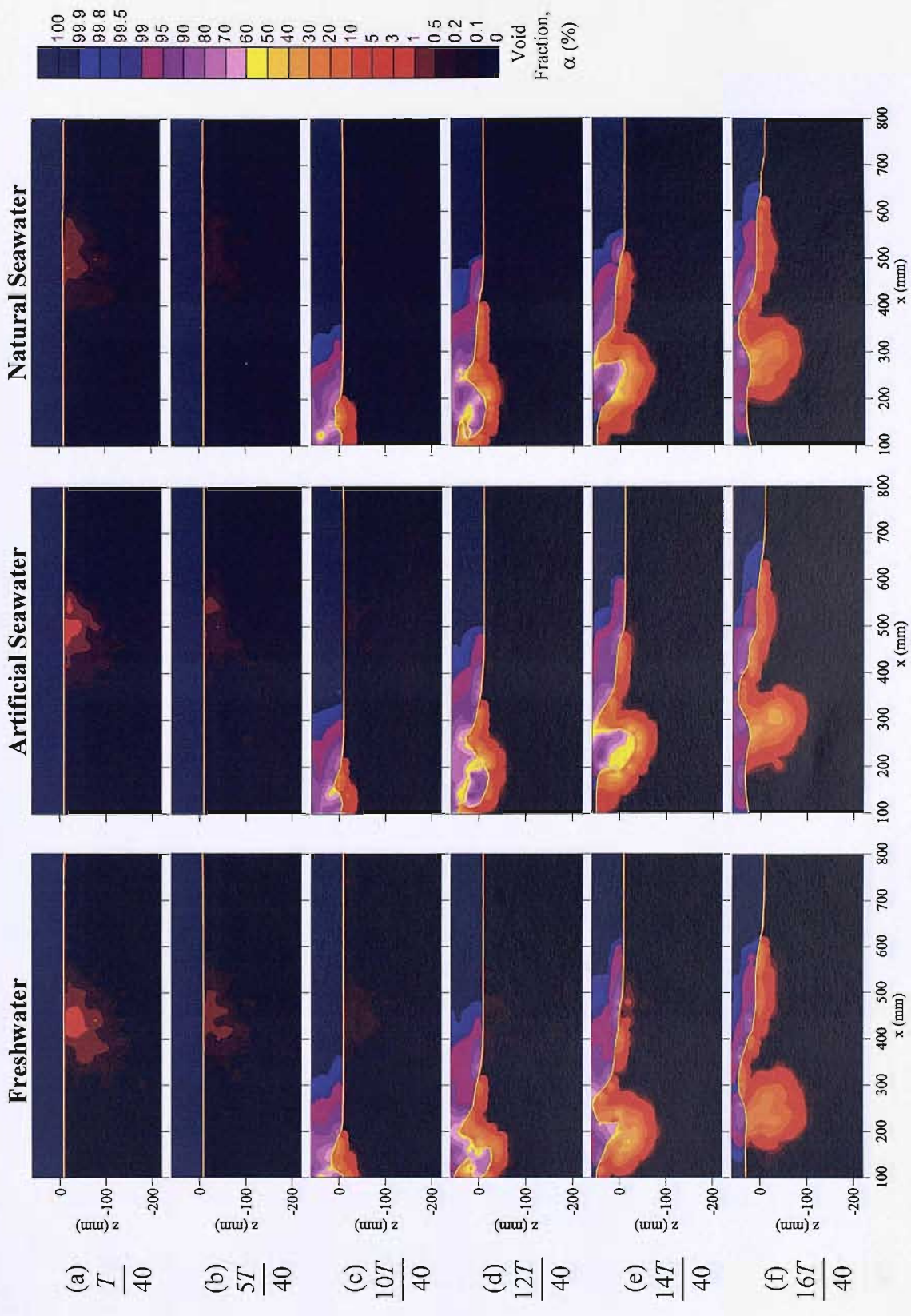

Figure 7.9 Void fraction distributions beneath plunging breaking waves in freshwater, artificial seawater and natural seawater.

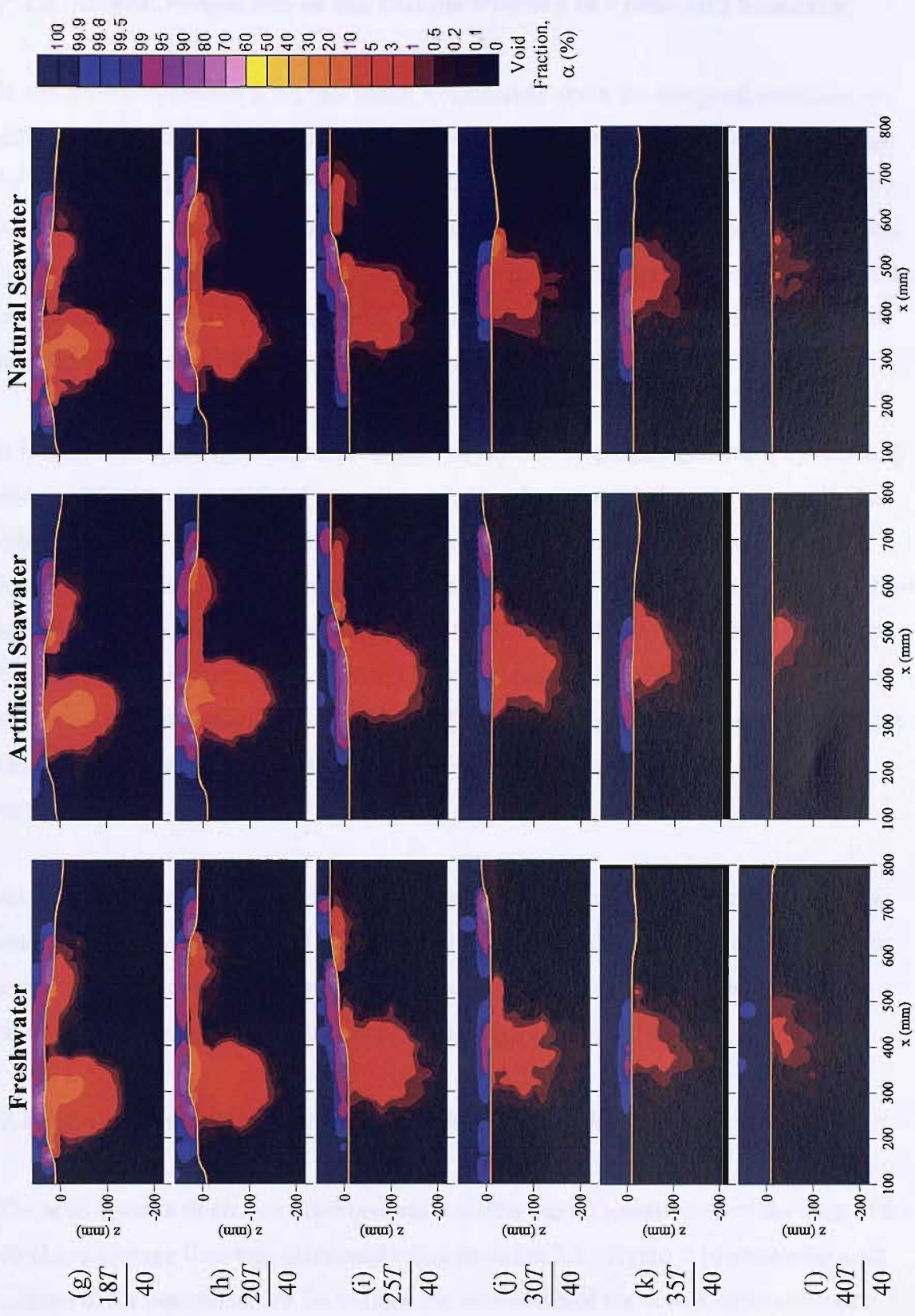

Figure 7.9 (continued).

7.3.3 Integral Properties of the Bubble Plumes in Fresh and Seawater

It was shown in section 5.3.2 that useful information about the temporal evolution of different quantities of the bubble plumes entrained by breaking waves can be obtained by calculating integral properties of the void fraction field. Similar integral properties are presented in this section to allow direct comparison of the bubble plumes generated in the three water types under examination. It is noted that due to the smaller size of the measurement area in the current tests, only moments of the bubble plume were taken and were confined within the region 100 mm<x<600 mm.

It is seen below that the integral properties of the bubble plumes generated by breaking waves in freshwater, artificial seawater and natural seawater behave in a very similar manner. This is a very interesting result and confirms the observations made in the previous sections that there are no significant differences in the distribution of entrained air and the temporal and spatial evolution of the bubble plumes generated by laboratory breaking waves in freshwater, artificial seawater and natural seawater. The data also supports the observations of Loewen *et al.* (1996) who reported that the bubble plumes created by laboratory wind waves behaved in a similar manner in both fresh and saltwater.

As the overall trends seen in each property are very similar to those for the freshwater case and these were discussed in some detail in section 5.3.2, the following discussion concentrates predominantly on any observed differences between the results for the three different water types rather than commenting on general trends.

7.3.3.1 Volume per unit Width of Air in the Bubble Plume

The total volume of air entrained beneath the 50% void fraction contour[2] for each of the 40 phase average bins was calculated using equation 5.2. Figure 7.10 shows the total volume of air normalised by the volume per unit width of the vortex of air enclosed

[2] As in Chapter 5, the 50% void fraction contour was used to approximate the position of the free surface as it is very difficult to accurately define the water surface during the period of most active breaking.

between the underside of the plunging jet and the wave face V_p/V_v plotted as a function of time normalised by the bubble rise time as described in section 5.3.2.1.

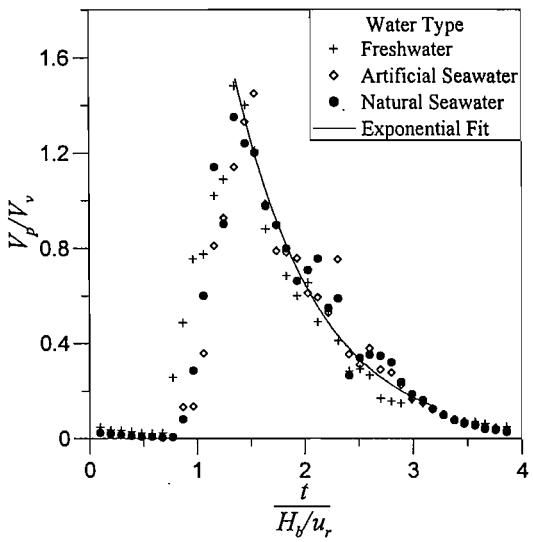

Figure 7.10 Volume of entrained air per unit width as a function of time.

It is seen in figure 7.10 that the three plots are very similar, displaying approximately the same peak values and subsequently decaying according to the same exponential. This confirms the observations made in section 7.3.1 that the volume of air entrained by breaking appears to be the same for all three water types and that the increased small bubble population observed during the later stages of the rise phase of the plume evolution does not contribute significantly to the total volume of entrained air.

This result contradicts the previous work of Chanson *et al.* (2002a) whose measurements of void fraction beneath plunging jets in freshwater and seawater suggested that a significantly smaller total volume of air was entrained in the seawater case. The current data also disagrees with Wu (2000) who reanalysed the measurements of the bubble size distribution beneath large scale laboratory waves made by Cartmill & Su (1993) and found that their results indicated that up to 12 times more air was entrained by breaking waves in seawater than in freshwater.

The data presented in Figure 7.10 indicates that at the scale of the current experiment, almost identical volumes of air are entrained by breaking waves in freshwater and artificial and natural seawater. Based on observations of the experiment and the photos

presented in figure 7.5 this is not a surprising result as the air entrainment process appeared to be very similar in all three cases. In addition it is noted in section 7.4.1 that air entrainment in breaking waves is mostly dependent on the wave geometry and gravity effects and so it seems likely that the total volumes of air entrained in fresh and seawater will be similar because, as noted in section 7.1, the bulk properties of the fluids are almost identical.

The results presented in figure 7.10 also indicate that once air has been initially entrained during the formation and injection phases, the volume of air in all three bubble plumes subsequently evolves in a very similar manner and this provides support for the observations made in the previous section that the bubbles in the plumes are predominantly of a similar size and the small bubble population present in the seawater cases has little effect on the overall behaviour of the plume.

7.3.3.2 Horizontal Movement of the Bubble Plume Centroid

Figure 7.11 shows the variation in the position of the horizontal centroid of the bubble plume as a function of time for the three different water types. It is seen that in all three cases, the centroid of the bubble plume moves at a velocity approximately equal to the shallow water wave speed during the period immediately after breaking while the formation and injection phases of the bubble plume are taking place. At later times when the plume moves into the rise phase, the horizontal velocity of the centroid reduces in a similar manner for all three cases. It is observed that the movement of the horizontal centroid in the two seawater cases is almost identical, but while the freshwater case displays the same trend, the position of the centroid is closer to the reef crest at all times. This is in agreement with the void fraction plots presented in figure 7.9 which show that the bubble plumes generated in artificial and natural seawater are consistently slightly downstream of the plume in the freshwater case.

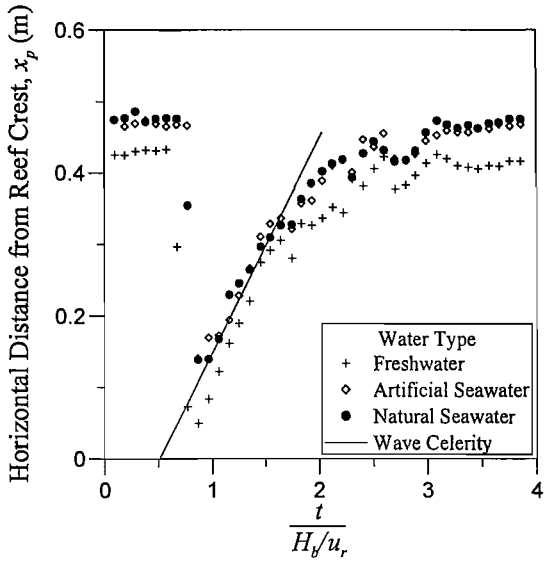

Figure 7.11 Horizontal movement of the bubble plume centroid as a function of time.

7.3.3.3 Vertical Movement of the Bubble Plume Centroid

The movement of the vertical centroid of the bubble plume normalised by the breaking wave height H_b as a function of time is shown in figure 7.12 and once again we see that the behaviour is very similar in all three cases. The only obvious difference between the three plots is that the bubble plume centroid reaches a slightly greater depth in the freshwater case and is consistently slightly closer to the surface in the natural seawater case. The similarities in the movement of the bubble plume centroid for all three water types provide further support for the observations made in section 7.3.1 that the bubbles in the plumes are predominantly of a similar size and consequently evolve in a similar manner after they have been entrained in the water column.

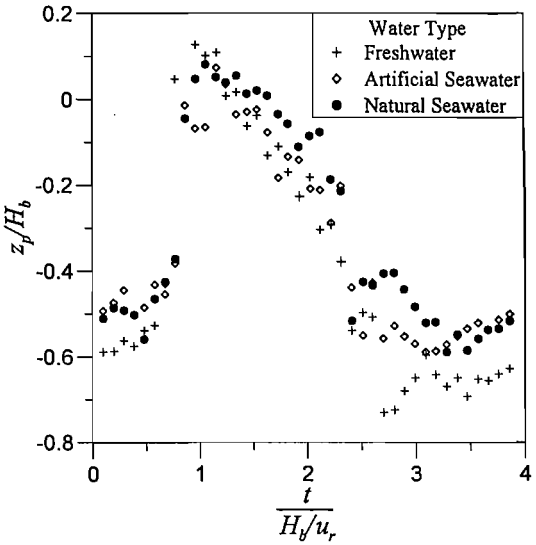

Figure 7.12 Vertical movement of the bubble plume centroid as a function of time.

7.3.3.4 Mean Void Fraction in the Bubble Plume

The variation of the mean void fraction in the bubble plume with time is presented in figure 7.13. To be consistent with the results of section 5.3.2.4, the 50% and 0.3% void fraction contours were used to define the bubble plume boundaries. Figure 7.13 demonstrates again that the results for all three water types display very similar behaviour with the mean void fraction rapidly rising to a peak value after the arrival of the new breaking wave and then decaying according to a power law. It is noted that the peak mean void fraction is noticeably larger in the two seawater cases, primarily because the cross-sectional area of the bubble plume is slightly larger in the freshwater case as demonstrated in section 7.3.3.5 below.

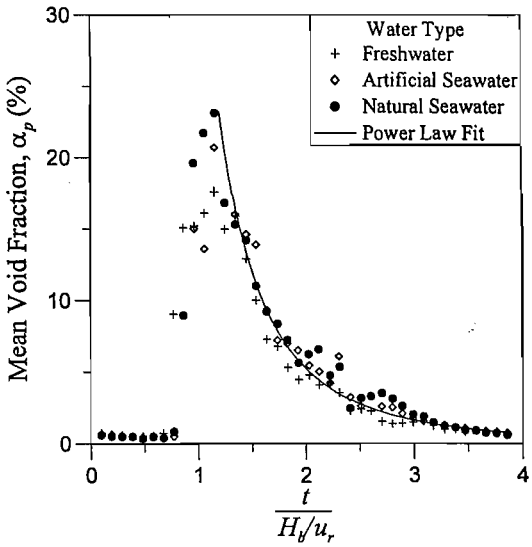

Figure 7.13 Variation of the mean void fraction in the bubble plume as a function of time.

7.3.3.5 Cross-Sectional Area of the Bubble Plume

For consistency with the results presented in section 5.3.2.5, the cross-sectional area of the bubble plume was calculated as the area enclosed between the 0.3% and 50% void fraction contours. The variation of the bubble plume area normalised by the cross-sectional area of the vortex as a function of time is presented in figure 7.14. It is observed that the peak value for the freshwater case is slightly greater than the two seawater cases, however in general the plumes display a similar overall trend which was described in section 5.3.2.5.

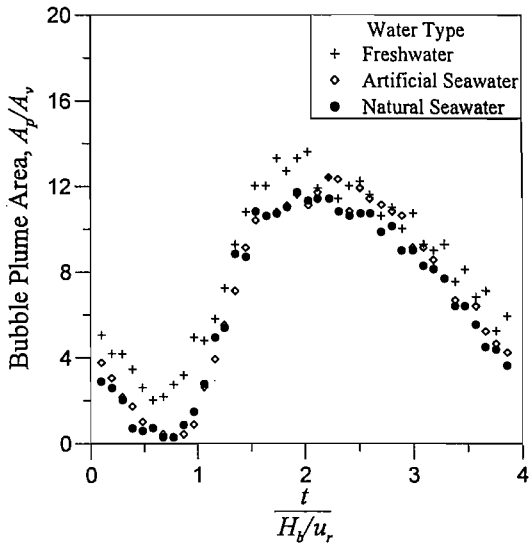

Figure 7.14 Variation of the bubble plume area as a function of time.

7.3.3.6 Bubble Penetration Depth

The temporal variation of the maximum depth of the 0.5% and 1% void fraction contours normalised by the breaking wave height are presented in figure 7.15. As with all of the previous plots, it is seen once again that the bubble plume behaves in a very similar manner in all three water types. Although any differences are small, the penetration depth is generally greatest for the freshwater case and smallest in the natural seawater plume.

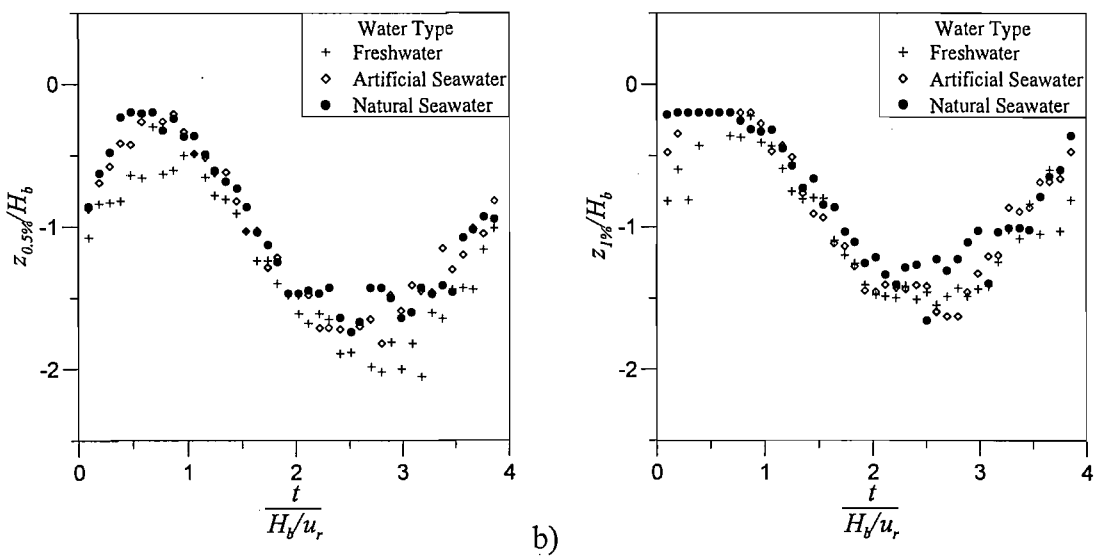

Figure 7.15 Variation of the maximum depth of **(a)** the 0.5% void fraction contour and **(b)** the 1% void fraction contour as a function of time.

7.3.3.7 Potential Energy of the Entrained Air Volume

The work per unit width required to keep the measured air volume entrained against buoyancy was calculated for each phase average bin using equation 5.5 in order to investigate the amount of incident wave energy dissipated during wave breaking. The temporal variation of the potential energy of the bubble plume normalised by the incident wave energy is presented in figure 7.16.

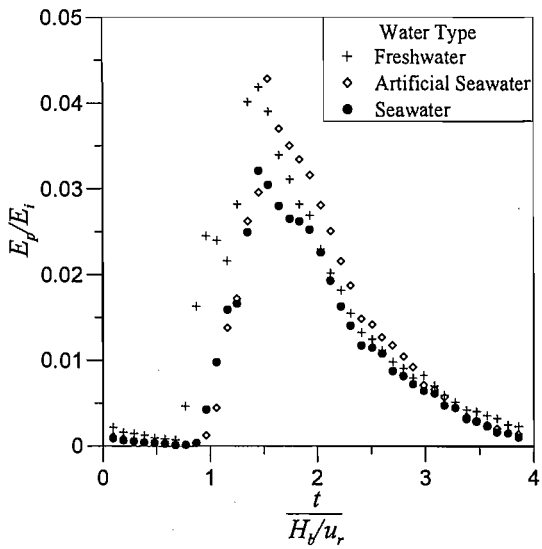

Figure 7.16 Temporal variation of the potential energy of the entrained bubble plumes normalised by the incident wave energy.

Figure 7.16 demonstrates that the potential energy of the bubble plume varies in a similar manner with time for all three water types. However it is clear that the peak value for the natural seawater case is 20% lower than the corresponding values in freshwater and artificial seawater. As the potential energy is calculated by taking moments of the void fraction field about the 50% void fraction contour, it is thought that this difference in the peak values is caused by the slightly smaller penetration depths reached by the natural seawater plume. Additionally, it may be significant that the largest differences between the natural seawater curve and the freshwater and artificial seawater results occur during the period of most active entrainment when the position of the free surface is difficult to define and the 50% void fraction contour is highly distorted. Away from the peak of the curves, the potential energy of the bubble plumes is quite similar in all three cases.

7.3.4 Validity of Freshwater Experiments for Modelling Oceanic Processes

The results discussed in section 7.3 show that at the scale of the current experiments, the bubble plumes entrained by breaking waves in freshwater and artificial and natural seawater are very similar. The only major differences observed in the experiments were that in the seawater cases an appreciable amount of foam developed on the water surface and a population of very small bubbles became evident during the latter phases of the plume evolution and was seen to accumulate in the region of wave breaking over several wave periods.

Measurements showed that the number of the small bubbles observed in the seawater cases was not sufficient to significantly contribute to the total volume of entrained air or make a notable difference to the measured void fraction distributions. However, their presence will alter the compressibility of the water. Consequently it is concluded that in most cases, the use of freshwater in models of oceanic processes at the scale examined in this chapter appears to be valid, although care must be taken when examining phenomena where compressibility effects are important or the level of surface foam is of interest. It is noted that there were no significant measurable or observable differences between the bubbly flow generated in artificial and natural seawater, thus it suggested that in situations where it is practically or economically prohibitive to obtain real seawater, artificial seawater should provide a good substitute.

7.4 SCALING AIR ENTRAINMENT

The results presented in the previous section have suggested that at the scale of the current experiments, the use of freshwater in physical models to examine oceanic processes is reasonably valid in most cases. It is noted however that the experimental data used to examine the differences in air entrainment in freshwater and seawater breakers was obtained using waves with a breaker height of just 100 mm. It is useful therefore to comment on the applicability of these small scale measurements of air entrainment to full scale, field conditions.

The problem of scaling laboratory results to full sized ocean waves is always difficult and few authors have commented on the issues involved in scaling air entrainment processes. Chanson (1997) noted that for high velocity two-phase flows, different scaling laws are valid for different aspects of the flow. In general, free surface flows are geometrically scaled and Froude similarity is applied. However he suggested that the processes which control the evolution of the bubble plume, such as bubble breakup and coalescence are dominated by surface tension effects which implies the need for Weber scaling. Based on these conclusions and the results of a series of laboratory tests examining the aeration around plunging jets at different scales, Chanson *et al.* (2002a) concluded that air entrainment in the sea cannot be accurately modelled by small scale laboratory tests but that such experiments provide useful information on the mechanisms of entrainment and the interaction between the different processes. By contrast, Lamarre (1993) made measurements of the integral properties of the void fraction field in both small 2D and large 3D laboratory waves and found that they scaled well with the wave height and wavelength, suggesting that scaling measurements of air entrainment processes in the laboratory to field conditions may be appropriate.

In this section, the issues involved in scaling three major aspects of the two-phase flow generated by breaking waves will be examined.

7.4.1 Initial Entrainment Process and the Total Volume of Entrained Air

In the following discussion it is assumed that all of the air entrained by a single breaking event occurs due to the primary entrainment mechanisms as described in section 2.3.2 and these are examined separately.

7.4.1.1 Collapse of the Vortex of Air Enclosed Beneath the Overturning Jet

If it is assumed that all of the air trapped within the vortex is subsequently entrained into the water column, this entrainment mechanism is entirely dependent on the geometry of the overturning wave. It is noted that in three-dimensional breaking waves, this assumption will not be entirely valid as some air will escape laterally as the wave breaks, however it is a reasonable first assumption for the purpose of this discussion. The scale effects that affect the vortex shape beneath a plunging jet at small scale were

discussed by Couriel *et al.* (1998), who suggested that surface tension can have a significant effect on the breaker geometry if the breaking wave height is smaller than 50 mm. As the present tests use a breaking wave height of 100 mm, surface tension effects are likely to be unimportant. Further support for this conclusion can be taken from the work presented in section 4.3.3 where it was found that the values of the vortex length to vortex width ratios measured in laboratory scale breaking waves were within the range of values found in the field studies of Mead & Black (2001) and Sayce *et al.* (1999). Consequently, it is assumed that the vortex dimensions will scale geometrically and there should be no significant scale effects associated with this entrainment mechanism.

7.4.1.2 Air Entrained by the Action of the Overturning Jet

Ledesma (2004) suggested that the air entrainment caused by the action of the overturning jet from a breaking wave is most suitably modelled by considering an impacting water jet. A summary of the previous work that has been completed on unsteady plunging jets is given in section 2.3.2.2.

Prosperetti & Oguz (1997) and Oguz *et al.* (1995) developed potential flow models of an impacting planar jet and falling water mass respectively and showed that for strong impacts, the effects of surface tension and viscosity were negligible and the process of air entrainment was dominated by gravity and inertia effects. Prosperetti & Oguz (1997) went on to present values of the volume of air per unit width entrained by a single jet impact normalised by the square of the jet width and showed that it was dependent solely on the jet Froude number. Based on these studies it seems reasonable to assume that there should be no significant scale effects associated with the plunging jet entrainment mechanism and the total volume of entrained air will scale geometrically.

The arguments outlined above suggest that the mechanisms of air entrainment are similar at model and field scale and that the total volume of air entrained during breaking will scale with the wave geometry.

7.4.2 Bubble Size Distribution

As detailed in section 2.3.4, a large number of previous studies examining the bubble size distribution in both the laboratory and field have been undertaken but there has been very little comment on how the measurements at these two scales compare. The results of previous authors listed in table 2.2 suggest that bubble size distributions beneath breaking waves at all scales follow a power law scaling, however beyond this there is little consistency within the available results and no obvious scale dependence is evident.

Garrett *et al.* (2000) argued that the bubble size spectra beneath breaking waves are the result of a simple dimensional cascade where air is initially entrained into relatively large bubbles which subsequently fragment into smaller bubbles at a rate that depends on the dissipation rate of turbulent kinetic energy ε. Garrett *et al.* went on to show that the process of bubble breakup depends on the differential forces on the surface of the bubble exceeding the restoring forces associated with surface tension. This implies that the bubble size should reach a minimum radius at the Hinze scale r_H (Hinze, 1955) which is dependent on the value of ε and below which bubbles are stabilised by surface tension forces and do not fragment.

Garrett *et al.* noted however that published bubble size distribution measurements showed the existence of large numbers of bubbles smaller than the Hinze scale. Deane & Stokes (2002) explained this by suggesting that bubbles larger than the Hinze scale are predominantly created by the fragmentation of the vortex of air trapped beneath the overturning jet, while smaller bubbles are entrained in the shear layer formed by the impact of the plunging jet. This conclusion was supported by their measurements of the bubble size distribution beneath breaking waves in a seawater laboratory flume which showed a change in spectral slope at a bubble radius of 1 mm that corresponded well with a value of the Hinze scale deduced from observations of bubble fragmentation. Deane & Stokes (1999 & 2002) also found a similar break point in the gradient of bubble size distributions obtained in oceanic waves at $r \approx 1$ mm and suggested that this was evidence that the Hinze scale is also relevant in the open ocean, implying that the same bubble formation mechanisms operate at both model scale and field conditions.

Further support for the existence of an oceanic Hinze scale has been provided by Gemmrich & Farmer (2004) who calculated a value of r_H=2 mm (of the same order as that found by Deane & Stokes (2002)) based on their measurements of near-surface turbulence.

From the discussion above, it is concluded that the same bubble formation and breakup mechanisms are observed in both the laboratory and ocean, and consequently it is expected that the distributions of bubble sizes after the initial entrainment event will be similar at both scales. Support for this conclusion is obtained from the field results of Bowyer (2001), whose near-surface measurements of bubble spectra in the vicinity of breaking waves in both seawater and freshwater show spectral slopes and a range of bubble sizes that compare well with the experimental data presented in section 6.4 and the measurements of Deane & Stokes (1999 & 2002).

7.4.3 Evolution of the Bubble Plume

The discussions above have concluded that while the total volume of air entrained is expected to scale geometrically with the wave height, the absolute sizes of bubbles present after initial entrainment has taken place are expected to be comparable at all scales. Consequently, the rise velocities of the bubbles making up the bubble plume will remain constant, independent of the scale of the breaking wave.

It was shown in section 5.3.2.1 that the characteristic time scale of air detrainment is the bubble rise time H_b/u_r and the bubble plume evolution was seen to scale well according to this time scale. It follows that when scaling results from model to full scale, the time scale of bubble plume evolution will follow the length scale S, while a Froude model used to scale the wave properties implies a time scale $\sqrt{S}$. It is expected therefore that there will be large differences in the temporal evolution of bubble plumes generated at model and full scale.

Evidence for this was observed during the experiments described in this chapter. It was noted that the bubble plume generated by laboratory breakers in seawater had almost entirely dispersed within a single wave period, leaving just a small senescent population

of very small bubbles and a limited amount of surface foam. By contrast, observations of waves breaking in the ocean show that a large number of bubbles and significant surface foam frequently remain in the water after one wave period. This effect can be seen in figure 7.17, which shows an aerial view of waves breaking along a headland. In this picture, the path of the breaking part of the waves can be clearly seen as the high levels of air remaining in the water as well as surface foam cause the water surface to appear white.

Figure 7.17 Highly aerated water left by the passage of repeated breaking waves.

In order to further examine the post-breaking behaviour of the bubble plumes generated by breaking waves at different scales, a numerical bubble model which describes the evolution of the void fraction distribution within a rising plume of bubbles was developed.

7.4.3.1 Bubble Plume Evolution Model

The model presented in this section is a two-dimensional, Lagrangian finite-difference model which traces individual bubbles and incorporates the effects of turbulent diffusion, bubble dissolution, buoyancy and hydrostatic bubble expansion. The model is similar to those presented by Thorpe (1984), Woolf (1993) and Woolf & Thorpe (1991) used to examine gas transfer in the upper ocean as described in section 2.3.7. The current model is designed to investigate the rapid evolution of the dense, transient bubble plumes generated directly beneath breaking waves and is used to compute the time-varying void fraction distribution of bubble plumes at different scales.

Initial Conditions

As mentioned in section 2.3.7, the process of wave breaking and initial bubble entrainment are highly complex and no successful models of these phenomena currently exist. Consequently, the current model ignores the injection and formation phases of the bubble plume evolution described in section 2.3.1 and the initial condition corresponds to the end of the injection phase when the plume is at its maximum penetration depth. The model then examines the subsequent evolution of the bubble plume in the rise phase.

For its start conditions, the model requires an initial void fraction distribution within the bubble plume to be entered on a 2 dimensional, square grid. This void fraction data is then converted into an initial bubble size distribution *N(r)* for each grid square by assuming a simplified bi-modal bubble size distribution as shown in figure 7.18.

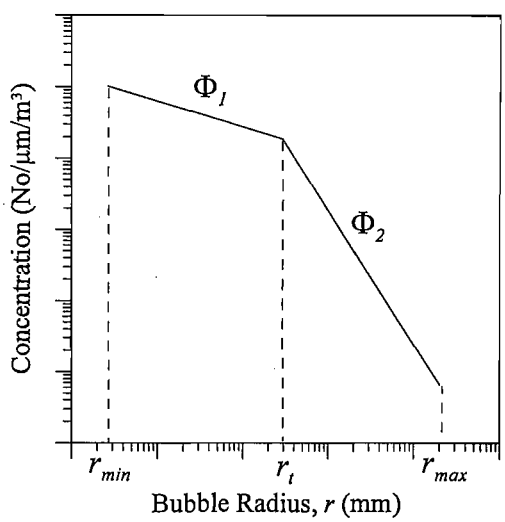

Figure 7.18 Idealised bi-modal bubble size distribution used by the bubble plume evolution model.

The equation for the bubble size distribution is

$$N(r) = A_1 r^{-\phi_1} \qquad \text{for } r<r_t, \tag{7.1a}$$

$$N(r) = A_2 r^{-\phi_2} \qquad \text{for } r>r_t, \tag{7.1b}$$

where A_1 and A_2 are constants.

The values of Φ_1 and Φ_2 can be taken from the results presented in section 6.4.1 or from the previously published results shown in table 2.2. The values of constants A_1 and A_2 for each grid point are dependent on the value of the void fraction

$$\alpha = V_a / V_m = \frac{4\pi}{3V_m} \int_{r_{min}}^{r_{max}} N(r) r^3 dr \tag{7.2}$$

where V_a is the total volume of air within the measurement volume and V_m is the measurement volume.

These initial size distributions are then divided up into a series of individual bubbles which a randomly distributed in space within each grid square. The subsequent evolution of the size and position of each bubble under the influence of turbulence, dissolution, buoyancy and hydrostatic expansion are then calculated based on the expressions detailed below using a finite-difference technique.

Change in Bubble Size due to Bubble Dissolution and Hydrostatic Expansion

Calculations of the change of the bubble radius due to dissolution and hydrostatic expansion are based on the ideal gas equation

$$P_B V_B = NRT\,, \tag{7.3}$$

where P_B is the pressure of the gas within the bubble, V_B is the bubble volume, N is the number of moles of gas within the bubble, R is the molar gas constant and T represents the temperature of the gas in degrees Kelvin.

Derivations of this equation allow the change of bubble radius to be calculated depending on the change of molar content and pressure of the gas within the bubble, given that the temperature remains constant.

The total pressure of all gases within a bubble is

$$P_B = P_A + \rho_w g z + \frac{2\sigma}{r}, \tag{7.4}$$

where P_A is the atmospheric pressure, ρ_w is the density of water and σ is the surface tension.

In this expression, the second term is the contribution due to hydrostatic pressure and the final term is the Laplace pressure due to the curvature of the bubble surface. These factors contribute to the pressure of the gas in the bubble so that in general, the partial gas pressures in the bubble are greater than those of the same gases in air. Because of this effect there is additional transfer of gases when compared to the ocean surface forced by the excess pressure in the bubbles and the extra surface area available for exchange.

In the current model we will consider the temporal evolution of air bubbles entrained in the water column. For simplicity we will follow the assumption of Thorpe (1984) and Weber *et al.* (2005) and assume that air consists of just its two major constituents, oxygen and nitrogen which make up 21.5% and 78.5% of the total molar content respectively. In this situation, the ideal gas law can be applied for each gas in the bubble, where the partial pressures of each gas can be calculated using Dalton's law

$$P = P_1 + P_2 + P_3 + \ldots\ldots P_n. \tag{7.5}$$

Thus, according to the ideal gas law, for each gas constituent, i,

$$P_{Bi} V_B = N_i R T. \tag{7.6}$$

As a bubble rises in the water column it undergoes size changes due to gas flux across the bubble surface and changes in the hydrostatic pressure. The equation describing the rate of change of bubble radius, *dr/dt* can be derived from the ideal gas law. If we assume that the situation is isothermal, the differential form of the ideal gas law is,

$$P_{Bi}\frac{\partial V_B}{\partial t}+V_B\frac{\partial P_{Bi}}{\partial t}=RT\frac{\partial N_i}{\partial t}. \tag{7.7}$$

By substituting the bubble volume

$$V_B=\frac{4\pi r^3}{3}, \tag{7.8}$$

and using equation 7.4, the differential form of the ideal gas law for 2 gases, oxygen (O_2) and nitrogen (N_2) becomes

$$\frac{\partial r}{\partial t}=\frac{RT\left[\frac{\partial N_{O2}}{\partial t}+\frac{\partial N_{N2}}{\partial t}\right]-\frac{4\pi r^3}{3}\rho_w g\frac{\partial z}{\partial t}}{4\pi r^2\left(P_A+\rho_w gz+\frac{2\sigma}{r}\right)-\frac{4\pi r^3}{3}\frac{2\sigma}{r^2}}. \tag{7.9}$$

The last term in the numerator of equation 7.9 describes the expansion of the bubble due to changes in the hydrostatic pressure caused by changes in depth as it rises through the water column. The first term in the numerator of equation 7.9 describes the change in bubble size due to gas diffusion into or out of the bubble and the time rate of change of the molar content N_i for each gas constituent i can be computed based on the following derivation.

The basic equation that governs gas transfer across a gas-liquid interface is a simplification of the Fickian diffusion equation and assumes that the gas and liquid phases are well-mixed reservoirs and a concentration difference is present across a thin boundary layer in each phase. The gas flux due to a concentration difference is

$$F=k_L\Delta C=k_L\left(C-\frac{P_A}{H}\right), \tag{7.10}$$

where F is the gas flux, k_L is the gas transfer velocity, C is the aqueous concentration and H is the Henry's law constant.

The instantaneous diffusion of gases between a bubble and the surrounding water is controlled by transfer through a concentration boundary layer with a thickness that is comparable to the bubble size and is complicated by the bubbles curved surface, finite volume and buoyant rise through the water column. By integrating equation 7.10 over the bubble surface, we get the bubble mass flux, F_i which is equal to the change in the molar content for gas i per second

$$\frac{\partial N_i}{\partial t} = F_i = k_{Bi} 4\pi r^2 \left(C_i - \frac{P_{Bi}}{H_i} \right), \tag{7.11}$$

where k_B is the individual bubble gas transfer velocity and P_{Bi} is the partial pressure of gas i in the bubble. According to this equation, the system is in equilibrium when $H_iC_i=P_{Bi}$, when $H_iC_i<P_{Bi}$, the gas invades the ocean and a reduction in the bubble size occurs and this is generally the case for bubbles in water because of the increased pressure inside the bubble due to hydrostatic pressure and surface tension.

It is assumed that the concentration of nitrogen and oxygen in the upper ocean is equivalent to saturated conditions at the surface, thus the aqueous concentration of oxygen and nitrogen can be written as

$$C_{O2} = \frac{P_{0,O2}}{H_{O2}}, \tag{7.12a}$$

and

$$C_{N2} = \frac{P_{0,N2}}{H_{N2}}, \tag{7.12b}$$

where $P_{0,O2}$ and $P_{0,N2}$ are the partial pressures of oxygen and nitrogen at sea level. For the current calculations, the aqueous concentrations are taken from Weber *et al.* (2005) who give values of 0.2203 mol/m^3 for oxygen and 0.4067 mol/m^3 for nitrogen.

Weber *et al.* (2005) suggest the following formula for the individual gas transfer velocity based on the expression for the total mass diffusion at low Reynolds numbers given by Levich (1962)

$$k_B = 2\sqrt{\frac{1}{2\pi}\frac{D_i v_B}{r}}, \tag{7.13}$$

where v_B is the differential velocity between the bubble and the surrounding fluid which is assumed to be equal to u_r, the buoyant rise velocity. The diffusion coefficients, D_i for each gas constituent are taken from Wise & Houghton (1966) and are equal to 2.3 x 10^{-9} m^2/s and 2.6 x 10^{-9} m^2/s for oxygen and nitrogen respectively. This expression for the transfer velocity is valid only for "clean" bubbles which retain a mobile surface. Bubbles in the ocean are generally considered to become "dirty" soon after their creation, causing their skins to become immobilised and significantly reducing the gas transfer rate. However as the current study is concerned with the dense, highly transient bubble plumes generated directly beneath breaking waves it was suggested that the bubble behaviour during the period of interest would approximate that of "clean" bubbles (D. Woolf, pers. comm.).

Bubble Rise Velocity

The rise speed of bubbles was calculated according to the "clean" bubble parameterisation of Leifer & Patro (2002).

Newly formed bubbles accelerate to a terminal rise velocity u_r which is determined by the balance between the buoyancy and drag forces within a few milliseconds (Park *et al.*, 1995). Small bubbles associated with low Reynolds numbers ($\mathrm{Re}=2ru_r/\nu_a$) are assumed to be spherical and non-oscillating, and as such their rise velocity u_r can be calculated explicitly using the Hadamard Rybczynsky modification of Stokes's Law

$$u_r = \frac{2}{3}\frac{gr^2\left(\rho_w - \rho_g\right)}{\mu_B}\left(\frac{1+\kappa}{2+3\kappa}\right), \tag{7.14}$$

where ρ_g is the gas density in the bubble ρ_w is the density of water and κ is the viscosity ratio ν_g/ν_ω, where ν_g and ν_w are the kinematic viscosities of the gas and water respectively.

As the bubble radius increases (Re>20), the flow around the bubble becomes increasingly asymmetric, leading to flow separation and bubble deformation. Experimental results have shown that equation 7.14 is only valid for r<60 μm. A modification is needed for larger bubbles (Leifer *et al.*, 2000) and a completely different form is required when Re>400 and bubbles begin to oscillate as they rise. For non-oscillating bubbles, Leifer & Patro (2002) parameterised u_r by fitting a modified version of equation 7.14 to the parameterisation of u_r presented by Clift *et al.* (1978)

$$u_r = \frac{1}{3} agr^b \nu_w^{\ m}, \tag{7.15}$$

where a and b are coefficients and $\nu_\omega^{\ m}$ describes the temperature dependency. The value of m was calculated by Leifer & Patro (2002) using a least-squares regression analysis of m with r from observed and theoretical values and was found to be

$$m = 10.52r - 1.04. \tag{7.16}$$

Thus the temperature dependency decreases with increasing bubble radius.

A second least-squares analysis was performed by Leifer & Patro (2002) using data from Clift *et al.* (1978) and Leifer *et al.* (2000) to calculate values of the constants a and b and these are shown in table 7.3 for different ranges of radius r.

Table 7.3 Bubble rise velocity coefficients for non-oscillating bubbles from Leifer & Patro (2002).

Re	r (μm)	a	b
<1	<60	1.00	2.00
1-35	60-275	0.75	2.00
35-120	275-475	50.67	3.17
120-425	475-665	75150	5.57
425-520	665-785	1277	4.07
520-540	785-900	5042	4.61

The peak radius r_p at which bubbles begin to oscillate as they rise is dependent on the Reynolds number and temperature. For example, at a temperature of 20°C, bubbles begin to oscillate at Re≈400 which is equivalent to a peak radius r_p of 670 μm. The value of the peak radius r_p in μm was given by Leifer *et al.* (2000) as

$$r_p = 1086 - 16.05T_p, \tag{7.17}$$

where T_p is in °C and in the range $0<T_p<35$°C.

When $r>r_p$, bubbles oscillate as they rise through the water column and a different form to that presented in equation 7.15 is required for the calculation of the bubble rise velocity. The parameterisation shown in equation 7.18 was developed by Leifer *et al.* (2000) from observations of oscillating bubbles and is in good agreement with the results of Clift *et al.* (1978). Equation 7.18 is applicable for oscillating bubbles and is valid for $0<T<30$°C and $r_p<r<4000$ μm

$$u_r = \left(u_{rm} + j_1\left(r - r_c\right)^{m_1}\right)e^{\left(j_2 T\left(r-r_c\right)^{m_2}\right)}. \tag{7.18}$$

The values of j_1, j_2, m_1, m_2, u_{rm} and r_c are given in table 7.4.

Table 7.4 Bubble rise velocity coefficients for oscillating bubbles from Leifer & Patro (2002).

Parameter	Value
r (μm)	$r_p<r<4 \times 10^3$
j_1	0.733
j_2	4.792×10^{-4}
r_c	0.0584
u_{tm}	22.16
m_1	-0.849
m_2	-0.815

For bubbles with a radius greater than 4000 μm, a constant rise velocity of u_r=0.25 ms^{-1} was used in agreement with Woolf (1993).

Thorpe *et al.* (2003) state that the mean rise speed of bubbles within a plume differs from that of a single bubble and present a correction to account for this effect

$$u_{rp} = u_r\left(1-6.55\alpha\right), \tag{7.19}$$

where u_{rp} is the mean rise speed of a bubble within a bubble plume and α is the local void fraction.

Turbulence

A simple approximation of turbulence within the water column after the passage of a breaking wave is simulated using a random walk model as used by Thorpe (1984), Woolf & Thorpe (1991) and Leifer (1995). It is accepted that random walk turbulence is not physically valid for modelling the flow beneath breaking waves, however it is thought to be sufficient for the purpose of the model described here.

Turbulence in the model is simulated by displacing each bubble through a distance L_b in a random direction θ at each timestep, where the value of L_b is randomly chosen from a normal distribution with a mean and standard deviation equal to L. The value of L is calculated based on a chosen effective turbulent diffusion coefficient K_v

$$K_v = \frac{L^2}{4\Delta t}, \tag{7.20}$$

where Δt is the model timestep.

Thorpe (1984) suggested that the value of K_v was in the range 64 to 320 cm^2s^{-1} for breaking waves in the ocean. Thus the position of each bubble calculated at each timestep based on the bubble rise velocity described above is adjusted by the following horizontal and vertical displacements

$$\Delta x = L_b \sin\theta, \tag{7.21a}$$

$$\Delta z = L_b \cos\theta. \tag{7.21b}$$

7.4.3.2 Comparison of the Model Predictions to Measured Data

To assess the accuracy of the model at predicting the evolution of the void fraction distribution within bubble plumes generated by breaking waves, the model was compared with measured void fraction data from the natural seawater case described above. Measured data on a 0.02 m grid was used for the initial void fraction distribution taken from the time when the penetration depth was a maximum, t_{p0}. It should be noted that in order to avoid the effects of surface waves, the grid does not extend right up to the free surface, but only to a depth of 0.02 m below the still water level.

The values of the other parameters required by the model are discussed below and presented in table 7.5. The spectral slopes of the bubble size distribution, Φ_1 and Φ_2 and the transition point between the two slopes d_{trans} were taken from the data of Deane & Stokes (2002). It was tempting to use the slopes presented in chapter 6, however these were measured in freshwater and while observations suggested that the size distributions in fresh and seawater were similar, the data of Deane & Stokes (2002) was used to ensure that the additional small bubble population was taken into account. The maximum bubble size d_{max} in the model was also taken from Deane & Stokes (2002), but the small bubble end of the distribution d_{min} was extended to include the

very small bubbles (d=60 μm) measured in seawater breakers by Terrill & Melville (2000), Farmer *et al.* (1998), Phelps *et al.* (1997) and Phelps & Leighton (1998).

Table 7.5 Parameters used for validation of the numerical bubble model.

Parameter	Value
Φ_1	-1.5
Φ_2	-10/3
d_{trans} (μm)	2000
d_{min} (μm)	60
d_{max} (μm)	20000
K_v (cm^2/s)	10

The model results are presented in figure 7.19 along with the measured data at various intervals during the rise phase of the bubble plume starting at time t_{p0}, when the plume is at its maximum penetration depth. It should be noted that the model does not account for the slow horizontal drift that the plume experiences during the rise phase in the laboratory, however it is seen that the model compares well with the measured data and captures the main features of the time-varying void fraction distribution. The major notable difference between the two plots is that the plume rises slightly faster in the model than in the measured data. This is thought to be because in the laboratory case, a limited number of bubbles continue to be carried downwards into the plume even after the maximum penetration depth has been reached which slows the mean rise speed of the plume. Closer agreement with the measured data can be achieved if a "dirty" bubble formulation for the bubble rise velocity is used, however it was suggested by D. Woolf (pers. comm.) that the "clean" bubble equation was more physically valid in the dense, transient bubble plumes generated immediately beneath breaking waves.

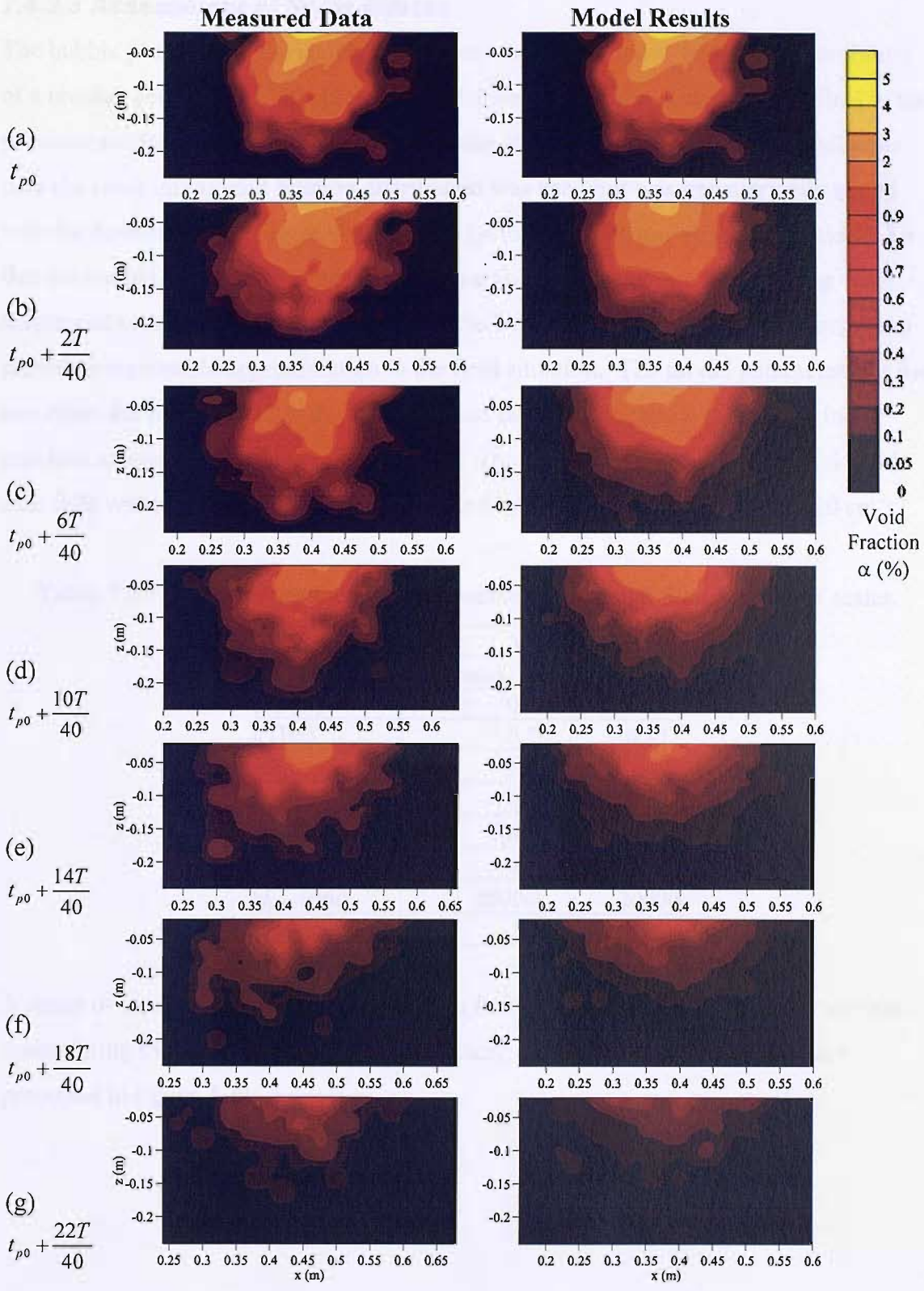

Figure 7.19 Comparison of model results and measured laboratory data at various times during a single wave period. Measured data is taken from the seawater laboratory data discussed in this chapter.

7.4.3.3 Assessment of Scale Effects

The bubble plume model described above was used to examine the temporal evolution of a breaker generated bubble plume at model and field scale. The case described in the previous section was used to represent a plume at model scale, while for the full scale case the same initial void fraction distribution was used but was geometrically scaled with the breaking wave height using a scale factor of 20. It was shown in section 4.3.4 that the bubble penetration depth is at least partially dependent on the breaking wave height and so a direct geometric scaling of the bubble plume dimensions is assumed to provide a reasonable approximation to the field situation. The model parameters for the two cases are predominantly the same as those used for the model calibration in the previous section and are shown in table 7.6. The chosen value of K_v for the field scale case falls within the range of values suggested by Thorpe (1984) of $64<K_v<320$ cm^{2}s^{-1}.

Table 7.6 Parameters used to compare bubble plume evolution at different scales.

Parameter	Value	
	Model	**Field**
H_b (m)	0.1	2.0
f (Hz)	0.7	0.157
Φ_1	-1.5	-1.5
Φ_2	-10/3	-10/3
d_{trans} (μm)	2000	2000
d_{min} (μm)	60	60
d_{max} (μm)	20000	20000
K_v (cm^2/s)	10	200

A series of contour plots of the void fraction field at model and field scale for various times during the plume evolution were produced using the bubble model and are presented in figure 7.20.

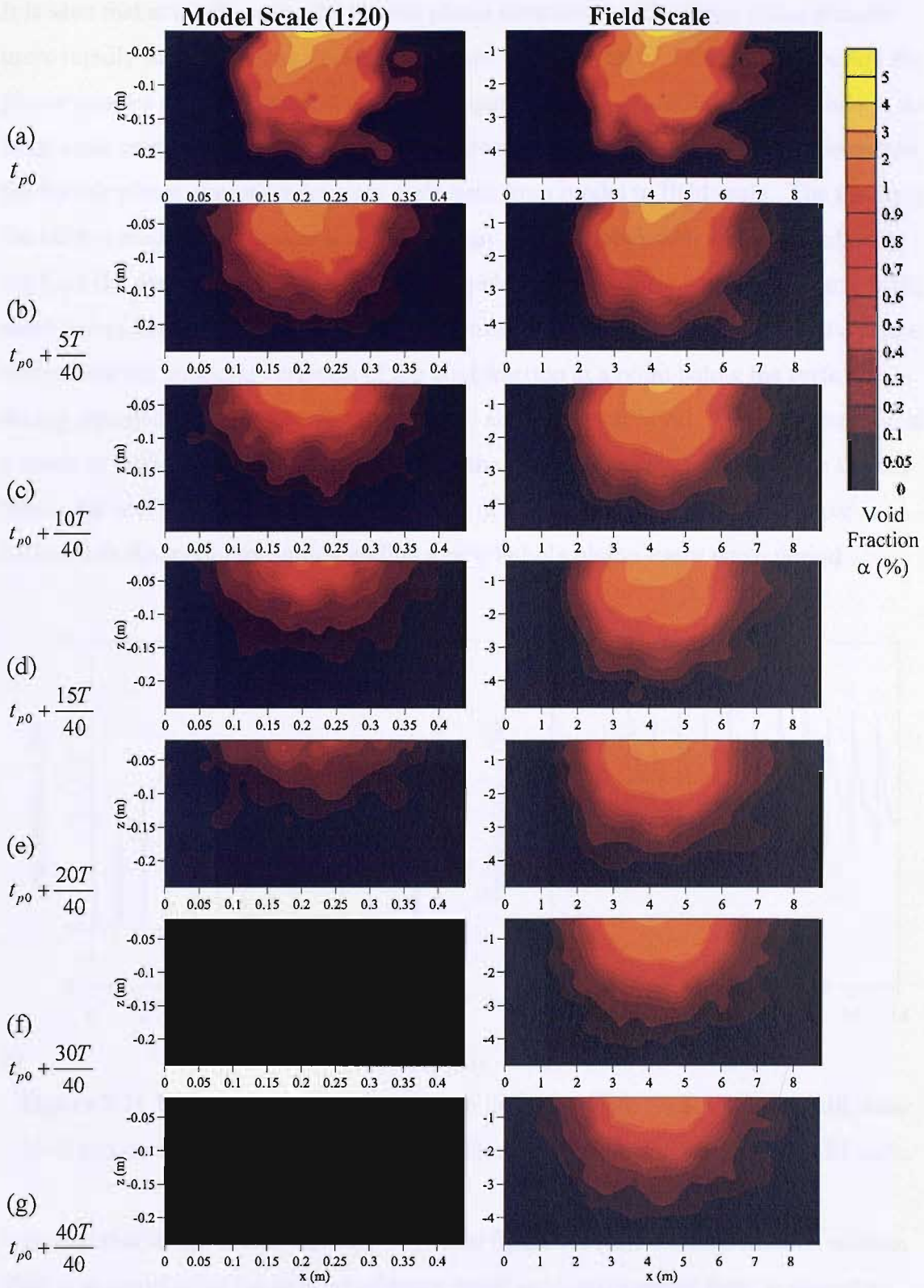

Figure 7.20 Void fraction distributions at various times during a single wave period at model (1:20) and field scale calculated using the bubble plume evolution model.

It is seen that at model scale, the bubble plume rises through the water column much more rapidly than in the large scale case. Indeed by the end of a single wave period the plume appears to have almost completely dispersed in the model scale case, while in the large scale case a significant plume still remains. Thus the bubble model confirms that the bubble plume evolution does not scale well from model to field scale. The results of the bubble model also suggest that a significant bubble population will accumulate in the field if a series of waves break at the same location, such as when a group of similar sized waves break on a submerged reef. To examine this phenomenon, it is informative to examine the temporal variation of the void fraction at a point below the surface during repeated breaking events. Figure 7.21 shows the variation of the void fraction at a depth of $H_b/5$ below the still water line on the centreline of the bubble plume in both the model and large scale cases over a series of 14 identical waves. A new wave is included in the model by simply adding a new bubble plume every wave period.

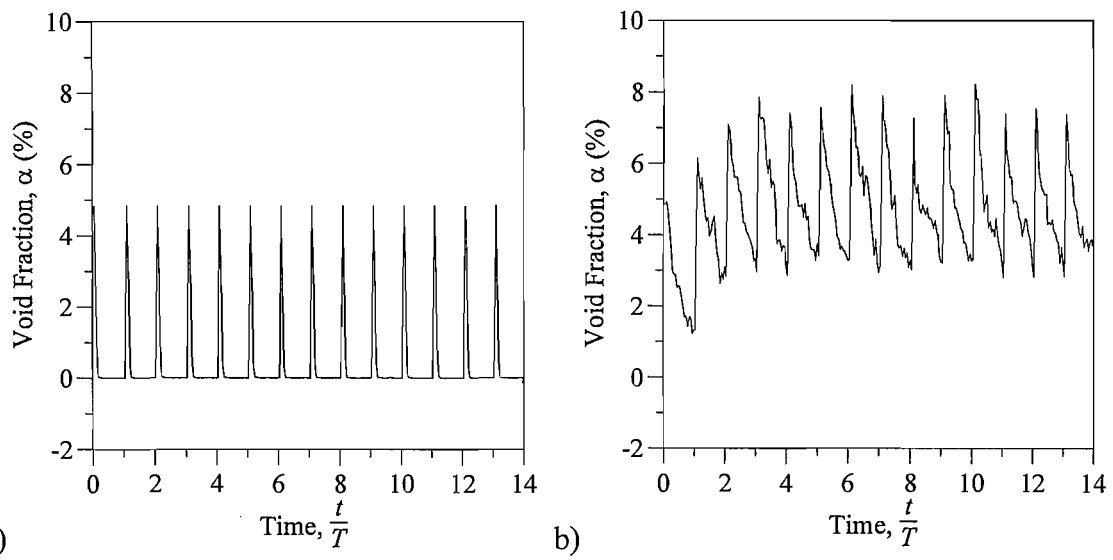

Figure 7.21 Variation of void fraction with time at a depth $H_b/5$ below the still water level and on the centreline of the bubble plume at **(a)** model scale and **(b)** field scale.

It is seen that in the small scale case shown in figure 7.21(a), the void fraction reduces almost to zero during the passage of every wave and consequently there is almost no accumulation of air over repeated waves. This is consistent with observations made during the experiment described above, where only a small population of fine bubbles which had a negligible contribution to the total void fraction was seen to accumulate with time over repeated breaking events. By contrast, figure 7.21(b) shows that in the

field scale case the volume of air in the water column accumulates over the first 3 wave periods and the void fraction reaches a maximum value that is almost twice as great as the initial value. After the first three breaking events, a constant ambient void fraction has been entrained into the water column and the value of α does not fall below 2.35%. This is of the same order of magnitude as the measurements of Bullock *et al.* (2001) who found that the mean ambient void fraction in front of a breakwater exposed to repeated breaking waves was 8.4%. Consequently, this analysis explains the white, aerated appearance of the ocean surface after a series of repeated breaking waves in the surf zone (figure 7.17) and shows that high volumes of air can accumulate beneath the free surface.

The discussion presented in this section has implications for the applicability of results from small scale physical models of breaking waves to field conditions. The results from the experiment described in section 7.3 showed that the differences between air entrainment by breaking waves in freshwater and seawater were small and thus in most cases, physical model tests using freshwater should be reasonably applicable to seawater conditions at the same scale. The discussion presented in this section suggests however that due to the similar bubble sizes likely to be present at all scales, the evolution of the bubble plume after entrainment and hence the average level of aeration in the region of breaking waves is far more dependent on the scale of the breaking wave than the water type. As it has been shown by previous authors that the presence of air can significantly affect wave impact pressures (Bullock et al., 2001; Peregrine, 2003), this result may have considerable effects on laboratory models of engineering structures and so scale effects on air entrainment should be taken into account by future researchers.

7.5 DISCUSSION AND SUMMARY

Chapter 7 describes a series of comprehensive measurements of the time-varying void fraction field beneath laboratory breaking waves in artificial and natural seawater and compares them with the freshwater data presented in chapter 5. To this author's knowledge, these measurements represent the first attempt to examine the distribution of entrained air and the spatial and temporal variations of the bubble plumes generated by laboratory breakers in seawater. As the majority of laboratory tests of coastal

processes are completed using freshwater, the information presented in this chapter is highly important as it helps to assess the validity of such experiments. In addition to the void fraction measurements, this chapter provides a discussion of the issues involved in scaling air entrainment in breaking waves from laboratory models to field conditions.

A large amount of work has been presented in this chapter, and the primary conclusions that have been drawn from it are listed below.

1. Analysis of the wave field both upstream and downstream of the reef crest suggests that the waves transmitted downstream of the reef crest after wave breaking are very similar in fresh and artificial seawater and there is no significant difference in the energy dissipated during breaking in the two liquids at the scale of the current measurements.

2. Observations of the bubbly flow generated by laboratory breakers in natural and artificial seawater in the current experiments suggest that the process of air entrainment is very similar to that in freshwater discussed in chapters 5 and 6. In all three cases, air is initially entrained predominantly in the form of large air cavities which are subsequently broken into smaller bubbles as they are driven into the water column.

3. While no measurements of bubble size were made, observations of the bubble plumes suggested that the bubbles generated in the main plume in freshwater and natural and artificial seawater are of a similar size and relatively large bubbles with diameters of the order of 1 mm or greater are visually predominant. However in the two seawater solutions, an additional population of fine bubbles becomes apparent during the rise phase as the large bubbles rise out of the water column. The slow rise velocity of these small bubbles leads to an accumulation of fine bubbles in the region of breaking waves. These bubbles are so small and not sufficiently numerous that they do not contribute significantly to the total volume of entrained air, but their presence will make a difference to the compressibility of the water.

4. A noticeable amount of surface foam which remained present for durations greater than a single wave period was observed in the two seawater cases. The increased presence of foam at the surface in seawater breaking waves was explained by Scott (1975) who showed that bubbles in seawater are stabilised by the presence of salt once they have reached the surface and thus can persist for long periods, while freshwater bubbles burst rapidly upon reaching the surface.

5. The optical fibre probe technique described in chapter 5 was used to produce contour plots of the time-varying void fraction field for the three different water solutions. These plots were very similar at all times and suggest that there are no significant differences in the distribution of entrained air or the temporal and spatial evolution of the bubble plume for the three test cases.

6. A number of integral properties of the void fraction field were calculated in order to examine the temporal variation of different aspects of the bubble plume, including the volume of entrained air, the horizontal and vertical movement of the plume centroid and the cross-sectional area. It was seen that in all cases, the bubble plumes behaved in a very similar manner. In particular it was found that an almost identical volume of air was entrained by the breaking waves in all three water types.

7. A discussion of the issues involved in applying small scale measurements of air entrainment to field conditions concluded that the total volume of air entrained should scale geometrically but the bubble size distribution would not scale and approximately the same absolute bubble sizes should be expected at all scales.

8. In order to investigate the effect of scale on bubble plume evolution, a two-dimensional, Lagrangian, finite-difference model which traces individual bubbles and incorporates the effects of turbulent diffusion, bubble dissolution, buoyancy and hydrostatic bubble expansion was developed. This model was shown to provide good predictions of the evolution of the void fraction distribution within a bubble plume when compared to measured data from the seawater case described in this chapter.

The bubble model was used to examine the evolution of a bubble plume over the course of a single wave period at model scale (1:20) and field scale. The results showed that at model scale the bubble plume almost entirely dispersed within a single wave period, while in the full scale case a significant volume of air remained. Further analysis showed that over repeated wave breaking events, an ambient void fraction which did not fall below 2.35% accumulated at a depth of $H_b/5$ in the full scale case, while at model scale the void fraction at the end of each wave period was close to zero. It is suggested therefore that while the experiment described in section 7.3 showed that in most cases, physical model tests using freshwater should be reasonably applicable to seawater conditions, the variation in bubble plume evolution after entrainment and hence the average level of aeration in the region of breaking waves is far more dependent on the scale of the breaking wave than the water type and this should be taken into account by future researchers.

CHAPTER 8 – CONCLUSIONS AND FURTHER WORK

8.1 CONCLUSIONS

This thesis has reported on a series of laboratory experiments designed to examine air entrainment, splash-up and energy dissipation in breaking waves. The findings of the experiments conducted during this study have been discussed within each chapter and the following summarises the main conclusions that have been drawn from this work.

Breaking waves are the predominant source of air entrainment in the oceans, charging the surface layer with a plume of bubbles which rapidly evolves in time and space. The presence of bubbles at the ocean surface is an important factor in a large number of physical processes, including the enhancement of gas transfer across the air-sea interface. While the importance of air entrainment by breaking waves is understood, knowledge of the mechanisms involved and detailed quantitative information is limited due to the complexity of the wave breaking process and the difficulties in making suitable measurements. The main focus of this study was to make use of a novel measurement technique to provide quantitative information about the air volume entrained by breaking laboratory waves. The properties examined include the evolution of bubble sizes and the time-dependent distribution of the entrained air volume during the period immediately after breaking, when large volumes of air are present in the form of a concentrated bubble plume. In addition, the energy dissipated by breaking waves was examined and estimates were made of the contribution of the processes of air entrainment and splash to the total dissipation.

The first series of experiments were designed to provide information about the energy dissipated by waves breaking over a submerged reef and its relationship with the incident wave conditions and the wave breaking intensity. These tests provided a large amount of quantitative information about the nature of wave breaking over low gradient submerged slopes which will be of interest to those designing submerged coastal

structures, or examining wave breaking on natural reefs and sandbars. They also provided an understanding of the experimental conditions used for subsequent tests on air entrainment.

Measurements of the transmitted wave field after waves broke over the crest of a submerged reef demonstrated that for given incident wave conditions, the proportion of wave energy dissipated during breaking increases systematically within the range 17% to 86% as the water depth above the reef crest decreases. A corresponding increase in the intensity of the wave breaking event was also observed as the water level was reduced, suggesting that there is a relationship between the violence of wave breaking and the total energy dissipation during wave breaking.

To provide a quantitative parameter to describe the intensity of breaking waves, measurements were made of the dimensions of the vortex enclosed between the overturning jet and the wave face. It was found that the area of the vortex, normalised by the square of the breaking wave height provided a suitable parameter to describe breaking intensity and measurements showed that for a wave with constant deepwater properties this parameter increased as the water depth over the crest of the submerged reef was reduced and the violence of breaking increased. Using the vortex area as a measure of the breaking intensity, it was seen that there is a relationship between the energy dissipated by wave breaking and the violence of wave breaking and waves with identical deepwater conditions broke more intensely and dissipated more energy as the water depth was reduced, providing support for the suggestion made in the previous paragraph. As the majority of the air volume contained within the vortex enclosed by the overturning jet is subsequently entrained into the water column, these results suggest that air entrainment by this mechanism becomes more significant as the wave breaking intensity and energy dissipation increases. A corresponding increase in the maximum bubble entrainment depth with increasing energy dissipation and breaking intensity was also observed. These results support the conclusions of previous authors that part of the wave energy dissipated during breaking must be accounted for by the work done against the buoyancy of bubbles and suggest that the contribution of the air entrainment mechanism to the total energy dissipated at breaking becomes more significant as the breaking intensity increases. Further support for this relationship was obtained from the void fraction measurements described in chapter 5.

In an extensive laboratory programme, detailed measurements were made of the time-varying void fraction field in the dense, rapidly varying bubble plumes entrained immediately beneath breaking waves using a novel optical fibre probe technique. The optical fibre probes were found to perform well in the violent flow and dense bubble plumes generated by breaking waves and allowed comprehensive measurements of void fractions beneath breaking laboratory waves to be made. In addition, the probes allowed measurements to be taken in the splash region above the free surface, as far as this author is aware for the first time. The results from these aeration measurements were used to produce contour plots of the phase-averaged void fraction over a large spatial domain at intervals of $T/40$ for three different wave cases. These plots were found to correctly capture the spatial and temporal variations of the two-phase flow in the region of breaking waves and demonstrated the rapid evolution of the bubble plume and splash-up.

The variation of some of the flow characteristics, including the areas of the bubble plume and splash-up and the movements of their centroids were examined by taking moments of the void fraction distribution. In general, it was found that the bubble plumes and splash-up volumes behaved in a similar manner for all wave cases, although some quantitative differences were observed. Previous authors had assumed that the temporal evolution of the bubble plume would scale with the wave period, but this was found not to be the case. Once entrained, the properties of the bubble plume had little or no dependence on the surface wave motion. Instead, an alternative scaling using the characteristic time of bubble detrainment was found to be more satisfactory and produced excellent results.

Calculations of the total volumes of the air and splash showed that the maximum values of the splash volume were of the same order as the peak volumes of air in all cases. The peak volume of entrained air normalised by the volume of the vortex enclosed between the underside of the plunging jet and the wave face V_p/V_v varied between 1.3 and 1.6, which is greater than the result of $V_p/V_v=1$ presented by Lamarre (1993). These measurements indicate that the breakup of the vortex of air enclosed beneath the overturning jet contributes significantly to the total volume of air entrained during wave breaking (between 62% and 74% in the current tests) and that this mechanism of air

entrainment is more important in strongly plunging breakers where the size of the vortex is relatively large, than in spilling breaking waves.

The work required to entrain bubbles against buoyancy makes some contribution to the total energy dissipated at breaking. Measurements of the potential energy of the entrained bubble plume showed that a minimum of 2.5% to 5% of the incident wave energy was dissipated in this way and the proportion increased with the intensity of the breaking event. Thus it is concluded that as the size of the vortex enclosed beneath the overturning jet increases with the breaking intensity, a higher proportion of the total volume of air will be entrained by submergence and breakup of this air volume and the energy dissipated by air entrainment will increase.

Based on measurements of the total energy dissipation made during the first series of experiments, it was seen that the energy expended in entraining air bubbles against buoyancy in the current tests accounted for a minimum of 4%, 6% and 9% of the total energy dissipated during wave breaking for the spilling, plunging and strongly plunging wave cases respectively. These values are considerably smaller than those of previous authors who estimated that air entrainment was responsible for between 20% (Hoque, 2002) and 30% to 50% (Lamarre, 1993) of the energy dissipated at breaking.

The work required to elevate the water in the splash-up generated at breaking must also contribute to the total energy dissipation. Measurements of void fraction in the splash region made using the optical fibre probe technique suggest that this mechanism accounts for a minimum of approximately 3.5% of the incident wave energy for both of the plunging wave cases under examination, and 1.7% for the spilling wave case. These values correspond to 2.5% of the total energy dissipated during breaking for the spilling wave case and 5% for the two plunging waves. To this author's knowledge, these are the first estimates of the direct contribution of splash generation to the total energy dissipated during wave breaking and suggest that the dissipation due to splash becomes more significant as the breaking intensity of the wave increases.

The measurements discussed above suggest that air entrainment and the generation of splash make an important contribution to the total energy dissipated during wave breaking. However, as the dissipation due to air entrainment and splash measured in the

experiments described in chapter 5 accounts for less than 20% of the total dissipation during breaking, it is clear that these are not the dominant mechanisms of dissipation and further work should examine the contributions of other processes in detail, in particular the generation of turbulence.

The optical fibre probes were also used to make measurements of the bubble size distributions in the dense bubble plumes entrained directly beneath both spilling and plunging laboratory waves in freshwater. Previous measurements of bubble sizes in this region have been restricted by the practical difficulties of making reasonable estimates in such a complex and rapidly varying two-phase flow. The optical fibre probes were found to perform well and produced reasonable measurements of bubble size which agreed well with flow visualisations. The good performance of this novel technique represents a significant advance, allowing the spatial variation of the bubble size distribution in the concentrated initial bubble plume to be examined in detail.

The measurements showed that the bubble size distribution in the large bubble range (d>2.4 mm) followed an obvious power law scaling in agreement with the findings of previous investigators. The exponent of the power law scaling Φ_2 decreased with distance from the active entrainment region and varied in the range $-1.4<\Phi_2<-3.15$ for a strongly plunging wave case and $-2.1<\Phi_2<-2.9$ for a spilling wave. The low gradient of the distribution close to the active entrainment region occurs because at this point there is a high proportion of large bubbles and air cavities formed by the breakup of the vortex, particularly in plunging waves. Further away from the region of active entrainment, the exponent of the power law scaling decreases as the larger bubbles break up or rise back to the surface and Φ_2 approaches the theoretical value of -10/3 presented by Garrett *et al.* (2000). A distinct change in the slope of the bubble size distribution plotted on a log-log scale was evident at a bubble diameter of between 1.7 and 2.4 mm. It is concluded that this change in the gradient of the distribution corresponds to the Hinze scale as suggested by Deane & Stokes (2002). Further measurements showed that the proportion of small bubbles present in the plume increases with time as larger bubbles break up or rise back to the surface. This temporal variation of bubbles sizes leads to a gradual increase in the gradient of the bubble size distribution with time, in agreement with the theoretical model of Garrett *et al.* (2000).

The concept of "plume age" was introduced in order to bring together the measured temporal and spatial evolution of the gradient of the bubble size distribution, where the plume age increases with distance and/or time away from the point of active air entrainment. Due to the difficulties in accurately measuring the plume age in the complex two-phase flow conditions, the mean void fraction at a point in the bubble plume α_m was used to approximate this value. The results demonstrated a systematic increase in the power law scaling with increasing void fraction as the measurement location moved closer to the point of active air entrainment. Encouragingly, the data from both plunging and spilling wave cases collapsed well onto a single curve, suggesting that α_m provides a good approximator for plume age independent of the breaker type.

Measurements of the void-fraction distribution in the dense bubble plumes entrained beneath breaking waves in artificial and natural seawater were completed and compared with the freshwater data discussed above. Knowledge of any differences in air entrainment in fresh and seawater is essential for assessing the validity of experimental models of oceanic processes which are almost always conducted in freshwater. In fact observations suggested that the process of air entrainment and the subsequent behaviour of the entrained bubble plume is very similar to that in freshwater. This was confirmed by measurements of the void fraction field made using the optical fibre probes which showed that the position of the plume centroid, the plume area, the mean void fraction and the total volume and distribution of air within the plume varied with time in an almost identical manner in all three test cases.

While no bubble size measurements were made, observations suggested that the bubbles generated in the main bubble plume in freshwater and natural and artificial seawater are of a similar size, and relatively large bubbles with diameters of the order of 1 mm or greater are visually predominant. However in the two seawater solutions, an additional population of fine bubbles became apparent during the rise phase of the bubble plume as the large bubbles rose back to the free surface. Owing to their slower rise velocity, there is an accumulation of fine bubbles in the region of wave breaking, though they are too small and not sufficiently numerous to contribute significantly to the total volume of

entrained air. It was concluded that due to the small differences between air entrainment by breaking waves in fresh and seawater, in most cases physical model tests using freshwater should be reasonably applicable to seawater conditions. However for problems where the compressibility of water is a consideration the use of freshwater will have a significant effect due to the reduced accumulation of fine bubbles over repeated breaking events.

The problem of applying small scale measurements of air entrainment to field conditions was also examined. It was concluded that the total volume of entrained air per unit width should scale geometrically with the square of the wave height, but that approximately the same bubble sizes would be expected at all scales and therefore the characteristic time scale of the bubble plume would not scale with the wave period. To investigate the effect of scale on bubble plume evolution, a two-dimensional, Lagrangian, finite-difference bubble tracking model was developed. This model was used to examine the evolution of a bubble plume over the course of a single wave period at model scale (1:20) and field scale. The results demonstrated that at model scale the bubble plume almost entirely dispersed within a single wave period, while in the full scale case a significant volume of air remained. Further analysis showed that over repeated wave breaking events, an ambient void fraction which did not fall below 2.35% accumulated at a depth $H_b/5$ in the full scale case, while at model scale the void fraction at the end of each wave period was almost zero. It is suggested therefore that while the fresh and seawater measurements described above showed that in general, physical model tests using freshwater should be reasonably applicable to seawater conditions at the same scale, the variation in bubble plume evolution after entrainment and hence the average level of aeration in the region of breaking waves is far more dependent on the scale of the breaking wave than the water type and this should be taken into account by future researchers.

In summary, this thesis has presented measurements of properties of the dense bubble plumes generated by laboratory breaking waves in freshwater and seawater to a resolution that has not previously been achieved. These results confirm the applicability of optical fibre phase detection probes for making measurements in breaking waves and provide a large amount of new information about the two-phase flow generated by wave breaking. In particular, the current work presents high quality measurements of the

distribution of the air entrained and splash generated by breaking waves as they vary with time and discusses the contribution of these mechanisms to the total energy dissipated during wave breaking.

8.2 FURTHER WORK

The experiments completed in chapter 4 provided interesting new information about wave transmission over submerged, low gradient coastal structures. In order to extend these results to provide guidance for the design of such structures, it would be useful to repeat the measurements over a range of reef gradients using both regular and irregular waves.

The optical probe measurement technique described in this thesis proved to be highly effective for making measurements of void fraction in the bubble plumes entrained by small scale breaking waves in the laboratory, although it is noted that development of a technique to allow the instruments to be calibrated over the full range of void fractions from 0% to 100% would be highly beneficial. However, it was found that the evolution of the bubbly flow entrained by wave breaking is subject to significant scale effects and this can have implications for the applicability of small scale models to full scale oceanic processes. It is suggested that the same optical fibre probe technique could be successfully used to provide similar void fraction data in the field and/or in a large scale laboratory facility. The information obtained from these studies would allow the effect of scale on air entrainment in breaking waves to be examined in more detail and enable further assessment of the validity of laboratory measurements made at small scale.

By taking moments of the void fraction field about the 50% void fraction contour to calculate the variation in the potential energy of the bubble plume and splash-up it was shown that entrainment of air and generation of splash accounted for a minimum of 6.5% to 14% of the total energy dissipated during wave breaking for the wave cases under examination. It is clear therefore that while these processes provide a significant contribution to the total dissipation, they are not the dominant mechanisms for the wave cases examined in this study and further work should examine the contributions of other processes in detail, with particular focus on turbulence generation.

The applicability of optical fibre probes for making bubble size measurements was demonstrated by the experiment described in chapter 6 which presents detailed measurements of the bubble size distribution in the dense bubble plumes entrained beneath breaking waves in freshwater. However, due to the limited time that seawater could be kept in the laboratory it was not possible to make measurements of the bubble sizes using the optical fibre probes. In order to provide confirmation of the observations made in the current study that the bubble sizes in freshwater and seawater are generally comparable but that an additional population of very fine bubbles exists in seawater, it is suggested that the bubble size measurements presented in chapter 6 could be repeated using seawater. The optical fibre probe technique could also be used to measure bubble sizes in breaking waves at different scales to allow an assessment of the suggestion made in section 7.4.2 that the distribution of bubble sizes beneath breaking waves is approximately constant at all scales.

As it has been noted by previous authors (Slauenwhite & Johnson, 1999) that the biological content of seawater can have an effect on bubble sizes, it is suggested that future experiments using seawater should include an assessment of the biological activity such as a Biochemical Oxygen Demand (BOD) or Chemical Oxygen Demand (COD) test in addition to a chemical analysis.

At present, no complete model of air entrainment in breaking waves exists, owing to the complex nature and lack of existing knowledge of the individual processes involved. While achieving a comprehensive model of this phenomenon is still some way off, such a model would represent a significant contribution and it is suggested that work in this area would be very valuable. This thesis has presented a large amount of detailed information which describes the nature of the two-phase flow in the region of breaking waves and this data will be useful for the validation of future models.

LIST OF REFERENCES

Abadie S, Caltagirone J-P & Watremez P. 1998. Splash Generation in a Plunging Breaker. *Computational Fluid Mechanics* 326: 553-559.

Agrawal YC, Terray EA, Donelan M, Hwang PA, Williams III AJ, Drennan WM, Kahma KK, Kitaigorodski SA. 1992. Enhanced Dissipation of Kinetic Energy Beneath Surface Waves. *Nature* 359: 219-220.

Ahrens JP. 1987. Characteristics of Reef Breakwaters. *Technical Report CERC-87-17*, WES, CERC, Vicksburg.

Allsop NHW. 1983. Low-crest Breakwaters, Studies in Random Waves. *Proceedings of Coastal Structures '83, ASCE*, Arlington, pp 94-107.

Asher WE & Farley PJ. 1995. Phase-Doppler Anemometer Measurement of Bubble Concentrations in Laboratory-Simulated Breaking Waves. *Journal of Geophysical Research* 100: 7045-7056.

Baldy S. 1988. Bubbles in the Close Vicinity of Breaking Waves: Statistical Characteristics of the Generation and Dispersion Mechanism. *Journal of Geophysical Research* 93: 8239-8248.

Banner ML & Peregrine DH. 1993. Wave Breaking in Deep Water. *Annual Review of Fluid Mechanics* 25: 373-397.

Barrau E, Riviere N, Poupot C & Cartellier A. 1999. Single and double optical probes in air-water two-phase flows: real time signal processing and sensor performance. *International Journal of Multiphase Flow* 25: 229-256.

Basco DR. 1985. A Qualitative Description of Wave Breaking. *Journal of Waterway, Port, Coastal and Ocean Engineering* 111: 171-188.

Battjes JA. 1974. Surf Similarity. *Proceedings of 14th International Conference on Coastal Engineering*, Copenhagen, pp 466-480.

Battjes JA. 1988. Surf-Zone Dynamics. *Annual Review of Fluid Mechanics* 20: 257-293.

Bin AK. 1988. Minimum Air Entrainment Velocity of Vertical Plunging Liquid Jets. *Chemical Engineering Science* 43: 379-389.

Bin AK. 1993. Review Article No. 43 - Gas Entrainment by Plunging Liquid Jets. *Chemical Engineering Science* 48: 3585-3630.

Black KP & Mead ST. 2001. Wave Rotation for Coastal Protection. *Proceedings of Coasts and Ports*, Gold Coast, Queensland, Australia.

Blanchard DC. 1963. The Electrification of the Atmosphere by Particles from Bubbles in the Sea. *Progress in Oceanography* 1: 71-202.

Blanchard DC & Woodcock AH. 1957. Bubble Formation and Modification in the Sea and its Meteorological Significance. *Tellus* 9: 145-158.

Bonmarin P. 1989. Geometric Properties of Deep-Water Breaking Waves. *Journal of Fluid Mechanics* 209: 405-433.

Bowyer PA. 2001. Video Measurements of Near-Surface Bubble Spectra. *Journal of Geophysical Research* 106: 14179-14190.

Boyer C, Duquenne AM & Wild G. 2002. Measuring Technique in Gas-Liquid and Gas-Liquid-Solid Reactors. *Chemical Engineering Science* 57: 3185-3215.

Bullock GN, Crawford AR, Hewson PJ, Hewson PJ, Walkden MJA & Bird PAD. 2001. The Influence of Air and Scale on Wave Impact Pressures. *Coastal Engineering* 42: 291-311.

Bullock GN, Obhrai C, Muller G, Wolters G, Peregrine DH & Bredmose H. 2005. Advances in the Understanding of Wave-Impact Forces. *Proceedings of Coastlines, Structures and Breakwaters*, London, pp 111-120.

Carey WM, Fitzgerald JW, Monahan EC & Wang Q. 1993. Measurement of the Sound Produced by a Tipping Trough with Fresh and Salt Water. *Journal of the Acoustic Society of America* 93: 3178-3192.

Cartellier A. 1990. Optical Probes for Local Void Fraction Measurements: Characterisation of Performance. *Review of Scientific Instruments* 61: 874-886.

Cartellier A. 1992. Simultaneous Void Fraction Measurement, Bubble Velocity and Size Estimate Using a Single Optical Probe in Gas-Liquid Two-Phase Flows. *Review of Scientific Instruments* 61: 874-886.

Cartellier A. 2001. Optical Probes for Multiphase Flow Characterisation: Some Recent Improvements. *Chemical Engineering Technology* 24: 535-538.

Cartellier A & Barrau E. 1998. Monfiber Optical Probes for Gas Detection and Gas Velocity Measurements: Conical Tips. *International Journal of Multiphase Flow* 24: 1265-1294.

Cartmill J & Su M-Y. 1993. Bubble Size Distribution Under Saltwater and Freshwater Breaking Waves. *Dynamics of Atmospheres and Oceans* 20: 25-31.

Chabot J, Lee SLP, Soria A & de Lasa HI. 1992. Interaction Between Bubbles and Fiber Optic Probes in a Bubble Column. *Canadian Journal of Chemical Engineering* 70: 61-68.

Chang K-A, Lim H-J & Su CB. 2003. Fiber Optic Reflectometer for Velocity and Fraction Ratio Measurements in Multiphase Flows. *Review of Scientific Instruments* 74: 3559-3565.

Chanson H. 1988. A Study of Air Entrainment and Aeration Devices on a Spillway Model. PhD thesis. University of Canterbury, Christchurch, NZ

Chanson H. 1997. *Air Bubble Entrainment in Free-surface Turbulent Shear Flows*. London: Academic Press. 401 pp.

Chanson H, Aoki S & Hoque A. 2002a. Scaling Bubble Entrainment and Dispersion in Vertical Circular Plunging Jet Flows: Freshwater Versus Seawater. *Proceedings of 5th International Conference on Hydrodynamics ICHD2002*, Taiwan, pp 431-436.

Chanson H, Aoki S & Hoque A. 2004. Physical modelling and similitude of air bubble entrainment at vertical plunging jet. *Chemical Engineering Science* 59: 747-758.

Chanson H, Aoki S & Maruyama M. 2002b. Unsteady Air Bubble Entrainment and Detrainment at a Plunging Breaker: Dominant Time Scales and Similarity of Water Level Variations. *Coastal Engineering*: 139-157.

Chanson H & Cummings PD. 1992. Aeration of the Ocean Due to Plunging Breaking Waves. *Research Report No. CE142*, Dept. of Civil Engineering Research Report Series, University of Brisbane.

Chanson H & Cummings PD. 1994. Effects of Plunging Breakers on the Gas Contents in the Ocean. *Marine Technology Society Journal* 28: 22-32.

Chanson H & Lee JF. 1997. Plunging Jet Characteristics of Plunging Breakers. *Coastal Engineering* 31: 125-141.

Chanson H & Toombes L. 2002. Air-Water Flows Down Stepped Chutes: Turbulence and Flow Structure Observations. *International Journal of Multiphase Flow* 28: 1737-1761.

Chen G, Kharif C, Zaleski S & Li J. 1999. Two-dimensional Navier-Stokes Simulation of Breaking Waves. *Physics of Fluids* 11: 3390-3400.

Chirichella D, Ledesma RG, Kiger KT & Duncan JH. 2002. Incipient Air Entrainment in a Translating Axisymmetric Plunging Laminar Jet. *Physics of Fluids* 14: 781-790.

Christensen ED & Deigaard R. 2001. Large Eddy Simulation of Breaking Waves. *Coastal Engineering* 42: 53-86.

Cipriano RJ & Blanchard DC. 1981. Bubble and Aerosol Spectra Produced by a Laboratory Breaking Wave. *Journal of Geophysical Research* 86: 8085-8092.

Clark NN & Turton R. 1988. Chord Length Distributions Related to Bubble Size Distributions in Multiphase Flows. *International Journal of Multiphase Flow* 14: 413-424.

Clift R, Grace JR & Weber ME. 1978. *Bubbles, Drops and Particles*. New York: Academic Press. 380 pp.

Cokelet ED. 1977. Breaking Waves. *Nature* 267: 769-774.

Cokelet ED. 1978. Breaking Waves-The Plunging Jet and Interior Flow Field. In *Mechanics of Wave-Induced Forces*. ed. TL Shaw, pp. 287-301. London: Pitman.

Collins JI & Weir W. 1969. Probabilities of Wave Characteristics in the Surf Zone. *Tetra Tech Report #TC-149*, Pasadena, CA.

Couriel ED, Horton PR & Cox DR. 1998. Supplementary 2-D Physical Modelling of Breaking Wave Characteristics. *WRL Technical Report 98/14*, Water Research Laboratory, University of New South Wales, Sydney.

Cox DT & Shin S. 2003. Laboratory Measurements of Void Fraction and Turbulence in the Bore Region of Surf Zone Waves. *Journal of Engineering Mechanics*: 1197-1205.

Cummings PD. 1996. Aeration due to Breaking Waves. PhD thesis. University of Queensland, Brisbane, Australia. 230 pp.

Cummings PD & Chanson H. 1997. Air Entrainment in the Developing Flow Region of Plunging Jets - Part 2: Experimental. *Journal of Fluids Engineering* 119: 603-608.

Dally WR, Dean RG & Dalrymple RA. 1985. Wave Height Variation Across Beaches of Arbitrary Profile. *Journal of Geophysical Research* 90: 11917-11927.

De Leeuw G & Leifer I. 2002. Bubbles Outside the Plume During the LUMINY Wind-Wave Experiment. In *Gas Transfer at Water Surfaces*. ed. M Donelan, pp. 295-301: American Geophysical Union.

Deane GB. 1997. Sound Generation and Air Entrainment By Breaking Waves in the Surf Zone. *Journal of the Acoustic Society of America* 102: 2671-2689.

Deane GB & Stokes MD. 1999. Air Entrainment Processes and Bubble Size Distributions in the Surf Zone. *Journal of Physical Oceanography* 29: 1393-1403.

Deane GB & Stokes MD. 2002. Scale Dependence of Bubble Creation Mechanisms in Breaking Waves. *Nature* 418: 839-844.

Detsch RM, Sharma RN. 1990. The Critical Angle for Gas Bubble Entrainment by Plunging Liquid Jets. *Chemical Engineering Journal* 44: 157-166.

Detsch RM, Stone TA & Sharma RN. 1992. Air Entrainment and Bubble Spectra of Plunging Liquid Jets at Acute Angles. *A.I.C.H.E. Symposium Series* 88: 119-125.

Duncan JH. 1981. An Experimental Investigation of Breaking Waves Produced by a Towed Hydrofoil. *Proceedings of the Royal Society of London A* 377: 331-348.

Duncan JH. 1983. The Breaking and Nonbreaking Wave Resistance of a Two-Dimensional Hydrofoil. *Journal of Fluid Mechanics* 126: 507-520.

Elmore PA, Chahine GL & Oguz HN. 2001. Cavity and Flow Measurements of Reproducible Bubble Entrainment Following Drop Impacts. *Experiments in Fluids* 31: 664-673.

Ervine DA, McKeogh E & Elsawy EM. 1980. Effect of Turbulence Intensity on the Rate of Air Entrainment by Plunging Water Jets. *Proceedings of the Institution of Civil Engineers* Part 2: 425-445.

Ervine DA & Elsawy EM. 1985. The Effect of a Falling Nappe on River Aeration. *Proceedings of 16th IAHR Congress*, Sao Paulo, Brazil, pp 390-397.

Farmer DM, Vagle SV & Booth AD. 1998. A Free-Flooding Acoustical Resonator for Measurement of Bubble Size Distributions. *Journal of Atmospheric and Oceanic Technology* 15: 1132-1146.

Friedl MJ & Fannelop. 2000. Bubble Plumes and their Interaction with the Water Surface. *Applied Ocean Research* 22: 119-128.

Führböter A. 1970. Air Entrainment and Energy Dissipation in Breakers. *Proceedings of 12th International Conference on Coastal Engineering*, Washington DC, pp 391-398.

Galvin CJ. 1968. Breaker Type Classification on Three Laboratory Beaches. *Journal of Geophysical Research* 73: 3651-3659.

Galvin CJ. 1969. Breaker Travel and Choice of Design Wave Height. *Journal of the Waterways and Harbours Division, ASCE, WW2* 95: 175-200.

Garrett C, Li M & Farmer DM. 2000. The Connection between Bubble Size Spectra and Energy Dissipation Rates in the Upper Ocean. *Journal of Physical Oceanography* 30: 2163-2171.

Gemmrich JR & Farmer DM. 2004. Near-Surface Turbulence in the Presence of Breaking Waves. *Journal of Physical Oceanography* 34: 1067-1086.

Govender K, Mocke GP & Alport MJ. 2002. Video-Imaged Surf Zone Wave and Roller Structures and Flow Fields. *Journal of Geophysical Research* 107: 1-21.

Haines MA & Johnson BD. 1995. Injected Bubble Populations in Seawater and Freshwater Measured by a Photographic Method. *Journal of Geophysical Research* 100: 7057-7068.

Hasselmann K. 1974. On the Spectral Dissipation of Ocean Waves due to Whitecapping. *Boundary Layer Meteorology* 6: 107-127.

Herringe RA & Davis MR. 1976. Structural Development of Gas-Liquid Mixture Flows. *Journal of Fluid Mechanics* 73: 97-123.

Hinze JO. 1955. Fundamentals of the Hydrodynamic Mechanism of Splitting in Dispersion Processes. *American Institute of Chemical Engineering Journal* 1: 289-295.

Hong M, Cartellier A & Hopfinger E. 2004. Characterisation of Phase Detection Optical Probes for the Measurement of the Dispersed Phase Parameters in Sprays. *International Journal of Multiphase Flow* 30: 615-648.

Hoque A. 2002. Air Bubble Entrainment by Breaking Waves and Associated Energy Dissipation. PhD thesis. Toyohashi University of Technology, Toyohashi. 151 pp.

Hoque A & Aoki S. 2005. Distributions of Void Fraction Under Breaking Waves in the Surf Zone. *Ocean Engineering* 32: 1829-1840.

Horikawa K & Kuo C. 1966. A Study on Wave Transformation Inside the Surf Zone. *Proceedings of 10th Conference on Coastal Engineering*, Tokyo, Japan, pp 217-233.

Hutt JA, Black KP & Mead ST. 2001. Classification of Surf Breaks in Relation to Surfing Skill. *Journal of Coastal Research* Special Issue No. 29: 66-81.

Hwang PA, Hsu Y-HL & Wu J. 1990. Air Bubbles Produced by Breaking Wind Waves: A Laboratory Study. *Journal of Physical Oceanography* 20: 19-28.

Hwung HH, Chyan JM & Chung YC. 1992. Energy Dissipation and Air Bubbles Mixing Inside Surf Zone. *Proceedings of 23rd International Conference on Coastal Engineering*, Venice, Italy, pp 308-321.

Irribarren CR & Nogales C. 1949. Protection des Ports. *Proceedings of XVIIth International Navigation Congress*, Lisbon, pp 31-80.

Isaacson I. 1991. Measurement of Regular Wave Reflection. *Journal of Waterway, Port, Coastal and Ocean Engineering* 117: 553-569.

Iversen HW. 1952. Laboratory Study of Breakers. *National Bureau of Standards, Circular 52*, Washington D.C.

Iwata K & Tomita T. 1992. Variation of Potential and Kinetic Energy in the Surf Zone. *Proceedings of 23rd International Conference on Coastal Engineering*, Venice, Italy, pp 336-349.

Jansen PCM. 1986. Laboratory Observations of the Kinematics in the Aerated Region of Breaking Waves. *Coastal Engineering* 9: 453-477.

Johnson BD & Cooke RC. 1979. Bubble Populations and Spectra in Coastal Waters: A Photographic Approach. *Journal of Geophysical Research* 84: 3761-3766.

Kabdasli MS & Turker U. 2002. The Wave Breaking Phenomena as a Tool for Environmentally Friendly Shore Protection. *Water Science and Technology* 46: 153-160.

Kalvoda PM, Xu L & Wu J. 2003. Macrobubble Clouds Produced by Breaking Wind Waves: A Laboratory Study. *Journal of Geophysical Research* 108: 1-8.

Kalvoda PM. 1992. Macrobubble Clouds Produced by Breaking Wind Waves. M.S. thesis. University of Delaware. 80 pp.

Katsaros KB & Atakturk SS. 1992. Dependence of Wave-Breaking Statistics on Wind Stress and Wave Development. *Proceedings of IUTAM Symposium*, Sydney, Australia, pp 119-132.

Keeling RF. 1993. On the Role of Large Bubbles in Air-Sea Gas Exchange and Supersaturation in the Ocean. *Journal of Marine Research* 51: 237-271.

Knudsen VO, Alford RS & Emling JW. 1948. Underwater Ambient Noise. *Marine Research* 7: 410-429.

Koehr BE. 2002. An Experimental Study of the Mechanism of Air Entrainment by Plunging Liquid Jets at a Free Surface. PhD thesis. John Hopkins University, Baltimore, Maryland. 262 pp.

Koga M. 1982. Bubble Entrainment in Breaking Wind Waves. *Tellus* 34: 481-489.

Kolovayev DA. 1976. Investigation of the Concentration and Statistical Size Distribution of Wind-Produced Bubbles in the Near Surface Ocean. *Oceanology* 15: 659-661.

Komar PD & Gaughan MK. 1973. Airy Wave Theory and Breaker Height Prediction. *Proceedings of 13th Conference on Coastal Engineering, ASCE*, Vancouver, Canada, pp 405-418.

Komen GJ, Cavaleri M, Donelan M, Hasselmann K, Hasselmann S & Jansen PEAM. 1994. *Dynamics and Modelling of Ocean Waves*: Cambridge University Press. 532 pp.

Lamarre E. 1993. An Experimental Study of Air Entrainment by Breaking Waves. PhD thesis. M.I.T., Cambridge, Massachusetts. 237 pp.

Lamarre E & Melville WK. 1991. Air Entrainment and Energy Dissipation in Breaking Waves. *Nature* 351: 469-472.

Lamarre E & Melville WK. 1992. Instrumentation for the Measurement of Void-Fraction in Breaking Waves: Laboratory and Field Results. *IEEE Journal of Oceanic Engineering* 17: 204-215.

Lamarre E & Melville WK. 1994. Void-fraction Measurements and Sound-Speed Fields in Bubble Plumes Generated by Breaking Waves. *Journal of the Acoustic Society of America* 95: 1317-1328.

Landrini M, Colagrossi A, Greco M & Tulin MP. 2005. SPH Simulation of Onshore Bores with Counter Rotational Vortical Structures. *Proceedings of 20th International Workshop on Water Waves and Floating Bodies*, University Centre in Svalbard, Longyearbyen, Article No. 34.

Le Mehaute B. 1962. On Non-Saturated Breakers and the Wave Run-Up. *Proceedings of 8th International Conference on Coastal Engineering*, Mexico City, Mexico, pp 77-92.

Ledesma RG. 2004. An Experimental Investigation on the Air Entrainment by Plunging Jets. PhD thesis. University of Maryland, Maryland. 192 pp.

Leifer I. 1995. A Validation Study of Bubble Mediated Air-Sea Gas Transfer Modelling. Georgia Institute of Technology, Atlanta, Georgia

Leifer I & De Leeuw G. 2002. Bubble Measurements in Breaking-Wave Generated Bubble Plumes During the LUMINY Wind-Wave Experiment. In *Gas Transfer at Water Surfaces*. ed. M Donelan, pp. 303-309: American Geophysical Union.

Leifer I, De Leeuw G & Cohen LH. 2000. Secondary Bubble Production from Breaking Waves : The Bubble Burst Mechanism. *Geophysical Research Letters* 27: 4077-4080.

Leifer I, De Leeuw G & Cohen LH. 2003. Optical Measurement of Bubbles: System. *Journal of Atmospheric and Oceanic Technology* 20: 1317-1332.

Leifer I, Patro R. 2002. The Bubble Mechanism for Methane Transport from the Shallow Sea Bed to the Surface: A Review and Sensitivity Study. *Continental Shelf Research* 22: 2409-2428.

Leifer I, Patro R & Bowyer P. 2000. A Study on the Temperature Variation of Rise Velocity for Large Clean Bubbles. *Journal of Atmospheric and Oceanic Technology* 17: 1392-1402.

Levich VG. 1962. *Physicochemical Hydrodynamics*. Upper Saddle River, N.J: Prentice-Hall. 700 pp.

Lim H-J & Chang K-A. 2004. Using Fibre Optic Reflectometry for Velocity and Void Fraction Measurements in Aerated Region of Breaking Waves (ABSTRACT ONLY). *Proceedings of 29th International Conference on Coastal Engineering*, Lisbon, Portugal.

Lin C & Hwung HH. 1992. External and Internal Flow Fields of Plunging Breakers. *Experiments in Fluids* 12: 229-237.

Lin TJ & Donnelly HG. 1966. Gas Bubble Entrainment by Plunging Laminar Liquid Jets. *American Institute of Chemical Engineering Journal* 12: 563-571.

Liu TJ & Bankoff SG. 1993. Structure of Air-Water Bubbly Flow in a Vertical Pipe -1: Liquid Mean Velocity and Turbulence Measurements. *International Journal of Heat and Mass Transfer* 36: 1049-1060.

Liu W. 1995. Data Interpretation Techniques for Inferring Bubble Size Distributions from Probe Measurements. PhD thesis. West Virginia University, Morgantown.

Liu W & Clark NN. 1995. Relationships Between Distributions of Chord Lengths and Distributions of Bubble Sizes Including Their Statistical Parameters. *International Journal of Multiphase Flow* 21: 1073-1089.

Liu W, Clark NN & Karamavruc AI. 1996. General Method for the Transformation of Chord-Length Data to a Local Bubble-Size Distribution. *AIChE Journal* 42: 2713-2720.

Loewen MR & Melville WK. 1991. Microwave Backscatter and Acoustic Radiation from Breaking Waves. *Journal of Fluid Mechanics* 224: 601-623.

Loewen MR & Melville WK. 1994. An Experimental Investigation of the Collective Oscillations of Bubble Plumes Entrained by Breaking Waves. *Journal of the Acoustic Society of America* 95: 1329-1343.

Loewen MR, O'Dor MA & Skafel MG. 1996. Bubbles Entrained by Mechanically Generated Breaking Waves. *Journal of Geophysical Research* 101: 20759-20769.

Longuet-Higgins MS. 1982. Parametric Solutions for Breaking Waves. *Journal of Fluid Mechanics* 121: 403-424.

Longuet-Higgins MS. 1992. The Crushing of Air Cavities in a Liquid. *Proceedings of the Royal Society of London A* 439: 611-626.

Longuet-Higgins MS & Cokelet ED. 1976. The Deformation of Steep Surface Waves on Water. A Numerical Method of Computation. *Proceedings of the Royal Society of London* Series A: 1-26.

Mackay D & Shiu WY. 1984. Physical-Chemical Phenomena and Molecular Properties. In *Gas Transfer at Water Surfaces*. ed. W Brutsaert, GH Jirka, pp. 3-16: D. Reidel Publications Co.

McCowan J. 1891. On the Solitary Wave. *Philosophical Magazine, 5th Series* 32: 45-58.

Mead ST & Black K. 2001. Predicting the Breaking Intensity of Surfing Waves. *Journal of Coastal Research* SI29: 103-130.

Medwin H. 1970. In-Situ Acoustic Measurements of Bubble Populations in Coastal Ocean Waters. *Journal of Geophysical Research* 75: 599-611.

Medwin H. 1977. In-Situ Acoustic Measurements of Microbubbles at Sea. *Journal of Geophysical Research* 82: 971-976.

Medwin H & Breitz ND. 1989. Ambient and Transient Bubble Spectral Densities in Quiescent Seas and Under Spilling Breakers. *Journal of Geophysical Research* 94: 12751-12759.

Melville WK. 1982. The Instability and Breaking of Deep Water Waves. *Journal of Fluid Mechanics* 115: 165-185.

Melville WK. 1994. Energy Dissipation by Breaking Waves. *Journal of Physical Oceanography* 24: 2041-2049.

Melville WK. 1996. The Role of Surface Wave Breaking in Air-Sea Interaction. *Annual Review of Fluid Mechanics* 28: 279-321.

Melville WK, Loewen MR & Lamarre E. 1992. Sound Production and Air Entrainment by Breaking Waves: A Review of Recent Laboratory Experiments. In *Breaking Waves*. ed. ML Banner, RHJ Grimshaw, pp. 139-146: Springer-Verlag.

Melville WK, Loewen MR & Lamarre E. 1993. Bubbles, Noise and Breaking Waves: A Review of Laboratory Experiments. In *Natural Physical Sources of Underwater Sound*. ed. BR Kerman, pp. 483-501: Kluwer Academic Publishers.

Melville WK & Rapp RJ. 1985. Momentum Flux in Breaking Waves. *Nature* 317: 514-516.

Miller RL. 1976. Role of Vortices in Surf Zone Prediction: Sedimentation and Wave Forces. *Beach and Nearshore Sedimentation, Society of Economic Paleantologists and Mineralogists, Special Publication No. 24*

Mizuguchi M. 1980. An Heuristic Model of Wave Height Distribution in Surf Zone. *Proceedings of 17th International Coastal Engineering Conference, ASCE*, Sydney, Australia, pp 278-289.

Monahan EC, Wang Q, Wang X & Wilson MB. 1994. Air Entrainment by Breaking Waves: A Laboratory Assessment. *Aeration Technology* 187: 21-26.

Monahan EC & Zietlow CR. 1969. Laboratory Comparisons of Fresh-Water and Salt-Water Whitecaps. *Journal of Geophysical Research* 74: 6961-6966.

Müller G, Wolters G & Cooker MJ. 2003. Characteristics of Pressure Pulses Propagating Through Water-Filled Cracks. *Coastal Engineering* 49: 83-98.

Munk WH. 1949. The Solitary Wave and its Application to Surf Problems. *Annual NY Academy of Science* 51: 376-424.

Murzyn F, Moaze D & Chaplin JR. 2004. Optical Measurements of Bubbly Flow in Hydraulic Jumps. *International Journal of Multiphase Flow* 31: 141-154.

Nadaoka K. 1986. A Fundamental Study on Shoaling and Velocity Field Structure of Water Waves in the Nearshore Zone. Tokyo Institute of Technology, Tokyo.

Nadaoka K, Hino A & Koyano Y. 1989. Turbulent Flow Field Structure of Breaking Waves in the Surf Zone. *Journal of Fluid Mechanics* 204: 359-387.

New AL. 1983. A Class of Elliptical Free-Surface Flows. *Journal of Fluid Mechanics* 130: 219-239.

Oguz HN & Prosperetti A. 1989. Surface Tension Effects in the Contact of Liquid Surfaces. *Journal of Fluid Mechanics* 203: 149-171.

Oguz HN & Prosperetti A. 1990. Bubble Entrainment by the Impact of Drops on Liquid Surfaces. *Journal of Fluid Mechanics* 219: 143-179.

Oguz HN, Prosperetti A & Kolaini AR. 1995. Air Entrainment by a Falling Water Mass. *Journal of Fluid Mechanics* 294: 181-207.

O'Hearn TJ, d'Agostino L & Acosta AJ. 1988. Comparison of Holographic and Coulter Counter Measurements of Cavitation Nuclei in the Ocean. *Journal of Fluids Engineering* 110: 200-207.

Papanicolaou P & Raichlen F. 1988. Wave and Bubble Characteristics in the Surf Zone. In *Sea Surface Sound.* ed. BR Kerman, pp. 97-109: Kluwer Academic Publishers.

Papanicolaou P & Raichlen F. 1992. Wave Characteristics in the Surf Zone. *Proceedings of Coastal Hydrodynamics*, pp 765-780.

Park WC, Klausner JF & Mei R. 1995. Physicochemical Hydrodynamics. *Experiments in Fluids* 19: 167-172.

Peregrine DH. 1979. Mechanics of Breaking Waves - A Review of Euromech 102. In *Mechanics of Wave-Induced Forces on Cylinders*. ed. TL Shaw, pp. 204-211. London: Pitman.

Peregrine DH. 1981. The Fascination of Fluid Mechanics. *Journal of Fluid Mechanics* 106: 59-80.

Peregrine DH. 1983. Breaking Waves on Beaches. *Annual Review of Fluid Mechanics* 15: 149-178.

Peregrine DH. 2003. Water Wave Impact on Walls. *Annual Review of Fluid Mechanics* 35: 23-43.

Peregrine DH, Cokelet ED & McIver P. 1980. The Fluid Mechanics of Waves Approaching Breaking. *Proceedings of 17th International Conference on Coastal Engineering*, Sydney, Australia, pp 512-518.

Peregrine DH & Thais L. 1996. The Effect of Entrained Air in Violent Water Wave Impacts. *Journal of Fluid Mechanics* 325: 377-397.

Phelps AD & Leighton TG. 1998. Oceanic Bubble Population Measurements Using a Buoy-Deployed Combination Frequency Technique. *IEEE Journal of Oceanic Engineering* 23: 400-410.

Phelps AD, Ramble DG & Leighton TG. 1997. The Use of a Combination Frequency Technique to Measure the Surf Zone Bubble Population. *Journal of the Acoustic Society of America* 101: 1981-1989.

Phillips OM. 1985. Spectral and Statistical Properties of the Equilibrium Range in Wind Generated Gravity Waves. *Journal of Fluid Mechanics* 156: 505-531.

Prosperetti A & Oguz HN. 1997. Air Entrainment Upon Liquid Impact. *Philosophical Transactions of the Royal Society London A* 355: 491-506.

Pumphrey HC & Elmore PA. 1990. The Entrainment of Bubbles by Drop Impacts. *Journal of Fluid Mechanics* 220: 539-567.

Raichlen F & Papanicolaou P. 1988. Some Characteristics of Breaking Waves. *Proceedings of 21st International Conference on Coastal Engineering*, Torremolinos, Spain, pp 377-392.

Ramberg SE, Barber ME & Griffin OM. 1985. Laboratory Studies of Steep and Breaking Deep Water Waves in a Convergent Channel. *Naval Research Laboratory Memo. Report 5610*, U.S. Dept. of the Navy, Washington, USA.

Rapp RJ & Melville WK. 1990. Laboratory Measurements of Deep-Water Breaking Waves. *Philosophical Transactions of the Royal Society London* A331: 735-800.

Saberi S, Shakourzadeh K, Bastoul D & Militzer J. 1995. Bubble Size and Velocity Measurements in Gas-Liquid Systems: Application of Fiber Optic Technique to Pilot Plant Scale. *Canadian Journal of Chemical Engineering* 73: 253-257.

Sawaragi T & Iwata K. 1974. Turbulence Effect on Wave Deformation After Breaking. *Coastal Engineering In Japan* 17: 39-49.

Sayce A, Black K, Gorman R. 1999. Breaking Wave Shape on Surfing Reefs. *Proceedings of Coasts and Ports '99*, Perth, Australia. pp. 596-603.

Scott JC. 1975. The role of salt in whitecap persistence. *Deep-Sea Research* 22: 653-657.

Seelig WN. 1980. Two-Dimensional Tests of Wave Transmission and Reflection Characteristics of Laboratory Breakwaters. *Technical Report No. 80-1*, WES, CERC, Vicksburg.

Sene KJ. 1988. Air Entrainment by Plunging Jets. *Chemical Engineering Science* 43: 2615-2623.

Serdula CD & Loewen MR. 1998. Experiments Investigating the Use of Fibre-Optic Probes for Measuring Bubble-Size Distributions. *IEEE Journal of Oceanic Engineering* 23: 385-399.

Serizawa A, Tsuda K & Michiyoshi I. 1984. Real-time Measurements of Two-Phase Flow Turbulence Using Dual-Sensor Anemometry. In *Measuring Techniques in Gas-Liquid Two-Phase Flows*. ed. JM Delhaye, G Cognet, pp. 495-523. New York: Springer.

Singamsetti SR & Wind HG. 1980. Characteristics of Breaking and Shoaling Periodic Waves Normally Incident on to Plane Beaches of Constant Slope. *Report M1371*, Delft Hydraulic Laboratory, Delft, Netherlands.

Slauenwhite DE & Johnson BD. 1999. Bubble Shattering: Differences in Bubble Formation in Fresh Water and Seawater. *Journal of Geophysical Research* 104: 3265-3275.

Smith ER & Kraus NC. 1990. Laboratory Study on Macro-Features of Wave Breaking Over Bars and Artificial Reefs. *Technical Report CERC-90-12*, WES, CERC, Vicksburg.

Smith ER & Kraus NC. 1991. Laboratory Study of Wave Breaking over Bars and Artficial Reefs. *Journal of Waterway, Port, Coastal and Ocean Engineering* 117: 307-325.

Stanton TP & Thornton EB. 2000. Profiles of Void Fraction and Turbulent Dissipation Under Breaking Waves in the Surf Zone. *Proceedings of 27th International Conference on Coastal Engineering*, Sydney, Australia, pp 70-79.

Stokes MD & Deane GB. 1999. A New Optical Instrument for the Study of Bubbles at High Void Fractions Within Breaking Waves. *IEEE Journal of Oceanic Engineering* 24: 300-311.

Storr GJ & Behnia M. 1999. Experiments with Large Diameter Gravity Driven Jets. *Experiments in Fluids* 27: 60-69.

Su M-Y, Burge R & Cartmill J. 1993. Measurement of Near-Surface Microbubble Density During SWADE.

Su M-Y, Ling SC & Cartmill J. 1988. Optical Microbubble Measurement in the North Sea. In *Sea Surface Sound.* ed. BR Kerman. Dordecht: Kluwer Publishers.

Sunamura T. 1981. A Laboratory Study of Offshore Transport of Sediment and a Model for Eroding Beaches. *17th Conference on Coastal Engineering, ASCE* 2: 1051-1070.

Svendsen IA. 1984. Wave Heights and Set-up in a Surf Zone. *Coastal Engineering* 8: 303-329.

Svendsen IA, Madsen PA & Buhr Hansen J. 1978. Wave Characteristics in the Surf-Zone. *Proceedings of 16th International Conference on Coastal Engineering*, Hamburg, Germany, pp 520-539.

Takikawa K, Yamada F & Matsumoto K. 1997. Internal Characteristics of Breaking Waves Over Submerged Breakwaters. *Proceedings of 7th International Offshore and Polar Engineering Conference*, pp 192-199.

Tallent JR, Yamashita T & Tsuchiya Y. 1990. Transformation Characteristics of Breaking Water Waves. In *Water Wave Kinematics*. ed. A Torum, OT Gudmestad, pp. 509-524: Kluwer Academic Publishers.

Terrill EJ & Melville WK. 2000. A Broadband Acoustic Technique for Measuring Bubble Size Distributions: Laboratory and Shallow Water Measurements. *Journal of Atmospheric and Oceanic Technology* 17: 220-239.

Terrill EJ, Lada G & Melville WK. 2001a. Surf Zone Bubble Populations. *Acoustical Oceanography* 23: 212-219.

Terrill EJ, Melville WK & Sramski D. 2001b. Bubble Entrainment by Breaking Waves and their Influence on Optical Scattering in the Upper Ocean. *Journal of Geophysical Research* 106: 16815-16823.

Thornton EB & Guza RT. 1983. Transformation of Wave Height Distribution. *Journal of Geophysical Research* 88: 5925-5938.

Thoroddsen ST, Etoh TG & Takehara K. 2003. Air Entrapment Under an Impacting Drop. *Journal of Fluid Mechanics* 478: 125-134.

Thorpe SA. 1984. The Role of Bubbles Produced by Breaking Wind Waves in Supersaturating the Near Surface Ocean Mixing Layer with Oxygen. *Annales Geophysicae* 2: 53-56.

Thorpe SA. 1984. A Model of the Turbulent Diffusion of Bubbles Below the Sea Surface. *Journal of Physical Oceanography* 14: 841-854.

Thorpe SA. 1993. Energy Loss by Breaking Waves. *Journal of Physical Oceanography* 23: 2498-2502.

Thorpe SA, Bowyer P & Woolf DK. 1992. Some Factors Affecting the Size Distributions of Oceanic Bubbles. *Journal of Physical Oceanography* 22: 382-389.

Thorpe SA, Osborn TR, Farmer DM & Vagle S. 2003. Bubble Cloud and Langmuir Circulation: Observations and Models. *Journal of Physical Oceanography* 33: 2013-2031.

Tsai C-P, Chen H-B & Hsu JRC. 2001. Calculations of wave transformation across the surf zone. *Ocean Engineering* 28: 941-955.

U.S. Army Corps of Engineers. 2002. Coastal Engineering Manual. *Engineer Manual 1110-2-1100*, U.S. Army Corps of Engineers, Washington D.C.

Vagle S. 1989. An Acoustical Study of the Upper-Ocean Boundary Layer. PhD thesis. University of Victoria & Institute of Ocean Science, B.C. Canada.

Vagle S & Farmer DM. 1992. The Measurement of Bubble Size Distributions by Acoustical Backscatter. *Journal of Atmospheric and Oceanic Technology* 9: 630-644.

Vagle S & Farmer DM. 1998. A Comparison of Four Methods for Bubble Size and Void Fraction Measurements. *IEEE Journal of Oceanic Engineering* 23: 211-222.

Van de Sande E & Smith JM. 1975. Mass Transfer from Plunging Water Jets. *The Chemical Engineering Journal* 10: 219-224.

Van der Meer JW. 1990. Data on Wave Transmission due to Overtopping. *Report H 986*, Delft Hydraulics, Delft, Netherlands.

Van der Meer JW & Angremond K. 1992. Wave Transmission at Low Crested Structures. *Proceedings of Coastal Structures and Breakwaters*, London, pp 25-41.

Vinje T & Brevig P. 1981. Numerical Simulation of Breaking Waves. *Advanced Water Resources* 4: 77-82.

Walsh AL & Mulhearn PJ. 1987. Photographic Measurements of Bubble Populations from Breaking Wind Waves at Sea. *Journal of Geophysical Research* 92: 14553-14565.

WAMDI Group. 1988. The WAM Model - A Third Generation Ocean Wave Prediction Model. *Journal of Physical Oceanography* 18: 1775-1810.

Wang P, Ebersole BA & Smith ER. 2003. Beach-Profile Evolution Under Spilling and Plunging Breakers. *Journal of Waterway, Port, Coastal and Ocean Engineering* 129: 41-46.

Wang Q & Monahan EC. 1995. The Influence of Salinity on the Spectra of Bubbles Formed in Breaking Wave Simulations. In *Sea Surface Sound '94*. ed. MJ Buckingham, JR Potter, pp. 312-319: World Scientific.

Waniewski TA, Brennen CE & Raichlen F. 2001. Measurements of Air Entrainment by Bow Waves. *Journal of Fluids Engineering* 123: 57-63.

Watanabe Y, Ohtsuka J & Saeki H. 2001. Evolution of Bubbly Flow in the Surf Zone. *Proceedings of 4th International Symposium on Waves (Ocean Wave Measurement and Analysis)*, San Francisco, California, pp 992-1001.

Weber TC, Lyons AP & Bradley DL. 2005. An Estimate of the Gas Transfer Rate from Oceanic Bubbles Derived from Multibeam Sonar Observations of a Ship Wake. *Journal of Geophysical Research* 110

Weggel JR. 1972. Maximum Breaker Height. *Journal of the Waterways and Harbours Division, ASCE, WW4*: 529-547.

Wise D & Houghton G. 1966. The Diffusion Coefficients of Ten Slightly Soluble Gases in Water at 10-60C. *Chem. Eng. Science* 21: 999-1010.

Wood IR. 1991. Air Entrainment in Free-Surface Flows. In *IAHR Hydraulic Structures Design Manual No. 4, Hydraulic Design Considerations*, pp. 149. Rotterdam, Netherlands: Balkema Publ.

Woolf DK. 1993. Bubble and the Air-Sea Transfer Velocity of Gases. *Atmosphere-Ocean* 31: 517-540.

Woolf DK, Thorpe SA. 1991. Bubbles and the Air-Sea Exchange of Gases in Near-Saturation Conditions. *Journal of Marine Research* 49: 435-466.

Wu CH & Nepf HM. 2002. Breaking Criteria and Energy Losses for Three-Dimensional Wave Breaking. *Journal of Geophysical Research-Oceans* 107: 1-18.

Wu J. 2000. Bubbles Produced by Breaking Waves in Fresh and Salt Waters: Notes and Correspondance. *Journal of Physical Oceanography* 30: 1809-1813.

Yasuda T, Mutsuda H & Mizutani N. 1997. Kinematics of Overturning Waves and Their Relations to Breaker Types. *Coastal Engineering* 29: 317-346.

Yasuda T, Mutsuda H, Mizutani N & Matsuda H. 1999. Relationships of Plunging Jet Size to Kinematics of Breaking Waves With Spray and Entrained Air Bubbles. *Coastal Engineering Journal* 41: 269-280.

Yuksel Y, Bostan T, Cevik E, Celikoglu Y & Gunal M. 1999. Two-Phase Flow Structure in Breaking Waves. *9th International Conference on Offshore and Polar Engineering* 3: 231-235.

Yuksel Y & Kapdasli MS. 1994. Breaking Waves-Plunging Point and its Effects. In *Sediment Transport Mechanisms in Coastal Environments and Rivers*. ed. RS Belorgey, pp. 299-307: World Scientific.

Zhao D & Toba Y. 2001. Dependenceof Whitecap Coverage on Wind-Wave Properties. *Journal of Oceanography* 57: 603-616.

Zhu Y, Oguz HN & Prosperetti A. 2000. On the Mechanism of Air Entrainment by Liquid Jets at a Free Surface. *Journal of Fluid Mechanics* 404: 151-177.

APPENDIX A – TIME-VARYING VOID FRACTION DISTRIBUTIONS

A.1 Wave Case 1 – Strongly Plunging Wave

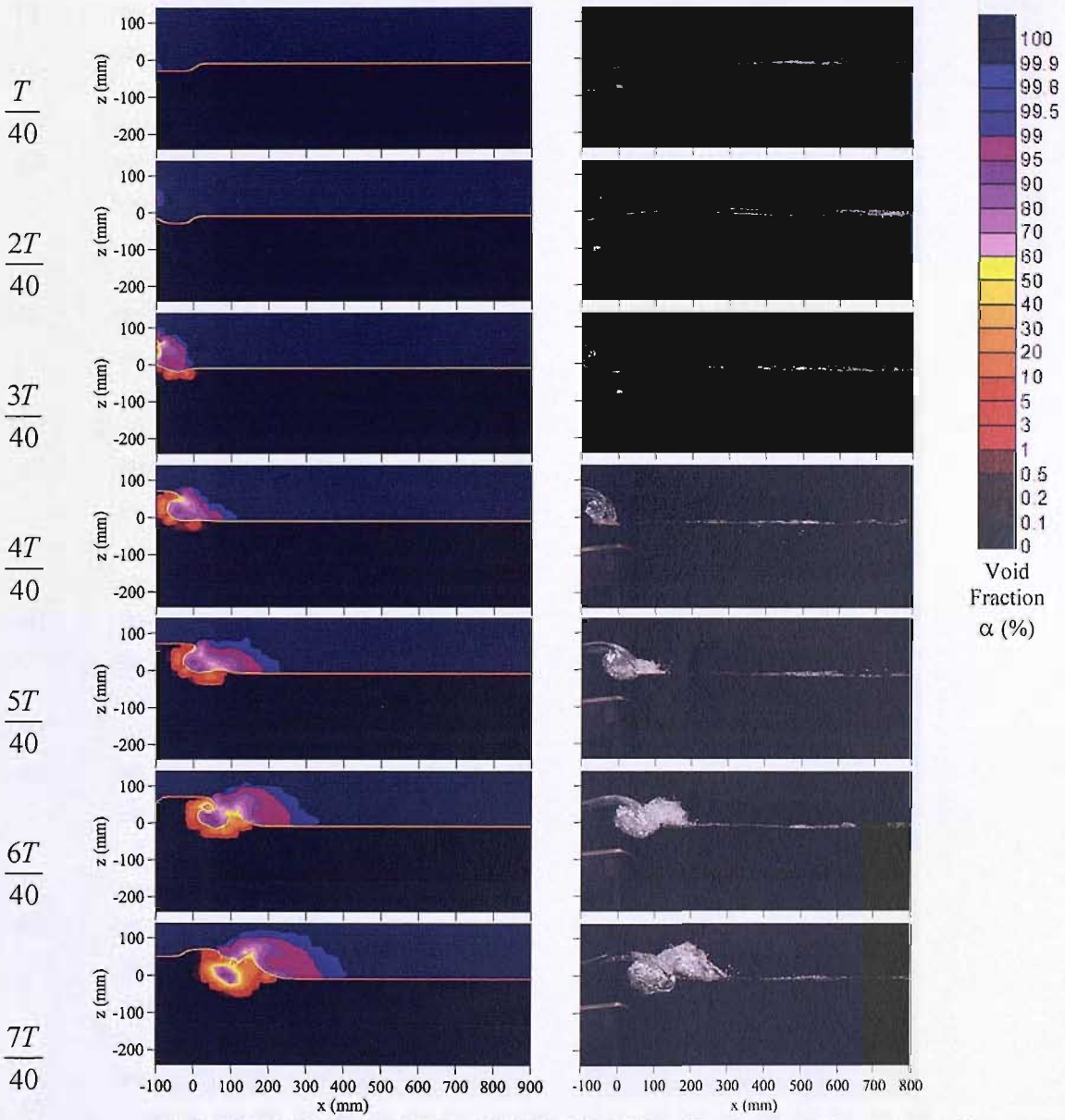

Figure A.1 Measured time-varying void fraction distributions and corresponding photographs for wave case 1. Phase averages begin at time t=T/40 and are presented at intervals of T/40.

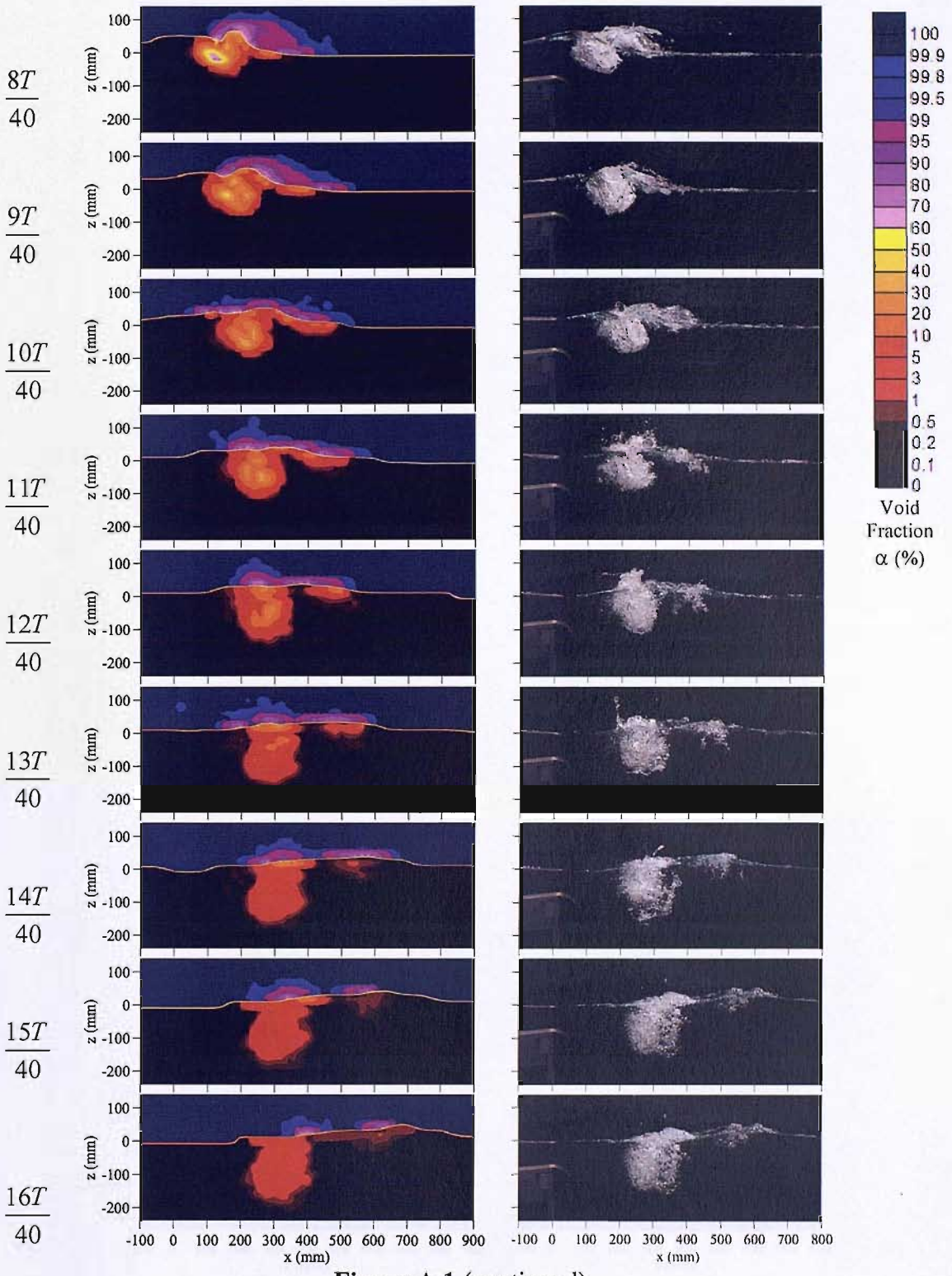

Figure A.1 (continued).

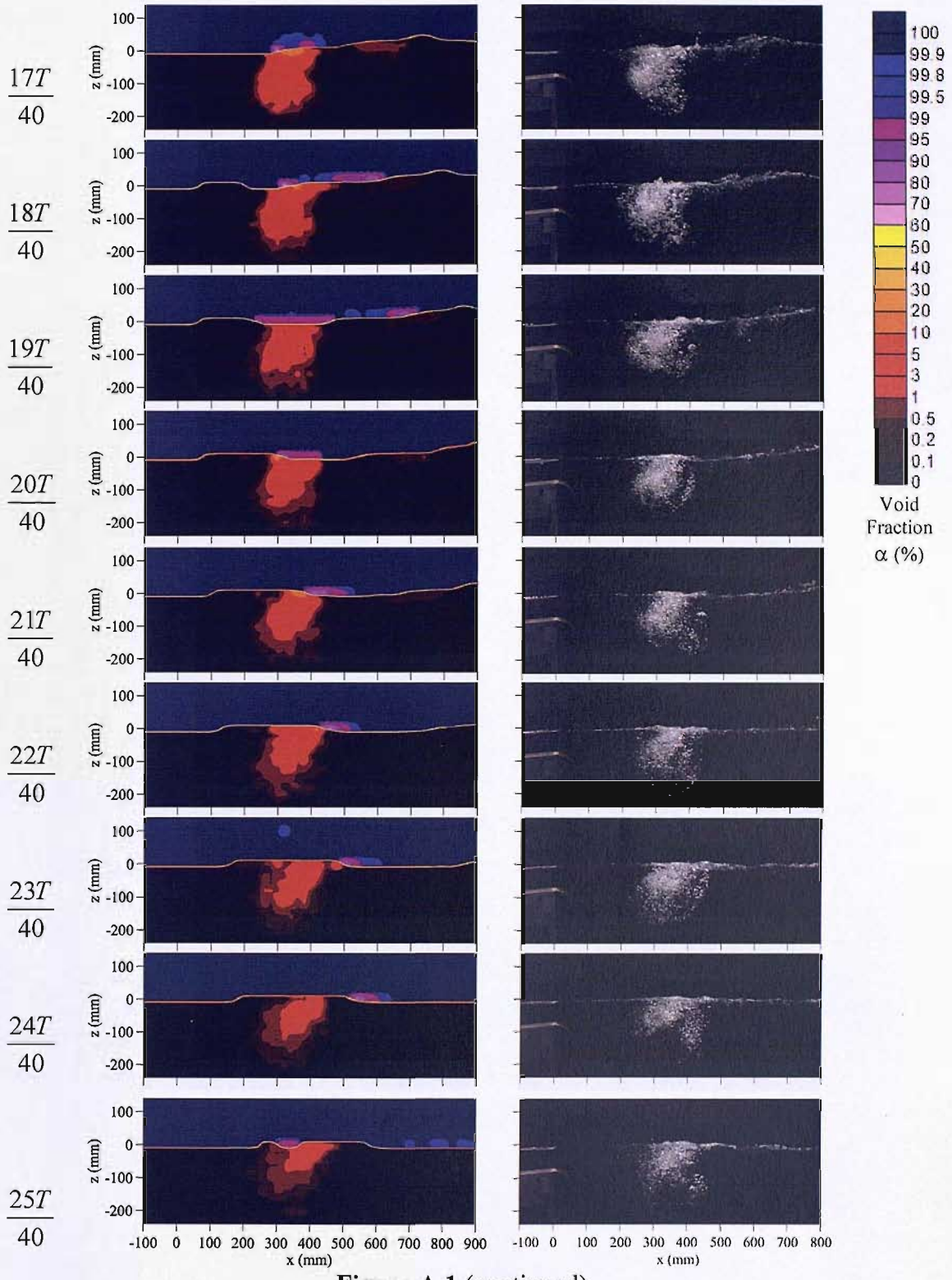

Figure A.1 (continued).

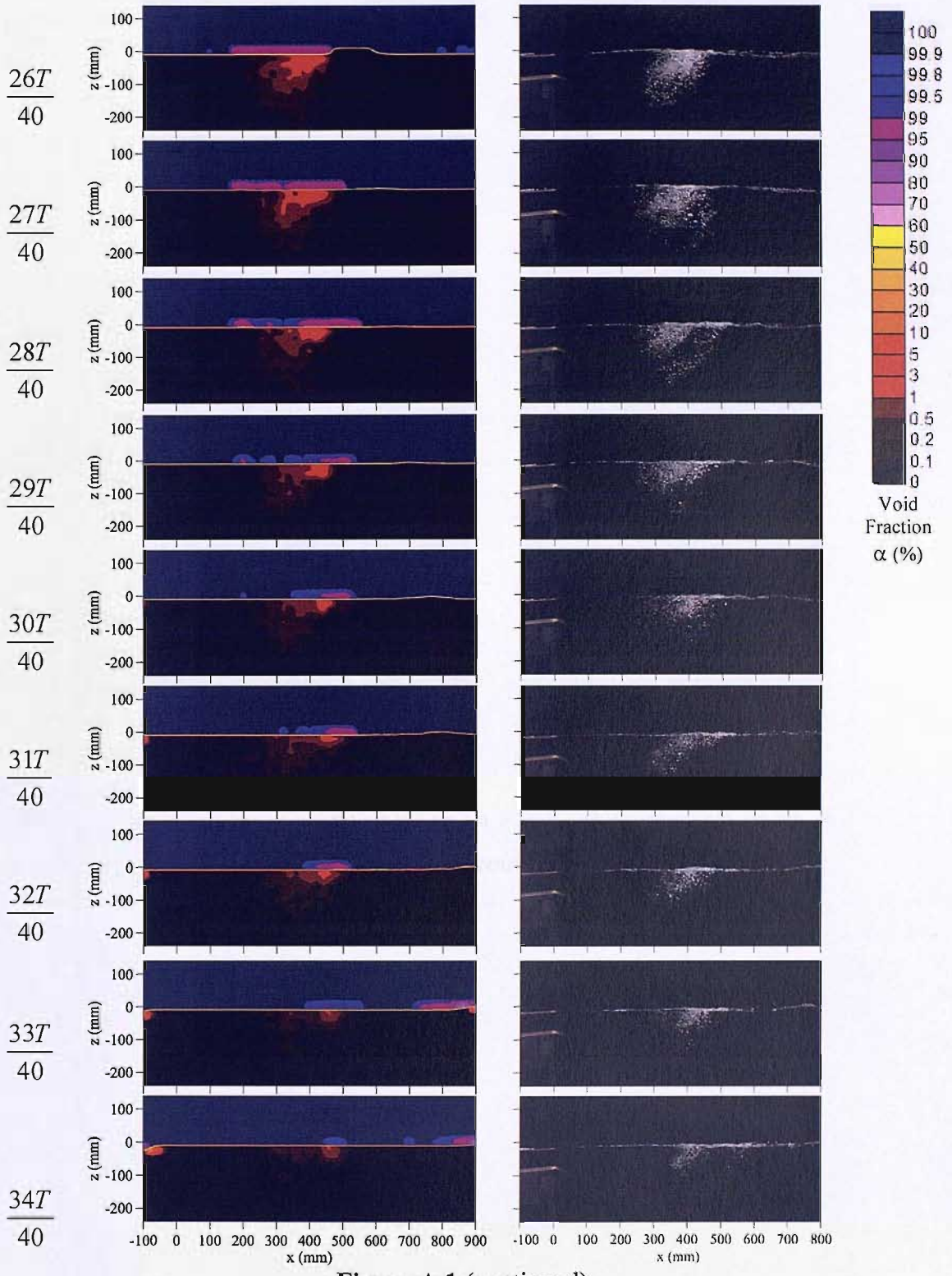

Figure A.1 (continued).

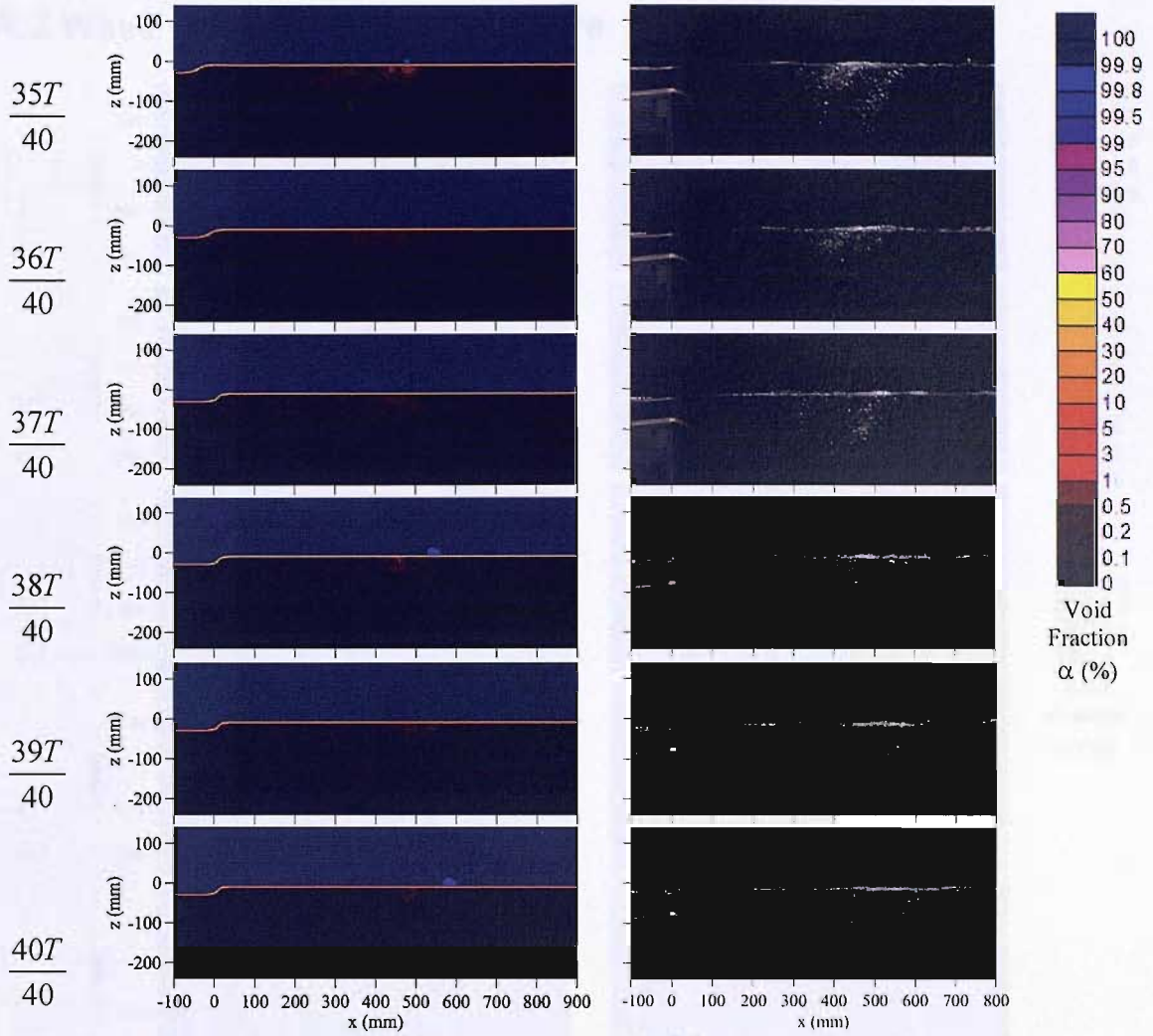

Figure A.1 (continued).

A.2 Wave Case 2 – Plunging Wave

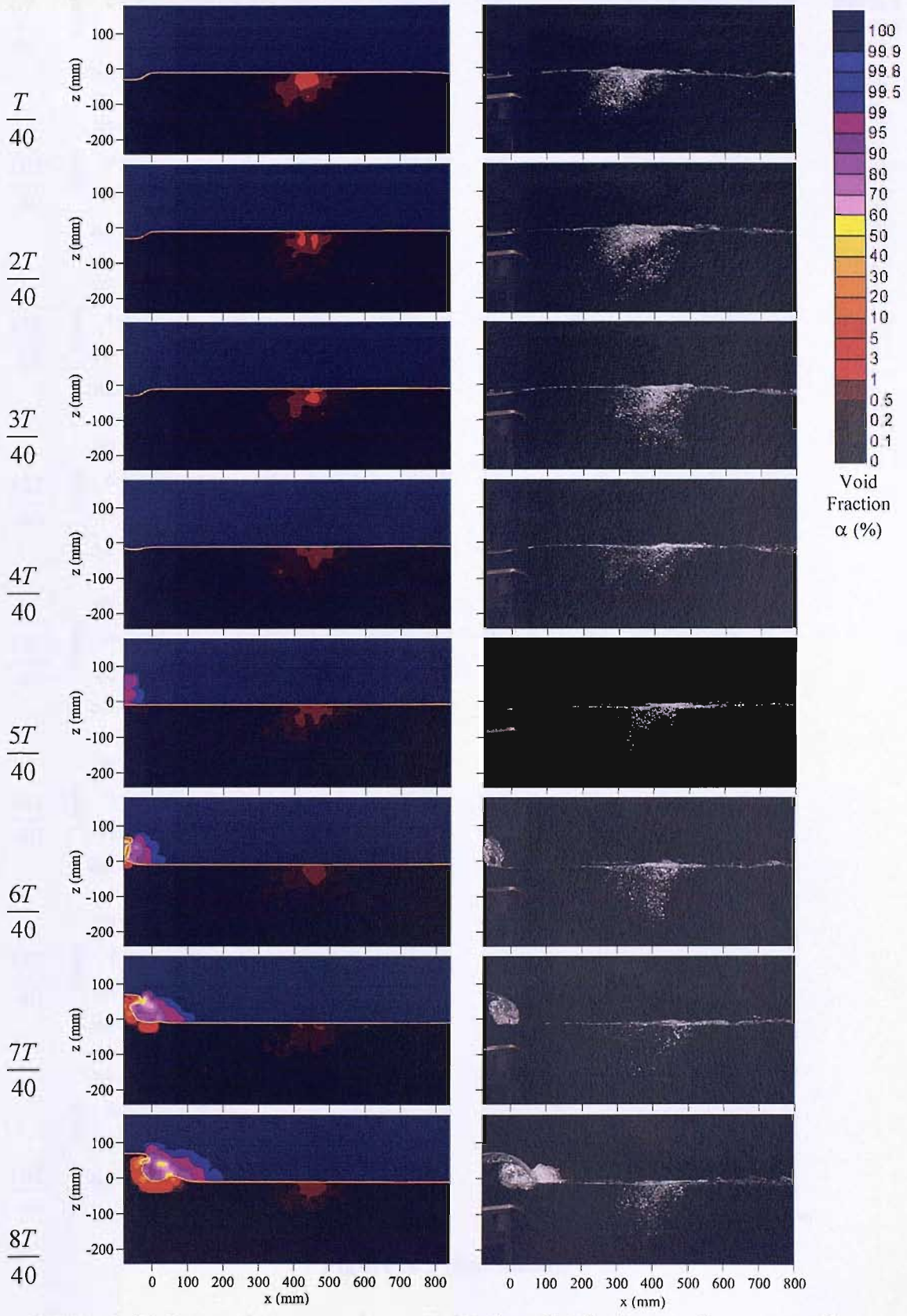

Figure A.2 Measured time-varying void fraction distributions and corresponding photographs for wave case 2. Phase averages begin at time $t=T/40$ and are presented at intervals of $T/40$.

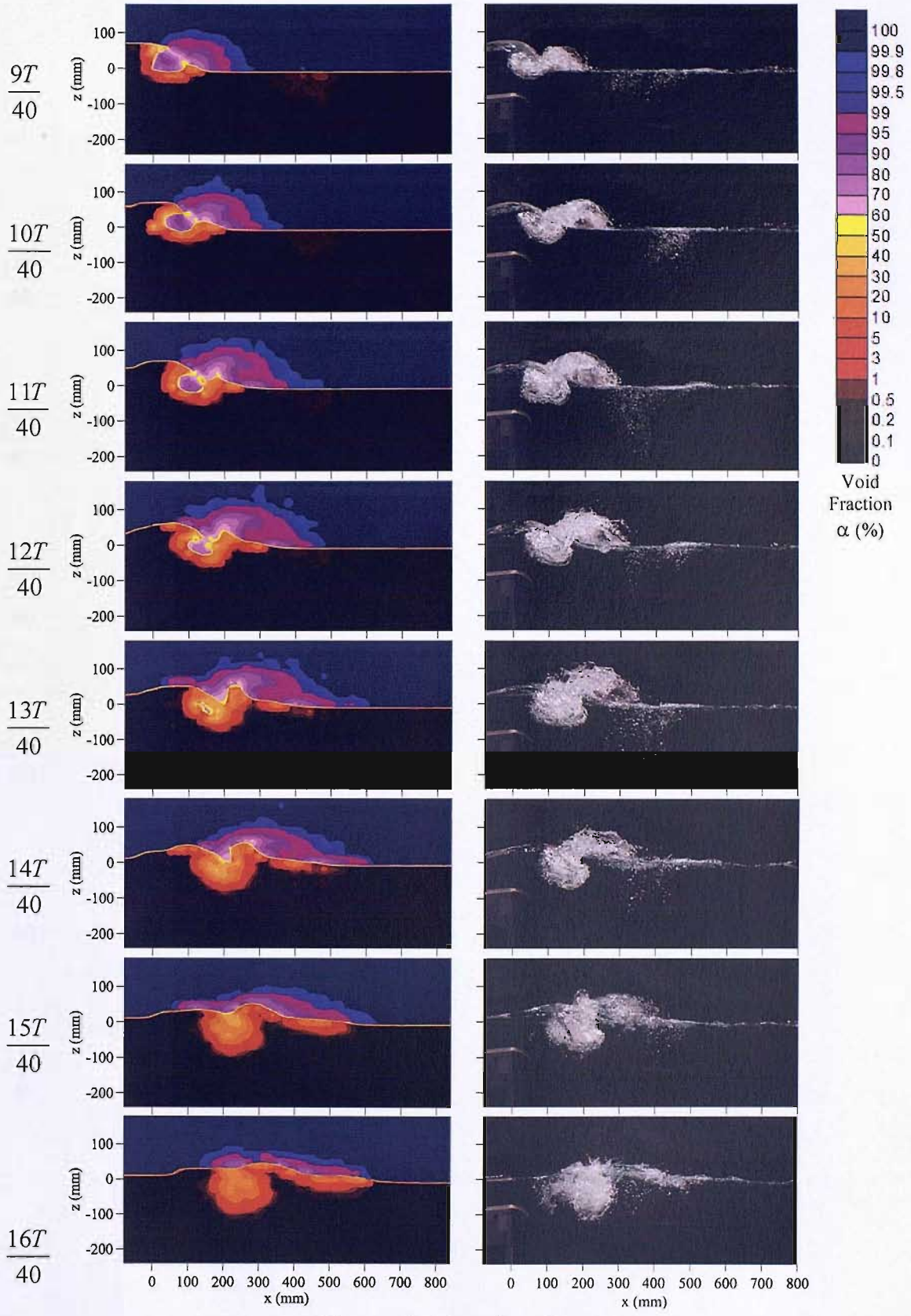

Figure A.2 (continued).

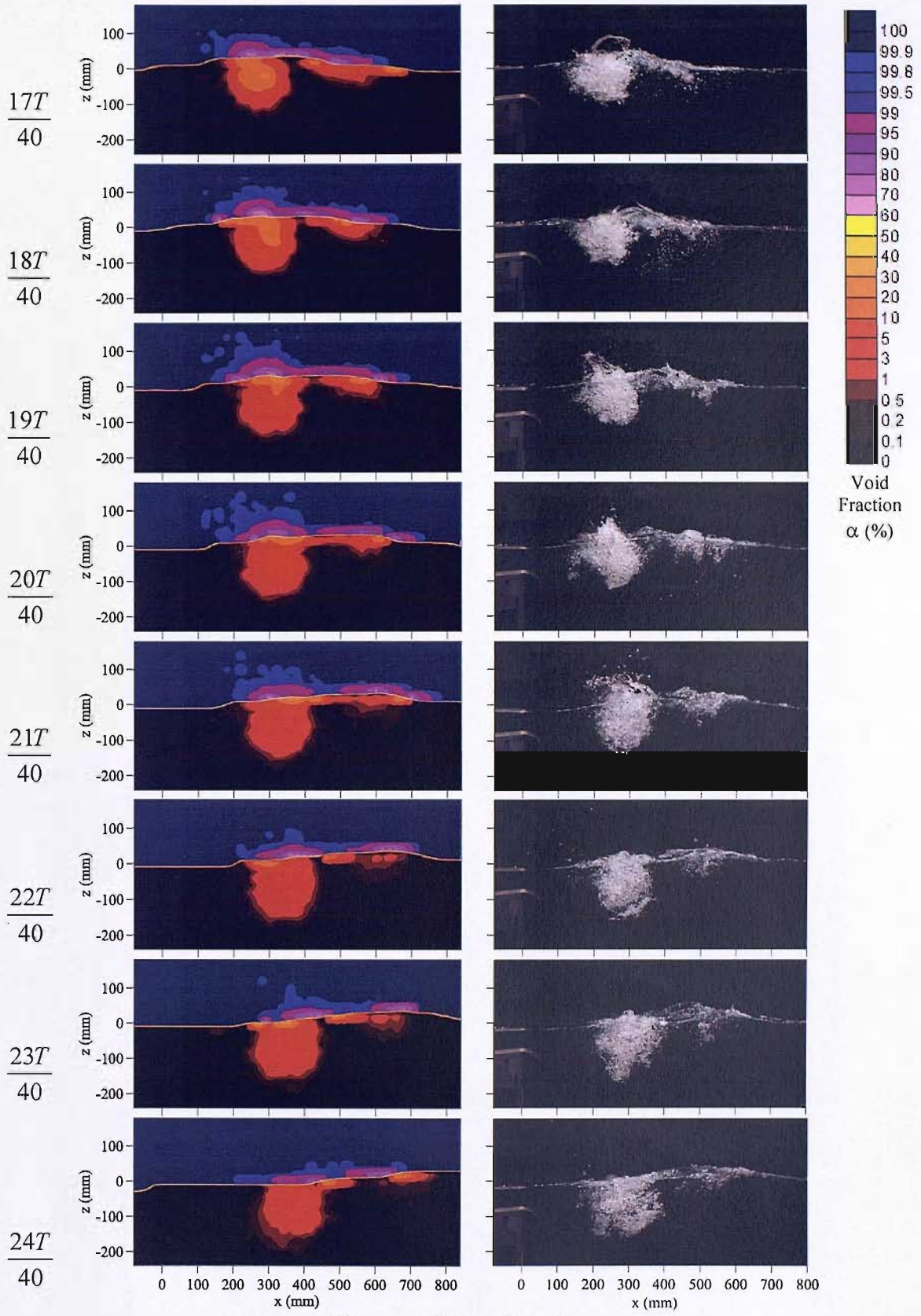

Figure A.2 (continued).

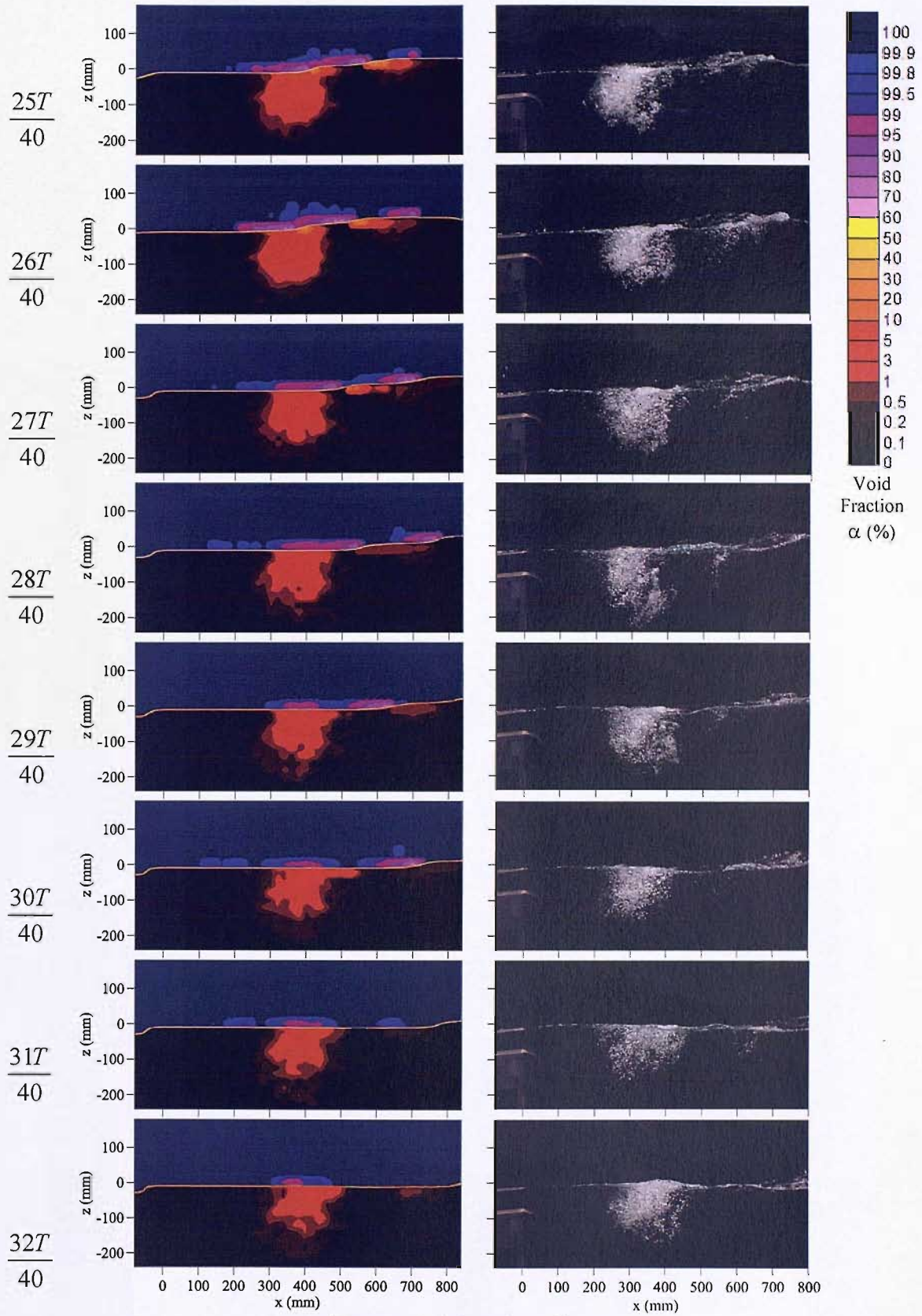

Figure A.2 (continued).

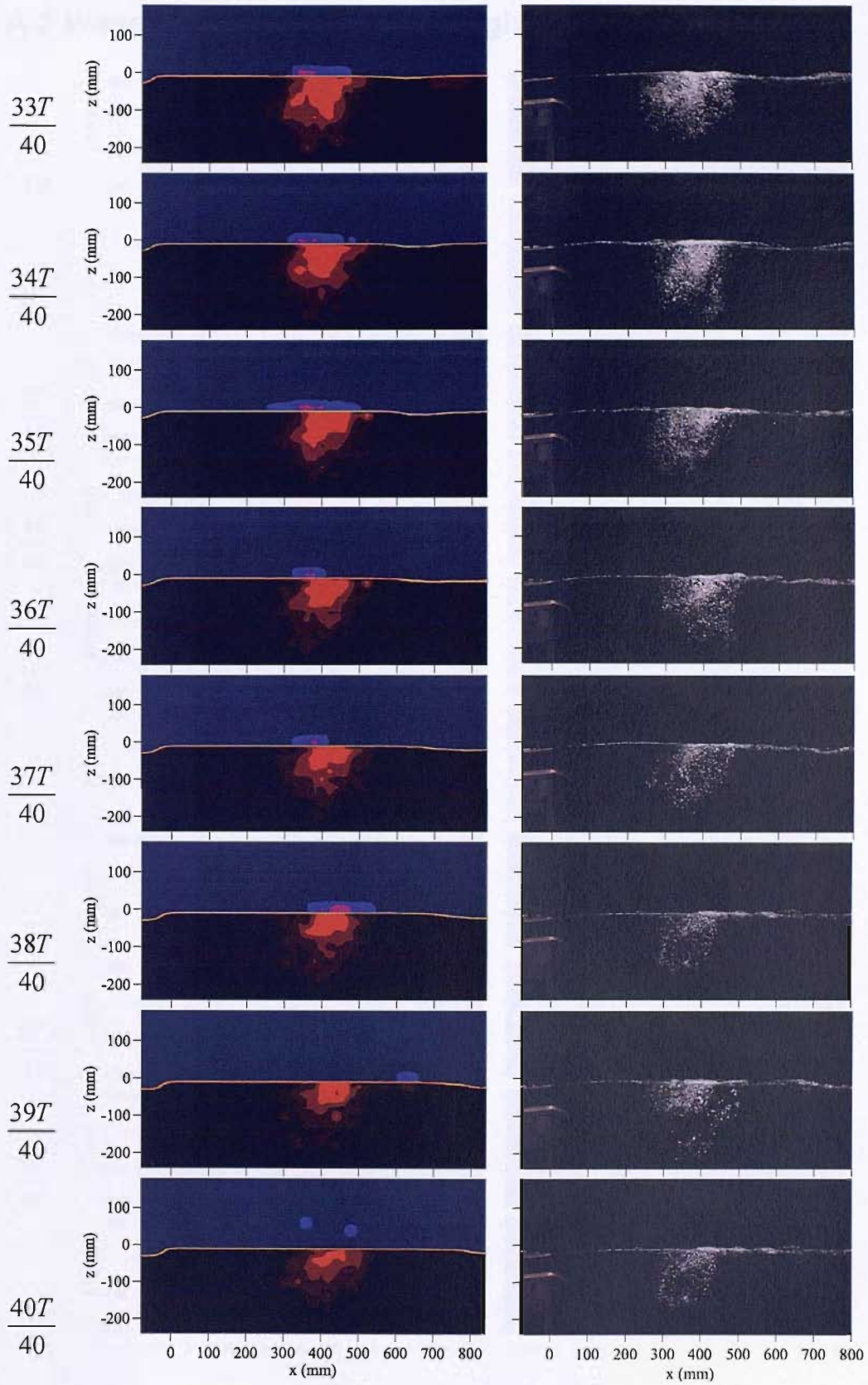

Figure A.2 (continued).

A.3 Wave Case 3 – Spilling/Plunging Wave

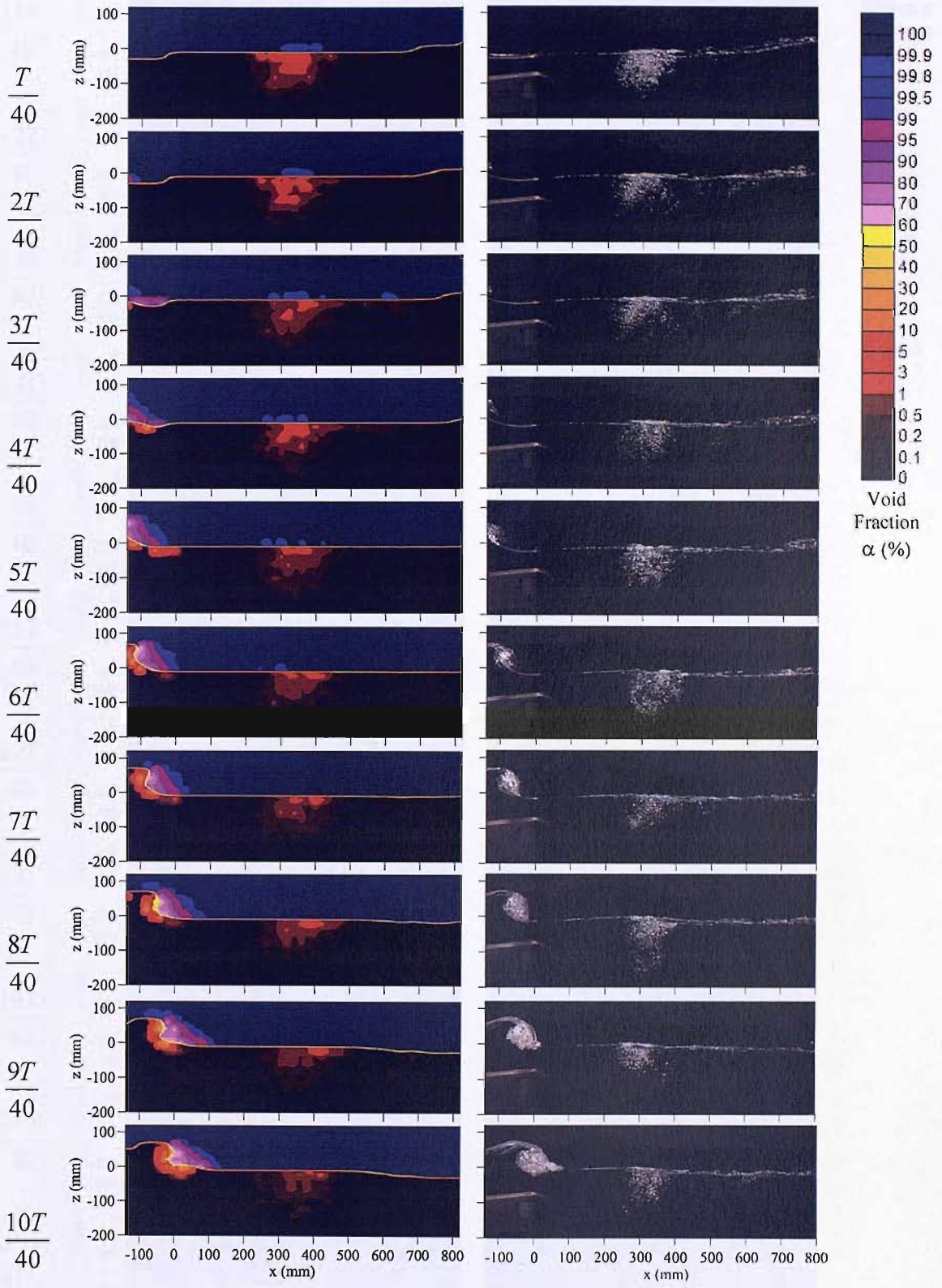

Figure A.3 Measured time-varying void fraction distributions and corresponding photographs for wave case 2. Phase averages begin at time $t=T/40$ and are presented at intervals of $T/40$.

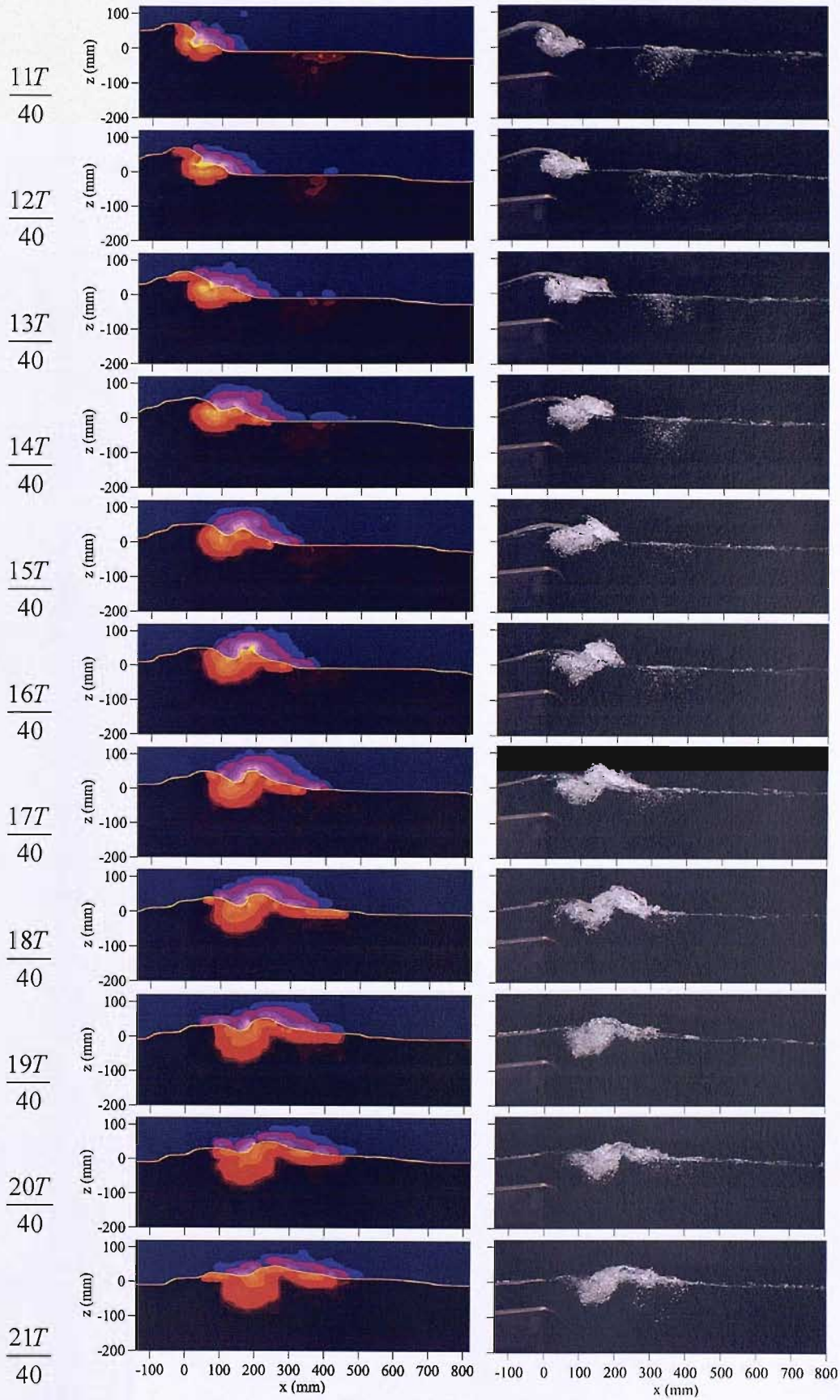

Figure A.3 (continued).

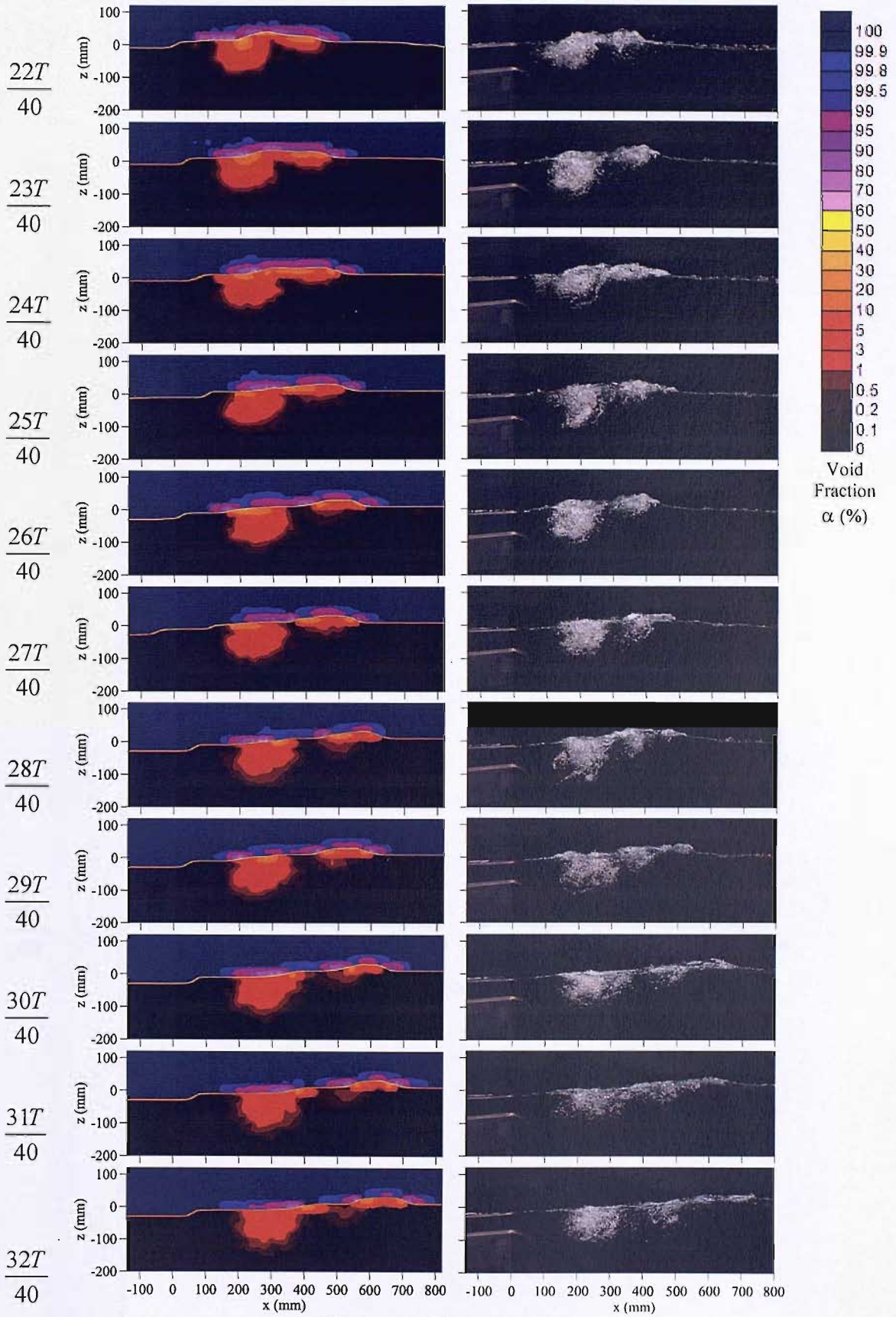

Figure A.3 (continued).

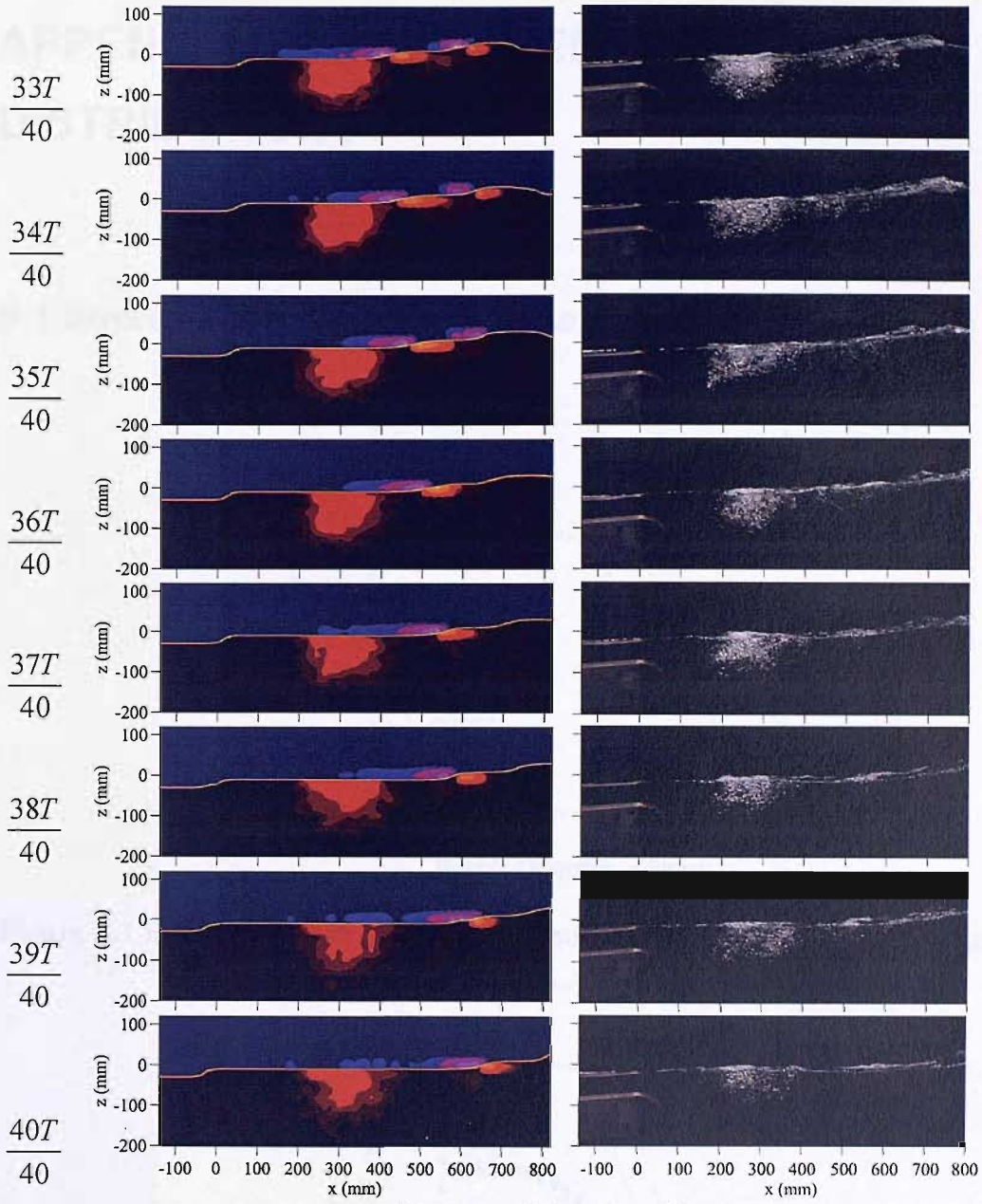

Figure A.3 (continued).

APPENDIX B – MEASURED BUBBLE SIZE DISTRIBUTIONS

B.1 Strongly Plunging Wave Case

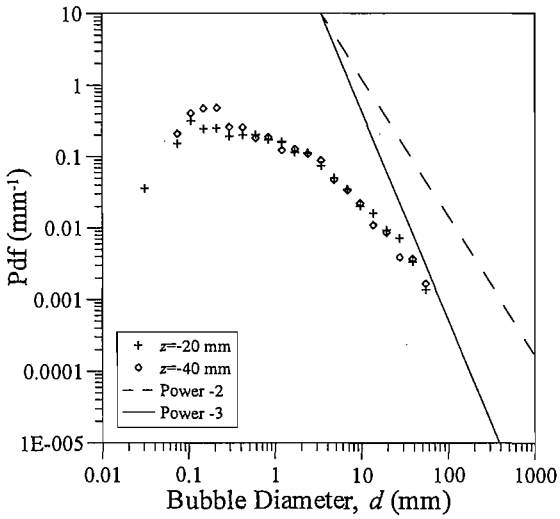

Figure B.1 Bubble size distributions for the strongly plunging wave case along vertical transects at x=200 mm.

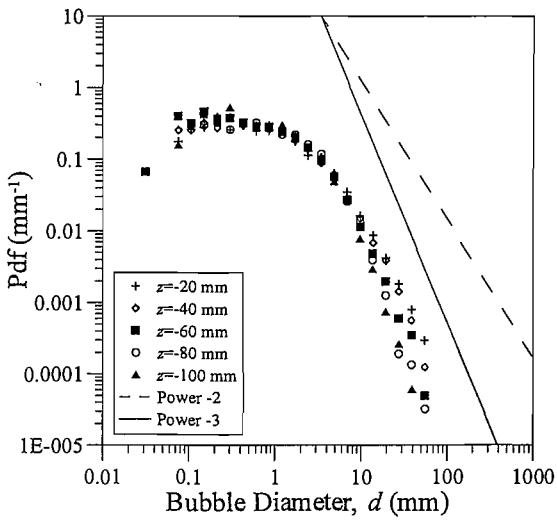

Figure B.2 Bubble size distributions for the strongly plunging wave case along vertical transects at x=280 mm.

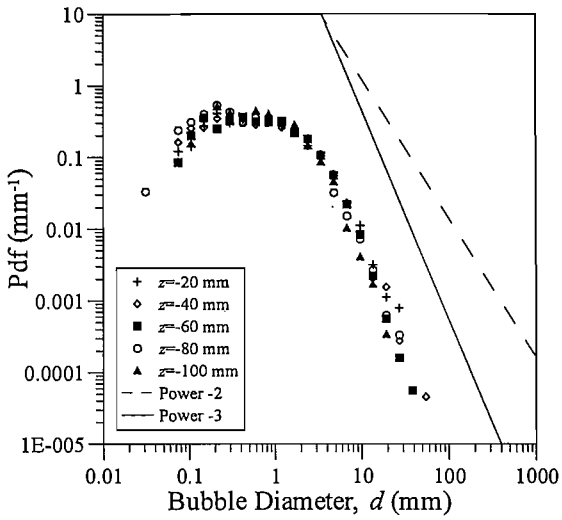

Figure B.3 Bubble size distributions for the strongly plunging wave case along vertical transects at x=360 mm.

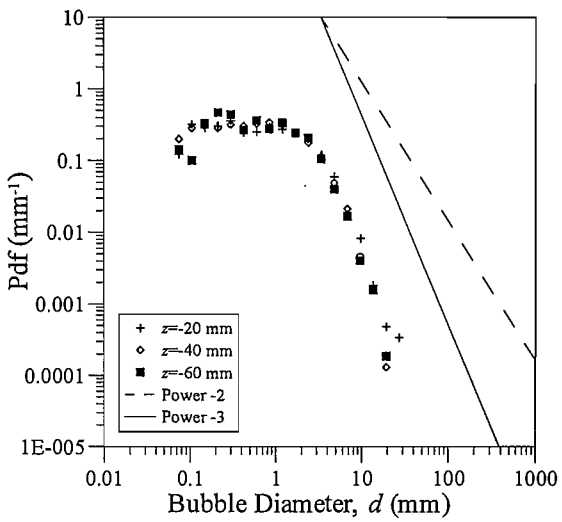

Figure B.4 Bubble size distributions for the strongly plunging wave case along vertical transects at x=420 mm.

B.2 Spilling/Plunging Wave Case

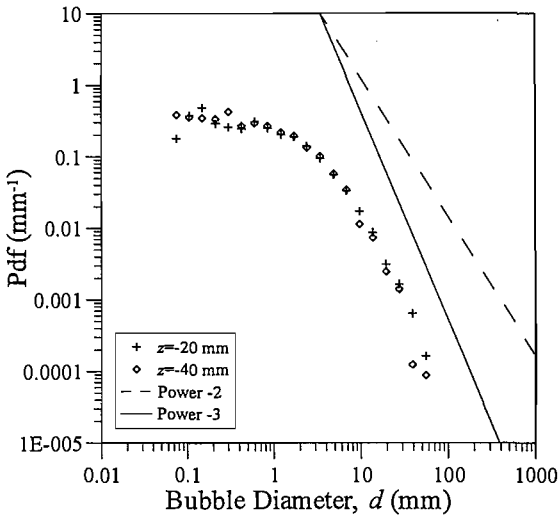

Figure B.5 Bubble size distributions for the spilling/plunging wave case along vertical transects at x=120 mm.

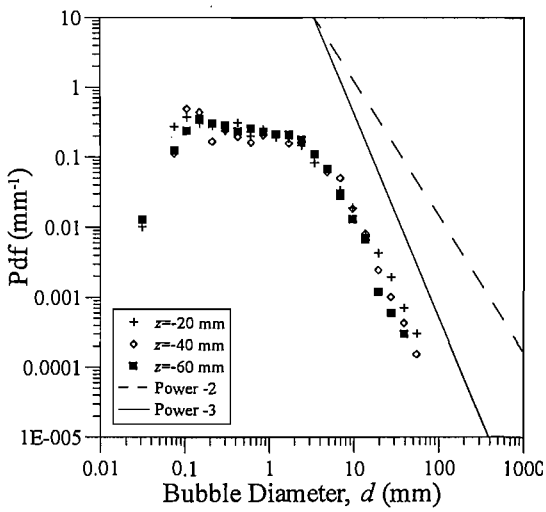

Figure B.6 Bubble size distributions for the spilling/plunging wave case along vertical transects at x=200 mm.

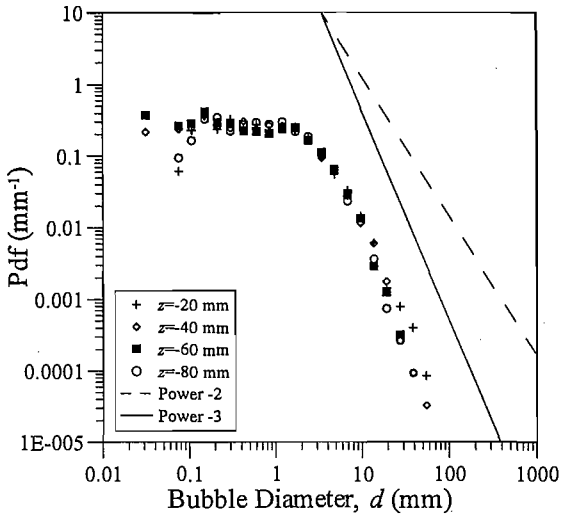

Figure B.7 Bubble size distributions for the spilling/plunging wave case along vertical transects at x=280 mm.

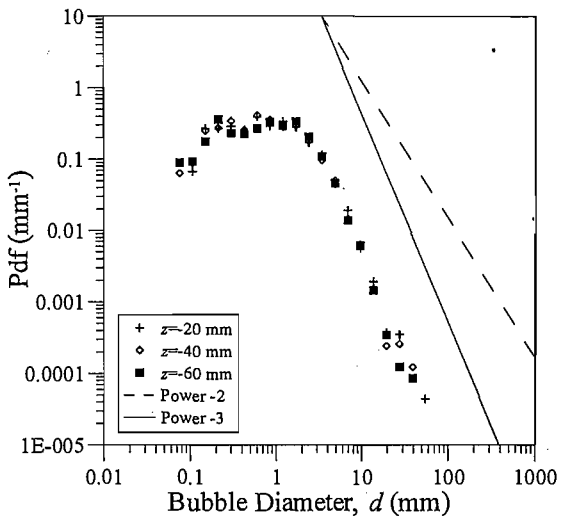

Figure B.8 Bubble size distributions for the spilling/plunging wave case along vertical transects at x=360 mm.

APPENDIX C – VOID FRACTION PLOTS IN FRESH AND SEAWATER

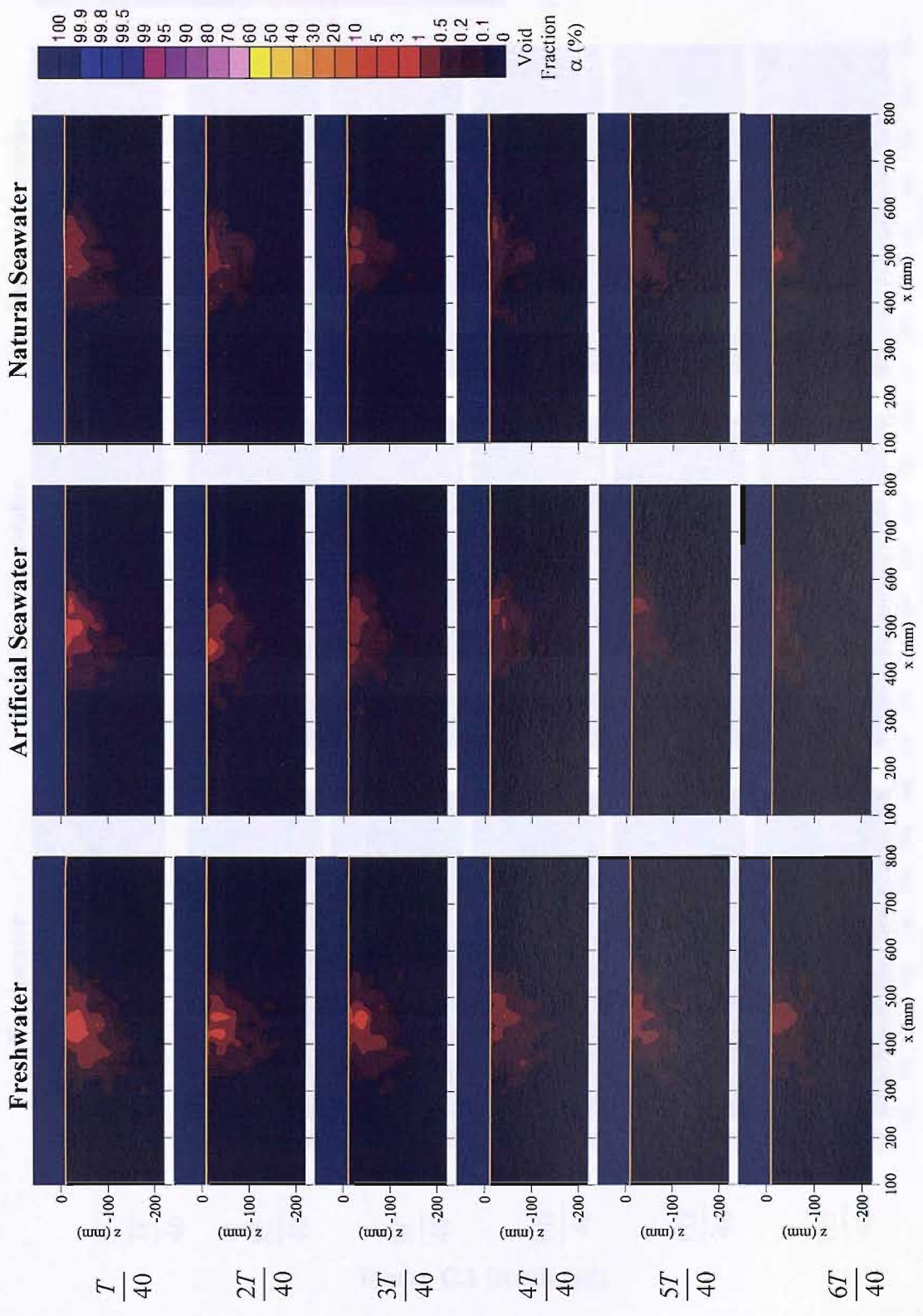

Figure C.1 Void fraction distributions beneath plunging breaking waves in freshwater, artificial seawater and natural seawater.

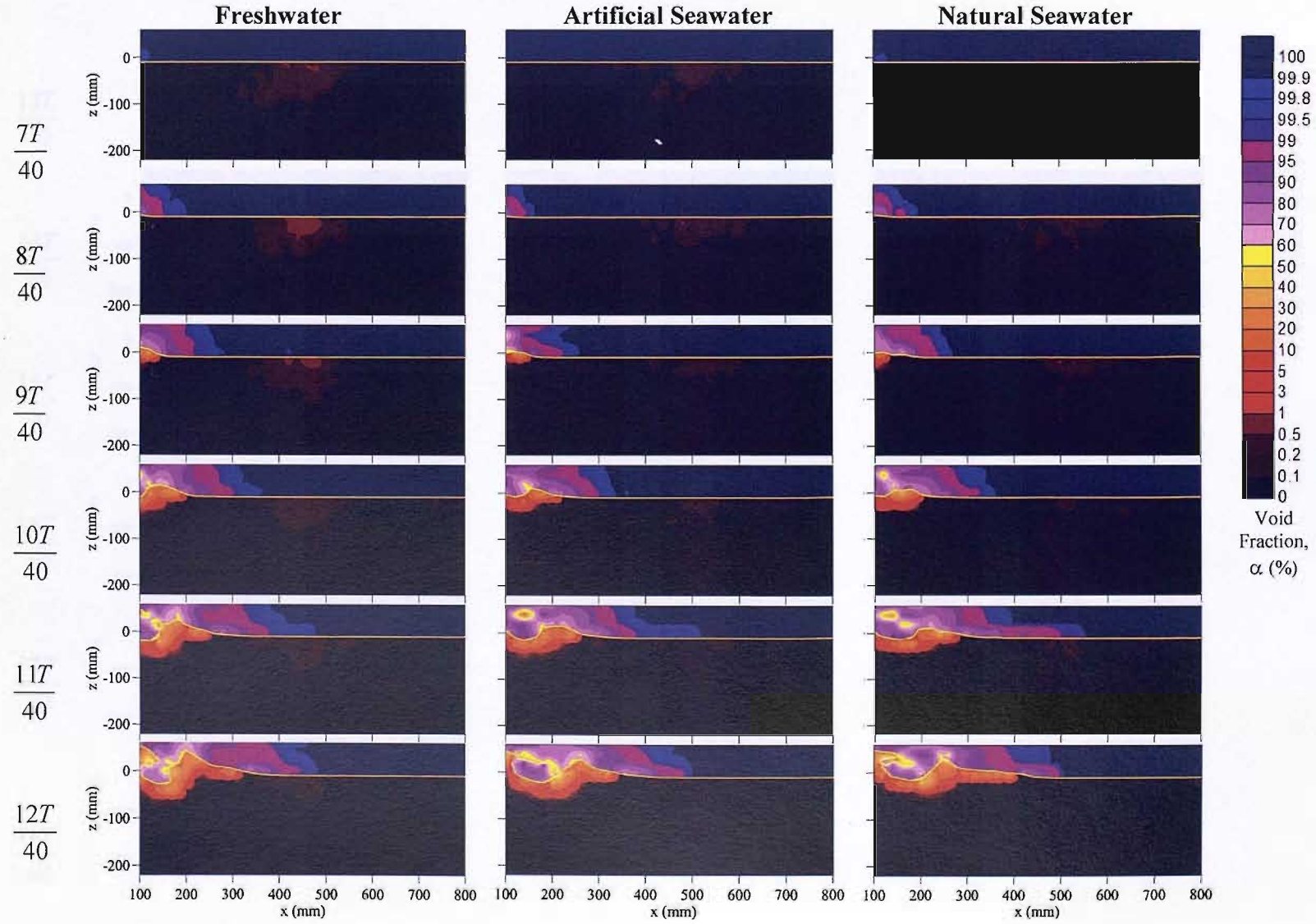

Figure C.1 (continued).

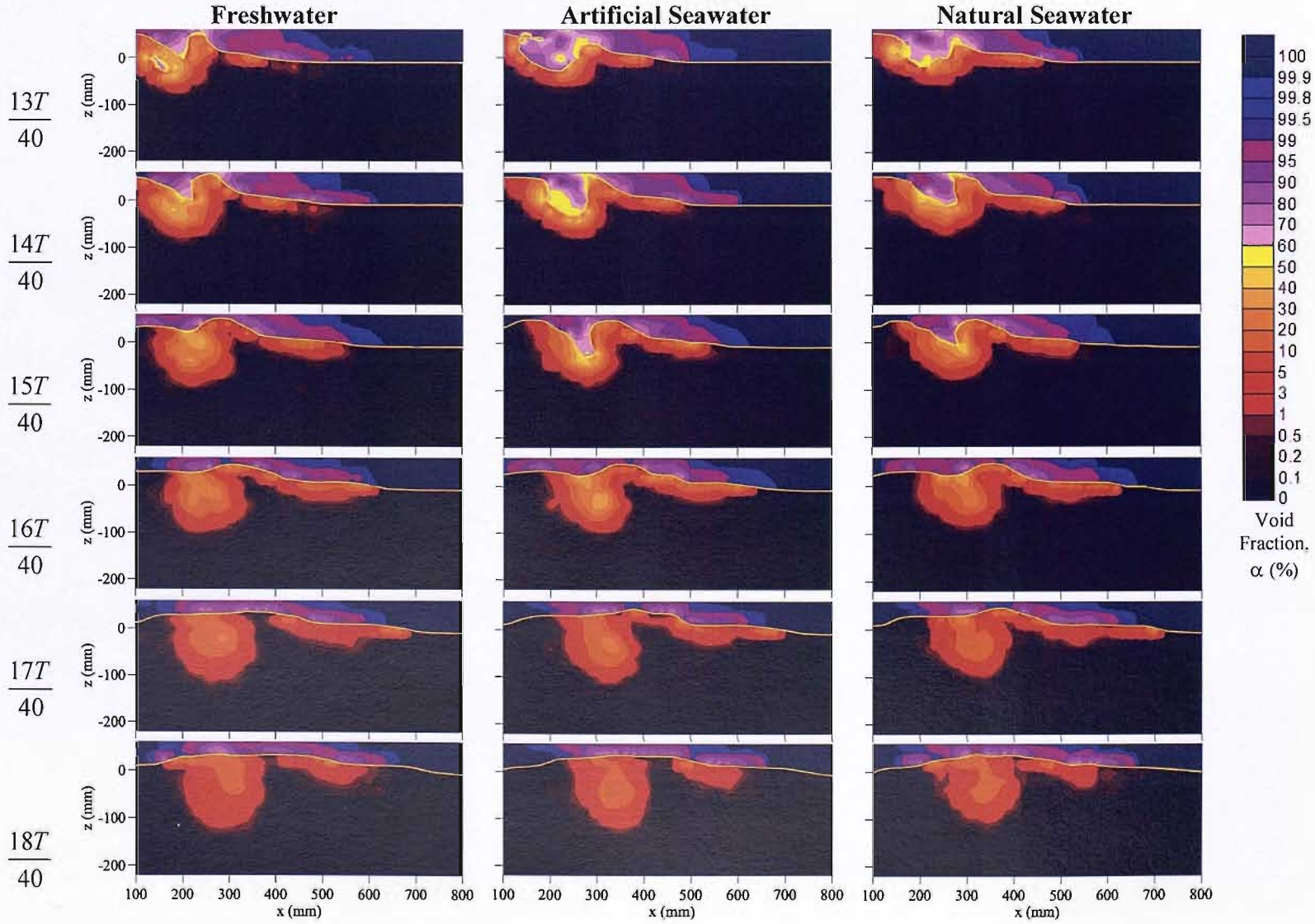

Figure C.1 (continued).

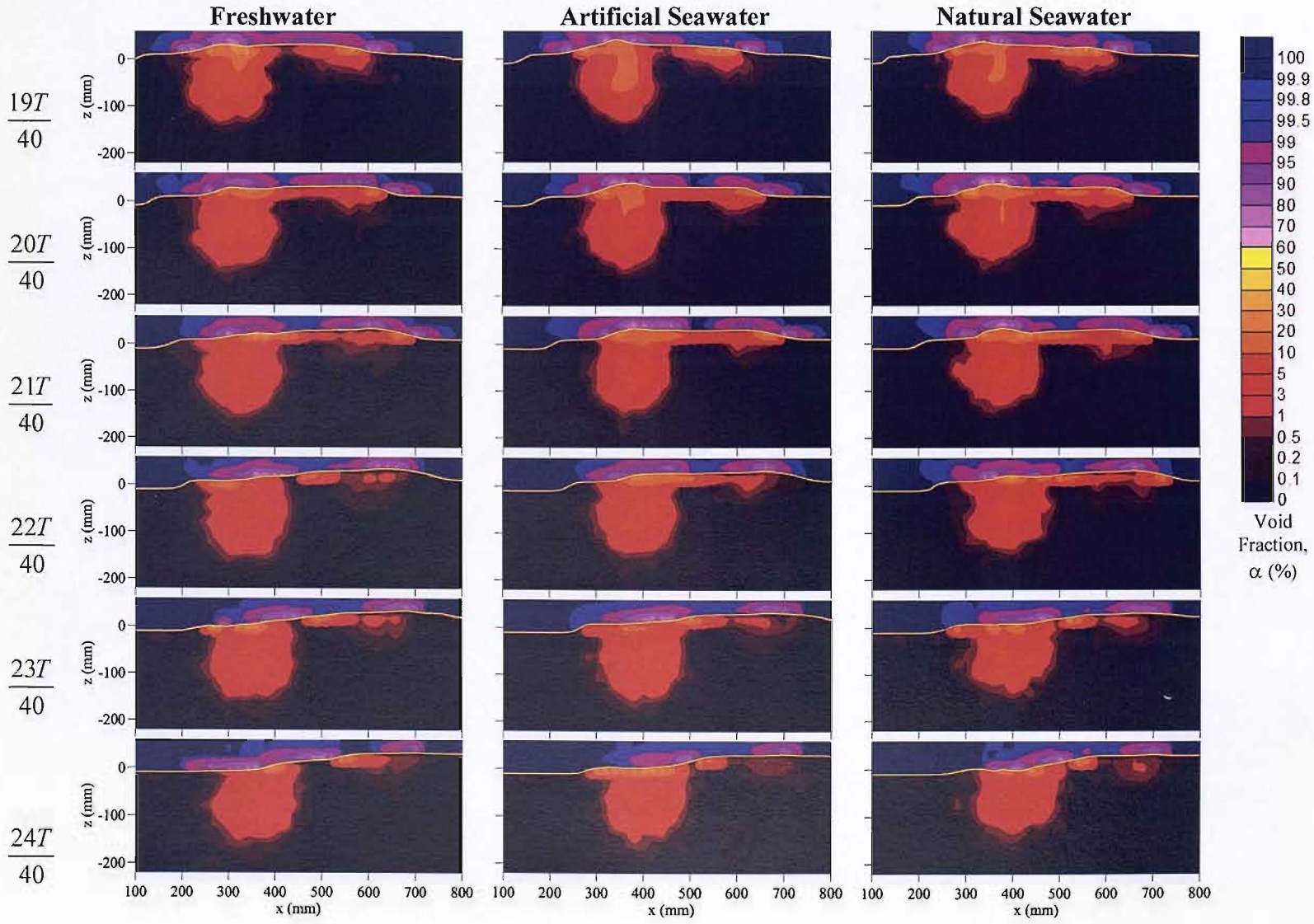

Figure C.1 (continued).

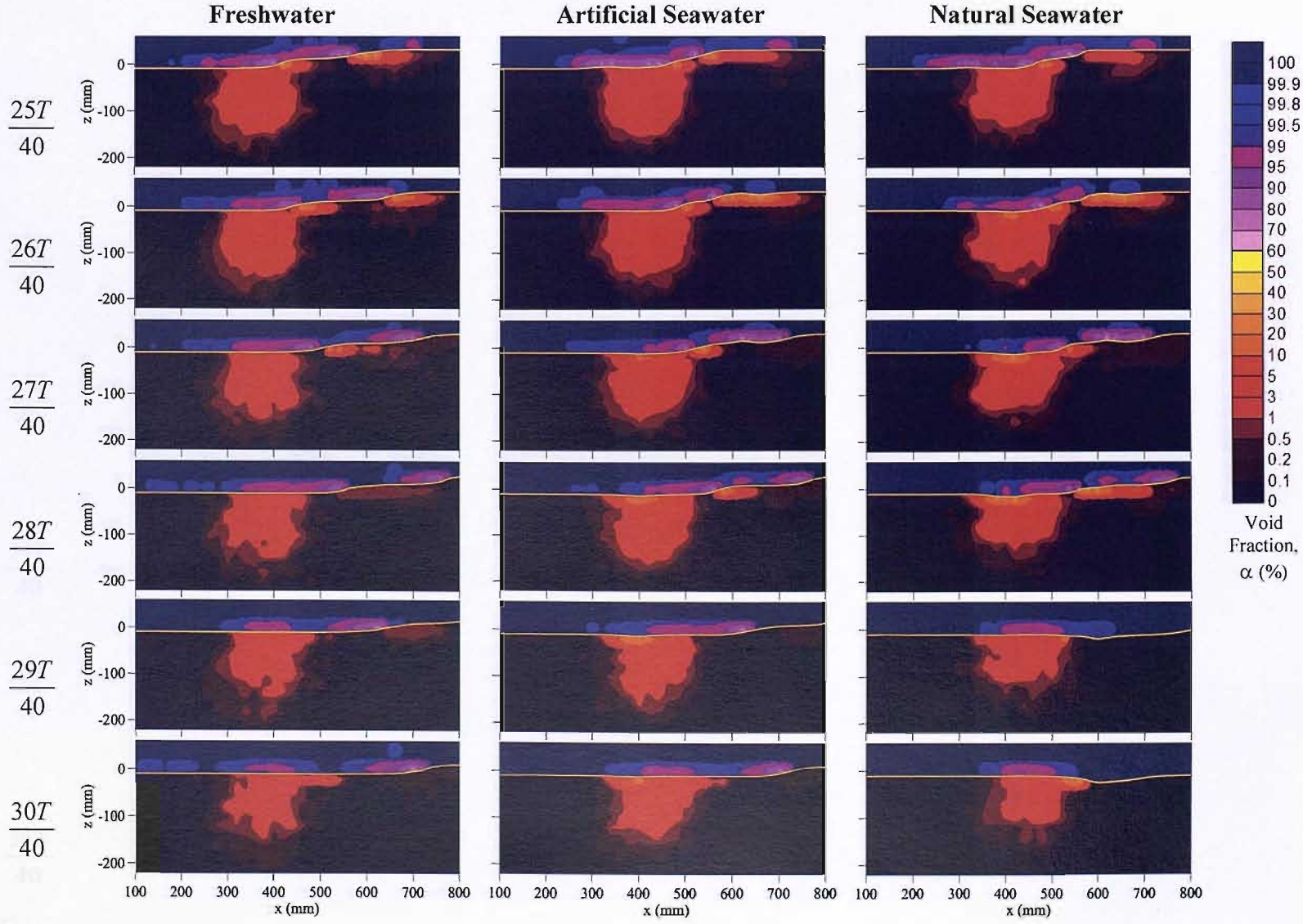

Figure C.1 (continued).

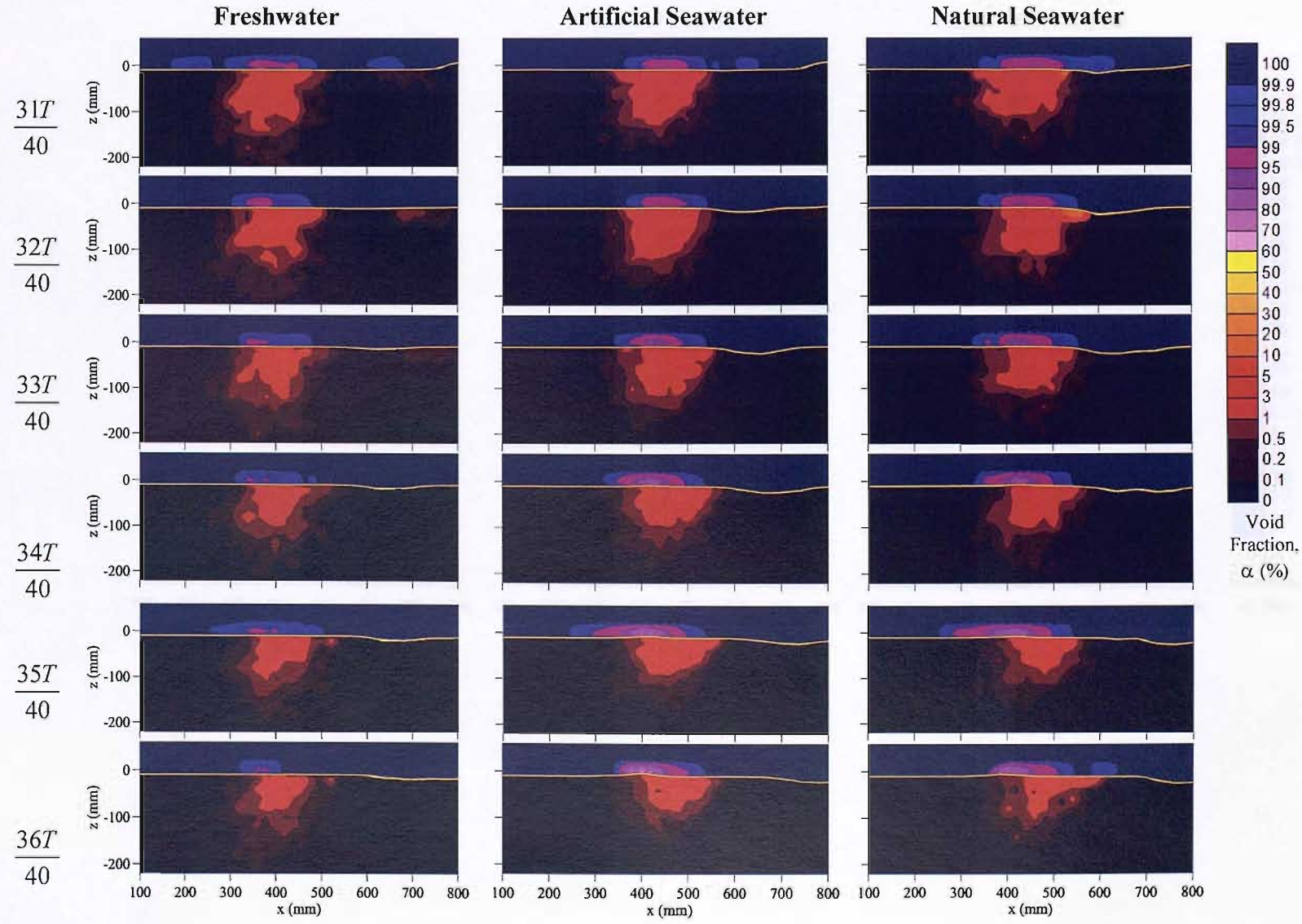

Figure C.1 (continued).

Figure C.1 (continued).